Development of Vascular Inspired Electrospun Hollow Fibre Membranes for use in 3D Tissue Culture



Risto John Martin

Lincoln College

Department of Engineering Science

University of Oxford

A thesis submitted for the degree of

Doctor of Philosophy

Michaelmas, 2022

Declaration of Originality

I, Risto Martin, hereby confirm that the work presented in this Thesis is my own. Where information has been derived from other sources, I confirm that this has been indicated in the Thesis. This work has not been submitted to another institution for any other degree or qualification.

To my mother, father, and sister.

Thank you.

Acknowledgements

It has been said that *"It takes a village to raise a child"*. Yet, I am sure that if you told many of those who helped me, that one day I would graduate from the University of Oxford with a DPhil, they would look at you sceptically. Yet, this thesis stands testament to the tireless efforts each made by those that have helped me on my way.

First and foremost, to my mother, father, and sister. Without your constant and unwavering support, none of this would be possible. I have always been able to trust that you have my back and that I can rely on your love and advice whenever I need it. Thank you.

It is fair to say my educational career has been anything but traditional. Without the support of many fantastic teachers, I do not know where I would be today. I would especially like to thank; Sally Davis, Rebecca Craig, Martin Scarratt, and Ms Hanzel. Each of you went above and beyond, helped inspire me, and ultimately helped me get to where I am today.

At each step throughout my university career, I have had the pleasure to attend a different institution, each remarkable in its own way, each teaching me its unique lessons, and I am incredibly grateful to have had the fortune to be a part of each one. To my undergraduate supervisor, Jesus Ojeda, thank you for nurturing my love of science and engineering, for teaching the fundamentals of academic rigour, and for inspiring me to pursue a career in research. To my Master's project supervisor, Sakis Mantalaris, thank you for giving me the opportunity to explore the wonders of tissue engineering. Your characteristic baptism of fire approach to presentation reviews has stood me in strength, such that every presentation or public speaking occasion now comes with ease. To my DPhil supervisors, Cathy, Pierre, and Sarah, I cannot thank you enough for all of your help and support over the last four years. I have truly enjoyed working with each of you. Your expert hand in allowing my curiosity to drift and explore new directions,

but knowing when to steer and apply pressure has left me a better researcher while allowing me to call this work my own.

In addition to my supervisors, I would like to thank those who have helped me with my work throughout my DPhil. Specifically, Jim Fisk and those at the IBME workshop. Not only did you fabricate some fantastic pieces of equipment, but you also provided many a laugh and some questionable advice on historical sites to visit. I would like to thank LIMA team, Kalin Dragnevski and Marzena Tkaczyk, for all your help with SEM over the years. Thanks to those at 3D life prints as well.

I am grateful to the University of Oxford and the Engineering and Physical Sciences Research Council (EPSRC) for the departmental scholarship which enabled me to pursue my research.

I am grateful to have had such wonderful friends throughout my DPhil. Hasan, thanks for all the mad adventures we have had over the last 11 years; while COVID and lockdown were awful, I think we made the best of it, and I look back at the fun we had with great fondness. You have been a fantastic friend, nurse, and confidant, wololo. Rand and Sahand, I greatly enjoyed our Sunday coffees at Peloton, and I look forward to all the sass you will serve in the future. Thank you to all those at LCBC; through you, I discovered my love for rowing, a passion I hope to keep with me for life. Jakob, thank you for all the fun on and off the water. And Ceren, thank you for all your support, for balancing me, all the fun, and love.

Risto

January 2023

Abstract

Long a mainstay in deciphering the mechanisms orchestrating cell behaviour in health and disease, now marred by insufficient cell-cell and cell-extracellular matrix interactions, the physiological relevance of two-dimensional tissue culture has been called into question. Modern three-dimensional tissue culture has been developed to mimic the cellular niche, yet these constructs remain limited to 200 μm in diameter or risk ischemic tissue damage. Utilising unconfined advective mass transfer perfusion bioreactors go some way in overcoming this size limitation. However, fluid shear forces in perfused media leave the cellular niche in these liable to disruption.

In vivo, blood vessels facilitate confined advective mass transfer, transporting dissolved gasses and nutrients throughout the body. Fulfilling this role *in vitro*, hollow fibre membranes (HFMs) have been used to support cell growth for, but not exclusively, erythroids, and endothelial cells (ECs). However, membranes used to date in these platforms are non-biodegradable, rigid, and monolithic, and, as such, are divorced in structure and nature from native tissues. In coronary artery bypass surgery, good procedural outcomes are associated with good morphological and mechanical similarities between the vessel transplanted and bypassed. To exhaustively mimic the physiological condition, HFMs used to support large three-dimensional tissue culture platforms should morphologically and mechanically mimic blood vessels of similar size.

From the meta-analysis of tissue engineered vascular grafts presented in this thesis, it was identified that electrospun polycaprolactone (PCL) and polydioxanone (PDO) conveyed mechanical properties akin to that of medium sized blood vessels. Additionally, it was noted that pyridine may be used as a controlled functional doping additive to modulate the properties of electrospun materials.

Given this state of affairs, it was hypothesised that HFMs may be fabricated continuously by

electrospinning in a reproducible way to mimic the morphological and mechanical properties of native medium-sized blood vessels while additionally facilitating nutrient exchange for tissue culture. Furthermore, these HFMs may be used as a substrate for biomedical research, potentially for the production of biomaterials intended for therapeutic application.

In answer to these hypotheses, this thesis presents a novel method for the continuous production of electrospun HFMs. Utilising this novel method PCL and PDO were solvent blended for the first time to produce defect free micro-fibre meshes, with a mass ratio of PCL/PDO of 0.43. Utilising this polymer blend, polymer concentration and pyridine were used to alter the micro-fibre diameter between 1.03 and 1.75 μm. These meshes were demonstrated to produce membranes which had porosities which ranged between 88-92 %. Permeability and particle rejection size were found to range between 1.21 - 1.89 $\times 10^{-14}$ m^2, and 5.8 - 4.8 μm, while tortuosity was found to decrease with pyridine concentration from 6.0 - 3.9. Consequently, cell ingress into the membrane layer is unlikely. Additionally, the blended PCL/PDO membranes were shown to be non-cytotoxic irrespective of pyridine concentration as determined with NIH 3T3s in accordance with ISO 10993. Furthermore, the EHFMs produced were found to match more of the mechanical properties of a medium sized blood vessel than any of the tissue engineered vascular grafts considered in the meta-analysis in presented this thesis.

Ensuring quality by design, mathematical modelling provides rationale when making experimental design decisions and thereby avoids the adoption of trial-and-error design evolution. Although all cell growth develops as a function of environmental conditions, ECs display a metabolic phenotype unlike most other cell types. Through a meta-analysis of data in the literature, a data-driven model of EC growth and behaviour was presented. EC growth in the prototype electrospun HFM bioreactor was thereby modelled by considering two-dimensional single-phase and porous media fluid flow with the Navier Stokes equations and Brinkman equations. Furthermore, we considered nutrient transport with an advection-diffusion-reaction model. Finally, we modelled EC growth with the data-driven model

previously presented. With this model, the influence of volumetric inlet flow rate and bioreactor outlet partial pressures on EC growth rate was evaluated. Of the conditions evaluated, the EC growth rate increased with the inlet media flow rate up to a maximum of 8.036E-6 s^{-1} at 7.5E-11 m^3/s, after which it began to decrease. However, an increase in the lumen to ECS outlet partial pressure was found to decrease the EC growth rate.

Finally, the fabrication of an electrospun HFM bioreactor was presented. HUVECs were cultured in the electrospun HFM lumen for 28 days under hydrostatic and hydrodynamic conditions. Irrespective of fluid flow conditions, by day 28 of the culture period, HUVECs were shown to have flattened, flow-aligned morphologies, reached confluency, and expressed VE-cadherin cell-cell interactions. In addition, μCT image analysis revealed that HUVEC density peaked within 5000 μm of the fibre inlet, after which it declined to a plateau, and that HUVEC growth was restricted to the lumen wall of the EHFM, with no cell ingress into the membrane wall.

It was concluded that in concert, our findings show that: electrospun HFMs may be continuously fabricated with morphological and mechanical properties akin to that of medium-sized blood vessels. The continuous production of these electrospun HFMs opens up the potential for scalable production of electrospun vascular grafts, which to date has otherwise been restricted to batch production of short sections which has otherwise in part inhibited their wide application. Additionally, electrospun HFMs could be used as a substrate for biomedical research. specifically, these membranes could potentially be incorporated into multi-modal mechanically dynamic bioreactors to facilitate membrane-bound advective mass transfer. This approach could minimize the risk of fluid shear stress disruption of the cellular niche and passive mechanical cues, thereby improving the physiological mimicry of platforms such as the humanoid bioreactor.

Dissemination

Peer-reviewed journal papers

R. Martin; H. Ye; S. Water; P. Mouthuy. *Morphological characterisation of electrospun hollow fibre membranes*. Journal of Membrane Science (Currently under review).

R. Martin; R. Lei; Y. Zeng; J. Zhu; H. Chang; H. Ye; Z. Cui. *Membrane Applications in Autologous Cell Therapy.* Membranes 2022, 12, 1182. https://doi.org/10.3390/membranes12121182

H. Ingram; **R. Martin**; J. Winterburn *Optimized cell growth and poly(3-hydroxybutyrate) synthesis from saponified spent coffee grounds oil*. Applied Microbiology and Biotechnology 106, 6033–6045 (2022). https://doi.org/10.1007/s00253-022-12093-9

Conference presentations and posters

R. Martin, P. Mouthuy; S. Water; H. Ye. *Physical and biological characterisation of mechanically and structurally mimetic small calibre vascular scaffolds.* 6th world congress of the Tissue Engineering and Regenerative Medicine International Society (TERMIS), Maastricht, The Netherlands, May 2021.

Contents

List of Figures **17**

List of Tables **26**

List of Abbreviations **28**

1 Introduction **30**

1.1 Thesis goals and overview 31

1.2 Thesis Structure 33

2 Literature review **34**

2.1 Two-dimensional *in vitro* culture 35

2.2 Hydrostatic bottom-up approach to 3D *in vitro* tissue culture 35

2.3 Hydrostatic top-down approach to 3D *in vitro* tissue culture 36

2.3.1 Solvent casting and salt leaching 36

2.3.2 Phase separation and freeze drying 37

2.3.3 Gas foaming 37

2.3.4 Self-assembly 37

2.3.5 3D printing 38

2.3.6 Electrospinning 38

2.4 Mechanical stimulation in bioreactors 40

2.5 The necessity of convective mass transfer 40

2.6 Membranes 41

2.7 Hydrodynamic membrane bioreactors 43

2.8 Lessons learnt from tissue engineered vasuclar grafts 44

2.9 Native Vasculature . . . 45
2.9.1 Structure . . . 45
2.9.1.1 The physiochemical landscape . . . 46
2.9.2 Cell signalling . . . 47
2.9.2.1 Metabolism . . . 48
2.9.3 Mechanical properties . . . 50
2.10 Tissue engineered vascular grafts . . . 52
2.10.1 Electrospun TEVG material selection . . . 53
2.10.1.1 Comparison of TEVG and native blood vessel mechanical properties 54
2.10.2 Postproduction functionalisation, topographic and physiochemical properties and of TEVGs . . . 56
2.10.3 Mathematical modelling of vascular graft remodelling . . . 57
2.10.3.1 Constituent properties . . . 58
2.10.3.2 Growth and repair . . . 58
2.11 Implications of the literature review . . . 59
2.12 Supplementary section . . . 62

3 Morphological and functional characterisation of vascular inspired electrospun hollow fibre membranes 66

3.1 Thesis integration and chapter structure . . . 66
3.2 Introduction . . . 68
3.3 Materials and methods . . . 69
3.3.1 Preparation of electrospinning solutions . . . 69
3.3.2 Design of EHFM collector . . . 70
3.3.3 Electrospinning . . . 70

3.3.4 EHFMs . . . 70
3.3.5 Electrospun flat sheet membranes . . . 72
3.3.6 Viscosity of the polymer solution . . . 72
3.3.7 Membrane recovery . . . 73
3.3.8 Scanning electron microscopy . . . 73
3.3.9 Micro-fibre diameter and orientation analysis . . . 73
3.3.10 Optical light microscopy . . . 73
3.3.11 Micro-computed tomography . . . 74
3.3.12 Porosity . . . 74
3.3.12.1 Mercury porosimetry . . . 74
3.3.12.2 EHFM μCT image analysis . . . 75
3.3.12.3 Gravimetric porosimetry . . . 76
3.3.13 Electrospun flat sheet membrane thickness . . . 76
3.3.14 Mechanical Properties . . . 77
3.3.15 Tortuosity . . . 77
3.3.16 Permeability . . . 79
3.3.17 Particle rejection . . . 80
3.3.18 Maintenance of BALB/c 3T3 cells . . . 81
3.3.19 NRU cytotoxicity assay . . . 81
3.3.20 Data and statistical analysis . . . 81
3.4 Results and Discussion . . . 82
3.4.1 Spinnability of polymer solutions . . . 82
3.4.1.1 Effect of mass ratio . . . 82
3.4.1.2 Effect of total polymer mass . . . 83
3.4.2 Electrospun hollow fibre membrane micro-topology . . . 83

3.4.2.1 Effect of total polymer mass 83
3.4.2.2 Effect of pyridine concentration 85
3.4.3 Electrospun hollow fibre membrane geometry and wall thickness 85
3.4.4 Porosity 87
3.4.5 Mechanical Properties 88
3.4.6 Tortuosity 91
3.4.7 Permeability 92
3.4.8 Particle rejection 93
3.4.9 Biocompatibility 94
3.5 Conclusion 95
3.6 Appendix 96
3.7 Supplementary section 96

4 Endothelial cell growth in an electrospun hollow fibre membrane bioreactor: A mathematical perspective 101

4.1 Introduction 103
4.2 Model description 106
4.3 Governing equations 109
4.3.1 Fluid model 109
4.3.1.1 Lumen and ECS 109
4.3.1.2 Membrane and cell layer 110
4.3.2 Transport model 111
4.3.3 Cell growth model 113
4.3.4 Boundary conditions 116
4.3.5 Initial conditions and parameter selection 119

4.4 Results and Discussion . . . 120
4.4.1 The role of inlet flow rate . . . 120
4.4.2 The role of EHFM bioreactor outlet partial pressures . . . 122
4.5 Model validation . . . 124
4.6 Conclusion . . . 126
4.7 Supplementary section . . . 128
4.7.1 Development of Endothelial Cell Growth Model . . . 128
4.7.1.1 Model development method . . . 128
4.7.1.2 Sub model selection . . . 130
4.7.1.2.1 Endothelial cell metabolism . . . 130
4.7.1.2.2 Endothelial cell signalling . . . 136
4.7.1.3 Endothelial cell growth model formulation . . . 139
4.7.2 Endothelial cell growth model formulation . . . 139
4.7.3 Dissolved gas concentration calculations . . . 139
4.7.4 Parameter values . . . 141
4.7.5 Cell culture dynamics profiles . . . 143

5 Prototyping of an electrospun hollow fibre membrane bioreactor 146

5.1 Materials and methods . . . 149
5.1.1 Preparation of electrospinning solutions . . . 149
5.1.2 Electrospinning . . . 150
5.1.2.1 EHFMs . . . 150
5.1.2.2 Electrospun flat sheet membranes . . . 150
5.1.3 Membrane pre-hydration testing . . . 151
5.1.4 Bioreactor Fabrication . . . 151

5.1.4.1 Fabrication of 3D printed parts 151
5.1.4.2 Bioreactor Assembly 152
5.1.5 Cell preparation and cell culture 153
5.1.5.1 Static scaffold culture 153
5.1.5.2 Bioreactor Operation 154
5.1.6 PrestoBlue cell viability assay 156
5.1.7 Scanning electron microscopy 156
5.1.8 Fixed confocal microscopy 157
5.1.9 Micro-computed tomography 158
5.1.10 Micro-computed tomography image analysis 158
5.1.10.1 Electrospun hollow fibre membrane morphology 158
5.1.10.2 Cell distribution 160
5.1.11 Metabolite analysis 161
5.1.11.1 GlucoRx X6 161
5.1.11.2 Abbot ARCHITECT 161
5.1.12 Statistical analysis and reproducibility 162
5.2 Results and Discussion 162
5.2.1 Membrane morphology 162
5.2.2 Static HUVEC culture 163
5.2.2.1 Hydro-static culture of HUVECs on electrospun flat sheet membranes 163
5.2.2.2 Hydro-static culture of HUVECs in EHFMs 165
5.2.2.3 Confocal microscopy imaging of HUVEC growth under hydro-static conditions 166
5.2.3 Culture of HUVECs under hydro-dynamic conditions in an EHFM bioreactor . 167
5.2.3.1 Cell distribution 170

5.2.3.2 Metabolic profiles 172

5.3 Conclusion 174

5.4 Appendix 176

5.5 Supplementary section 176

6 Conclusions, and future directions **181**

6.1 Limitations 185

6.2 Future directions 186

References **188**

List of Figures

Figure 2.1 Bottom-up vs. top-down approaches in tissue engineering, reprinted from [1]. 36

Figure 2.2 Schematic of (a) inception of instability and jet formation (b) basic electrospinning setup, reprinted from [2]. 39

Figure 2.3 Classification of membranes by materials, structures, and configuration, reprinted from:[3]. 42

Figure 2.4 Membrane process designation by solute and pore size, reprinted from:[3]. . . 42

Figure 2.5 Schematic and histology of a human muscular artery, adapted from [4]. 46

Figure 2.6 Pressure-diameter relationship of a viscoelastic artery showing the binary low and high pressure elastic moduli and the development of a hysteresis loop [5]. 51

Figure 2.7 Bar chart showing the number of electrospun tissue engineering vascular graft mechanical properties that were within the range of the corresponding property of the profile defined for healthy native medium-sized blood vessels, as given in table 2.1, labelled with the polymer, micro-fibre diameter, reference table 2.2 row number, and coloured according to micro-fibre alignment and polymer nature as given by the key. 55

Figure 3.1 (A) Schematic of EHFM collector with pictures of parts as fabricated, and (B) Screen capture of EHFM collector software control panel. 71

Figure 3.2 SEM micrographs of EHFMs produced from a blended polymer PCL/PDO solution with a mass ratio of 0.43 and; (A) a total polymer concentration of 7.05, 9.25, 12.33, 15.86, and 19.38 %, respectively, and doped with 5 ppm pyridine. (B) a total polymer concentration of 9.25 % and doped with 1, 5, 10, 25, and 50 ppm pyridine. . 84

Figure 3.3 EHFM micro-fibre diameter distributions determined from the analysis of SEM images captured at x3000 (n=3) produced with a blended polymer PCL/PDO solution with a mass ratio of 0.43 and a total polymer concentration (A) ranging between 7.05 and 19.38 % doped with 5 ppm pyridine, and (B) of 15.85 % doped 1, 5, 10, 25, and 50 ppm pyridine. Median wall thickness of PCL/PDO EHFMs (n=3) produced with a polymer solutions containing a total polymer concentration; (C) ranging between 7.05 and 19.38 % and doped with 5 ppm of pyridine; (D) of 15.85 % and doped with 0,1, 5, 10, 25, and 50 ppm pyridine as determined through the analysis of EHFM cross sectional images captured with μCT. 84

Figure 3.4 µCT images illustrating the cross sectional morphology of EHFMs produced from a blended PCL/PDO polymer solution with a mass ratio of 0.43 and; (A) a total polymer concentration of 7.05, 9.25, 12.33, 15.86, and 19.38 % doped with 5 ppm pyridine, and (B) a total polymer concentration of 9.25 % doped with 1, 5, 10, 25, and 50 ppm pyridine, respectively. 86

Figure 3.5 Porosity of EHFMs (n≥3) produced from a blended PCL/PDO polymer solution with a mass ratio of 0.43 and a total polymer concentration of 15.85 % and doped with 0 - 50 ppm pyridine as measured with (orange) mercury porosimetry, (green) gravimetric analysis, and (blue) µCT image analysis. 87

Figure 3.6 Stress-strain profiles of EHFMs (n=3) produced from a blended PCL/PDO polymer solution with a mass ratio of 0.43 and a total polymer concentration (A) ranging from 7.05 - 19.38 % and doped with 5 ppm pyridine, and (B) of 15.85 % and doped with 1 - 50 ppm pyridine. 89

Figure 3.7 Tortuosity of electrospun flat sheet membranes (n=3) produced from a blended PCL/PDO polymer solution with a mass ratio of 0.43 and a total polymer concentration 15.86 % and doped with 1- 50 ppm pyridine. 92

Figure 3.8 Permeability of electrospun flat sheet membranes (n≥3) produced from a blended PCL/PDO polymer solution with a mass ratio of 0.43 and a total polymer concentration 15.86 % and doped with 1- 50 ppm pyridine. 93

Figure 3.9 Particle cut size off size of electrospun flat sheet membranes (n=9) produced from a blended PCL/PDO polymer solution with a mass ratio of 0.43 and a total polymer concentration 15.86 % and doped with 1- 50 ppm pyridine. 94

Figure 3.10 Cytotoxicity of EHFMs (n=3) produced from a blended PCL/PDO polymer solution with a mass ratio of 0.43 and a total polymer concentration 15.86 % and doped with 1- 50 ppm pyridine as determined by the NRU test. N represents undiluted extract. N/2, N/4, and N/8 represent 2-fold, 4-fold, and 8-fold dilutions of N, respectively. SLS (sodium dodecyl sulphate) represent positive control group; PEC (polyethylene caps) represents negative control group. 95

Figure S3.1 Assembled diffusion cell with electrospun flat sheet membrane sandwiched between two chambers fitted with Rushton turbine impellers. Each chamber has ports on the side to allow water to flow through the jacketed layer to maintain a constant temperature. Atop each chamber there are two sampling ports to facilitate the initial filling of the cell and subsequent circulation of the working fluid to sensors to enable the monitoring of glucose concentration. 97

Figure S3.2 Polar plots of the change in PCL/PDO EHFM micro-fibre orientation (n=3) produced with blended PCL/PDO polymer solution with a mass ratio of 0.43 and (A) a total polymer concentration ranging between 7.05 and 15.85 % doped with 5 ppm pyridine, or (B) a total polymer concentration of 15.86 % and doped with 0, 1, 5, 10, 25, and 50 ppm pyridine. 97

Figure S3.3 Change in aspect ratio of PCL/PDO EHFMs (n=3) produced with; (A) a polymer solutions containing a total polymer concentration ranging between 7.05 and 19.38 % and doped with 5 ppm of pyridine; (B) a polymer solution containing a 15.85 % total polymer concentration and with 0,1, 5, 10, 25, and 50 ppm of pyridine as determined through the analysis of EHFM cross sectional images captured with μCT. 98

Figure S3.4 Electrospun flat sheet membrane micro-fibre diameter distributions determined from the analysis of SEM images captured at x3000 (n=3) produced with a blended polymer PCL/PDO solution with a mass ratio of 0.43 and a 15.85 % total polymer concentration doped with 0,1, 5, 10, 25, and 50 ppm pyridine. 98

Figure S3.5 Wall thickness of blended PCL/PDO electrospun flat sheet membranes (n=3), produced with a blended polymer PCL/PDO solution with a mass ratio of 0.43 and a 15.85 % total polymer concentration doped with 0,1, 5, 10, 25, and 50 ppm pyridine, as determined through the analysis of cross sectional images captured with μCT. 99

Figure 4.1 Schematic of the data-driven phenomenological model of endothelial cell growth sensitive to environmental, cell signalling, and mechanical stimuli. 106

Figure 4.2 Block flow diagram of the reactor configuration showing the flow paths of each media stream. 107

Figure 4.3 A 3D schematic representation of an electrospun hollow fibre bioreactor with the membrane and cell layer highlighted in the grey and dotted layers. The radii of the cell layer, lumen, membrane and ECS are demarcated as r_c, r_l,r_m and r_e, respectively. . 107

Figure 4.4 A schematic representation of an axisymmetric cross section of an EHFM bioreactor with the membrane and cell layer highlighted in the grey and dotted layers. The radii of the cell layer, lumen, membrane and ECS are r_c, r_l, r_m, and r_e, respectively. Similarly, the inlet media flow rate, lumen and ECS outlet pressures are labeled as $Q_{l,0}$, $P_{l,L}$, and $P_{e,L}$. 108

Figure 4.5 Variation in the endothelial cell growth rate with inlet media flow rate 121

Figure 4.6 Variation in EC growth rate with the change in the proportion of ECS:lumen outlet partial pressure pressures. 123

Figure 4.7 The change in simulated EC density as predicted by the full model (green) and reduced model (orange) compared to experimentally measured values taken from [6], as shown as blue points. 125

Figure S4.1 (A) Endothelial cell specific glucose uptake rate in response to glucose concentration and (B) Cell specific growth rate as a function of glucose concentration, with associated models, and experimental data from the literature are shown as blue points. 132

Figure S4.2 (A) Endothelial cell specific glutamine uptake rate in response to glutamine concentration and (B) Cell specific growth rate as a function of glutamine concentration, with associated models, and experimental data from the literature are shown as blue points. 133

Figure S4.3 Endothelial cell ammonia dose dependent change in cell specific growth rate with associated models and experimental data from the literature shown as blue points. 134

Figure S4.4 (A) Endothelial cell specific oxygen uptake rate in response to oxygen concentration and (B) Cell specific growth rate as a function of oxygen concentration, with associated models, and experimental data from the literature are shown as blue points. 135

Figure S4.5 Endothelial cell specific VEGF release rate in response to lactate concentration and (B) Cell specific growth rate as a function of VEGF concentration, with associated models, and experimental data from the literature are shown as blue points. 137

Figure S4.6 (A) Endothelial cell specific Lactate release rate in response to oxygen concentration and (B) Cell specific death rate as a function of shear stress, with associated models, and experimental data from the literature are shown as blue points. 138

Figure S4.7 (A-G) EC culture dynamic profiles showing the influence of inlet media flow rate on endothelial cell growth and the change in concentration of the species of interest in an electrospun hollow fibre bioreactor, with bars illustrating the range in EC number and concentration in the cell layer. in which the colours shown in the key correspond with the adjacent flow rate in m^3/s. (H) The change in liquid shear stress in the cell layer with inlet flow rate. 143

Figure S4.8 (A-G) Culture dynamics profiles showing the influence of the bioreactor ECS and lumen outlet partial pressure differential, δ, on endothelial cell growth and the change in concentration of the species of interest in an electrospun hollow fibre bioreactor, with bars illustrating the range in EC number and concentration in the cell layer. in which the colours shown in the key correspond with the adjacent δ value. (H) The change in liquid shear stress in the cell layer with inlet flow rate. 144

Figure 5.1 A schematic of the assembly of an electrospun hollow fibre membrane bioreactor. 152

Figure 5.2 (A) piping and instrumentation diagram of the electrospun hollow fibre membrane bioreactor configuration. 155

Figure 5.3 (A) Profile and (B) Side view SEM micrographs of EHFM. Quantified EHFM morphological characteristics, including the (C) median wall thickness, (D) elliptical major axis length, and (E) aspect ratio, as measured by μCT image analysis. 163

Figure 5.4 (A) Change in HUVEC viability as quantified by the change in PrestoBlue fluorescence relative to day 0 when cultured under hydro-static conditions on electrospun PCL/PDO flat sheet membranes doped with 25 ppm pyridine. (B) SEM micrographs of HUVECs cultured; on electrospun flat sheet membranes for (B) 6 hours, and (C) 2 days, in which scale bars are 60 μm. 164

Figure 5.5 (A) Change in HUVEC viability as quantified by the change in PrestoBlue fluorescence relative to day 0 when cultured under hydro-static conditions on EHFMs. SEM micrographs of HUVECs cultured on EHFMs for (B) 6 h, (C) 2, (D) 8, (E) 22, and (F) 28 days, in which the scale bar represents 200 μm. 165

Figure 5.6 Confocal microscopy micrographs of HUVECs cultured on EHFMs, for 6 hours - 28 days under static conditions, or within an EHFM bioreactor when designated with a BR, stained for nuclei (blue), F-actin (red), and VE-cadherin (green). 168

Figure 5.7 (A) EHFM mounted in bungs with open enclosure (B) Clamped EHFM bioreactor enclosure with epoxy. (C) EHFM bioreactor plumbed in the piping configuration in accordance with block flow diagram seen in figure 5.2. (D) Change in HUVEC viability as quantified with PrestoBlue fluorescence relative to day 0 when cultured under hydro-dynamic conditions in an EHFM bioreactor (n=3). SEM micrographs of HUVECs cultured in an EHFM bioreactor under hydro-dynamic conditions for 28 days, with a scale bar equivalent to (E) 100 μm, and (F) 600 μm. (G) Confocal micrograph of HUVECs cultured in an EHFM bioreactor under hydro-dynamic conditions for 28 days, stained for nuclei (blue), F-actin (red), and VE-cadherin, with scale bar equivalent to 500 μm. 169

Figure 5.8 (A) μCT image of EHFM bioreactor hollow fibre with HUVECs in lumen isolated through pipeline described in section 5.1.10.2 and seen in supplementary figure S5.7. (B) The radial and (C) longitudinal HUVEC distribution in an EHFM bioreactor as determined through μCT image analysis. 171

Figure 5.9 Change in (A) Glucose and (B) Lactate concentrations (n=3) in an EHFM bioreactor during the culture of HUVECs over a 28 day period, as measured with the GlucoRx meter (dashed line) and Architect system (solid line). 173

Figure S5.1 Change in HUVEC viability as quantified by the change in PrestoBlue fluorescence relative to day 0 when cultured under hydro-static conditions on (A) electrospun flat sheet membranes, and (B) electrospun hollow fibre membranes (n=3) produced with 0 (Blue), 1 (Green), 5 (Red), 10 (Cyan), 25 (Magenta), 50 (Black) ppm pyridine. 176

Figure S5.2 SEM micrographs of HUVECs cultured on electrospun flat sheet membranes for (A) 6 hours, (B) 2, (C) 4, (D) 6, (E) 8, and (F) 10 days, in which scale bars are 60 μm. 176

Figure S5.3 SEM micrographs of HUVECs cultured on EHFMs for 6 hours, and 2, 4, 6, 8, 10, 12, 14, 16, 18, 20, 22, 24, 26, and 28 days, in which scale bars are 100 μm. 177

Figure S5.4 SEM micrographs of; HUVECs cultured on electrospun flat sheet membranes for (A) 6 hours and 10 days, in which scale bars are 600 μm. HUVECs cultured on EHFMs under hydro-static conditions (C), and hydro-dynamic conditions (D), in which scale bars are 600 μm. Blank EHFMs treated with osmium staining as used in all SEM and μCT samples. 177

Figure S5.5 Central cuts of confocal microscopy micrographs of HUVECs cultured on EHFMs, for 6 hours - 28 days under static conditions, stained for nuclei (blue), F-actin (red), and VE-cadherin (green), in which the scale bar is equivalent to (A) 2 mm and (B) 250 μm. Uncut versions of the confocal micrographs for the full 28 day culture period may be seen in supplementary figure 5.6. 178

Figure S5.6 (A) Profile and (B) Side view SEM micrograph of single EHFM mounted into mounting bung and fixed with epoxy glue. (C) Profile Side view SEM micrograph of multiple EHFMs mounted into mounting bung and fixed with epoxy glue. 178

Figure S5.7 (A) Raw μCT image of EHFM bioreactor hollow fibre with HUVECs in the lumen. (B) Binary mask of μCT EHFM bioreactor fibre (C) Isolated μCT image of EHFM bioreactor hollow fibre with HUVECs in the lumen. (D) Thresholded image of μCT image of EHFM bioreactor hollow fibre showing regions which have pixel values significantly greater than that of a blank EHFM. (E) Centroid location of blobs in a single thresholded μCT EHFM image. (F) DBSCAN clusters of centroids along the entire EHFM bioreactor fibre, those highlighted in purple are considered outliers and removed as noise in final cluster distribution analyses. 179

List of Tables

Table 2.1 Range of characteristic mechanical properties of medium sized blood vessels. . 52

Table 2.2 Table of morphological and functional properties of tissue engineered vascular grafts reviewed in meta-analysis. 62

Table 3.1 Mass ratio of PCL and PDO evaluated and the resultant spinnability and presentation of fibre defects of the solutions spun 82

Table 3.2 Effect of total polymer mass on PCL/PDO polymer solution spinability and presentation of fibre defects 83

Table 3.3 Comparison of the mechanical properties of healthy medium sized human arteries with those of EHFM in which yellow, green, and red cell colours signify properties below, within, or above the range defined by that of the healthy medium sized human arteries. 90

Table 4.1 Table of bioreactor geometry taken as representative experimentally measured values from [7] 108

Table 4.2 Table of model dependent variables 109

Table 4.3 Table of EC reaction model parameter definitions 113

Table 4.4 Table of EC growth model parameter definitions 114

Table 4.5 Table of EC growth limitation, and inhibition parameter definitions 116

Table 4.6 Table of EC seeding density, membrane material property parameters, inlet concentrations and diffusivities for the species of interest 119

Table 4.7 Suite of substrate limitation and inhibition models evaluated to describe cell specific growth, protein expression, metabolite consumption, and waste metabolite excretion rates. 131

Table 4.8 Fitted model parameters for endothelial cell glucose dose dependent cell specific uptake and growth rate. 132
Table 4.9 Fitted model parameters for endothelial cell glutamine dose dependent cell specific uptake and growth rate. 134
Table 4.10 Fitted model parameters for endothelial cell ammonia dose dependent cell specific uptake and growth rate equation parameters. 135
Table 4.11 Fitted model parameters for endothelial cell oxygen dose dependent cell specific uptake and growth rate equation parameters. 136
Table 4.12 Fitted model parameters for endothelial cell VEGF dose dependent cell specific uptake and growth rate equation parameters. 137
Table 4.13 Fitted model parameters for endothelial cell oxygen dose dependent lactate production and shear stress dependent cell specific growth rate. 139
Table 4.14 Table of EC seeding density, membrane material property parameters, inlet concentrations and diffusivities for the species of interest 140
Table 4.15 Endothelial cell reaction model parameter values 141
Table 4.16 Endothelial cell growth model parameter values 142

List of Abbreviations

2D . . . . . Two-dimensional

3D . . . . . Three-dimensional

AA . . . . . Amino Acid

ADP . . . . . Adenosine diphosphate

ANG . . . . . Angiopoietin

ATP . . . . . Adenosine triphosphate

EC . . . . . Endothelial cells

ECM . . . . . Extra-cellular matrix

ECS . . . . . Extra capillary space

EHFM . . . . . Electrospun hollow fibre membrane

FGF . . . . . Fibroblast growth factor

G-6-P Glucose-6-phosphate

G-6-PDH . . . . . Glucose-6-phosphate dehydrogenase

G&R . . . . . Growth and repair

H2O2 . . . . . Hydrogen peroxide

HFM . . . . . Hollow fibre membrane

HK . . . . . Hexokinase

HUVEC . . . . . Human umbilical vein endothelial cells

KLF2 . . . . . Krüppel-like factor 2

NAD . . . . . Nicotinamide adenine dinucleotide

NADH . . . . . Nicotinamide adenine dinucleotide reduced

NRU . . . . . Neutral red uptake

PCL . . . . . Polycaprolactone

PDGF . . . . . Platelet derived growth factor

PDO . . . . . Polydioxanone

PEC . . . . . Polyethylene caps

RGD . . . . . Arginine-glycine-aspartic acid

SMC . . . . . Smooth muscle cell

TEVG . . . . . Tissue engineered vascular graft

VEGF . . . . . Vascular endothelial growth factor

WSS . . . . . Wall shear stress

Chapter 1

Introduction

Historically, two-dimensional (2D) tissue culture paved the way for the development of our understanding of the biochemical and mechanical mechanisms regulating cell function. However, the lack of physiological cell-cell and cell-ECM interactions in 2D models necessitates the development of new *in vitro* models [8, 9]. Modern static three-dimensional (3D) tissue culture scaffolds and mechanically actuated bioreactors better mimic the cellular micro-environment [10, 11]. However, the size of these scaffolds is limited by the short effective range of diffusive mass transfer. To supply sufficient nutrient and gas exchange in thick scaffolds, hollow fibre membranes (HFMs), as pseudo vasculature, have been used [12, 13]. However, the rigid and monolithic surface of HFMs prevents their use in actuated bioreactors and disrupts passive mechanical cues. To exhaustively mimic physiological conditions, HFMs should have characteristics similar to their closest physiological analogue, vasculature. Tissue engineered electrospun vascular grafts (TEVGs) have been developed to emulate the morphology and mechanical properties of native blood vessels for use in cardiac bypass surgery, yet they are not regularly used as HFMs to support tertiary cell growth in scaffolds. Furthermore, the mismatch of polymer degradation rates has led to graft calcification or concerns over rupture. Therefore, novel polymers and blends should be considered [14, 15].

1.1 Thesis goals and overview

Considering this current state of affairs, this thesis aims to answer the question: Can HFMs be fabricated continuously by electrospinning in a reproducible way to mimic the morphological and mechanical properties of native vasculature as well as facilitate nutrients exchange in static and dynamic culture conditions as a substrate for biomedical research?

To answer these questions, my specific objectives are, therefore:

1. Produce electrospun HFMs which mimic the morphology and mechanical properties of native vasculature through a continuous process in a reproducible and controllable manner.

- Continuous production of electrospun HFMs is key to preventing a bottleneck in the production of bioreactors incorporating their use. By matching the morphology and mechanical properties of the HFMs and native vasculature, physiological passive mechanical cues, disrupted with existing HFMs, may be preserved.

2. Characterise the transport properties of the membranes and how they may change under mechanical loading.

    - By characterising the transport properties of the electrospun HFMs produced, the suitability of the membranes for nutrient and signalling molecule delivery may be evaluated.

3. Develop a mathematical model to describe the transport across the membranes.

    - By decoupling the flow regimens between the shell and lumen of the HFMs, it is possible to adopt dynamic feeding regimens. By modelling nutrient and gas transfer as well as cell growth, optimal feed regimens may be developed.

4. Develop static and mechanically dynamic HF bioreactor geometrically informed from electrospun HF transport model.

    - By taking the number of HFMs and bioreactor configuration as additional degrees of freedom, the geometry of the bioreactor may be informed to provide optimal culture conditions.

5. Evaluate the use of the electrospun HFMs for tissue culture in (a) static and (b) mechanically dynamic HF bioreactor configurations.

    - The influence of maintaining passive mechanical cues, through the use of electrospun HFMs, may be evaluated by testing the bioreactor configurations developed under culture conditions and comparing them to existing HF bioreactor platforms.

1.2 Thesis Structure

Thus in this thesis, the relevant literature on tissue engineering scaffolding techniques, membranes, TEVGs, and mathematical modelling are reviewed in chapter 2. A description of the design and assembly of a novel electrospinning apparatus is then described in Chapter 3, along with the morphological and functional characterisation of continuously produced blended PCL/PDO electrospun hollow fibre membranes. A model to describe fluid flow, mass transport and endothelial cell growth is presented in chapter 4. The model presented is used to explore the effect of inlet media flow rate on endothelial cell growth rates. The assembly of an electrospun hollow fibre membrane bioreactor is presented in chapter 5. Using the inlet flow rate which yielded the highest theoretical human umbilical vein endothelial cell growth rate according to the model presented in chapter 4, the biocompatability of electrospun PCL/PDO is then evaluated under hydro-static and hydro-dynamic conditions. Finally, conclusions, limitations of these works and future perspectives are finally given in chapter 6.

Chapter 2

Literature review

Since its inception in 1885, tissue culture has developed into an indispensable tool in deciphering the biochemical and mechanical mechanisms by which cells form tissue and function in both health and disease [8, 9]. To study these mechanisms, various tissue culture platforms have been developed, including *in vitro* two-dimensional (2D) and three-dimensional (3D) static culture, perfusion, hollow fibre membrane (HFM) and mechanically dynamic bioreactors.

2.1 Two-dimensional *in vitro* culture

2D tissue culture, in which cells are cultured in suspension or as a monolayer in Petri dishes or tissue flasks, is currently the most frequently used tissue culture technique. The importance of cell-cell and cell-ECM interactions in the cellular micro-environment on tissue development and function has called the validity of 2D models into question [16].

Sandwich culture and micro-patterning techniques have subsequently been developed to maintain the simplicity of 2D culture techniques while maintaining cell morphology, and phenotype [8]. These platforms, however, still depend on non-physiological conditions and therefore do not provide a good model [17]. To more faithfully mimic the native structure of the tissue of interest and recreate the cellular micro-environment, bottom-up and top-down production techniques have been used to develop 3D tissue culture platforms [1].

2.2 Hydrostatic bottom-up approach to 3D *in vitro* tissue culture

By fabricating micro-scale tissue building blocks with specific architecture to be assembled into larger tissues, bottom-up production of physiologically sized tissues holds great promise [18]. Spheroids, cell sheeting, hydro-gels, biological prefabricated scaffolds and microfluidic organ on a chip, have all been used for the production of micro-scale tissues. Facilitating cell-cell and cell-ECM interactions, spheroids and organoids provide a significant improvement over 2D culture, while microfluidics and

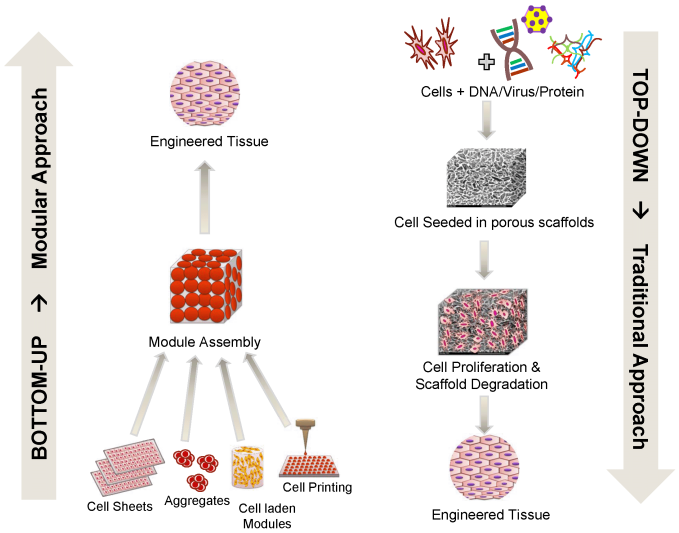


Figure 2.1. Bottom-up vs. top-down approaches in tissue engineering, reprinted from [1].

hydrogels are used to study cell-cell interactions in organ-like configurations and drug screening [8].

The ECM, formed from a range of extracellular biosynthetic products and signalling molecules excreted by adjacent cells, creates a complex organised 3D network of nanofibers and nanopores [19, 20]. Bottom-up scaffolds fail to mimic the fibre orientation and mechanical properties of the native ECM and therefore require further development. Top-down scaffold production may be used to more faithfully mimic these properties of native tissues.

2.3 Hydrostatic top-down approach to 3D *in vitro* tissue culture

Various top-down approaches capable of producing highly porous fibrous networks akin to that of native ECM have been developed. Methods developed include solvent casting, salt leaching, phase separation, freeze drying, gas foaming, self-assembly methods, 3D printing, and electrospinning.

2.3.1 Solvent casting and salt leaching

Highly porous scaffolds, with controlled pore size, may be produced by casting polymer solutions with suspended uniformly sized salt particles and subsequently removing the salt in a water bath [21]. PCL and thermally blended PCL and PDO were used to produce salt-leached scaffolds for the culture

of chondrocytes. However, these scaffolds were found to support fewer cell numbers than traditional tissue culture plates. This reduction in cell numbers was associated with the use of cytotoxic solvents and salts in the solvent casting and salt leaching process [22].

2.3.2 Phase separation and freeze drying

Thermal and non-solvent phase separation may be used to make foams and membranes. Heterogeneous pore distributions produced by non-solvents are usually unsuitable for tissue culture scaffolds but are widely used in the production of membranes [23]. Freeze drying and thermally induced phase separation, in contrast, produces a narrow controllable pore size distribution and has therefore been widely used to produce scaffolds from various polymers, including poly(L-lactic-co-glycolic acid), polyurethane, poly(methyl- methacrylate), poly(D, L-lactade), poly(caprolactone), and polystyrene [24]. While the low temperatures required for these techniques enables the incorporation of proteins, high cost and use of cytotoxic solvents limit their application [21].

2.3.3 Gas foaming

To forego the need for cytotoxic solvents, gas foaming, in which inert gases under high pressure are used to saturate polymers and create air bubbles, has been used to produce highly porous scaffolds. Limited interconnectivity of pores within these scaffolds inhibits cell infiltration, and therefore their use [25].

2.3.4 Self-assembly

Peptide filaments, formed by weak covalent and non-covalent bonds, act as cables that connect neighbouring cells and provide mechanical support, thereby creating a 3D network *in vivo*. Attempts to recreate these *ex vivo* have, however, so far only yielded high cost mechanically weak scaffolds that are susceptible to fragmentation [18].

2.3.5 3D printing

The production of scaffolds directly from computer aided design models may be achieved by 3D printing. 3D printing techniques developed include stereolithography, selective laser sintering, fused deposition modelling, 3D inkjet and extrusion printing. Through the chemical bonding of monomers, sintering or melting of polymers, these techniques can produce scaffolds with complex spatial geometries to recreate the cellular micro-environment within large scaffolds. The inability of these methods to produce scaffolds which mimic the structure of the ECM, however, currently limits their use [21].

2.3.6 Electrospinning

Dating back to the 1600s, electrospinning enables the drawing of micro-nano scale fibres from a polymer rich solution by overcoming the surface tension of the viscoelastic liquid through the manipulation of surface charge electrostatic repulsive coulombic forces [26, 27, 28, 29].

Electrospinning requires four general components namely: a high-voltage power supply, a syringe pump, a spinneret and a collector, as seen in figure 2.2. Scaffolds are produced by initially dissolving a polymer in an appropriate solvent. The solution is pumped through a capillary to a nozzle at which a droplet is maintained through surface tension. The application of a high voltage creates a balance between coulombic surface repulsive electrostatic force, surface tension, and the attractive electrostatic force between the droplet and the collector [30]. By increasing the voltage, the strength of the electrostatic field is increased, causing the droplet to destabilise, eventually resulting in the formation of a Taylor cone [31]. Once the electrostatic field is strong enough, a jet of polymer solution erupts from the Taylor cone, in which instabilities created by the balance between electrostatic repulsion and Rayleigh surface tension results in a "whipping" motion [32]. This whipping stretches and thins the jet, from which the solvent evaporates to form micro-nano scale fibres. These fibres are then collected on the earthed collector for subsequent use [33, 28]. As a result of solvent evaporation required for micro-fibre

production during electrospinning, electrospun scaffolds are inherently less prone to contamination with residual solvent compared to other top-down scaffold production techniques such as solvent casting.

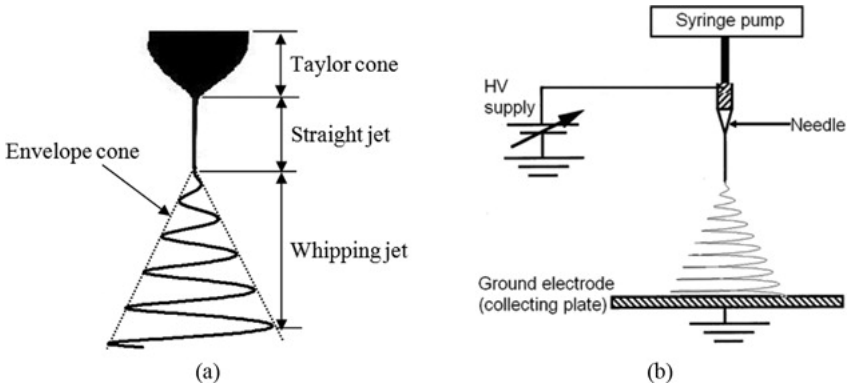


Figure 2.2. Schematic of (a) inception of instability and jet formation (b) basic electrospinning setup, reprinted from [2].

Micro-fibre morphology may be manipulated through the intrinsic properties of the solution, and ambient conditions such as conductivity, viscosity, the surface tension of the solution, temperature, humidity, and atmospheric pressure [34, 33, 35, 36, 30, 32].

The morphology of electrospun meshes is determined by the collector used. Static collectors may only be used to produce unaligned discontinuous meshes, while dynamic collectors may produce continuous sections with aligned fibres [37, 2, 29].

While 3D scaffolds produced by bottom-up or top-down techniques facilitate the mimicry of cell-cell and cell-ECM interactions, they are predominantly used under static conditions. Tissue specific adaptation to mechanical stresses *in vivo* and remodelling following disruption demonstrates the regulatory role of mechanical stimulation on tissue function. To deconvolve and harness the interplay of biochemical and mechanical regulatory cues, it is, therefore, necessary to study tissues under dynamic conditions [38].

2.4 Mechanical stimulation in bioreactors

Mechanical cues may be subdivided into passive and active. Passive cues originate from the active sensing of the environment in which cells are resident, while active cues directly impose mechanical stimulation onto the cell. Passive cues may be mimicked in static 3D tissue culture platforms by matching mechanical hardness, micro-fibre alignment, and porosity. Active cues may only be reproduced by dynamic systems, hydrostatic pressure, fluid shear stress, compression, and stretching [39, 38].

To date, spinner flasks, rotating wall, compression, and perfusion reactors have provided insight into the role of mechanical cues in the regulation of chondrocytes [40], osteocytes [41], and vascular tissue [39]. Although combinations of forces have been evaluated [42], these systems fail to accurately mimic physiological tissue specific multi-directional forces. Recent developments in humanoid bioreactor technologies may now create a platform on which physiological mechanical forces can be recreated. The combining of these humanoid robots with a flexible bioreactor system, therefore, presents the opportunity to develop a platform which would capture physiological mechanical complexity [10, 11].

2.5 The necessity of convective mass transfer

3D tissue culture techniques and mechanically dynamic bioreactors collectively facilitate the deciphering of mechanical and biochemical cues on tissue function [40]. To ensure good cell viability, it is important to maintain adequate oxygen and nutrient concentrations. In 3D tissue culture scaffolds, mass transport occurs solely through diffusion, since they lack native vasculature. The potential flux of dissolved species depends in part on the tortuosity and structure of the scaffold. Hydrogel scaffolds tend to have low tortuosity and therefore tend to have relatively good diffusive mass transport characteristics. However, even in hydrogel scaffolds, cell growth is limited to a depth of only 200 μm from a fresh media supply, due to the rate at which cells consume oxygen and nutrients [43, 12]. Moulded and 3D printed channels within hydrogel scaffolds have been used to facilitate advective mass transfer to

support localised cells survival in complex geometries [44, 45, 46]. However, the lack of selectivity of hydrogel fluid-solid interface inhibits the use of dynamic feed regimens necessitating the incorporation of a selective layer such as a membrane.

2.6 Membranes

Membranes, defined as "a region of discontinuity interposed between two phases" [47], have many beneficial properties for tissue culture, including low energy consumption for separation, high surface area to volume ratio, tuneable pore size, and ease of preparation [48, 49].

Synthetic membranes are principally segregated by the nature of the material from which they are constructed, as organic or inorganic. While membranes used are predominantly organic, the inability to use organic membranes in harsh operating conditions sometimes necessitates the use of more expensive inorganic membranes [48, 50].

The rate of flux through a membrane, as described by Fick's law, is dependent on the thickness of the separating layer. Consequently, a cross-sectional structure is also used for classification as either symmetric (isotropic), in which the cross-sectional structure is constant, or asymmetric (anisotropic), which typically consists of a thin selective surface layer and a thicker non-selective support layer. Furthermore, the structure of the selective layer may be used to classify membranes. While the majority of membranes are porous and achieve separation through sieving, other common selective layer structures include homogeneous dense layers, ion exchange, liquid, and fixed carriers [50]. A schematic of the classification of membranes may be seen in figure 2.3.

The separation achieved through porous membranes by sieving is determined by pore size by which they are commonly classified by [3, 50]. Porous membranes may be classified as porous, mesoporous, microporous and non-porous, or alternatively as micro (MF), ultra (UF) and nano (NF) filtration media

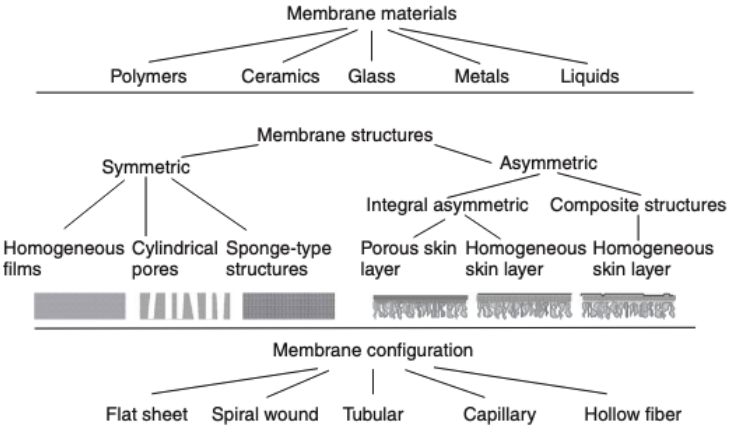


Figure 2.3. Classification of membranes by materials, structures, and configuration, reprinted from:[3].

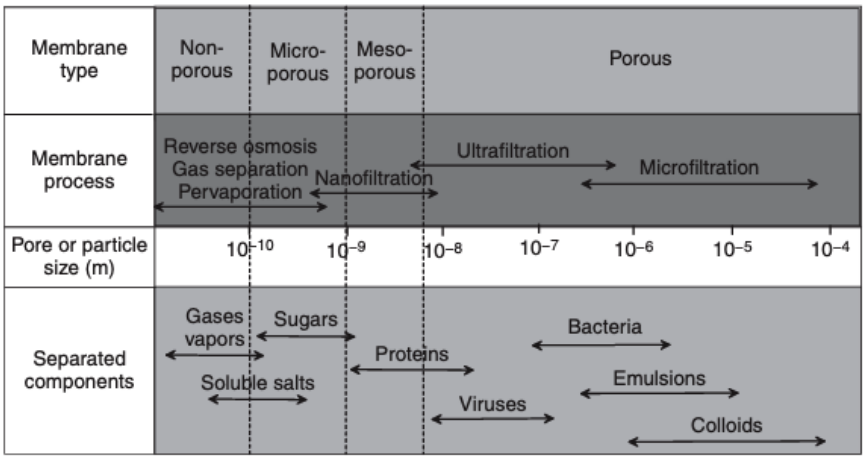


Figure 2.4. Membrane process designation by solute and pore size, reprinted from:[3].

and reverse osmosis (RO) membranes [3, 23]. The designation of membrane types according to pore size may be seen in figure 2.4.

The wide range of synthetic membranes developed that are capable of low temperature *in situ* separations, around 37 °C, provides a highly attractive platform for bioprocessing separation applications, owing to their ability to facilitate low-cost separations without the risk of damaging biological materials, which may otherwise occur at temperatures above 37 °C. Consequently, membranes have been used to develop various cell culture and tissue culture platforms [51].

2.7 Hydrodynamic membrane bioreactors

Through membrane compartmentalisation or immobilisation, bioactive substances may be conserved and protected from fluid shear stress to enable their use over an extended period [52]. In tissue culture, the compartmentalisation and selectivity facilitated by membranes enable the use of convective mass transfer to supply nutrients without disrupting the cellular micro-environment. Due to their inherently high surface area to volume ratio, HFMs are most frequently used [53].

Porous organic and inorganic HFMs have been used in bioreactor configurations as pseudo vasculature, decoupling lumen and shell fluid side shear stresses to enable dynamic alterations in culture feed regimens.

Mathematical models have been developed incorporating the mass transfer characteristics of the membranes used, module configuration and cell growth kinetics to optimise culture conditions [54, 55, 56, 57, 58].

Clinical cell therapies require high numbers of cells, ranging between $10^5 - 10^{13}$ cells, of highly controlled populations, [57]. Owing to their high surface area, the potential use of pulsatile flow and optimised feed regimens means that, compared to 2D culture techniques, HFM bioreactors are capable of supporting higher cell numbers [59]. To date, HFM bioreactors have been used for the expansion of lymphocytes [60], erythroids [13, 61], mesenchymal stromal progenitor cells [62], and human embryonic stem cells [63]. The need for tissue specific platforms has to date, inhibited the adoption of HFM bioreactors for the large-scale production of biopharmaceuticals. However, as stem cell therapies continue to be developed, the tight control of culture conditions required to maintain pluripotency of stem cells is likely to necessitate HFM bioreactors to produce the high volumes required [57].

Further to the expansion of cell numbers for cell therapies, HFMs may facilitate the generation of physiologically relevant tissues. HFMs have been used as pseudo vasculature for vascular grafts [64, 15], osteogenic [65, 66], cartilage and neural tissues. The compartmentalisation and the selectivity of HFMs has also enabled the development of bio-hybridised blood purification systems to support the metabolic functions of patients with organ damage [59].

HFMs are predominantly non-biodegradable, rigid and monolithic in nature. The monolithic nature of existing membranes is exemplified by ceramic membranes which have take the form of a single, solid, and continuous piece of material [13]. These stand in contrast to the fibrillar micro-structure of the ECM which constitutes the vascular wall [67]. While flexible HFMs have been developed for potential application in kidney dialysis, separation of blood components, gas separations, and water treatment [68, 69, 70], their monolithic structure means they fail to mimic physiological passive mechanical cues afforded by cellular fibrillar ECM interactions. As HFMs are used as pseudo vasculature, they should exhaustively mimic the mechanical and morphological properties of natural vasculature to maintain physiological passive mechanical cues.

2.8 Lessons learnt from tissue engineered vasuclar grafts

Coronary diseases, including stenosis and thrombosis, if untreated, can lead to ischemic tissue damage or vessel rupture [71]. Consequently, cardiovascular disease is the leading cause of death worldwide and is projected to continue to be until at least 2030 [72]. Coronary autologous artery bypass is the current gold standard in the treatment of stenosis, in which good procedural outcomes have been associated with good morphological and mechanical similarities between the vessel transplanted and bypassed [71]. With the aim to minimise the complications associated with autologous transplants, tissue engineered vascular grafts (TEVGs) have been developed. As with autologous transplants, an ideal TEVGs should be morphologically and mechanically similar to the vessel bypassed while ensuring;

long-term maintained graft compliance, an antithrombotic surface and be resistant to kink formation and aneurysms [73, 74]. Similarly, when developing next-generation vascular mimetic HFMs to ensure exhaustive mimicry of the physiological condition, not only is it pertinent to consider the morphology and mechanical characteristics of native vasculature, but their properties should be mimicked as closely as possible.

2.9 Native Vasculature

Blood vessels are responsible for the transport of nutrients and dissolved gases to tissues through arteries and the removal of waste metabolites in veins. Moving distally blood vessels bifurcate numerous times while decreasing in size, leading to an increase in cross-sectional area and a decrease in pressure. To account for these changes, the structure of the vessels varies, and as such, blood vessels may be segregated and profiled accordingly [4, 75].

2.9.1 Structure

Blood vessels are generally comprised of three concentric laminae: the intima, media and adventitia. Venous vessels are characterised by a thicker adventitia and thinner media, while arterial vessels have a thicker media and thinner adventitia. The decrease in blood vessel size distal is associated with a thinning of each of the laminae until the capillaries, which are comprised of an intima layer only. Blood vessels may, therefore, be broadly classified as large, medium, small, arterioles, muscular venules, capillaries, and postcapillary venules [76]. A schematic of this general structure may be seen in figure 2.5.

The endothelium is a monolithic layer of flat elongated polygonal squamous flow-aligned endothelial cells (ECs) located on a basal lamina associated with pericytes, collectively forming the intima. The media is formed of concentrically aligned layers of smooth muscle cells (SMCs) alternatively sandwiched between thin sheets of elastin and collagen. Elastin provides elastic recoil, while collagen

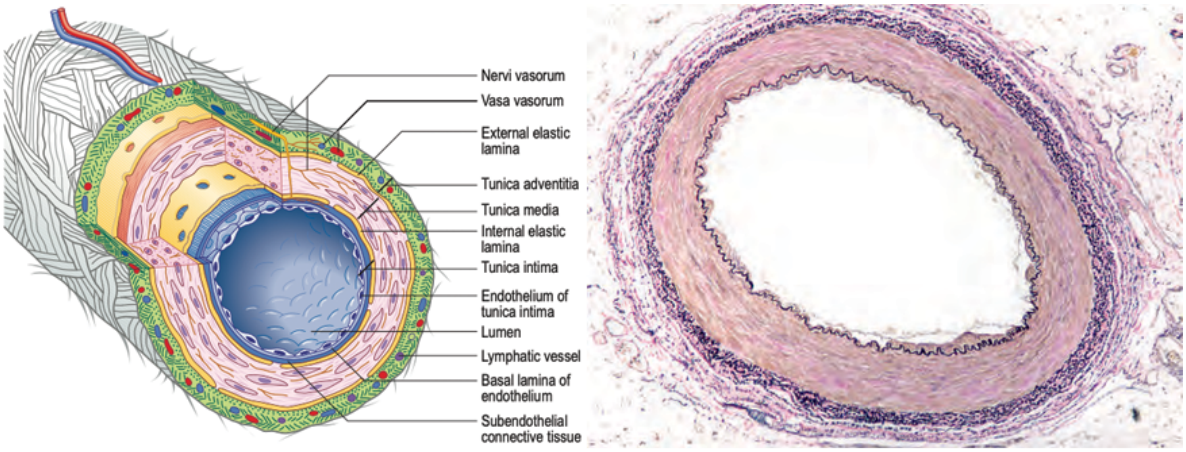


Figure 2.5. Schematic and histology of a human muscular artery, adapted from [4].

provides retentive stress on vessel walls to prevent over-expansion from intraluminal pressure, thereby enacting complementary mechanical characteristics. Finally, the adventitia, comprised of axially aligned collagen fibres, maintains the length and calibre of vasculature while facilitating vessel integration into surrounding connective tissues. Larger vessels, in which wall thickness is such that diffusive mass transfer is insufficient to prevent ischemic tissue damage, have *vasa* and *nervi* vasorum that provide an auxiliary nutrient supply to the tissue and regulate the degree of vascular constriction [76].

Blood vessels have been shown to be highly structurally plastic, capable of dynamically altering their degree of constriction and structure in response to environmental stimuli [77]. By considering the cellular constituents of blood vessels, it is thereby possible to appreciate the myriad of physiochemical mechanisms orchestrating this plasticity and *de novo* vessel formation.

2.9.1.1 The physiochemical landscape

Depending on the developmental stage, blood vessels develop *in vivo* through various mechanisms, including embryonic vasculogenesis, *de novo* adult vasculogenesis, angiogenesis and finally through the splitting of existing vessels. In adults, neovascularization predominantly occurs through angiogenesis whereby, briefly, quiescent phalanx cells reversibly differentiate into highly proliferative tip and stalk cells before returning to a quiescent state. Orchestrating the transition between each of these states,

growth factors and cell signalling molecules, including vascular endothelial growth factor (VEGF), NOTCH, angiopoietin (ANG), platelet-derived growth factor (PDGF) and fibroblast growth factors (FGFs), which are therefore integral to vasculogenesis [78].

2.9.2 Cell signalling

In contrast to the myriad of soluble growth factors orchestrating various cellular differentiation and maturation pathways, such as haematopoiesis, a single soluble growth factor, VEGF, presides as the dominant regulatory factor over vasculogenesis [79]. To modulate the reversible transition between quiescence and a proliferative phenotype, the growth factor VEGF-A binds with the receptor VEGFR-2. The subsequent tug-of-war interplay between Notch receptor (NOTCH) and Delta-like 4 (DLL4) expression in adjacent ECs facilitates the VEGF modulation of EC proliferation, vessel branching, and enlargement [80]. Providing further modulatory effect to this process, two isoforms, B and C, mediate the response to VEGF-A and regulate the tip and stalk cell phenotypic specification and lymphangiogenesis respectively [81].

Subsequent to the proliferation of ECs, to ensure proper vessel function, EC mediated pericyte and SMC recruitment is imperative to blood vessel maturation. Pericytes, which stabilise blood vessels and maintain EC quiescence, are recruited through EC secretion of the chemoattractant PDGF-β. Similarly, EC expressed sphingosine-1-phosphate has been found to modulate migration, proliferation and survival of SMCs, which maintain vessel dilation and medial ECM protein composition. To ensure EC quiescence during blood vessel maturation, the TIE family receptor and their ANG antagonists have been found to act as a binary switch while enabling response to angiogenic stimuli [81]. Additionally, perivascular cells have also been shown to modulate EC and SMC behaviour orthogonally through SMC and EC secretion of VEGF and ANG in response to mural cell FGF and TGF-β, production [82].

Further to the action of cell signalling molecules, following the onset of vessel perfusion, flow

induced wall shear stress (WSS) has been found to activate Krüppel-like factor 2 (KLF2), consequently upregulating EC expression of nitric oxide, evoking a shift towards quiescence [82]. WSS has also been implicated in the regulation of arteriovenous differentiation, with arterial high-pressure flow driving ECs towards arterial phenotypes [78]. In addition to the onset of flow induced WSS, improved oxygen supply facilitated by the onset of convection lowers localised EC VEGF secretion to further their shift towards quiescence [78]. While the differentiation of ECs into each of these phenotypes is guided by growth factors, there is growing evidence that these factors modulate metabolic shifts that themselves drive phenotypic differentiation and vasculogenesis [83].

2.9.2.1 Metabolism

Metabolism serves three primary purposes: energy production, redox homeostasis and biomass synthesis. Strikingly cellular metabolism is vastly similar between different species in the animal kingdom. However, ECs display metabolic adaptations different to most cell types [84]. In contrast to most healthy cell types, ECs are glycolysis addicts, producing 85% of their ATP glycolytically, converting glucose to lactate [85]. In spite of the loss of a potential 34 extra ATP molecules, which may be produced through oxidative glycolysis, predominant energy production through anaerobic glycolysis offers various potential benefits to ECs. These benefits include faster kinetics of anabolic ATP production, reduced reactive oxygen species produced compared to oxidative phosphorylation, preservation of oxygen for perivascular cells, the production of glycogen for the vascularisation of glucose poor milieus, energy production to support vascularisation of hypoxic milieus and the potential exploitation of the feed forward angiogenic loop created by the lactate produced [86]. Furthermore, the shunting of glucose derived glycolysis intermediates into the pentose phosphate pathway, and the hexosamine biosynthesis pathway have been associated with further modulation of the redox status, nitric oxide synthesis, nucleotide synthesis and as a nutrient sensor respectively [83, 86, 87]. Mechanical stimulation has also been found to mediate EC metabolism through the suppression of anaerobic glycolysis through

WSS mediated activation of KLF217. The significance of anaerobic glycolysis to EC proliferation and migration has been exemplified through the inhibition of glycolysis intermediates, which in turn resulted in a reduced EC proliferation and migration [83]. Further exemplifying the significance of anaerobic glycolysis EC function, during proliferation, tip cells were found to over express glycolysis transgenes in spite of strong anti-angiogenic Notch signalling. This revelation has subsequently been taken as confirmation that EC metabolic states may independently drive EC proliferative phenotypes [84]. While glucose is integral to EC survival, ECs utilise several other metabolites.

Glutamine, the most abundant non-essential amino acid (AA) in circulation, is the AA most consumed by ECs. Predominantly catabolised by ECs for ROS homeostasis, protein and nucleotide production, ECs with deficient glutamine have been found to be more susceptible to oxidative stress, inhibited proliferation and motility. Surprisingly, in spite of its abundance, ECs have been found to synthesise negligible amounts of glutamine. Inhibition of this synthesis, however, inhibits EC proliferation and migration [87]. Further to glutamine; asparagine, arginine and serine have been identified to be vital to EC functionality, without which motility and proliferation are inhibited[84].

Unlike many other cell types, ECs depend on fatty acid oxidation for nucleotide synthesis. Additionally, lipids are used by ECs as signaling molecules and are catabolised to supplement intermediates in the tricarboxylic acid cycle. Accordingly, shortages of fatty acids are associated with inhibited EC migration and proliferation [87]. Unexpectedly, despite the ability of ECs to absorb lipids from the bloodstream, disruption of EC synthesis of palmitate results in the inhibition of EC proliferation but not migration [84].

By considering the distal variation in blood vessel morphology, one can begin to appreciate the modulatory effects these mechanisms may serve towards the regulation of blood vessel plasticity. By considering the variation in mechanical properties, however, it is possible to appreciate the functional

role these mechanisms serve to ensure appropriate vessel functionality.

2.9.3 Mechanical properties

In view of the change in blood vessel structure and the associated constituent components moving distally, it is pertinent to consider their mechanical properties according to size. Accordingly, blood vessels may be categorised as large, medium, small and capillaries. Furthermore, it has been demonstrated that mechanical properties vary with various disease states and, as such, should be segregated accordingly. Various methods have been used to measure the mechanical properties of blood vessels. However, uniaxial tensile testing has predominantly been used and therefore affords the most comparisons to be made [88].

From the stress-strain response curve obtained from uniaxial tensile testing of blood vessels, as exemplified in figure 2.6, it was hypothesised that the different components constituting the vascular wall conferred the two distinct linear regions. The initial low pressure region was accredited to SMCs and elastin in the media, and the subsequent stiffer response to extra-physiological pressures was associated with collagen. Blood vessels should therefore be characterised by both the low and high pressure moduli. Furthermore, the component dependency of these characteristics suggests that moving distally, morphological variation will confer differences in response to mechanical loading [89, 90]. Collectively, three blood vessel mechanical properties may be determined, including the Young's modulus, ultimate tensile strength and ultimate tensile stress. Blood vessels also display hysteresis in response to the cycling loading and therefore have no resting configuration and so may be considered viscoelastic in nature [77].

The association of variation in blood vessel mechanical properties with structure variations in blood vessels between locations and patients makes comparative studies difficult. To enable comparisons between studies, mechanical evaluation standards for blood vessels were therefore developed. These

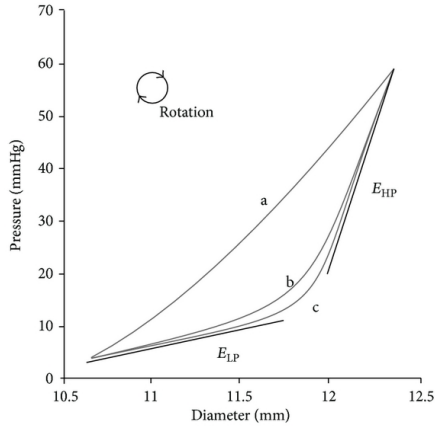


Figure 2.6. Pressure-diameter relationship of a viscoelastic artery showing the binary low and high pressure elastic moduli and the development of a hysteresis loop [5].

standards included Peterson's elastic modulus defined by equation 2.1, to create a relative measure of cross-sectional compliance [91].

$$\mathrm{C}(\%\mathrm{mmHg}^{-1} \times 10^2) = \left(\frac{D_s - D_d}{D_d(P_s - P_d)} \right) \times 100 \tag{2.1}$$

where, C is the compliance of the blood vessel, D_s is the blood vessel diameter systole, D_d is the blood vessel diameter diastole, P_s is the blood pressure systole and P_d is the blood pressure diastole. Accordingly, blood vessel compliance is a measure of the capacity of the vessel to elongate and enlarge when exposed to variations in pressure. It is an indicator of how easily the vessel walls undergo deformation under mechanical stress. Mathematically, compliance and the Young's modulus of a blood vessel have an inverse relationship through the stress-strain relationship of the blood vessel wall. Subsequently, it has been demonstrated that the stiffness of arteries increases with aging. Neither the low- nor high-pressure Young's modulus have, however, been found to correlate with age, while compliance has, and so may be considered a better indicator of vessel health [92].

Collectively, blood vessels may be profiled by size and health status by considering the low- and high-pressure Young's modulus, ultimate tensile strength, maximum strain, burst strength and retention strength in both axial and radial directions [93]. Consequently, by comparing studies evaluating the

mechanical properties of blood vessels, a mechanical profile of similar size blood vessels were created, as seen in table 2.1. Having profiled the variation in structural, physiochemical and mechanical properties of native vasculature, one can prospectively evaluate the merits of the methods by which TEVGs may be produced.

Table 2.1. Range of characteristic mechanical properties of medium sized blood vessels.

Property	Radial/Axial	Healthy Native Vessel Range	Ref
Low Pressure Young's Modulus	Radial	0.15-1.7 MPa	[94, 95]
High Pressure Young's Modulus	Radial	1.27 – 8 MPa	[94, 96]
	Axial	0.22 – 2.61 MPa	[91, 97]
Ultimate Tensile Stress	Radial	4.1 MPa	[98, 99]
	Axial	1.44 – 2.37 MPa	[94, 100]
Maximum Strain	Radial	134-242%	[99]
	Axial	35 - 83%	[94]
Burst Strength	N/A	1250 – 3200 mmHg	[94, 101]
Compliance	N/A	2.1 - 12.2 %	[102, 103]

TEVGs have to date been predominantly developed as alternatives to autologous artery transplants for coronary bypass surgeries, in which morphological and mechanical similarity between the vessel transplanted and bypassed is associated with good procedural outcomes [71]. In view of the morphological and mechanical variation between blood vessels, TEVGs with a luminal diameter of less than 6 mm should match the mechanical properties as seen in Table 1. To create a scaffold which matches this profile, various methods have been employed.

2.10 Tissue engineered vascular grafts

TEVGs have been produced in adherence to one of four philosophies, including the use of

1. biostable polymers intended for permanent residence within the body,

2. native or biodegradable synthetic polymers to be dynamically replaced with native tissue *in vivo*,

3. scaffolds made from native or biodegradable synthetic polymers initially primed with autologous, cellular constituents before transplant, and finally,

4. the development of conduits made entirely of natural tissue *ex vivo*.

To date, only large calibre TEVGs, with diameters larger than 6 mm, produced from biostable polymers have been approved for clinical use. Below this size, biostable polymeric TEVGs fail due to thrombosis, chronic foreign body reactions, intimal hyperplasia and graft calcification [104]. Small calibre scaffolds primed with autologous cells and those produced entirely of natural tissue have shown great promise; however, long lead times and the high cost of production have inhibited their use. To overcome these issues, electrospun TEVGs produced from biodegradable polymers have shown great promise [73, 104, 105, 77].

2.10.1 Electrospun TEVG material selection

To date, electrospinning has been used to produce micro-fibrous meshes from more than 100 polymers [106], of these TEVGs have been produced from synthetic polymers including Polycaprolactone (PCL) [107], Polydioxanone (PDO) [108], polylactic acid [109] and polyurethane [110]. Synthetic polymers are biologically inert, to improve biocompatibility and cell attachment, natural polymers, including collagen [111, 112], silk [113], and tropoelastin [114] have been evaluated. Natural polymers alone, however, have poor mechanical properties. To combine the superior mechanical properties and biocompatibility of synthetic and natural polymers, respectively, co-spinning and blending have been considered [115, 116, 117]. Furthermore, different collector configurations and layering have been used to recreate a hierarchical structure and variation in the alignment of fibrous ECM proteins found in native vasculature [109, 117, 118, 119]. Further to the native biocompatibility of materials used, by considering the gross mechanical properties achieved with each material it is possible to identify materials and micro-fibre morphologies which confer those most akin to native vasculature.

2.10.1.1 Comparison of TEVG and native blood vessel mechanical properties

By comparing the mechanical properties of TEVGs with the range of that measured for healthy blood vessels of comparable size, as defined in table 2.1, it is possible to identify the micro-fibre diameter range, alignment and polymers which confer mechanical properties similar to that of native vasculature. Of the 106 TEVGs considered, as detailed in the supplementary table 2.2, only 72 of them had at least one mechanical property which fell within the range of that for healthy blood vessels of a similar size. By considering figure 2.7 the polymers and associated micro-fibre diameters, associated with each of the TEVGs in table 2.2, which gave mechanical properties within the range of healthy blood vessels of a similar size may be determined. From this comparison, it may be seen that TEVGs produced from PCL and PDO with unaligned micro-fibres approximately 0.7 μm in diameter have mechanical properties that are most frequently akin to that of medium-sized blood vessels. It should be noted that, while micro-fibre alignment in the direction of stress is physiologically accurate [39], it yielded extra-physiological values for all properties considered except for maximum strain. TEVGs should match all the mechanical properties of native blood vessels. However, to ensure successful engraftment, cellular adhesion, infiltration, proliferation, and migration are key [117, 120].

It should be noted that while this analysis begins to attempt to compare TEVGs and the mechanical profile defined for medium-sized blood vessels, the comparisons made are limited by the number of mechanical properties reported for each in the literature. Furthermore, these comparisons are between medium-sized blood vessels and similarly sized TEVGs. However, if TEVGs are to be developed to target smaller blood vessels then a profile for smaller vessels, less than 6 mm, should be defined. The lack of quantitative data for smaller blood vessels in the literature and difficulties in measuring these data currently inhibit these comparisons. Research into defining the mechanical profile for blood vessels with diameters less than 6 mm would therefore be useful.

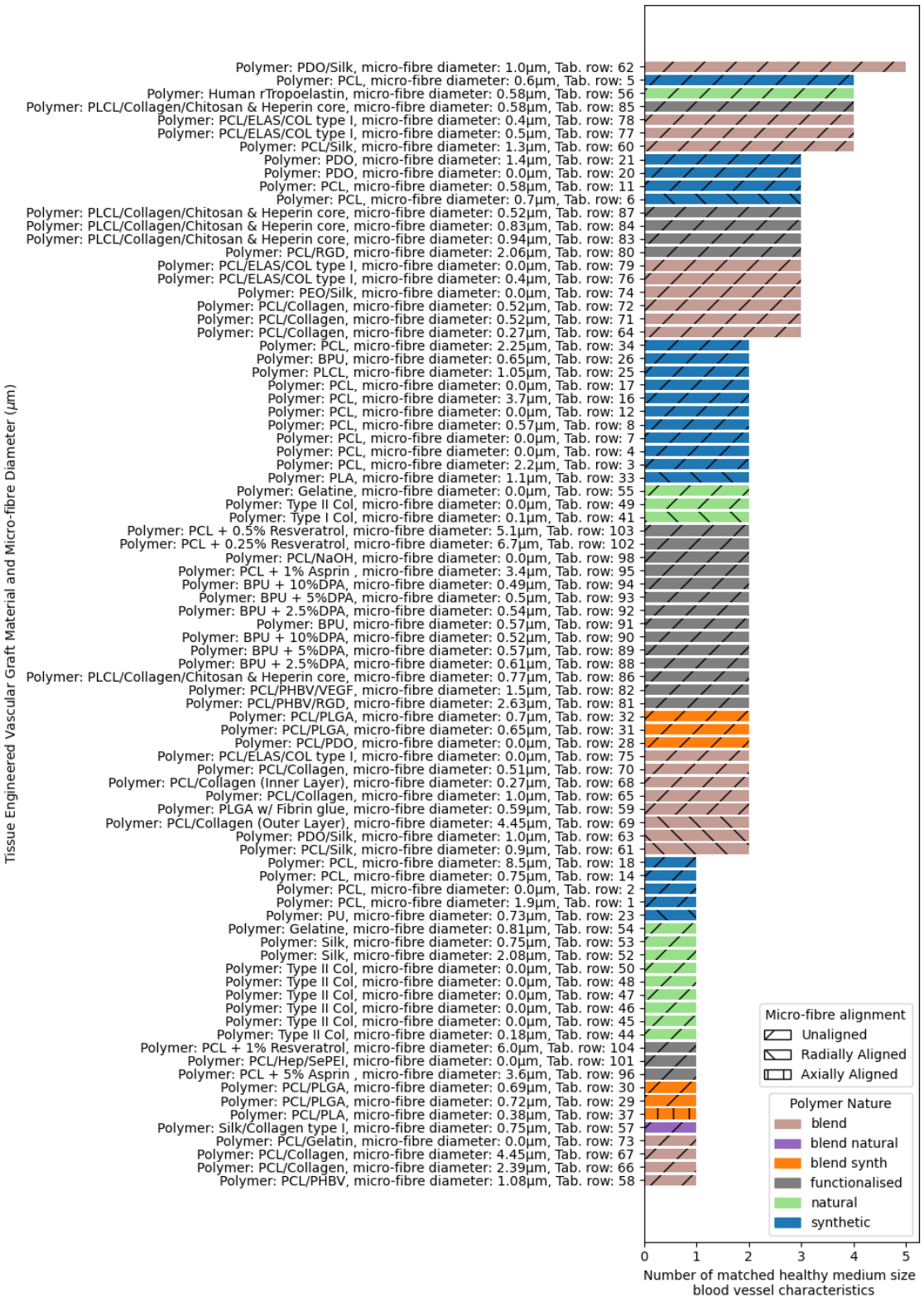


Figure 2.7. Bar chart showing the number of electrospun tissue engineering vascular graft mechanical properties that were within the range of the corresponding property of the profile defined for healthy native medium-sized blood vessels, as given in table 2.1, labelled with the polymer, micro-fibre diameter, reference table 2.2 row number, and coloured according to micro-fibre alignment and polymer nature as given by the key.

2.10.2 Postproduction functionalisation, topographic and physiochemical properties and of TEVGs

Further to the biocompatibility of the materials selected for the production of TEVGs, topographic and physiochemical properties, including micro-fibre alignment, porosity and hydrophobicity, have been identified as key to ensuring successful engraftment. By aligning micro-fibre orientation with the direction of stress imparted on the mesh, it was found that the Young's moduli, ultimate tensile stress, maximum strain and burst pressure could be increased while compliance was found to decrease [113, 116, 118]. Furthermore, ECs and SMCs were shown to align in the direction of micro-fibre orientation [118, 121]. To enable the cellular infiltration of TEVGs and migration of cells, sufficient pore size is vital. It has been hypothesised that a pore size similar to that of cells is required to enable cell infiltration. For SMCs, a pore size of roughly 10 μm should therefore be adequate [106]. Subsequently, a pore size below 7.46 μm was found to inhibit SMC infiltration [74]; a pore size above this should therefore be maintained. In view of the direct correlation between fibre diameter, pore size and mechanical properties, it is vital to find a material with appropriate mechanical properties while maintaining a sufficient pore size at the associated micro-fibre diameter [122]. Further to preventing physical obstruction of cellular infiltration, good cellular adhesion aids cellular proliferation, migration and differentiation [120]. Polymer hydrophobicity and biofunctionalization of synthetic materials have therefore been considered as a means to improve TEVG engraftment.

Due to the loss of micro-fibre morphology, the use of purely hydrophilic materials is not possible [112]. Blending of hydrophilic and hydrophobic polymers has consequently been used to maintain micro-fibre morphology *in vitro* and was associated with an increase in cellular proliferation. The increase in hydrophilicity, however, also corresponded to an increase in non-specific binding, including that of Lactate dehydrogenase, an enzyme associated with platelet adhesion. An increase in hydrophobicity may, therefore, also confer greater thrombotic tendency due to non-specific binding [109]. The specificity of surface modification may increase cell adhesion without increasing the thrombogenic tendencies of

grafts.

Through covalent and non-covalent bonding, macromolecules, including heparin, cell-adhesion peptides, growth factors and other pharmaceutical agents, have been used as surface modifications [123]. Non-covalent bonding of heparin, through blending, decreased the formation of thrombosis [124, 125], and provided a binding site for subsequent attachment of VEGF. Covalently bonded VEGF was found to improve endothelisation and, when bonded to heparin, improved cell attachment [126, 127]. Similarly, PDGF has also been found to confer a step-wise increase in proliferation with concentration [128]. Arginine-glycine-aspartic acid (RGD) is a cell adhesion motif displayed on the surface of many ECM proteins and is the most extensively evaluated cell-adhesion peptide [98, 129]. Covalent bonding of RGD to PCL was found to improve SMC infiltration, capillary formation, luminal endothelial lining and alignment [130]. The blending of the pharmaceutical drug rosuvastatin was found to increase endothelisation and reduce platelet adhesion [131].

Despite the numerous advancements made towards the development of a suitable TEVG, difficulties in online and inline diagnostics and the complex interconnected nature of biological systems forced the adoption of a trial-and-error methodology toward their development. However, mathematical modelling offers a means to expedite the process by providing a rationale for experimental design decisions [132].

2.10.3 Mathematical modelling of vascular graft remodelling

In order to evaluate the large expanse of TEVG property parameters to determine a theoretically optimal design, it is imperative to accurately model the mechanical properties of vasculature and cell behaviour in health and disease. Since it was initially hypothesised that the different components constituting the vascular wall conferred the two distinct linear regions, as seen in figure 2.6, efforts have been made to model the stress-strain response of the vascular wall [89]. Early attempts relied on phenomenological models. However, these gave no insight into the role of the constitutive wall structure

[133, 134]. To better predict vessel wall mechanics, constitutive models were subsequently developed [135].

2.10.3.1 Constituent properties

It was initially suggested that the initial low pressure stress-strain response, as seen in figure 2.6, could be accredited to SMCs and elastin in the media and that the subsequent stiffer response to extra-physiological pressures was associated to collagen [89]. Subsequently, further investigations have sought to determine the constitutive effects of each vascular wall component. To separate the mechanical contributions of elastin and collagen, enzymatic digestion has been used to isolate each from arterial tissues [136, 137]. However, the realisation that the two are physically linked suggests that data obtained from these experiments may be flawed [138]. Similarly, due to the plasticity in vascular remodelling, vessels from mouse models with altered ECM proteins display compensatory changes in ECM contributions within the vessel wall [139]. The contribution of each component, therefore, remains to be fully elucidated. In spite of these shortcomings, models accounting for layer specific collagen and elastin abundancies [140], fibre orientation [141] and waviness [138] have shown promise towards describing the mechanical properties of vessel walls. In light of the development of these constitutive models, Growth and repair (G&R) models have been developed to model the variation in mechanical properties with time.

2.10.3.2 Growth and repair

Since the conception of the first constitutive vascular G&R model, evaluating the effect of WSS and neointimal hyperplasia, there have been significant advances in vascular G&R modelling [135, 142]. Specifically, Miller et al. developed a phenomenological model describing the influence of macrophages and shear stress on collagen deposition along with polymer degradation [143]. By marrying the fibre diameter and porosity alongside the existing phenomenological model, it was determined that a decrease

in porosity and fibre diameter corroborated a decreased inflammation response which in turn resulted in neo-tissue formation with characteristics similar to that of native vasculature [144]. Subsequently, this model was also used to determine optimal scaffold parameters [145]. Following the development of a chemo-mechano-bio mechanistic G&R model by Wattaon et al., biochemical and mechanical influences along with macrophage mediated inflammation response on fibroblast ECM remodelling could be examined while alleviating the dependency on phenomenological cell behaviour modelling [146]. A modified form of this mechanistic model was subsequently used to examine the role of scaffold characteristics on neo-tissue development and graft stenosis [147, 148]. More recently, a multiscale mechanistic model has been developed to capture the effect of inter- and intra-cell signalling cascades originating from mechanical stimuli. However, it has yet to be applied to tissue scale G&R modelling [149]. Along the same vein, G&R models have also been used to study the remodelling of autologous vein transplants following bypass surgery [150, 151, 152, 153, 154]. Despite these developments towards mechanistic G&R modelling, the lack of three 3D special fidelity in these models limits their usefulness as TEVG failure is often local [155]. Accordingly, 3D G&R models have been developed, their dependency on the use of an overly simplistic cell growth model [156], lack of nutrient transport model and rigid vascular walls [157], however, limits the conclusions drawn from these models.

2.11 Implications of the literature review towards the production of vascular inspired electrospun hollow fibre membranes

The insufficient mimicry of the cellular niche afforded by traditional 2D tissue culture necessitates new technologies capable of recreating the cellular micro-environment. 3D tissue culture techniques satisfy this requirement but are limited in size, to just 200 μm in order to prevent necrotic regions from forming. HFMs have been used to support cell growth in 3D tissue culture scaffolds larger than 200 μm. However, these membranes disrupt passive mechanical cues and prevent the use of auxiliary actuation in mechanically dynamic bioreactors. To prevent this disruption, new membranes, which mimic the

structure and mechanical properties, should therefore be developed.

As the gold standard for the treatment of cardiovascular stenosis, the development of TEVGs represents a means towards attenuating comorbidities associated with allogenic transplants used to date in bypass surgery. However, complications associated with the use of small-calibre TEVGs have so far prevented their use clinically. As with their autologous counterparts, by matching the structure and mechanical properties, it may be possible to develop an optimal TEVG to enable their use. Similarly, next-generation HFMs developed to prevent the disruption of passive mechanical cues in tissue engineered scaffolds should mimic the structural and mechanical properties as exhaustively as possible.

To aid the design of a next-generation HFM, which exhaustively mimics native blood vessels, a structural and mechanical profile of native, medium-sized blood vessels was defined. In order to match these properties various top-down and bottom-up tissue engineering strategies were considered. Top-down approaches were selected as these ensured a membrane with appropriate mechanical properties could be produced as an off-the-self-like product, which would not be possible with bottom-up approaches. Of the various methods used to produce TEVGs, electrospinning has shown great promise. The mechanical properties of electrospun TEVGs were compared to that of the profile of medium-sized blood vessels defined. Through this comparison, it was identified that PCL and PDO electrospun TEVGs with an unaligned micro-fibre mesh and a micro-fibre diameter of 0.7 μm most frequently had properties within the bounds of native medium-sized blood vessels. PCL and PDO may therefore be suitable materials for a next-generation vascular mimetic electrospun HFM.

While such a meta-analysis of existing electrospun TEVGs allows for the reduction of the electrospun hollow fibre membrane property parameter space considered, the dependency on trial-and-error development is slow, costly and labour-intensive. Mathematical modelling provides an alternative

means by which parameter spaces may be rapidly evaluated and inform future experiments. To this end, developments towards constitutive and G&R modelling have shown great promise in the development of TEVGs. However, as electrospun HFMs have not been developed, models for these should be investigated to aid in their development.

In concert, these finds suggest that next-generation HFMs are required to prevent the disruption of passive mechanical cues and facilitate confined advective mass transport in multi-modal mechanical dynamic bioreactors, such as the anthropomorphic humanoid bioreactor which has been developed to exhaustively mimic the cellular environment in the supraspinatus tendon in the human shoulder [11]. To prevent the disruption of passive mechanical cues, next-generation HFMs should mimic their closest physiological relative, vasculature. To date, TEVGs have been developed to morphologically and mechanically mimic bypassed vessels to ensure the best clinical outcomes. To learn from these developments, A meta-analysis of existing TEVGs was conducted and revealed that, electrospun PCL and PDO conferred mechanical properties closest to that of medium-sized blood vessels. The production of electrospun HFMs should therefore be investigated as a means to developing next-generation HFMs for tissue engineering.

2.12 Supplementary section

Table 2.2. Table of morphological and functional properties of tissue engineered vascular grafts reviewed in meta-analysis.

Row No.	Polymer	Micro-fibre Diameter (μm)	Vessel Size	Micro-fibre alignment	Pore Size (μm)	Porosity (%)	Young's Modulus (MPa)		Ultimate Tensile Stress (MPa)		Maximum Strain (%)		Ref.
							X-Axis	Y-Axis	X-Axis	Y-Axis	X-Axis	Y-Axis	
Synthetic Polymers													
1	PCL	1.90	N/A	Unaligned						4.80		600	[158]
2			Small	Unaligned						5.40			[159]
3		2.20	N/A	Unaligned						4.10		1092	[104]
4			Small	Unaligned	24			1		4.10		260	[108]
5		0.60	Small	Unaligned			9.40	7.30	3.90	2.60	90	130	[116]
6		0.70	Medium	Radial			42.70	0.60	20	1.40	100	600	[116]
7			Medium	Unaligned				4.98		2.70		126	[106]
8		0.57	N/A	Unaligned				12.35		4.14		147	[160]
9		0.40	Medium	Radial									[118]
10		0.40	Medium	Axial									[118]
11		0.58	Medium	Unaligned	5.19			7.50		1.50		417	[161]
12			Medium	Unaligned				4.98		2.70		126	[106]
13			N/A	Unaligned									[120]
14		0.75	N/A	Unaligned	1					4.90		180	[162]
15		0.11	Medium	Axial	10.99	16.23		806.69		37.16			[121]
16		3.70	Small	Unaligned			2.90		1.80		660		[163]
17			Medium	Unaligned				0.93		6.80		150	[127]
18		8.50	N/A	Unaligned	42.90			10				600	[164]
19	PLA	0.10	Small	Axial	12.08	6.57		409.34		11.19			[121]
20	PDO		Small	Unaligned	18			4.80		9		50	[108]
21		1.40	Small	Unaligned			12.30	9.90	4.60	5.10	240	330	[116]
22		1.20	Medium	Radial			35.70	0.20	12.50	0.70	70	570	[116]
23	PU	0.73	Medium	Radial						5.85		295.40	[110]
24		2	Medium	Unaligned	1					21		320	[162]
25	PLCL	1.05	Medium	Unaligned				0.85		1.91		135	[107]
26	BPU	0.65	Medium	Unaligned				1.40		3.40		227	[165]
27	Gortex		Medium	Monoalythic				31.61		14.03		27.80	[107]
Co-spun and Blended Synthetic Polymers													
28	PCL/PDO		N/A	Unaligned	20.06			2.60		6.50		121.31	[108]

Row No.	Polymer	Micro-fibre Diameter (μm)	Vessel Size	Micro-fibre alignment	Pore Size (μm)	Porosity (%)	Young's Modulus (MPa)		Ultimate Tensile Stress (MPa)		Maximum Strain (%)		Ref.
							X-Axis	Y-Axis	X-Axis	Y-Axis	X-Axis	Y-Axis	
29	PCL/PLGA	0.72	Small	Unaligned						31.73		215.92	[166]
30		0.69	Small	Unaligned						20.19		144.11	[166]
31		0.65	Small	Unaligned						9.17		116.36	[166]
32		0.70	Small	Unaligned						6.29		63.42	[166]
33	PLA (Part of PCL-PLA Multilayer)	1.10	Small	Radial	10	79		30.90		4.30		47	[119]
34	PCL (Part of PCL-PLA Multilayer)	2.25	Medium	Unaligned	15			10.70		1.20		260	[119]
35	PCL/PVA		Medium	Unaligned									[120]
36	PCL/PU		N/A	Unaligned	10					18		375	[162]
37	PCL/PLA	0.38	Medium	Axial	23.72	194				2.60		1.80	[109]
39		0.43	Medium	Axial	9.71	20.80				1		7.40	[109]
40		0.35	Medium	Axial	9.02	14.77		1529.20		44.06			[121]
					Natural Polymers								
41	Type I Col	0.10	N/A	Unaligned									[111]
42		0.10	Medium	Radial			26.10	52.30	0.70	1.50			[111]
43	Type III Col	0.25	Medium	Radial									[111]
44	Type I & III Col	0.39	Medium	Radial									[111]
45	Type II Col	0.18	Medium	Unaligned				51.45		2.39		9.53	[167]
46			Medium	Unaligned				0.73		0.60		159.23	[167]
47			Medium	Unaligned				0.92		0.57		128.27	[167]
48			Medium	Unaligned				0.75		0.54		131.80	[167]
49			Medium	Unaligned				0.57		0.35		111.83	[167]
50			Medium	Unaligned				0.51		0.30		78.27	[167]
51			Medium	Unaligned				0.89		0.76		127.30	[167]
52	Silk	0.96	Medium	Unaligned	19	88.81				0.36		26	[168]
53		2.08	Medium	Unaligned	15	80.85				3.57		12	[168]
54		0.75	N/A	Unaligned								27.34	[169]
55	Gelatine	0.81	Medium	Unaligned				33.80	2.90		11.70		[113]
56			Medium	Unaligned				105		2.50		64	[106]
57	Human rTropoelastin	0.58	N/A	Unaligned			0.82	0.99	0.34	0.38	79	75	[114]

Row No.	Polymer	Micro-fibre Diameter (μm)	Vessel Size	Micro-fibre alignment	Pore Size (μm)	Porosity (%)	Young's Modulus (MPa)		Ultimate Tensile Stress (MPa)		Maximum Strain (%)		Ref.
							X-Axis	Y-Axis	X-Axis	Y-Axis	X-Axis	Y-Axis	
Co-spun and Blended Natural Polymers													
58	Silk/ Collagen type I	0.75	Medium	Unaligned								28.76	[170]
Hybrid of Natural and Synthetic Polymers													
59	PCL/ PHBV	1.08	N/A	Unaligned	30.65			28		7.05		431.33	[126]
60	PLGA with Fibrin glue	0.59	N/A	Unaligned				2.26					[171]
61	PCL/ Silk	1.30	Small	Unaligned			13.40	15.60	1.40	1.40	50	50	[116]
62		0.90	Medium	Radial			16.20	0.80	4.80	0.70	50	270	[116]
63	PDO/ Silk	1	Medium	Unaligned			1.70	2.20	2.30	2.70	150	140	[116]
64		1	Medium	Radial			20.50	0.50	7.60	0.70	60	270	[116]
65	PCL/ Collagen	0.27	Medium	Unaligned	1.33			2.03		3.13		90	[74]
66		1	Medium	Unaligned	7.46			0.58		2.03		142	[74]
67		2.39	Medium	Unaligned	11.98			0.45		0.71		211	[74]
68		4.45	Medium	Unaligned	34.64			0.26		0.75		734	[74]
69		0.27	Medium	Unaligned	1.33			1.28		1.45		204	[117]
70		4.45	Medium	Radial	34.64			1.28		1.45		204	[117]
71		0.51	Medium	Unaligned				4.59		1.93		187.11	[160]
72		0.52	Medium	Unaligned	4.76			2.70		4		140	[161]
73		0.52	Medium	Unaligned	4.76			3.80		8.30		62	[161]
74	PCL/ Gelatin		Medium	Unaligned				30.80		1.29		138	[106]
75	PEO/ Silk		N/A	Unaligned				2.45		2.42		83	[172]
76	PCL/ ELAS/ COL type I		Medium	Unaligned				12		6.50		135	[173]
78		0.40	Small	Unaligned	2.50			2		1		90	[173]
79		0.50	Small	Unaligned	4			3		1.50		70	[173]
80		0.40	Small	Unaligned	5.50			4		2		65	[173]
81			Small	Unaligned				11		4		90	[173]
Biofunctionalized Polymers													
82	PCL/ RGD	2.06	N/A	Unaligned	4.87	50		18		2		320	[174]
83	PCL/ PHBV/ RGD	2.63	Small	Unaligned	6.41	50		44		2.50		320	[174]
84	PCL/ PHBV/ VEGF	1.50	Small	Unaligned	1.87	45		12		3		190	[174]

Row No.	Polymer	Micro-fibre Diameter (μm)	Vessel Size	Micro-fibre alignment	Pore Size (μm)	Porosity (%)	Young's Modulus (MPa)		Ultimate Tensile Stress (MPa)		Maximum Strain (%)		Ref.
							X-Axis	Y-Axis	X-Axis	Y-Axis	X-Axis	Y-Axis	
85	PLCL/ Collagen/ Chitosan & Heperin core	0.94	Small	Unaligned				5.40		12		73	[125]
86		0.83	Medium	Unaligned				5.70		8.80		74	[125]
87		0.58	Medium	Unaligned				2.20		2.50		59	[125]
88		0.77	Medium	Unaligned				2.50		7.80		184	[125]
89		0.52	Medium	Unaligned				7.80		8.80		87	[125]
90	BPU + 2.5 % DPA	0.61	Medium	Unaligned				2.40		4.90		130	[165]
91	BPU + 5 % DPA	0.57	Small	Unaligned				3.50		5.70		101	[165]
92	BPU + 10 % DPA	0.52	Small	Unaligned				7		7.40		107	[165]
93	BPU	0.57	Small	Unaligned				1.40		2.30		180	[165]
94	BPU + 2.5 % DPA	0.54	Small	Unaligned				1.60		4.40		150	[165]
95	BPU + 5 % DPA	0.50	Small	Unaligned				1.90		4.40		106	[165]
96	BPU + 10 % DPA	0.49	Small	Unaligned				2.80		6.20		117	[165]
97	PCL + 1 % Asprin	3.40	Small	Unaligned			2.40		2.70		840		[163]
98	PCL + 5 % Asprin	3.60	Medium	Unaligned			6.40		5.40		550		[163]
99	PCL + 10 % Asprin	3.50	Medium	Unaligned			13		9		900		[163]
100	PCL/NaOH		Medium	Unaligned				1.20		7		155.20	[127]
101	PCL/ Hep		N/A	Unaligned									[127]
102	PCL/ Hep/ VEGF		N/A	Unaligned									[127]
103	PCL/ Hep/ SePEI		N/A	Unaligned						2.50		180	[115]
104	PCL + 0.25 % Resveratrol	6.70	Small	Unaligned	32.90			8.30		1.60		600	[171]
105	PCL + 0.5 % Resveratrol	5.10	Small	Unaligned	26.20			7		1.30		600	[171]
106	PCL + 1 % Resveratrol	6	Small	Unaligned	27.40			5		1		600	[171]

Chapter 3

Morphological and functional characterisation of vascular inspired electrospun hollow fibre membranes

3.1 Thesis integration and chapter structure

This chapter presents the development of a novel electrospinning collector for the continuous production of electrospun hollow fibre membranes. Having identified PCL and PDO as conferring mechanical properties similar to that of healthy medium size blood vessels in chapter 2, first a polymer blend which enabled the production of defect free electrospun micro-fibres is identified. Having found suitable polymer solution blends, the morphological characterisation of the electrospun hollow fibre membranes produced with the novel collector and blended PCL/PDO polymer solution is presented. Finally, the functional characteristics of the electrospun hollow fibre membranes are measured and presented.

In this section all experimental work, data analysis, and writing was carried out by Risto Martin. Prof. Pierre Alexis-Mouthuy, Prof. Sarah Waters, and Prof. Hua (Cathy) Ye provided supervision and advice throughout.

Morphological and functional characterisation of vascular inspired electrospun hollow fibre membranes

Authors:

Risto Martin[1], Hua (Cathy) Ye[1]*, Sarah Waters[2], Pierre-Alexis Mouthuy [3]*

Affiliations:

[1]*Department of Engineering Science, University of Oxford, Oxford, OX3 7DQ, UK*

[2]*OCIAM, Mathematical Institute, University of Oxford, Radcliffe Observatory Quarter, Woodstock Road, Oxford, OX2 6GG, UK*

[3]*Nuffield Department of Orthopaedic Surgery, The Botnar Research Centre, Institute of Musculoskeletal Sciences, Oxford University, N.O.C. Headington, Oxford, OX3 7LD, UK*

***Corresponding author**:

hua.ye@eng.ox.ac.uk, pierre-alexis.mouthuy@ndorms.ox.ac.uk

Keywords:

Tissue Engineering — Electrospinning — Hollow fibre membrane — Vascular biology

Abstract

Hollow fibre membranes have been used to support cell growth in 3D tissue culture scaffolds larger than 200 μm in diameter. However, these membranes disrupt passive mechanical cues and prevent the use of auxiliary actuation in mechanically dynamic bioreactors. Herein, we present a novel method for the continuous production of electrospun hollow fibre membranes (EHFMs). We hypothesised that: solvent blended polycaprolactone and polydioxanone may be electrospun to produce EHFMs with micro-topography and functional characteristics akin to that of medium sized human arteries and that doping with pyridine may be used as a method by which these properties may be controlled. We

found that: it was possible to continuously produce EHFMs and that both total polymer and pyridine concentration may be used to modulate: micro-fibre diameter, gross EHFM morphology, mechanical properties, membrane tortuosity, permeability and pore size. The mechanical properties of blended PCL/PDO EHFMs were within the range of healthy medium sized human arteries and that all EHFMs produced with 50 ppm pyridine and below were non-cytotoxic. In summary, our findings show that EHFMs may be used as a substrate to support cell growth in 3D tissue culture or as an *ex vivo* model of vasculature with passive mechanical cues similar to those exacted by healthy medium sized human arteries.

3.2 Introduction

The indispensability of two-dimensional (2D) tissue culture techniques is marred by its insufficient mimicry of physiological conditions, particularly the lack of cell-cell and cell-extracellular matrix interactions. Static three-dimensional (3D) culture techniques aim to replicate these conditions. However, the short effective range of diffusive mass transfer of only 200 μm limits the size of these constructs [12, 13]. In lieu of vasculature in 3D tissue culture scaffolds, hollow fibre membranes (HFMs) have been used to facilitate advective mass transfer without the disruption of the cellular niche. Consequently, HFMs have been used to support several cell types at densities higher than that achievable in 2D static culture [13, 59, 61, 62, 63].

Discrepancies between HFMs and human vasculature, namely the rigid, monolithic and non-biodegradable nature of HFMs, prevents their use in mechanically actuated bioreactors and disrupts passive mechanical cues. To exhaustively mimic physiological conditions HFMs should have characteristics akin to that of vasculature of comparable size. By considering a structural and mechanical profile of healthy human arteries it is possible to determine the characteristics which an ideal vascular inspired HFM should have. From literature, we identified that electrospun polycaprolactone (PCL)

and polydioxanone (PDO) most frequently were found to have mechanical properties within the range defined as of that of medium sized human arteries. It was hypothesised HFMs constructed from electrospun materials, a macroscopic tubular structure with walls consisting of electrospun material, may take the form of a next-generation biomimetic HFM. However, PCL, was frequently too stiff and its slow degradation rate was associated with calcification *in vivo* [104]. Conversely, PDO was too elastic and degraded too quickly creating the potential for membrane rupture [108]. It was therefore hypothesised that a blend of the two polymers may confer a material with mechanical properties and a degradation rate akin to that of native medium sized human arteries [108]. Pyridine has previously been used as an additive to modulate micro-fibre morphology and mechanical properties of PCL and PDO alone [175, 176]. Consequently it was further hypothesised that pyridine may be used as a doping agent through which the properties of the electrospun PCL/PDO blends may be augmented.

In this paper the development of a novel continuous process for the production of small calibre electrospun hollow fibre membranes (EHFMs) is presented. Utilising this method, EHFMs are produced from solvent blended PCL and PDO, with varying mass ratios, total polymer masses and pyridine doping concentrations. EHFMs are then characterised in terms of their micro-topography, gross morphology, porosity, mechanical properties, tortuosity, permeability, and cytotoxicity.

3.3 Materials and methods

3.3.1 Preparation of electrospinning solutions

PDO (melting flow rate 4.5 g/10min at 170 °C, Riverpoint Medical, Portland, USA) and PCL (inherent viscosity of 1.11 dl/g Ashland Specialities, Dublin, Ireland) were dissolved in 1,1,1,3,3,3-hexafluoroisopropanol (HFIP, ultra-pure >99.99%, Halocarbon Product Corporation, Atlanta, USA) at different ratios and concentrations as specified. Pyridine (purity >99.5%, PhEur grade, EMSURE ACS, Merck, Darmstadt, Germany) was added to the polymer granules along with HFIP at concentrations of

1, 5, 10, 25 and 50 ppm. Prior to testing, the final solutions were agitated at room temperature on a roller for at least 24 hours to allow for complete dissolution of the polymer.

3.3.2 Design of EHFM collector

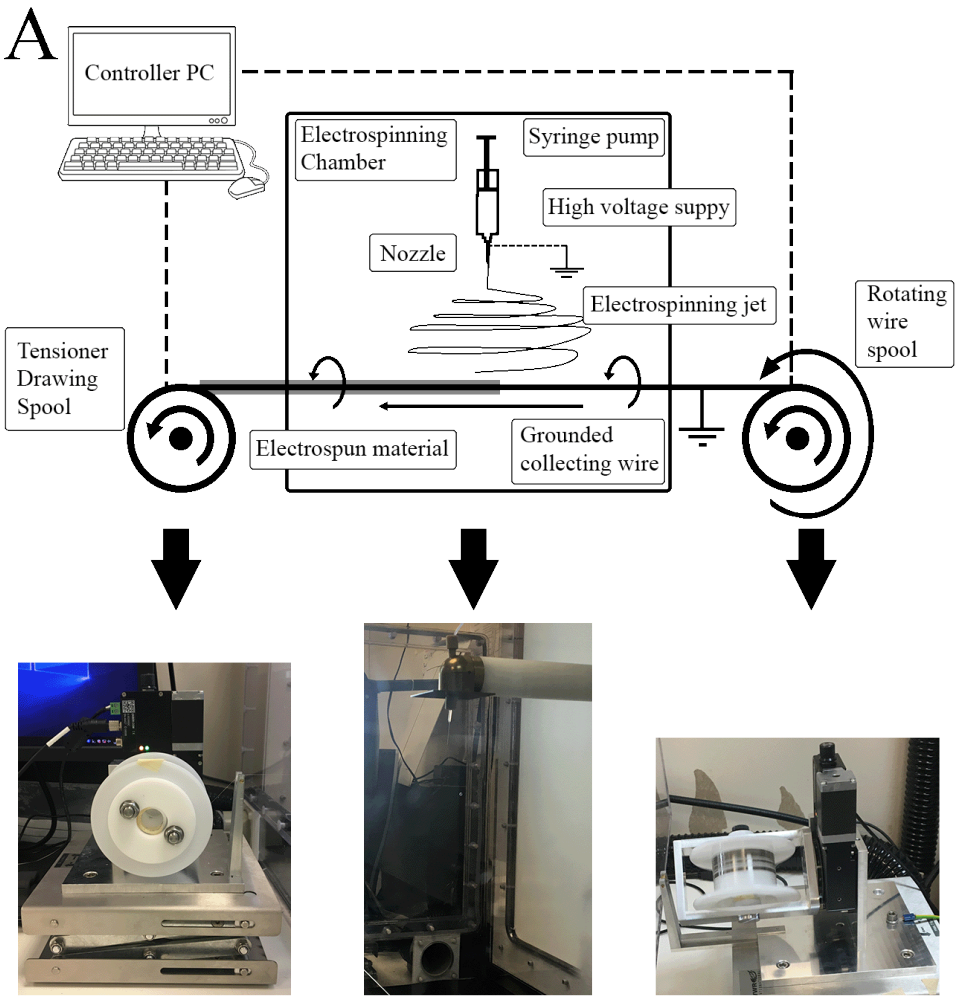
The EHFM collector, designed with computer aided design software (SOLIDWORKS 2022, Dassault Systèmes, France) and fabricated by the University of Oxford Engineering Science workshop, comprised of two units: a rotational spool bracket and a tensioner, as seen in figure 3.1A.

Stainless steel wire (100 μm in diameter, Goodfellow Cambridge Ltd, Huntingdon, UK) was unwound from a spool (⌀57 × 25.2 mm) mounted in the rotary spool bracket. The wire was hung under the electrospinner nozzle, with tension maintained by friction between the spool and the rotary spool bracket pin. The wire was grounded by feeding over the brass roller on the rotary spool bracket guiding arm, connected to an earth. The tensioner unit comprised of a secondary guiding arm for fine alignment of the wire and a second spool to collect the coated stainless steel. X-RSW60C motorized rotary stages (Zaber, Vancouver, Canada) were used to rotate the tensioner spool and the rotational spool bracket. The simultaneous rotation of the bracket and collector spool allowed for continuous drawing of rotating wire and thus the continuous collection of EHFMs. Software was written to control the collector process parameters, (LabVIEW 2019, National Instruments, Austin, Tx, United States) the control panel of which may be seen in figure 3.1B.

3.3.3 Electrospinning

3.3.4 EHFMs

EHFMs were fabricated with a single nozzle electrospinning setup connected to a high voltage power supply system (30 kV, SL30P30/230, Spellman, West Sussex, UK), fed with polymer solution from a syringe pump (World Precision Instruments Limited, Florida, US) at a flow rate of 1 ml/hr, with



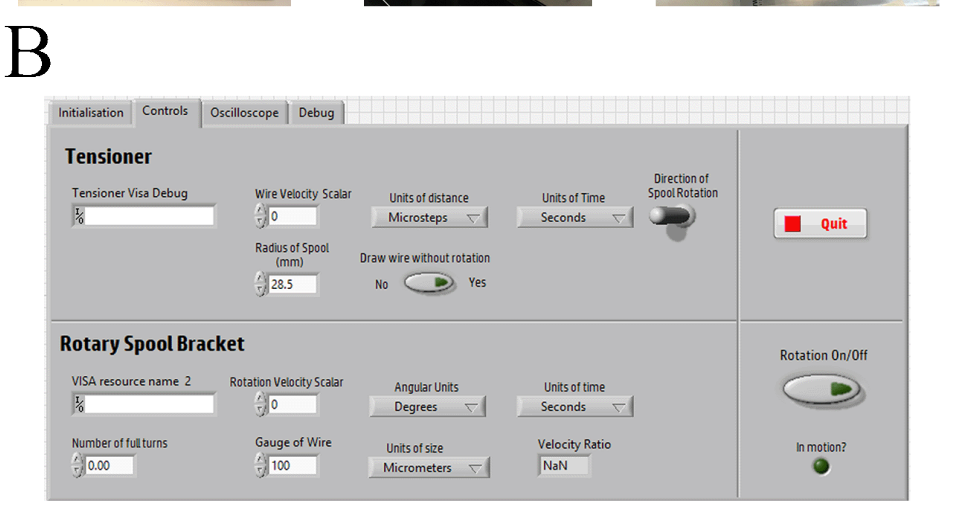


Figure 3.1. (A) Schematic of EHFM collector with pictures of parts as fabricated, and (B) Screen capture of EHFM collector software control panel.

a potential difference of 10-13 kV maintained between the nozzle and the collector. Prior to use, the collector wire was washed with 70 % ethanol. The nozzle and the wire collector were placed, with a constant gap of 19 cm, in a glove box circulated constantly with filtered air to eliminate HFIP vapours produced during operation. A distance of 1.5 m was maintained between the tensioner and rotary spool bracket. The wire draw, rotation speed and rotation direction oscillation frequency were maintained at 0.5 mm/s, 75 rpm and 10 rotations, respectively. The EHFMs were continuously collected on the tensioner spool which could be removed between spins and stored in a desiccator.

3.3.5 Electrospun flat sheet membranes

Electrospun flat sheet membranes were fabricated in an EC-DIG electrospinning system (IME Medical Electrospinning, Geldrop, the Netherlands), maintained at 50 % humidity and 20 °C. A constant gap of 19 cm was maintained between the nozzle and the 8 cm diameter rotating mandrel collector. The nozzle was set to pan the width of the rotating mandrel at 20 mm/s, which in turn rotated at 50 rpm. Polymer solution was fed from a syringe pump (Harvard Apparatus, Holliston, Massachusetts, United States) at a flow rate of 1 ml/hr and the potential difference of 10-13 kV maintained between the nozzle and the collector. Electrospun flat sheet membranes were collected on aluminum foil coating the rotating mandrel, which could be removed for storage.

3.3.6 Viscosity of the polymer solution

The dynamic viscosity of polymer solutions was measured using a rotational viscometer Viscopad R and TR8 spindle (Fungilab, Barcelona, Spain). 7.1 ml of polymer solution, prepared as described in section 5.1.1, was transferred in the stainless steel Viscopad R solution reciprocal. The TR8 spindle was submerged in the solution and the reciprocal was mounted on the Viscopad. The reciprocal was submerged in a water bath at a set 18 °C to ensure a temperature fluctuation of no more than 0.8 °C. Viscosity measurements were recorded with a spindle speed of 20 rpm over a period of 5 minutes.

3.3.7 Membrane recovery

Sections of EHFM were obtained by cutting lengths of wire coated in electrospun material to the desired length. The sections were wetted with 70% ethanol for a few seconds after which fine tweezers were used to pull the electrospun coating off of the wire. Similarly, sections of electrospun flat sheet membranes were obtained by cutting the desired area of electrospun material coated aluminum foil and wetting it with 70% ethanol.

3.3.8 Scanning electron microscopy

Sections of EHFM and electrospun flat sheet membrane, recovered as described in section 3.3.7, were gold coated using a SC7620 Mini Sputter Coater System (Quorum Technologies Ltd, East Sussex, UK). High resolution images were taken using an environmental scanning electron microscope (SEM, Carl Zeiss Evo LS15 Variable Pressure Scanning Electron Microscope). For each sample, representative sections were imaged at four magnifications of $\times$100, $\times$500, $\times$3,000 and $\times$10,000 respectively.

3.3.9 Micro-fibre diameter and orientation analysis

Electrospun membrane micro-fibre diameter and orientation were analysed from the SEM images (n = 3) taken at 3000x using the ImageJ plugin DiameterJ. The software is able to analyse an image to determine the distribution of fibre diameters and orientations present in an image [177]. The output distribution tables were analysed with a Python script which calculated representative distributions of micro-fibre diameter and orientation for each polymer solution and pyridine concentration evaluated.

3.3.10 Optical light microscopy

Sections of EHFM and electrospun flat sheet membrane were observed using an inverted light microscope (Nikon Eclipse Ti) under a 10x magnification for any macroscopic defects.

3.3.11 Micro-computed tomography

Sections of EHFM or electrospun flat sheet membrane, obtained as described in section 3.3.7, were mounted in a custom sample holder placed vertically in the micro computerised tomography machine (μCT, SkyScan 1172, SkyScan, Kontich, Belgium). 2.5 mm sections of the membranes were scanned with a set voltage of 40 kV, current of 250 mA and no filter used. 1200 projections were then used to reconstruct images with a pixel size of 0.98 μm using the NRecon software (SkyScan 1172, SkyScan, Kontich, Belgium) Feldkamp algorithm.

3.3.12 Porosity

Three methods were used to evaluate porosity including mercury porosimetry, μCT image analysis, and gravimetric analysis

3.3.12.1 Mercury porosimetry

Mercury porosimetry is the gold standard for the measurement of porosity and pore size. Mercury porosimetry is based on the capillary law for small pores, in which the porosity is determined as the ratio of the penetrating liquid volume at low and high pressure. Additionally, for a non-wetting liquid such a mercury, the diameter of cylindrical pores may be calculated by the Washburn equation, as seen in equation 3.1.

$$D = -\frac{1}{P} 4\gamma \cos\varphi \tag{3.1}$$

Where D is pore diameter, P is pressure, γ is the surface tension of the wetting liquid, and φ is the contact angle. Porosity and pore size distributions were measured by mercury intrusion with an Autopore IV 9500 mercury porosimeter (Micromeritics Instrument Co, Norcross, GA, USA). The

porosimeter had a max pressure range of 33,000 psia enabling pore size measurement from of 360μm to 0.005μm. Sections of electrospun membrane, recovered as described in 3.3.7, weighing 50 +/- 5 mg were placed into the penetrometer cup (s/n = 14,3 bulb, 0.412 stem, powder). The penetrometer was initially inserted in the low-pressure port where gases were evacuated from the penetrometer before it was filled with mercury. The penetrometer was then transferred into the high-pressure port in which samples (n = 3) were run with a mercury filing pressure of 0.49 psia and an equilibration time of 10 s.

3.3.12.2 EHFM μCT image analysis

Reconstructed μCT images of EHFMs were analysed with a Python image analysis routine to obtain EHFM wall thickness, lumen diameter, fibre aspect ratio and porosity. To minimise the image size and processing time, the image was trimmed to the region bounded by the outermost non-background colour pixels. The reduced image was then binarized and queried using a two-dimensional 7x7 convolutional screen, highlighting 7x7 regions containing at least 6 pixels. The largest region of connected pixels was isolated, and a canny edge detection filter was applied. Non-critical pixels, i.e. those which do not result in a change in shape, were removed by contouring [178], and an ellipse was fitted using a distance of least squares algorithm [179]. As the lumen of the fibre was theoretically to be found in the centre of the fibre and have a circular diameter of 100 μm, a region of 150 pixels squared was isolated from the centre point of the ellipse from the unadulterated image. The lumen position shape and size were then identified by querying this region with the same pipeline as the entire image. The dimensions identified were used to generate a binary mask to isolate only the pixels of interest from the unadulterated original image, which were binarized using Otsu's method [180]. The mask and binarised fibre image matrices were summed. The membrane porosity was taken as the percentage of the summed binarised imaged over that of the binary mask. Wall thickness was found by calculating the mean distance between 100 points around the lumen and outer wall bounding ellipses.

3.3.12.3 Gravimetric porosimetry

To determine the porosity of EHFMs through gravimetric analysis, the mean volume per unit length was taken as the area bounded by the inner and outer bounding ovals detected in section 3.3.12.2 multiplied by the length of section weighed. EHFM sections, obtained as in section 5.1.7, were weighed with a mass balance (Precisa 125A, Precisa, Livingston, UK). Density of each section was calculated from the measured mass over the mean section volume. Porosity was taken as the density of the section over that of raw blended PDO and PCL which were taken to have a density of 1.318 and 1.145 g/cm^3, respectively.

3.3.13 Electrospun flat sheet membrane thickness

Electrospun flat sheet membrane wall thickness was determined from reconstructed μCT images, captured as described in section 5.1.9, and analysed with a Python image analysis routine. Briefly, To remove background noise, the mean background pixel value was evaluated from a pre-selected background region of the image. All pixels below the mean value of this region were set to zero. A Gaussian blur was applied to mitigate the formation any artificial holes in the membrane layer after which the image was binarised using Otsu's method [180]. The binarized image was queried using a two-dimensional 2x2 convolutional screen, highlighting 2x2 regions containing at least 2 pixel. The coordinates of all pixels were recorded. The axis by which the membrane ran was evaluated by considering the interquartile range of the pixel coordinates in each axis. The axis with the largest range was taken as the long axis. Consequently, membrane thickness at each pixel height was taken as the coordinate range at each pixel height in the short axis. By multiplying the range by the pixel size the electrospun flat sheet membrane thickness was determined.

3.3.14 Mechanical Properties

The mechanical properties of EHFMs were determined through uni-axial tensile testing. 20 cm of dry sample ($n \geq 3$) was evaluated using a Zwick machine (5kN KAP-TX, Zwick Roell Group, Ulm, Germany) fitted with a custom mount, in which 8 cm of sample was deformed between two mount posts. As recommended for the tensile testing for vascular grafts, the deformation speed was set to 50 mm/s [93]. The resulting force extension data was evaluated using a Python script, which fitted a straight line to the first points until the R^2 value was lower than 0.95. This point was taken as the yield point and the gradient of the fitted line as the Young's modulus (MPa). While median values of the force at break (N), ultimate stress (MPa), and breaking strain (%) were taken as the first point at which a force was recorded with less than 95% of that of the maximum recorded force.

3.3.15 Tortuosity

Membrane tortuosity was determined from the measured effective and bulk water diffusion coefficients of glucose according to equation 3.2, in which ϕ is the membrane porosity, D_e^G is the effective glucose diffusion coefficient and D_w^G is the bulk water glucose diffusion coefficient.

$$\tau = \frac{\phi D_e^G}{D_w^G} \tag{3.2}$$

The bulk water diffusion coefficient of glucose at a given temperature was interpolated from a quadratic fit of experimental data using the dependence between log D_w^G and 1/T [181]. The effective diffusion coefficient was measured with a diffusion cell built to similar specification as Suhaimi *et al.* and C.Chenu *et al.* [182, 183]. The diffusion cell, as seen in the supplementary figure S3.1, consisted of two jacketed polyacrylate chambers of identical volume, designed in house and 3D printed (3D LifePrints, Headington, UK). To maintain a constant temperature the chamber jackets were filled and circulated with deionized water with a flow rate of 20 ml/min. The cell was assembled by sandwiching

a ⊘1/2" silicon gasket (Cole-Parmer, Illinois, United States) and an electrospun flat sheet membrane, produced as described in section 5.1.2.2 and prepared as described in section 3.3.7, between the two chambers and then screwing the chambers together. To prevent the formation of a concentration gradient in the chambers, each was fitted with a Rushton turbine impeller driven by a DC motor (McLennan Servo Supplies, Aldershot, UK) at 40 rpm. To measure the change in glucose concentration across the membrane the working fluid from the donor chamber was continuously pumped from the sample ports at 1 ml/hr through an in-line flow through B.LV5 biosensor (Jobst Technologies, Freiburg im Breisgau, Germany) and back to the chamber. As the system is closed, the glucose concentration in the receptor cell was taken as the initial glucose concentration minus the concentration in the donor cell. To enable the use of the sensors, a buffer solution was used as the working fluid which was comprised of; 94.12 mM NaCl, 5.37 mM KCl, 1.36 mM $CaCl_2 \cdot 2H_2O$, 0.86 mM $Na_2HPO_4 \cdot 7H_2O$, 0.81 mM $MgCl_2 \cdot 6H_2O$, 25 mM HEPES and 26 mM $NaHCO_3$ dissolved in deionized water. To ensure the accurate measurement of glucose concentrations, between each experiment the sensor was calibrated with solutions of known glucose concentration in working fluid. Between each experiment both chambers were washed with deionized water prior to assembly. The chambers were then filled with fresh buffer solution through the sample ports. The ports on the receptor chamber were sealed and 3ml of buffer solution was removed on the donor side to be replaced with a 3ml bolus shot of 833 mM concentrated glucose solution. The sensor was connected to the ports of the donor side and the Rushton turbine was started. After 30s the pump circulating the sensors was started, glucose concentration was then measured every 10 s for 24 hours or until equilibrium was reached. The effective diffusivity was taken as the straight line gradient of change in the natural log of the glucose concentration difference with time according to equation 3.3 [184].

$$\ln\left(\frac{C^G_{D,t}}{C^G_{D,t} - C^G_{D,t=0}}\right) = -\frac{D^G_e A}{l}\left(\frac{1}{V_A} + \frac{1}{V_B}\right)(t - t_0) \tag{3.3}$$

In which, $C^G_{D,t=0}$ is the initial glucose concentration in the donor chamber, $C^G_{D,t}$ is the glucose concentration in the donor chamber at time t, D^G_e is the effective diffusion coefficient of glucose, A is membrane area, l is membrane thickness, V_A is the volume of the donor chamber, V_B is the volume of the receptor chamber, t is time and t_0 is the initial time.

3.3.16 Permeability

Electrospun flat sheet membrane pure water permeability was measured with a Sterlitech HP4750 dead-end filtration cell. For each experiment an electrospun flat sheet membrane disk, produced and prepared as described in section 5.1.2.2 and section 3.3.7 respectively, was cut with a 51 mm diameter. The electrospun flat sheet membrane disk was placed on a custom membrane support layer, with 1 mm holes equally spaced with 1.5 mm between the centre of each hole, and sandwiched between two rubber gaskets in the filtration cell, giving an effective membrane area of $1.13 \times 10^{-3}\text{m}^2$. The cell was filled with 300 ml of deionized water and pressurized using compressed air from a cylinder. The tube from the cylinder was 2.01 m long and had an inner diameter of 6.4mm. On the permeate side water flowed through a 27 cm long 1.67 mm ID tube into a receptacle on a mass balance (AB54-2, Mettler Toledo, Ohio, US). By slowly opening the cylinder regulator the outlet pressure was set to 68947.6 Pa while the 300ml of dionized water was discharged, ensuring the membrane was fully wetted before permeability was measured. For each run the pressure drop from the gas cylinder to the filtration cell and from the filtration cell to the collection reciprocal was calculated with the Hagen–Poiseuille equation as given by equation 3.4.

$$\Delta P = \frac{8\mu LQ}{\pi R^4} \tag{3.4}$$

where ΔP is pressure drop, μ is the dynamic viscosity of the working fluid, L is the length of tube, Q is volumetric flow rate and R is the tube radius. By taking the inlet gas and outlet water volumetric flow

rate to be the same as the permeate flow rate. The cell was refilled with 30 ml of deionized water and the cell was pressurised at the set pressure previously determined. The permeate pure water mass flux was recorded through the RS232 output of the balance until the water in the filtration cell was depleted. The membrane pure water permeability, k, was calculated according to equation 3.5.

$$k = \frac{q\mu l}{\Delta P} \tag{3.5}$$

Where q is the pure water flux, μ is the dynamic viscosity of water, l is membrane thickness, and ΔP is the trans-membrane pressure.

3.3.17 Particle rejection

Electrospun flat sheet membrane particle rejection studies were carried out in a Sterlitech HP4750 dead-end filtration cell. A test slurry of micro polystyrene balls (Duke Scientific, CA, US) was prepared by combining slurries of defined particle size including 1, 4.7 ± 0.4 , 10, 15.5 ± 0.6, 21.4 ± 0.7, 25.2 ± 1.0 , 26.1 ± 1.0, and 30μm particles and diluting them in 600 ml of deionized water. Electrospun flat sheet membranes were prepared as in section 3.4.7 and the filtration cell was filled with 30 ml of the test slurry after being rinsed with deionized water. Trans-membrane pressure was set as in section 3.4.7 and the permeate was collected in a 50 ml falcon tube. Particle size counts of the test slurry and permeate were measured with a multisizer fitted with a 30 μm aperture (Beckman Coulter Multisizer 4e, Beckman Coulter, CA, US) by diluting 10 μl samples (n = 9) in 10 ml of filtered Isoton II buffer (Beckman Coulter, CA, US). From these counts particle rejection was calculated with equation 3.6 [185].

$$R = \left(1 - \frac{C_{per}}{C_{feed}}\right) \times 100 \tag{3.6}$$

where R is particle rejection, C_{per} and C_{feed} are the permeate and feed particle concentration.

3.3.18 Maintenance of BALB/c 3T3 cells

BALB/c 3T3 cells (Merck, Germany) were maintained at 37 °C in 5% CO2 in Dulbecco's Modified Eagle Medium (DMEM, Sigma-Aldrich, UK) supplemented with 10% (v/v) newborn calf serum (Sigma-Aldrich, UK), 4 mM l-glutamine (Thermo Fisher Scientific, UK), 20 mM HEPES (Thermo Fisher Scientific, UK), and 1% (v/v) penicillin/streptomycin (Invitrogen, UK). Cells were cultured in T25 tissue culture flasks (Corning, NY,US). The culture media was changed every third day. Once cells had reached approximately 90% confluency, they were mechanically scraped and sub-cultured under the same conditions to allow proliferation. Cells were regularly checked for Mycoplasma infection using a MycoAlert testing kit (Lonza, UK), according to the manufacturer's instructions.

3.3.19 NRU cytotoxicity assay

For the neutral red uptake (NRU) cytotoxicity test, BALB/c 3T3 cells which were seeded into 96-well plates (1×10^4 cells/well) and maintained in culture for 24 h to form a sub-confluent monolayer. Subsequently, cells were exposed to the test compounds over a range of concentrations. After 24 h exposure, NRU was determined for each treatment concentration and compared to that determined in control cultures – cell viability was calculated as the percentage of viable cells in the control group (cell culture media only). For the treatment extracts, all compounds were extracted at a ratio of 0.1 mg/mL in medium for 72 h before being added to cell culture.

3.3.20 Data and statistical analysis

All python rutines used for the analysis of experimental data presented herein may be found at: `https://github.com/ristojm`. Statistical analysis was performed with the SciPy.stats Python package in each data analysis routine. To determine the statistical significance of the results, distributions were compared using a two-way Mann-Whitney U test. Results were considered significant at $p<0.05$.

3.4 Results and Discussion

3.4.1 Spinnability of polymer solutions

3.4.1.1 Effect of mass ratio

To determine a suitable mass ratio at which to blend PCL and PDO for electrospinning, solutions with mass ratios as described in table 3.1 were prepared with a total polymer concentration of 9.25 % and 5 ppm of pyridine.

Table 3.1. Mass ratio of PCL and PDO evaluated and the resultant spinnability and presentation of fibre defects of the solutions spun

PCL/PDO Mass Ratio	Spinnable?	Beading?	Viscosity (cP)	S.D. (cP)
0	Yes	No	896	8
0.25	Yes	Yes		
0.43	Yes	No	1005	12
0.58	Yes	Yes		
0.70	Yes	Yes	1140	7
0.83	No	N/A	1510	3
0.84	Yes	Yes		
0.85	No	N/A		
0.86	Yes	Yes		
0.86	Yes	Yes		
0.87	Yes	Yes	1313	12
1	Yes	No	3794	9

To identify solutions theoretically capable of producing electrospun material free of beading, the viscosity of the solutions was measured. The viscosity of the blends was bounded by that of the neat polymer solutions. The blended polymer solutions were spun and screened for defects such, as beading or droplets, under an optical microscope, those which appeared defect free were further evaluated with SEM. Of the solutions evaluated, only the neat solutions and that with a PCL/PDO mass ratio of 0.43 were both spinnable and produced defect free micro-fibres. Defects in electrospun material occur due to an imbalance electrostatic repulsion and Rayleigh surface tension instabilities [32]. The persistence of beading may be explained by the immiscibility of PCL and PDO as this would inhibit polymer chain

entanglement thereby leading to the formation of beads [186, 32].

3.4.1.2 Effect of total polymer mass

Having identified a mass ratio at which defect free electrospun micro-fibres may be produced, polymer solutions with varying total polymer masses at a mass ratio of 0.43 PCL: PDO, as described in table 3.2, were evaluated. All solutions with a total polymer concentration ranging between 7.05

Table 3.2. Effect of total polymer mass on PCL/PDO polymer solution spinability and presentation of fibre defects

Total polymer concentration (% w/v)	Spinnable?	Beading?
7.05	Yes	No
9.25	Yes	No
12.33	Yes	No
15.86	Yes	No
19.38	Yes	No
22.91	No	N/A
26.43	No	N/A

to 19.38 % could be electrospun and produced defect free micro-fibres. From 22.91 % and above the solutions were too viscous to be pumped down capillary tubing and consequently were not suitable for electrospinning.

3.4.2 Electrospun hollow fibre membrane micro-topology

3.4.2.1 Effect of total polymer mass

To determine the effect of total polymer concentration on micro-fibre diameter and orientation, representative SEM images of EHFMs produced with each polymer solution were captured, as seen in figure 3.2A. As seen in figure 3.3A the median micro-fibre diameter increased from 1.03 to 1.75 μm with an increase in total polymer concentration from 7.05 to 15.86 %. However, there was no significant change in micro-fibre diameter between 15.86 and 19.39 %. Furthermore, the increase in micro-fibre diameter was accompanied by an increase in spread.

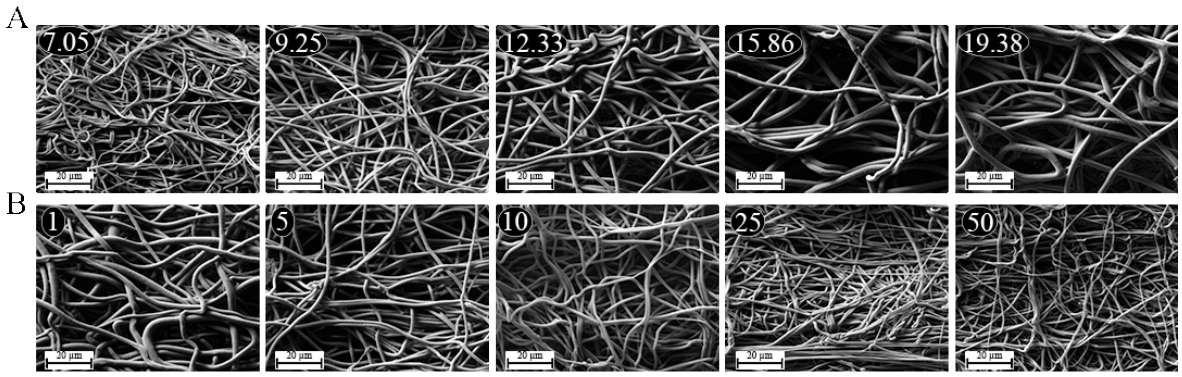


Figure 3.2. SEM micrographs of EHFMs produced from a blended polymer PCL/PDO solution with a mass ratio of 0.43 and; (A) a total polymer concentration of 7.05, 9.25, 12.33, 15.86, and 19.38 %, respectively, and doped with 5 ppm pyridine. (B) a total polymer concentration of 9.25 % and doped with 1, 5, 10, 25, and 50 ppm pyridine.

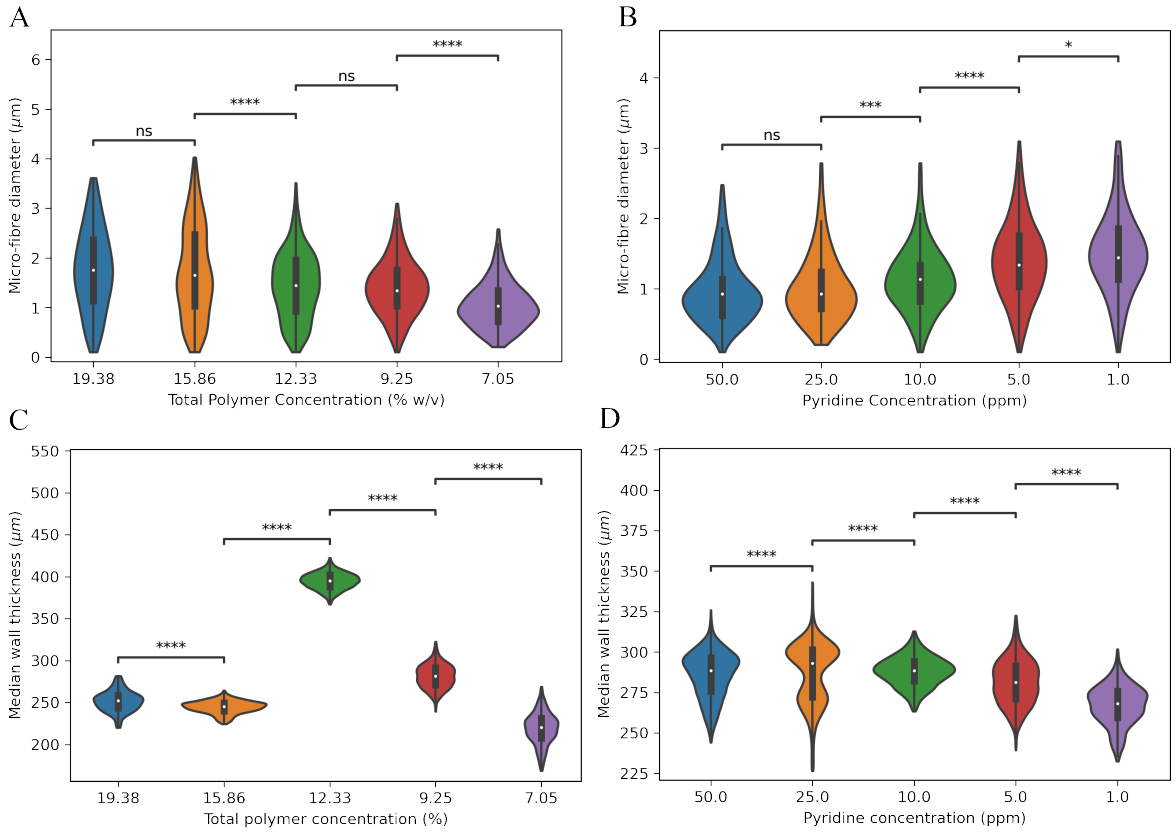


Figure 3.3. EHFM micro-fibre diameter distributions determined from the analysis of SEM images captured at x3000 (n=3) produced with a blended polymer PCL/PDO solution with a mass ratio of 0.43 and a total polymer concentration (A) ranging between 7.05 and 19.38 % doped with 5 ppm pyridine, and (B) of 15.85 % doped 1, 5, 10, 25, and 50 ppm pyridine. Median wall thickness of PCL/PDO EHFMs (n=3) produced with a polymer solutions containing a total polymer concentration; (C) ranging between 7.05 and 19.38 % and doped with 5 ppm of pyridine; (D) of 15.85 % and doped with 0,1, 5, 10, 25, and 50 ppm pyridine as determined through the analysis of EHFM cross sectional images captured with μCT.

Previously, electrospun materials with randomly aligned micro-fibres were found to have mechanical properties akin to that of medium sized arteries, matrices of unaligned micro-fibres were therefore desired [116, 114, 108]. For all total polymer concentrations no more than 2 % of micro-fibres were oriented in any given direction and were therefore be considered randomly aligned, as seen in supplementary figure S3.2A.

3.4.2.2 Effect of pyridine concentration

The effect of pyridine concentration on micro-fibre diameter and orientation was determined by spinning the solution with a total polymer concentration of 9.25 % with different pyridine concentrations as seen in the SEM images captured in figure 3.2B. As seen in figure 3.3B, The median micro-fibre diameter decreased with an increase in pyridine concentration from 1 – 25 ppm; however, there was no significant change in fibre diameter from 25 – 50 ppm, which is in agreement with the findings of Lach et al., [176].

As before, irrespective of pyridine concentration the meshes were found to be unaligned, with no more than 3.5% of the micro-fibres aligned in any given direction, as seen in supplementary figure S3.2B.

Further to the micro-topology of the EHFMs the effect of total polymer pyridine concentration on EHFM gross morphology was also considered.

3.4.3 Electrospun hollow fibre membrane geometry and wall thickness

As electrospun material is very soft and liable to compression when measured on contact with calipers, μCT image analysis, imaged as described in section 5.1.9 and analysed as described in section 3.3.12.2, was used as none contact and none destructive means for analysis. Cross sections of EHFMs as imaged with μCT may be seen in figure 3.4.

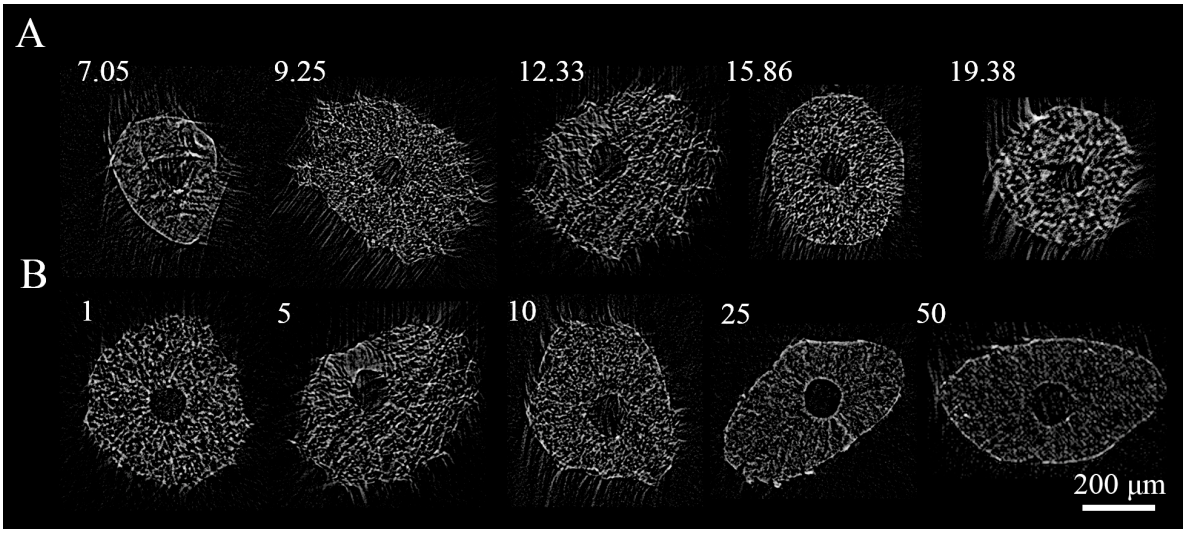


Figure 3.4. µCT images illustrating the cross sectional morphology of EHFMs produced from a blended PCL/PDO polymer solution with a mass ratio of 0.43 and; (A) a total polymer concentration of 7.05, 9.25, 12.33, 15.86, and 19.38 % doped with 5 ppm pyridine, and (B) a total polymer concentration of 9.25 % doped with 1, 5, 10, 25, and 50 ppm pyridine, respectively.

With an increase in total polymer concentration EHFM wall thickness was not seen to change, except at 12.33 % which had a wall thickness almost double that of the other concentrations, as seen in figure 3.3C. This change may have been due to instabilities during the electrospinning process which led to uneven micro-fibre deposition. Evidence for the uneven deposition may be seen in the increase in ovality in EHFMs produced with a total polymer concentration of 12.33 % compared to those produced from any of the other total polymer concentrations tested, as seen in figure 3.4A and quantified in figure S3.3A in the supplementary figures.

An increase in pyridine was found to result in an increase in the median EHFM wall thickness, as seen in figure 3.3D. This increase in wall thickness can be explained by the increase in EHFM ovality with pyridine concentration, as seen in figure 3.4B and quantified in figure S3.3B in the supplementary figures. As oxygen and nutrient concentration is only altered by the action of cells, diffusive mass transfer through the EHFM walls will not inhibit their ability to support cell growth in 3D tissue culture.

As it is possible to tune micro-fibre diameter through polymer and pyridine concentrations, the solution with a total polymer concentration of 15.86 % was selected as the polymer solution of preference

for future analyses, while pyridine concentration continued to be varied to facilitate the study of the effect of changes in micro-fibre diameter.

3.4.4 Porosity

With an increase in pyridine concentration the porosity, as measured with mercury porosimetry was found to increase, as seen in figure 3.5. However, the porosities measured were far below that of other comparable electrospun materials [119, 168]. To check these findings, μCT image analysis and gravimetric analysis were carried out as alternative measurements taken through operations based on different principles of measurement. Each of these techniques, therefore, evaluates porosity in a slightly different way. Mercury porosimetry is only capable of measuring open pore structures, while μCT and gravimetric analysis measure the total porosity, including closed and open but inaccessible pore structures.

The porosity the EHFMs was evaluated from representative samples using μCT, by this means, as seen in figure 3.5, porosity was found to range between 94-96% with no significant change irrespective of pyridine concentration. Through gravimetric analysis, the median porosity was found to range between 88-92%, again, with no significant change with an increase in pyridine concentration.

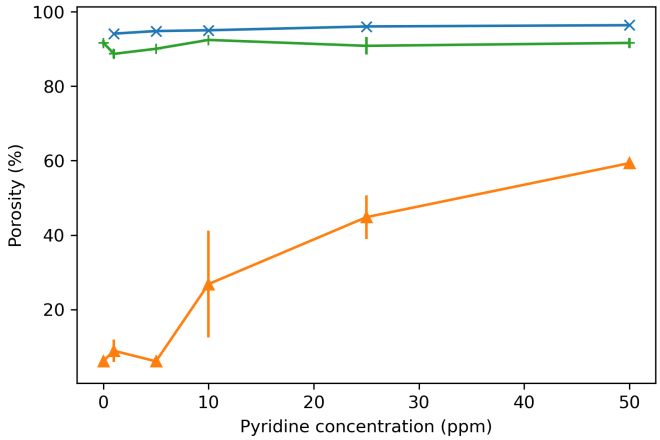


Figure 3.5. Porosity of EHFMs (n≥3) produced from a blended PCL/PDO polymer solution with a mass ratio of 0.43 and a total polymer concentration of 15.85 % and doped with 0 - 50 ppm pyridine as measured with (orange) mercury porosimetry, (green) gravimetric analysis, and (blue) μCT image analysis.

The miss-match between the porosity measured with mercury porosity compared to that measured with μCT and gravimetric analysis may have arisen due to the soft and compliant nature of electrospun material. As mercury porosimetry depends on the penetration of a non-wetting fluid into the material while under pressure to measure porosity and pore size, the soft electrospun material may buckle under the pressure required to penetrate the pores in the material. This would result in measurements lower than the true values being recorded. Consequently, alternative methods which do not rely on a penetrating fluid should be used when measuring the porosity of soft materials.

Porosity is determined from the ratio of white to black pixels in the detected volume in μCT image analysis. While, gravimetric analysis utilises the volume measured with μCT and the mass recorded to determine porosity. Although both of these methods use some measurements determined through μCT, the means by which porosity is calculated is different. Given the close agreement of the porosities measured with μCT and gravimetric analysis, it is likely these measurements better reflect the true value and suggests that mercury porosimetry may not be suitable for measuring the porosity of electrospun materials.

To determine whether the membranes have functional characteristics akin to that of native vasculature we first consider their mechanical properties.

3.4.5 Mechanical Properties

The mechanical properties of the EHFMs produced with each of polymer solution and 5 ppm pyridine were evaluated through uni-axial tensile testing, the resulting stress strain graphs may be seen in figure 3.6A.

Similarly, the mechanical properties of EHFMs produced with a polymer solution with a total polymer concentration of 15.85 % spun with pyridine concentrations ranging from 1-50 ppm were

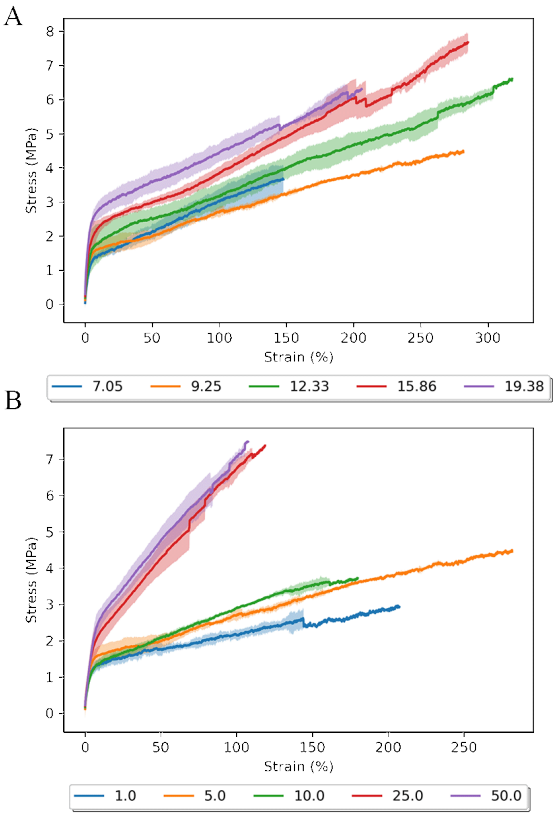


Figure 3.6. Stress-strain profiles of EHFMs (n=3) produced from a blended PCL/PDO polymer solution with a mass ratio of 0.43 and a total polymer concentration (A) ranging from 7.05 - 19.38 % and doped with 5 ppm pyridine, and (B) of 15.85 % and doped with 1 - 50 ppm pyridine.

evaluated in the same way, the stress strain profiles of which can be seen in figure 3.6B. Mechanically defining metrics, including the Young's modulus, yield stress and strength, ultimate tensile stress, and maximum strain determined from these profiles may be seen in table 3.3. With an increase in polymer and pyridine concentration there was an increase in the median yield stress. However, there was no statistically significant trend in the change in the Young's modulus, yield strain, ultimate tensile stress and maximum strain.

By comparing the mechanical properties to the mechanical profile of medium sized human arteries defined in table 3.3 we evaluated the degree by to which EHFMs mechanically mimic the properties of native human vasculature. As the EHFMs were found to be comprised of randomly aligned micro-fibre meshes the radial and axial properties were taken to be the same. From these comparisons, seen in table 3.3, it is evident that for all polymer solutions and pyridine concentrations tested that the EHFMs are

Table 3.3. Comparison of the mechanical properties of healthy medium sized human arteries with those of EHFM in which yellow, green, and red cell colours signify properties below, within, or above the range defined by that of the healthy medium sized human arteries.

	EHFM polymer solution					Pyridine concentration (ppm)					Range of medium sized healthy human arteries		
Property	7.05	9.23	12.33	15.86	19.38	1	5	10	25	50	Max	Min	Ref.
Radial Young's modulus (MPa)	2.75	3.51	3.35	3.69	3.71	1.89	3.51	2.83	3.81	4.64	23.70	0.22	[94, 95]
High Axial Young's modulus (MPa)	2.75	3.51	3.35	3.69	3.71	1.89	3.51	2.83	3.81	4.64	8.00	2.25	[94, 96]
Low Axial Young's modulus (MPa)	2.75	3.51	3.35	3.69	3.71	1.89	3.51	2.83	3.81	4.64	3.60	0.15	[91, 97]
Radial Ultimate Tensile Strength (MPa)	3.77	3.39	5.96	6.69	6.07	2.78	3.39	3.62	5.53	6.65	10.09	1.09	[98, 99]
Axial Ultimate Tensile Strength (MPa)	3.77	3.39	5.96	6.69	6.07	2.78	3.39	3.62	5.53	6.65	4.10	0.04	[94, 100]
Radial Maximum Strain (%)	39.31	39.87	73.26	57.69	45.16	40.06	39.87	38.89	19.91	23.36	99.40	40.80	[99]
Axial Maximum Strain (%)	39.31	39.87	73.26	57.69	45.16	40.06	39.87	38.89	19.91	23.36	242.00	134.00	[94]
Yield Stress (MPa)	0.70	0.93	0.90	1.87	2.89	1.34	0.93	0.79	1	0.87	N/A	N/A	N/A
Yield Strain (%)	0.26	0.26	0.28	4.53	10.97	7.75	0.26	0.28	0.27	0.21	N/A	N/A	N/A

within the range of the radial Young's modulus. Similarly, with the exception of those produced with a polymer solution with a total polymer concentration of 7.05 % and doped with 5 ppm pyridine, the EHFMs were found to be within the range of the high axial Young's modulus. EHFMs produced from a polymer solution with a total polymer concentration greater than and including 12.33 % had a Young's modulus which exceeded the low axial Young's modulus of medium sized human arteries. For the radial and axial ultimate tensile strength all EHFMs produced were within the range or exceed the range of medium sized arteries. Average resting blood pressure is 120mmHg (16 kPa) while maximal blood pressure while under stress is approximately 202.5 mmHg (27 kPa) [187]. Comparing the ultimate tensile strength of the EHFMs with these pressures, it is evident that all EHFMs produced should not burst while operating within physiologically relevant fluid pressures. While both the axial and radial maximum strains were found to be below the range of medium sized healthy arteries, the yield stress for all EHFMs tested was above the maximal physiological blood pressure. The EHFMs should therefore only deform elastically under physiological conditions and as such the low yield strain should therefore not present an issue.

The reasonable mechanical match between EHFMs and native human vasculature makes them a good candidate as a scaffold for vascular tissue engineering, however, to support cell growth sufficient nutrient supply within the matrix is vital. By evaluating the tortuosity of the EHFMs, we consider the limitation to diffusive nutrient transfer created by the EHFM walls.

3.4.6 Tortuosity

Models for nutrient transport are typically fitted to experimental data to determine effective diffusivities through HFMs. Nutrient transport models typically fitted to HFMs nutrient transport data assume a rigid wall. In contrast to most HFMs, EHFMs have a low Young's modulus similar to human arteries and therefore this assumption does not hold. Given the unique method by which EHFMs are produced and their isotropic structure, membranes with other conformations may be produced from the same micro-fibre mesh. Consequently, electrospun flat sheet membranes were produced. To validate this assumption the micro-fibre diameter and orientation distributions of electrospun flat sheet membranes were evaluated. As seen in the supplementary figure S3.4, as in the EHFMs, as pyridine concentration increases from 1-50 ppm the micro-fibre diameter decreases from 2.62 to 2.21, 2.41, 2.02, 1.86, and 1.84 μm, respectively. Having ensured structural comparability of the electrospun flat sheet membranes and EHFMs, the tortuosity of the electrospun flat sheet membranes was evaluated. As membrane thickness is a key parameter when determining the membrane tortuosity the wall thickness of the electrospun flat sheet membranes was measured through μCT image analysis. Irrespective of pyridine concentration, electrospun flat sheet membrane wall thickness was found to be around 200 μm, as seen in supplementary figure S3.5. Tortuosity was found to decrease with an increase in pyridine concentration from 6.01 to 3.94, as seen in figure 3.7. Compared to other measurements of electrospun flat sheet membrane tortuosity these values are higher, with PCL and PLLA membranes with median micro-fibre diameters of 3 and 1.85 μm, respectively, having previously being found to have a tortuosity ranging between 1.6-2.5 and 2.7-3.0 [182].

As an increase in tortuosity results in an increased effective diffusivity a decrease in tortuosity results in improved nutrient exchange. This suggests that EHFMs produced with higher pyridine concentrations are likely to be better for cell growth.

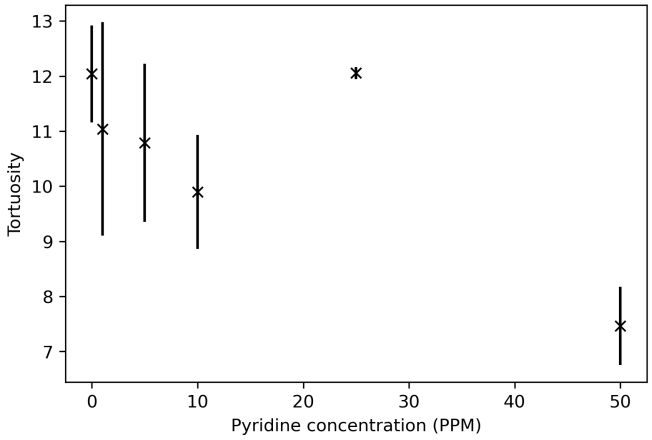


Figure 3.7. Tortuosity of electrospun flat sheet membranes (n=3) produced from a blended PCL/PDO polymer solution with a mass ratio of 0.43 and a total polymer concentration 15.86 % and doped with 1- 50 ppm pyridine.

3.4.7 Permeability

Membrane permeability should also be considered when evaluating the suitability of EHFMs for tissue culture purposes as this will dictate the degree of nutrient exchange facilitated by advective mass transfer. Similar to the measurement of effective diffusion coefficients in HFMs, when measuring the permeability of HFMs models for fluid flow in rigid tubes are typically fitted to experimental data. As the assumption of rigid tube walls does not hold for EHFMs, electrospun flat sheet membranes were used to measure the permeability. With an increase in pyridine concentration from 0 to 50 ppm, membrane permeability, as seen in figure 3.8, was found to range between 1.21 - 1.89 $\times 10^{-14}$ m^2. micro-fibre diameter has been suggested to play a dominant role in permeability, such that an increase in micro-fibre diameter is associated with an increase in permeability [188]. Previously permeabilities of electrospun flat sheet membranes produced from cellulose and polysulfone, with micro-fibre diameters ranging between 4.7-16.4 and 0.3-0.8 μm have been measured [189, 190]. The permeability of both these membranes were orders of two and one orders of magnitude lower than the PCL/PDO membrane tested here. PAN electrospun membranes have been found to have a permeability similar to that of the PCL/PDO membranes. However, micro-fibre diameters for these membranes were not reported limiting comparisons made [191]. Compared to electrospun membranes with similar sized micro-

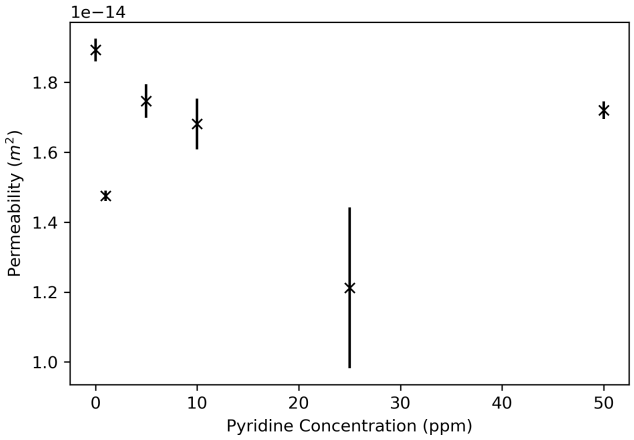


Figure 3.8. Permeability of electrospun flat sheet membranes (n≥3) produced from a blended PCL/PDO polymer solution with a mass ratio of 0.43 and a total polymer concentration 15.86 % and doped with 1- 50 ppm pyridine.

fibres the PCL/PDO membranes presented here have very high pure water permeabilities. These high permeabilities may be due to the high porosity of these membranes. However, microfiltration membranes more widely have pure water permeabilities which range between 1×10^{-16} to 1×10^{-13} these permeabilities are therefore well within the expected range [23].

3.4.8 Particle rejection

HFM bioreactors have been used to study cell behaviour for a wide range of both single cell types, such as endothelial cells, and co-culture systems, including umbilical cord derived mononuclear cells [6, 61]. When supporting growth of single cell types, cells are either grown in the lumen or the extra-capillary space between the membranes. Owing to size exclusion facilitated by membrane pore size co-culture systems may be developed such that the cell types are kept separate throughout the culture, with one population in the lumen while the other is retained in the extra-capillary space. Conversely, it is important that for membranes intended to be used as scaffolds, that the pore size is sufficient for cell ingress. The size exclusion capacity of a membrane may be functionally quantified as the particle cut off size. The particle cut off size of EHFMS was evaluated, as described in section 3.3.17. The particle rejection size was found to decrease with an increase in pyridine concentration from 5.8 to 4.8 μm, as seen in figure 3.9.

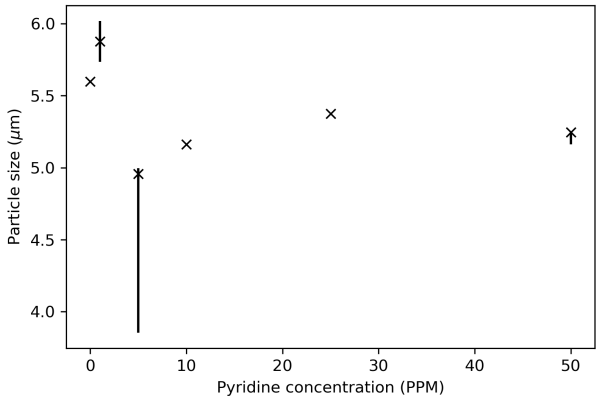


Figure 3.9. Particle cut size off size of electrospun flat sheet membranes (n=9) produced from a blended PCL/PDO polymer solution with a mass ratio of 0.43 and a total polymer concentration 15.86 % and doped with 1- 50 ppm pyridine.

Previously infiltration of smooth muscle cells have been shown to size excluded by pore sizes smaller than 7.46 µm [74, 106]. As the particle size cut off were found to be below this size, EHFMs may be used to facilitate non-integrated co-culture systems. Previously electrospun materials have been combined through a two step manufacturing step, first an inner layer mimicking the tunica initima and a second to mimic the medial layer [117, 173]. In these constructs the inner layer has ensured the partitioning of endothelial cells from the media layer, while the second layer facilitated the integration of smooth muscle cells. Similarly, the membranes described here may be combined with a secondary scaffold to create an artificial vascular graft or model. Furthermore, it is likely that as the PCL/PDO in the membrane degrades that pore size will increase enabling the integration of cells into the electrospun matrix.

3.4.9 Biocompatibility

In addition to appropriate morphological and functional characteristics to ensure EHFMs are suitable to support 3D tissue culture or as an *ex vivo* model for vasculature, it is essential that materials used for their production are non-cytotoxic.

ISO 10993-1 lays out standards for biological evaluation of medical devices in which ISO 10993-5

specifies testing procedure for *in vitro* cytotoxicity [192, 193]. Materials were prepared in line with ISO 10993-12 and tested as described in section 3.3.19 [194]. As seen in figure 3.10, all material tested were found support cell growth such that the NRU absorbance measured was above 75% of cells grown in the presence of fresh media only. Irrespective of the pyridine concentration used below 50 ppm, all EHFMs tested are therefore non-cytotoxic.

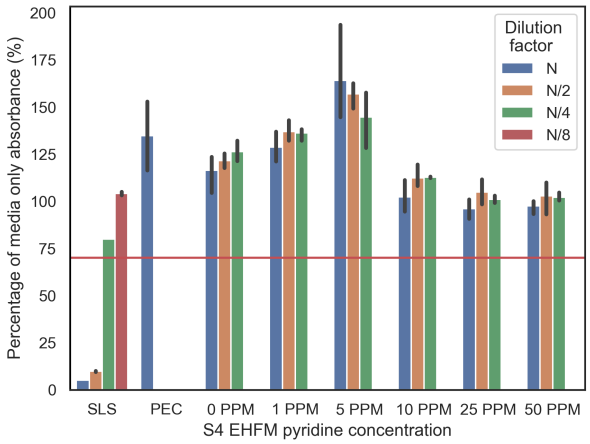


Figure 3.10. Cytotoxicity of EHFMs (n=3) produced from a blended PCL/PDO polymer solution with a mass ratio of 0.43 and a total polymer concentration 15.86 % and doped with 1- 50 ppm pyridine as determined by the NRU test. N represents undiluted extract. N/2, N/4, and N/8 represent 2-fold, 4-fold, and 8-fold dilutions of N, respectively. SLS (sodium dodecyl sulphate) represent positive control group; PEC (polyethylene caps) represents negative control group.

3.5 Conclusion

We present the development of a novel method for the continuous production of EHFMs. Pyridine has previously been used to augment micro-topographical and mechanical properties of electrospun material. It was hypothesised that blended PCL and PDO, doped with pyridine, may be used to produce EHFMs with micro-typographical structure and functional characteristics akin to medium sized human arteries. EHFMs produced with such properties may be used as a substrate to support cell growth in 3D tissue culture, without disruption of passive mechanical cues or as an *ex vivo* model for vasculature. Consequently, we demonstrate that PCL and PDO may be solvent blended to produce defect free micro-fibre meshes at a mass ratio of PCL/PDO of 0.43. Micro-fibre diameter was shown to be controllable with both total polymer and pyridine concentration and found to range between 1.03 and

1.75 μm in diameter. While gross morphological characteristics were found to be sensitive to pyridine concentration. Below, 25 ppm a regular cylindrical gross morphology was maintained, while at and above this concentration EHFMs became oval. EHFM porosity was measured with three methods, utilising three separate principals of operation. Mercury porosimetry was found to be unsuitable as the high operating pressure used resulted in the the soft electrospun material buckling. EHFMs were instead found to be 88-92% porous, as measured with gravimetric analysis. As determined through uni-axial tensile testing, EHFMs were found to have mechanical properties within the normal range of medium sized human arteries. Tortuosity was found to decrease with pyridine concentration, ranging from 6.0 - 3.9, while permeability ranged between 1.21 - 1.89 $\times 10^{-14}$ m^2, respectively. Particle rejection was found to range from 5.8 - 4.8 μm, and consequently cell ingress in likely to be inhibited such that EHFMs may facilitate isolated co-culture of cell types. Finally, irrespective of pyridine concentration all EHFMs produced were found to be non-cytotoxic. We therefore conclude that, EHFMs display morphological and functional characteristics akin to that of medium sized human arteries and may be useful as, a substrate to support cell growth without disrupting passive mechanical cues, an *in vitro* models for vasculature, or for the continuous production of multi-layer artificial vascular grafts.

3.6 Appendix

3.7 Supplementary section

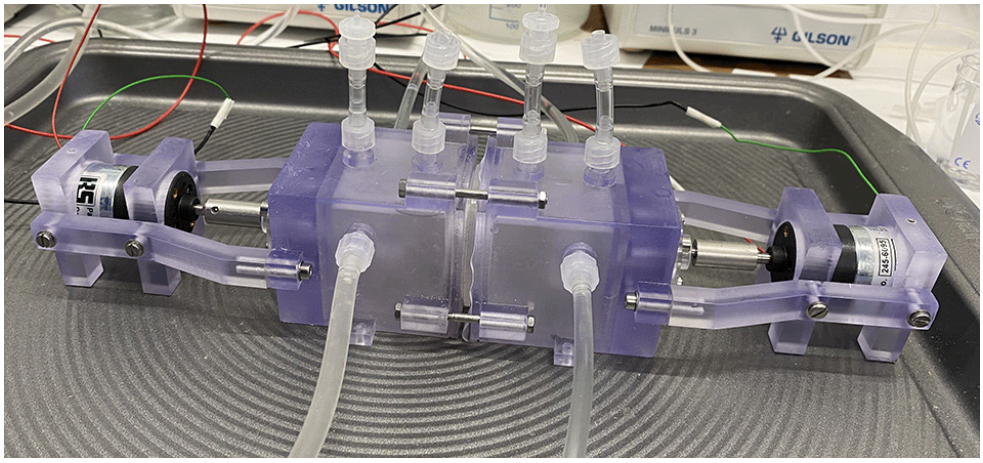


Figure S3.1. Assembled diffusion cell with electrospun flat sheet membrane sandwiched between two chambers fitted with Rushton turbine impellers. Each chamber has ports on the side to allow water to flow through the jacketed layer to maintain a constant temperature. Atop each chamber there are two sampling ports to facilitate the initial filling of the cell and subsequent circulation of the working fluid to sensors to enable the monitoring of glucose concentration.

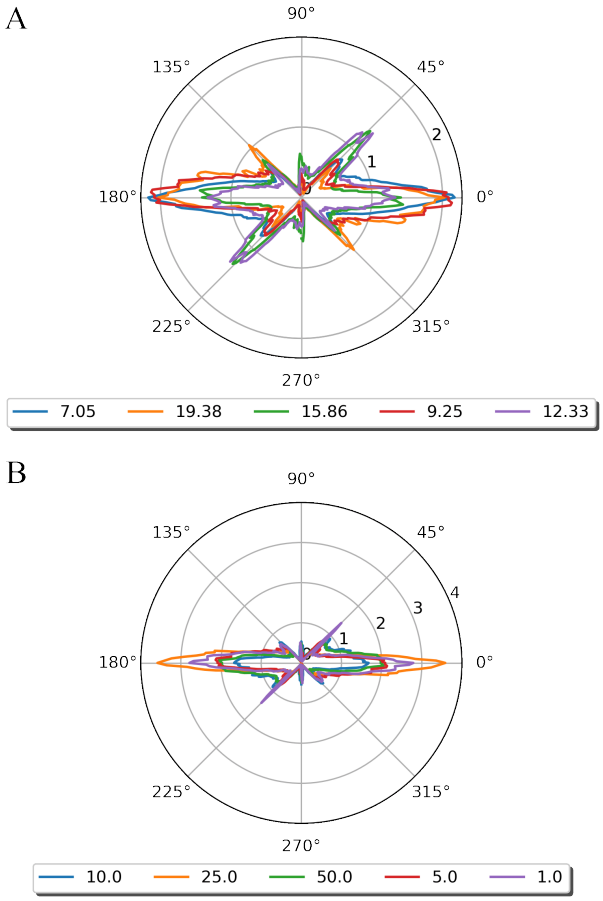


Figure S3.2. Polar plots of the change in PCL/PDO EHFM micro-fibre orientation (n=3) produced with blended PCL/PDO polymer solution with a mass ratio of 0.43 and (A) a total polymer concentration ranging between 7.05 and 15.85 % doped with 5 ppm pyridine, or (B) a total polymer concentration of 15.86 % and doped with 0, 1, 5, 10, 25, and 50 ppm pyridine.

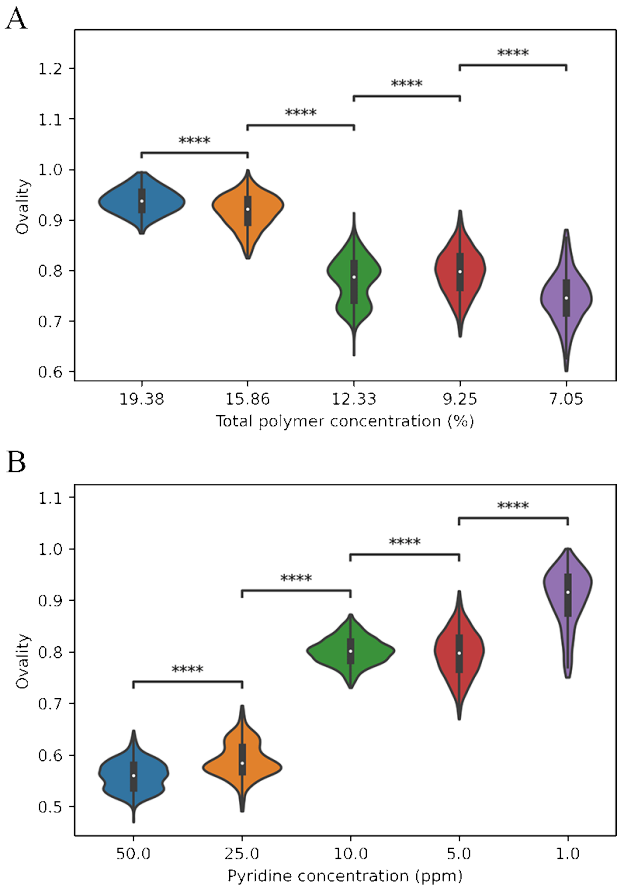


Figure S3.3. Change in aspect ratio of PCL/PDO EHFMs (n=3) produced with; (A) a polymer solutions containing a total polymer concentration ranging between 7.05 and 19.38 % and doped with 5 ppm of pyridine; (B) a polymer solution containing a 15.85 % total polymer concentration and with 0,1, 5, 10, 25, and 50 ppm of pyridine as determined through the analysis of EHFM cross sectional images captured with μCT.

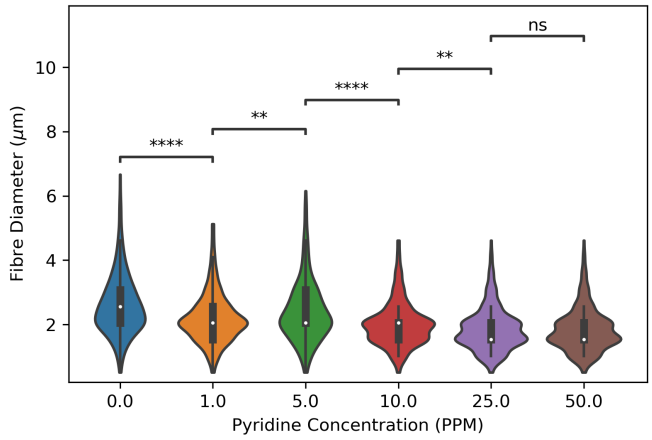


Figure S3.4. Electrospun flat sheet membrane micro-fibre diameter distributions determined from the analysis of SEM images captured at x3000 (n=3) produced with a blended polymer PCL/PDO solution with a mass ratio of 0.43 and a 15.85 % total polymer concentration doped with 0,1, 5, 10, 25, and 50 ppm pyridine.

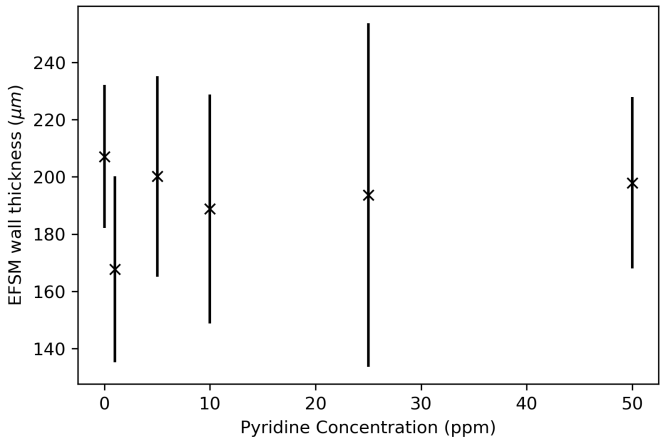


Figure S3.5. Wall thickness of blended PCL/PDO electrospun flat sheet membranes (n=3), produced with a blended polymer PCL/PDO solution with a mass ratio of 0.43 and a 15.85 % total polymer concentration doped with 0,1, 5, 10, 25, and 50 ppm pyridine, as determined through the analysis of cross sectional images captured with μCT.

Statement of Authorship for joint/multi-authored papers for PGR thesis

To appear at the end of each thesis chapter submitted as an article/paper

The statement shall describe the candidate's and co-authors' independent research contributions in the thesis publications. For each publication, there should exist a complete statement that is to be filled out and signed by the candidate and supervisor **(only required where there isn't already a statement of contribution within the paper itself).**

Title of Paper	Morphological and functional characterisation of vascular inspired electrospun hollow fibre membranes
Publication Status	□Published □ Accepted for Publication ☒ Submitted for Publication □Unpublished and unsubmitted work written in a manuscript style
Publication Details	e.g. Martin, R., Mouthuy, P., Waters, S., Ye, H., (2023) Morphological and functional characterisation of vascular inspired electrospun hollow fibre membranes

Student Confirmation

Student Name:	Risto John Martin		
Contribution to the Paper	All experimental work, data analysis and writing was carried out by Risto Martin. Prof. Pierre Alexis-Mouthuy, Prof. Sarah Waters, and Prof. Hua (Cathy) Ye provided supervision and advice throughout.		
Signature		Date	03/01/2023

Supervisor Confirmation

By signing the Statement of Authorship, you are certifying that the candidate made a substantial contribution to the publication, and that the description described above is accurate.

Supervisor name and title: Prof Hua Ye		
Supervisor comments The description above is accurate.		
Signature 	Date	5 Jan 2023

This completed form should be included in the thesis, at the end of the relevant chapter.

Chapter 4

Endothelial cell growth in an electrospun hollow fibre membrane bioreactor: A mathematical perspective

Electrospun hollow fibre membranes developed in chapter 3 may be integrated into an electrospun hollow fibre membrane bioreactor. To aid with the development of such a platform by providing rational to experimental design decisions, utilising experimentally measured membrane functional characteristic parameters from chapter 3, in this chapter, we present a two-dimensional fluid flow, nutrient transport, and endothelial cell growth model of an electrospun hollow fibre membrane bioreactor. With this model, we evaluate our hypotheses that: The media inlet flow rate alters endothelial cell growth rate, and that, the ratio of bioreactor outlet pressures may also indirectly alter endothelial cell growth rates.

In this section, the formulation of the model, simulation work, analysis and writing was carried out by Risto Martin. Prof. Sarah Waters, Prof. Pierre Alexis-Mouthuy, and Prof. Hua (Cathy) Ye provided supervision and advice throughout.

Endothelial cell growth in vascular mimetic electrospun hollow fibre membranes: A mathematical modelling perspective

Authors:

Risto Martin[1], Cathy (Hua) Ye[1]*, Pierre-Alexis Mouthuy [2], Sarah Waters[3]*

Affiliations:

[1]*Department of Engineering Science, University of Oxford, Oxford, OX3 7DQ, UK*

[2]*Nuffield Department of Orthopaedic Surgery, The Botnar Research Centre, Institute of Musculoskeletal Sciences, Oxford University, N.O.C. Headington, Oxford, OX3 7LD, UK*

[3]*OCIAM, Mathematical Institute, University of Oxford, Radcliffe Observatory Quarter, Woodstock Road, Oxford, OX2 6GG, UK*

***Corresponding author**:

hua.ye@eng.ox.ac.uk, waters@maths.ox.ac.uk

Keywords:

Tissue engineering — Bioreactor — Electrospun — Hollow fibre membrane — Vascular biology

Abstract:

We present a two-dimensional fluid flow, nutrient transport, and endothelial cell growth model of an electrospun hollow fibre membrane bioreactor. In the model system, endothelial cells are seeded in a cell layer on the lumen wall of the electrospun hollow fibre membrane. The Navier-Stokes equations describe single-phase flow in the lumen and extra-capillary space, while the Brinkman equation describes porous media fluid flow in the cell and membrane layers. The change in concentration of dissolved species of

interest in each system domain is governed by an advection-diffusion-reaction equation. Endothelial cell growth is modelled by a phenomenological data-driven model of endothelial cell metabolism and signalling, sensitive to shear stress, nutrient and signalling molecule concentrations.

We found that initially, between 5E-13 and 5E-9 m^3/s., the endothelial cell growth rate increased with the inlet media flow rate, reaching a maximum at 7.5E-11 m^3/s, after which it decreased. Conversely, the endothelial cell growth rate was found to decrease with an increase in the relative lumen to extra capillary outlet partial pressures.

Finally, we validate our model against exemplar experimental data from a study of endothelial cell growth in a hollow fibre membrane bioreactor previously described in literature. Additionally, we compare our model to a reduced version, similar to cell growth models previously described in literature, considering only the effect of local oxygen concentration and shear stress. In this comparison, we found our model better described the overall trend of endothelial cell growth in a hollow fibre membrane bioreactor.

4.1 Introduction

Hollow fibre membrane (HFM) bioreactors, facilitate membrane confined advective mass transfer, enabling cell growth in large tissue-engineered constructs made otherwise impossible by the short effective range of diffusive mass transfer [46, 59, 43, 12]. Yet, the non-biodegradable nature and the discrepancy in mechanical and micro-topographical properties between HFMs and native vasculature, prevents their use in many tissue-engineered constructs intended for clinical settings [70, 69, 195, 68]. To this end, we have previously developed electrospun HFMs (EHFMs) that are flexible, biodegradable, biocompatible, micro-topographically and mechanically vascular bio-mimetic [7]. Using these, EHFM bioreactors may now be developed.

EHFM bioreactors may be used to model vasculature *in vitro* or to support cell growth in larger tissue engineered constructs. Uniform cell growth in the shortest culture time possible is desirable in both of these roles. For an *in vitro* vascular model, a reduction in the time required to form a complete monolayer of endothelial cells (ECs), akin to that in vasculature *in vivo*, represents a reduction in the cost and lead time associated with the generation of a functional vascular model. Therefore rapid cell growth is desired in the development of a functional biomimetic vascular model [155].

Progression in the development of bioreactor systems is typically slow due to their trial-and-error style evolution. Mathematical modelling, however, offers a means to expedite this process by providing a rationale for experimental design decisions and may be applied in the development of a novel EHFM bioreactor platform [132]. EHFMs are structurally similar to electrospun scaffolds developed for vascular bypass surgery, for which models have been developed. However, these models neglect fluid flow and mass transport but rather revolve around the immune centric remodelling of these scaffolds following implantation *in vivo*. As there is no immune response *in vitro*, as in a bioreactor, these models are not appropriate for EHFM bioreactor development [143, 145, 144, 147, 148].

Previous models produced for electrospun tubes with a circular cross-section used in bioreactors have been developed. These models evaluated the role of scaffold structure and reactor configuration on oxygen dictated cell proliferation and taxi [196]. In this model, fluid flow was only considered in the porous media domain, and smooth muscle cell proliferation was taken to be dependent on local oxygen concentration only. Furthermore, as advective mass transport dominates in physiological fluid flow regimens, the model is limited in its neglection of free body flow and advective mass transfer.

Models have been developed for cell growth in HFM bioreactors which consider nutrient transport, free body and porous media fluid flow. These models have been used to evaluate the influence of cell seeding density on oxygen concentration dynamics, fluid flow on cell growth due to the role of chemo-

attractants and nutrient availability, shear stress on cell growth and cell layer growth [197, 198, 199, 58]. While these models were developed for HFMs, they may be adapted for EHFMs by taking structural differences into account with the substitution of appropriate porosity and permeability parameters.

In these models, cell growth has predominantly been considered to be dependent on local oxygen concentration only [198, 199, 58]. This may limit these models as cell growth develops as a function of environmental conditions including, nutrient availability, waste metabolite concentration, cell signalling, mechanical stimulation, and topographic effects. Similarly, the rate of cellular consumption and production of soluble factors and ECM proteins is dependent on environmental conditions. Reviews of physio-chemical factors modulating EC growth have identified vascular endothelial growth factor (VEGF) as the dominant cell signalling regulatory factor [78, 80, 81]. Furthermore, ECs display metabolic adaptations different to most cell types in that they produce the majority of their ATP glycolytically, converting glucose to lactate. Other metabolites identified as being of particular interest included glutamine, ammonia and oxygen. Similarly, wall shear stress was also recognised as playing a vital role in the maturation of ECs *in vivo*. On account of these findings, we produced a phenomenological data-driven model to describe EC growth in response to modulatory factors, as described in supplementary section 4.7.1 and summarised in figure 4.1. Owing to the data-driven nature of this model, aspects such as the influence of mechanical stimuli of cell death of shear stress on proliferation had to be neglected from this model. This we due to the lack of quantitative data in the literature. Consequently, to aid the development of future models, research into the measurement of the dose-response behaviour of cells would be beneficial.

Consequently, we hypothesised that, due to the change in shear stress and advective mass transfer with fluid velocity, the media inlet flow rate alters the EC growth rate. Additionally, we hypothesised that the ratio of bioreactor outlet pressures also indirectly alters EC growth rates by modulating the proportion of fluid flow through the lumen and extra capillary space (ECS), thereby changing the

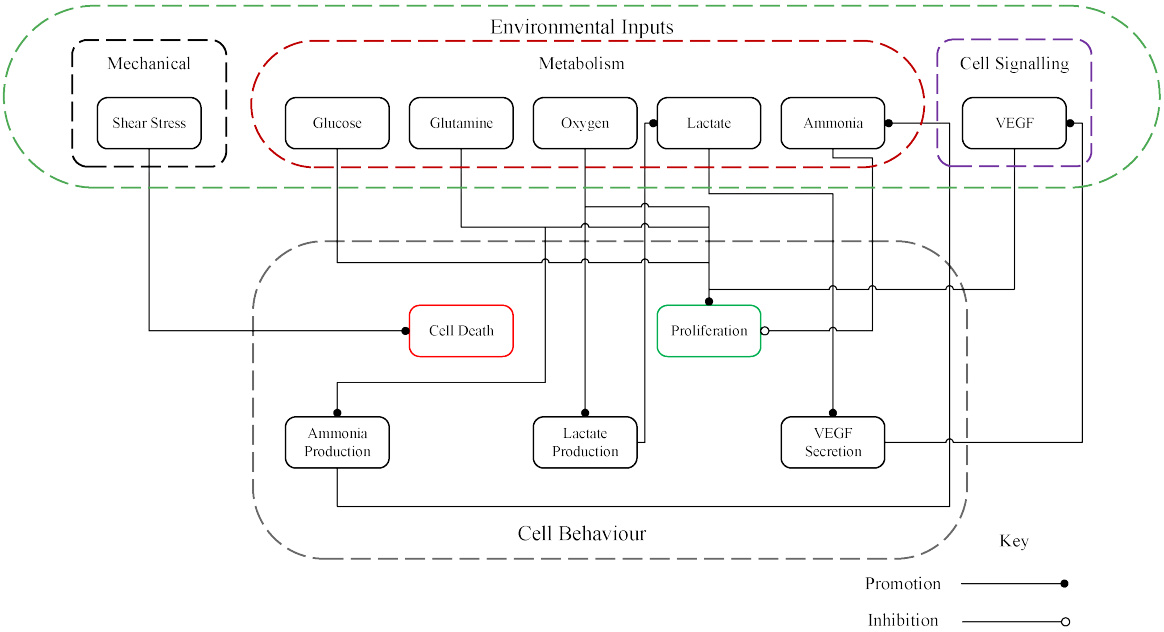


Figure 4.1. Schematic of the data-driven phenomenological model of endothelial cell growth sensitive to environmental, cell signalling, and mechanical stimuli.

proportional flux of nutrients in the lumen and ECS. This paper presents a model for fluid flow, nutrient transport, and EC growth in an EHFM bioreactor utilising the Navier Stokes single-phase fluid flow, Brinkman porous media fluid flow, advection-diffusion-reaction and the data-driven EC growth models. With this model, we evaluate the numerical solutions of time dependent EC growth under experimentally relevant conditions to test our hypotheses. To do so, we evaluate: (1) The effect of the inlet media flow rate on the EC growth rate and, (2), the influence of the EHFM bioreactor outlet port partial pressures on the EC growth rate. Finally, we validate our model against experimental EC growth data from the literature and compare the results against a reduced version of our EC growth model, similar to those already in the literature.

4.2 Model description

We consider a simplified model system that consists of a bioreactor continuously fed with fresh media. By considering the block flow diagram, as seen in figure 4.2, the flow paths in the model system may be visualised. In short, a stream of fresh media, with volumetric flux $Q_{l,0}$, is fed into the bioreactor

EHFM lumen. Once the media has passed through the reactor, it may exit out the lumen or ECS outlet, at which we specify pressure as $P_{l,L}$ and $P_{e,L}$, respectively. The resultant media stream is then sent to waste and leaves the system.

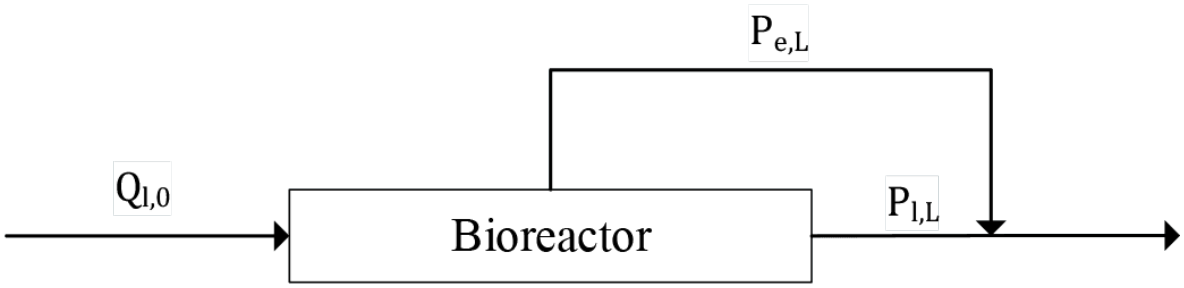


Figure 4.2. Block flow diagram of the reactor configuration showing the flow paths of each media stream.

In an EHFM bioreactor, the EHFM is a component of the repeating unit. For the purpose of simplicity we assume the model bioreactor to consist of a single EHFM unit, which is considered to be; porous, permeable, rigid and encased within an impermeable hard shell, as seen in figure 4.3.

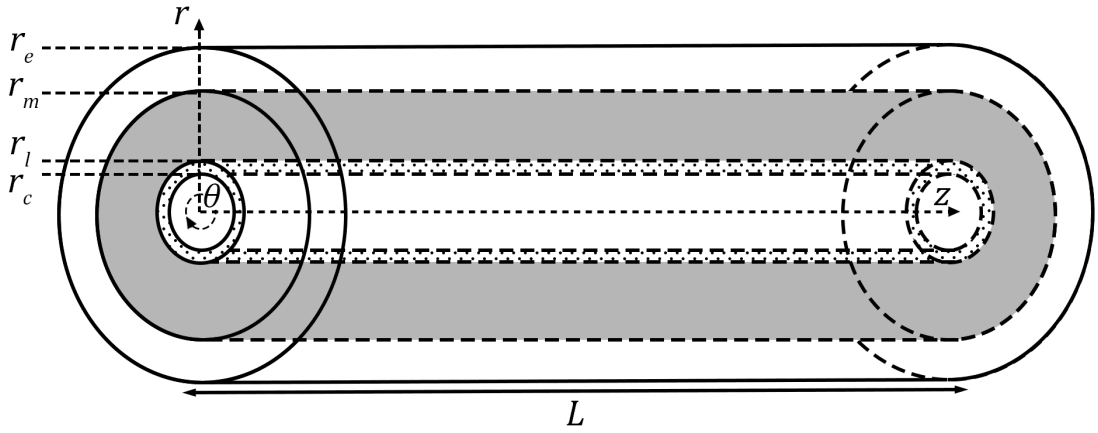


Figure 4.3. A 3D schematic representation of an electrospun hollow fibre bioreactor with the membrane and cell layer highlighted in the grey and dotted layers. The radii of the cell layer, lumen, membrane and ECS are demarcated as r_c, r_l,r_m and r_e, respectively.

We consider a cylindrical polar coordinate system (z, r, θ), with z aligned along the length of the bioreactor, r is the radial coordinate and θ is the azimuthal angle. We assume the system is axisymmetric. Accordingly, we neglect variations with respect to θ and any azimuthal components of velocity. We

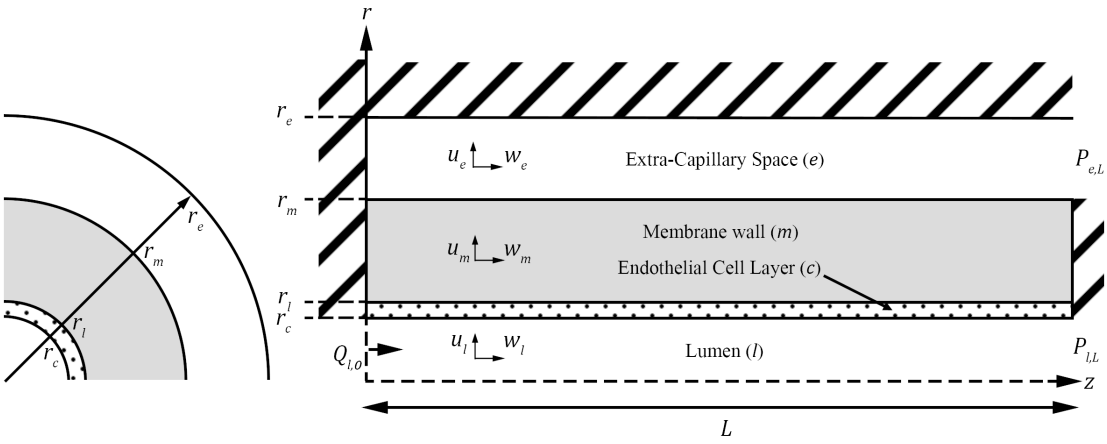


Figure 4.4. A schematic representation of an axisymmetric cross section of an EHFM bioreactor with the membrane and cell layer highlighted in the grey and dotted layers. The radii of the cell layer, lumen, membrane and ECS are r_c, r_l, r_m, and r_e, respectively. Similarly, the inlet media flow rate, lumen and ECS outlet pressures are labeled as $Q_{l,0}$, $P_{l,L}$, and $P_{e,L}$.

define $\hat{\mathbf{z}}$ and $\hat{\mathbf{r}}$ as unit vectors in the axial and radial directions and consider all dependent variables as a function of z, r, and time, t. Specifically, we denote the velocity components along z and r as w and u.

Figure 4.4 represents a cross section through the axisymmetric system. The bioreactor has length L, radius r_e and consists of four domains; the lumen $0 \leq r < r_{\mathrm{c}}$, cell layer $r_{\mathrm{c}} < r < r_{\mathrm{l}}$, membrane $r_{\mathrm{l}} < r < r_{\mathrm{m}}$, and finally the ECS $r_{\mathrm{m}} < r \leq r_{\mathrm{e}}$, for the entire length of the bioreactor $0 \leq z \leq \mathrm{L}$. The radii and lengths of each of these domains are set to match those of previously experimentally measured values and may be seen in table 4.1 [7].

Table 4.1. Table of bioreactor geometry taken as representative experimentally measured values from [7]

Inner most radius of	**Symbol**	**Value**	**Unit**
Cell layer	r_c	48.9	[μm]
Lumen	r_l	50	[μm]
Membrane	r_m	350	[μm]
Extra-capillary space	r_e	400	[μm]
Bioreactor length	L	3500	[μm]

In the cell layer, ECs are assumed to be seeded uniformly. ECs are then considered as immobile reactive species that may consume or produce species of interest and fluctuate in density according to the EC growth model. The cell layer is assumed to have the same fluid transport properties, porosity, and permeability as the membrane layer, irrespective of cell number. To aid model simplicity, it is

assumed that there is no degradation of the membrane layer and no deposition of ECM, so that it is fixed and inert. The effect of cell layer growth and change in ECM permeability has previously been evaluated [58]. In this case, it is likely that the cell layer would remain a mono-layer as is common for EC growth. However, it is likely the permeability of the cell layer would change with cell growth. The effect of this may be explored in future models.

Throughout the model, subscript α indicates the domain considered, where $\alpha = l, c, m$ and e for the lumen, cell layer, membrane, and ECS, respectively. Similarly, superscript (i) indicates the species of interest, where $i = 1, 2, 3, 4, 5$ and 6 for glucose, glutamine, oxygen, VEGF, lactate and ammonia, respectively.

The model system consists of governing equations for cell growth, mass transport, single-phase and porous media fluid flow. Boundary conditions are specified to couple the governing equations in each domain. Experimentally relevant initial conditions and parameter values are taken for each simulation to solve for the 5 unknown dependent variables, as seen in table 4.2, in the model system.

Table 4.2. Table of model dependent variables

Name	Units	Description
u_α	$[m/s]$	Culture medium radial velocity
w_α	$[m/s]$	Culture medium axial velocity
p_α	$[Pa]$	Fluid pressure
$c_\alpha^{(i)}$	$[mol/m^3]$	Concentration
N	$[1/m^3]$	EC Density

4.3 Governing equations

4.3.1 Fluid model

4.3.1.1 Lumen and ECS

Culture medium is considered to be; an incompressible Newtonian viscous fluid with constant density, ρ_w, and viscosity, μ, equal to that of water, and to contain dilute species of interest. In the lumen and ECS, there are no cells or porous material; we therefore model single-phase flow of culture

media with the Navier–Stokes continuity of mass and momentum equations, respectively,

$$\nabla \cdot \mathbf{u}_\alpha = 0, \tag{4.1}$$

$$\rho_w(\mathbf{u}_\alpha \cdot \nabla)\mathbf{u}_\alpha = \nabla \cdot [-p_\alpha \mathbf{I} + \mathbf{T}_\alpha], \tag{4.2}$$

where $\mathbf{T}_\alpha$ is the fluid viscous stress tensor given by,

$$\mathbf{T}_\alpha = \mu(\nabla \mathbf{u}_\alpha + (\nabla \mathbf{u}_\alpha)^{\mathrm{T}}), \tag{4.3}$$

where, $\alpha = l$ or e, p_α is the fluid pressure and $\mathbf{u}_\alpha = (w_\alpha, \mathrm{u}_\alpha)$ is the culture medium velocity.

4.3.1.2 Membrane and cell layer

As in the lumen and ECS, in the cell layer and membrane domains conservation of fluid mass for an incompressible fluid is governed by the continuity equation,

$$\nabla \cdot \mathbf{u}_\alpha = 0, \tag{4.4}$$

While porous media fluid flow conservation of momentum is modelled using Brinkman's equation,

$$0 = \nabla \cdot \left[-p_\alpha \mathbf{I} + \frac{\mathbf{T}_\alpha}{\phi} \right] - \left(\frac{\mu}{\kappa} \right) \mathbf{u}_\alpha, \tag{4.5}$$

where ϕ is the porosity and κ is the permeability of the domain. As the cell layer is assumed to have the same fluid transport properties, porosity, and permeability as the membrane layer, irrespective of cell number. We assume continuity of fluid velocity, stress, concentration and mass flux between the

cell and membrane layer. We therefore combine domains $\alpha = c$ and m into a single continuum when solving equations 4.4 and 4.5 such that $\alpha = m$ for both domains.

4.3.2 Transport model

The conservation of mass for the concentration of the dissolved dilute species of interest in all domains is given by an advection-diffusion-reaction equation given as,

$$\mathbf{u}_\alpha \cdot \nabla c_\alpha^{(i)} + \nabla \cdot \mathbf{J}_\alpha^{(i)} = \mathrm{R}_\alpha^{(i)}, \tag{4.6}$$

where,

$$\mathbf{J}_\alpha^{(i)} = -D_\alpha^{(i)} \nabla c_\alpha^{(i)}, \tag{4.7}$$

where $\mathbf{J}_\alpha^{(i)}$ is diffusive flux, $c_\alpha^{(i)}$ is concentration, $D_\alpha^{(i)}$ is the diffusion coefficient and $\mathrm{R}_\alpha^{(i)}$ is the reaction term. In the lumen and ECS the diffusion coefficient is given by that in water, so that $D_\alpha^{(i)} = D_w^{(i)}$. However, in the membrane and cell layer we consider an effective diffusion coefficient given by,

$$D_\alpha^{(i)} = \frac{\phi}{\Upsilon} D_w^{(i)}, \tag{4.8}$$

where $\alpha = c$ or m, and Υ is the membrane tortuosity. As $\mathrm{R}_\alpha^{(i)}$ is taken to occur due to the action of the ECs, in the lumen, membrane and ECS, where no cells are present, $\mathrm{R}_l^{(i)} = \mathrm{R}_m^{(i)} = \mathrm{R}_e^{(i)} = 0$. In the cell layer only, as there are ECs present, $\mathrm{R}_c^{(i)}$ is taken to be equal to the substrate limitation and inhibition model determined to best describe EC consumption or production of the given species of interest in the data-driven EC growth model seen in the supplementary section 4.7.1. For each species of interest, in

the cell layer, $R_c^{(i)}$ is therefore taken as,

$$R_c^{(1)} = \frac{NV_{max}^{(1)}(c_c^{(1)})^{n^{(1)}}}{(K_s^{(1)})^{n^{(1)}} + (c_c^{(1)})^{n^{(1)}}} \tag{4.9}$$

$$R_c^{(2)} = \frac{NV_{max}^{(2)}(c_c^{(2)})^{n^{(2)}}}{(K_s^{(2)})^{n^{(2)}} + (c_c^{(2)})^{n^{(2)}}} \tag{4.10}$$

$$R_c^{(3)} = \frac{NV_{max}^{(3)}(c_c^{(3)})^{n^{(3)}}}{(K_s^{(3)})^{n^{(3)}} + (c_c^{(3)})^{n^{(3)}}} \tag{4.11}$$

$$R_c^{(4)} = N\left(a^{(4)} + \frac{V_{max}^{(4)}c_c^{(5)}}{K_v^{(4)} - c_c^{(5)}}\right), \tag{4.12}$$

$$R_c^{(5)} = NV_{max}^{(5)}\left(1 - \frac{(c_c^{(3)})^{n^{(5)}}}{(K_s^{(5)})^{n^{(5)}} + (c_c^{(3)})^{n^{(5)}}}\right), \tag{4.13}$$

$$R_c^{(6)} = (R_c^{(2)} - K_d^{(2)})Y^{(6,2)}N. \tag{4.14}$$

Where N is EC density and the definition of all other reaction model terms may be seen in table 4.3, the value of which may be seen in table 4.15 in appendix 4.7.4.

Table 4.3. Table of EC reaction model parameter definitions

Name	Unit	Description
$V_{max}^{(i)}$	$[mol/s]$	Species maximum reaction rate
$n^{(i)}$		Reaction Moser constant
$K_s^{(i)}$	$[mol/m^3]$	Species reaction half saturation constant
$K_v^{(4)}$	$[mol/m^3]$	VEGF production maximal Lactate concentration
$a^{(i)}$	$[mol/s]$	Species basal reaction constant
$Y^{(i,j)}$		Ratio of species i production for each of species j consumed

4.3.3 Cell growth model

Finally, we consider EC growth, which occurs in the cell layer only. We model EC growth as follows,

$$\frac{\partial N}{\partial t} = (\zeta - \zeta_d)N, \tag{4.15}$$

where ζ and ζ_d are the cell growth and death rate given by,

$$\zeta = \zeta_{max} f_{lim} f_{inh} \left(1 - \frac{N}{N_{max}}\right), \tag{4.16}$$

$$\zeta_d = b^{(ss)} + \left(\frac{G_{max}^{(ss)} \tau}{K_G^{(ss)} + \tau}\right) \tag{4.17}$$

in which $b^{(ss)}$ is the basal EC death rate under static fluid conditions, $G_{max}^{(ss)}$ and $K_G^{(ss)}$ are the maximal death rate due to shear stress and shear stress half saturation constants, respectively. The magnitude of shear stress, τ, is taken as,

$$\tau = \dot{\gamma} \cdot \mu \tag{4.18}$$

Where $\dot{\gamma}$ is the shear rate given by the magnitude of the strain-rate tensor,γ, given by [200],

$$\dot{\gamma} = \sqrt{\frac{1}{2}\gamma : \gamma}, \tag{4.19}$$

where the contraction operator ':' is defined by

$$\mathbf{a} : \mathbf{b} = \sum_{n} \sum_{m} a_{nm} b_{nm} \tag{4.20}$$

and where γ is given by,

$$\gamma = (\nabla \mathbf{u}_{\alpha} + (\nabla \mathbf{u}_{\alpha})^{\mathrm{T}}) \tag{4.21}$$

The definition of all terms in EC growth model may be seen in table 4.4, the values of which may be seen in table 4.16 in appendix 4.7.4.

Table 4.4. Table of EC growth model parameter definitions

Name	Unit	Description
ζ_{max}	$[1/s]$	Maximum EC growth rate
N_{max}	$[1/m^3]$	Maximum EC density
$b^{(ss)}$	$[1/s]$	basal proliferation constant due to shear stress
$G^{(ss)}_{max}$	$[1/s]$	Shear stress maximum proliferation rate
$K^{(ss)}_{G}$	$[Pa]$	Shear Stress proliferation half saturation constant
τ	$[Pa]$	Shear stress

We model the inhibitory effect of limited nutrient availability and waste metabolite abundance on cell growth with f_{inh} and f_{lim}. The effect of each species of interest in each of these functions was taken as the model found to best describe EC growth in response to each species of interest, as determined in the data-driven model development as seen in the supplementary section 4.7.1. Consequently, f_{inh} and

f_{lim} are be given by,

$$f_{inh} = 1 - \frac{b_c^{(6)} + \frac{G_{max}^{(6)} c_c^{(6)} \left(1 + \frac{c_c^{(6)}}{K^{(6)}}\right)}{c_c^{(6)} + K_G^{(6)} + \frac{(c_c^{(6)})^2}{K_I^{(6)}}}}{Y_{max}^{(6)}}, \tag{4.22}$$

$$f_{lim} = G^{(1)} G^{(2)} G^{(3)} G^{(4)}, \tag{4.23}$$

where $G^{(i)}$ is the function of cell growth due to nutrient limitation given by,

$$G^{(1)} = \frac{G_{max}^{(1)} (c_c^{(1)})^{m^{(1)}}}{((K_G^{(1)})^{m^{(1)}} + (c_c^{(1)})^{m^{(1)}}) Y_{max}^{(1)}}, \tag{4.24}$$

$$G^{(2)} = \frac{b^{(2)} + \frac{G_{max}^{(2)} c_c^{(2)}}{K_G^{(2)} + c_c^{(2)}}}{Y_{max}^{(2)}}, \tag{4.25}$$

$$G^{(3)} = \frac{G_{max}^{(3)} c_c^{(3)}}{\left(K_G^{(3)} + c_c^{(3)} + \frac{(c_c^{(3)})^2}{K_I^{(3)}} \left(1 + \frac{c_c^{(3)}}{K^{(3)}}\right)\right) Y_{max}^{(3)}}, \tag{4.26}$$

$$G^{(4)} = \frac{G_{max}^{(4)} c_c^{(4)} \left(1 + \frac{c_c^{(4)}}{K^{(4)}}\right)}{\left(K_G^{(4)} + c_c^{(4)} + \frac{(c_c^{(4)})^2}{K_I^{(4)}}\right) Y_{max}^{(4)}}, \tag{4.27}$$

in which $Y_{max}^{(i)}$ is a normalisation condition with value equal to the maximum of the function so that each function gives a value between 0-1. By this means fluctuations in the local concentration of species

of interest modulate the effective fraction of ζ_{max}. The definition for each term in the EC the growth limitation and inhibition functions may be seen in table 4.5, while their values may be seen in table 4.16 in appendix 4.7.4.

Table 4.5. Table of EC growth limitation, and inhibition parameter definitions

Name	Unit	Description
$G_{max}^{(i)}$	$[mol/s]$	Maximum EC growth rate
$m^{(i)}$		Cell growth Moser constant
$K_G^{(i)}$	$[mol/m^3]$	EC growth rate half saturation constant
$Y^{(i)_{max}}$	$[mol/s]$	EC growth function normalisation condition
$b^{(i)}$	$[mol/s]$	Species basal proliferation constant
$K_I^{(i)}$	$[mol/m^3]$	Species proliferation Inhibition constant
$K^{(i)}$	$[mol/m^3]$	Species proliferation constant

We now close the problem by imposing boundary conditions.

4.3.4 Boundary conditions

We impose symmetry conditions at the centre line so that at $r = 0$,

$$\frac{\partial w_l}{\partial r} = 0, \frac{\partial c_l^{(i)}}{\partial r} = 0, \qquad u_l = 0. \tag{4.28}$$

On the ECS-reactor wall boundary no slip and no flux boundaries are imposed at $r = r_e$ so that,

$$\mathbf{u}_e = \mathbf{0}, \qquad \hat{\mathbf{r}} \cdot \mathbf{J}_e^{(i)} = 0. \tag{4.29}$$

We couple single phase and porous media flow at the lumen-cell layer and membrane-ECS interfaces by considering a continuity of concentration, mass flux, velocity and the normal component of the stress tensor at each interface [201], so that at $r = r_c$,

$$c_l^{(i)} = c_c^{(i)}, \qquad D_l^{(i)} \frac{\partial c_l^{(i)}}{\partial r} = D_c^{(i)} \frac{\partial c_c^{(i)}}{\partial r}, \tag{4.30}$$

$$\mathbf{u}_l = \mathbf{u}_c, \qquad (-p_l\mathbf{I} + \mathbf{T}_l) \cdot \hat{\mathbf{r}} = (-p_c\mathbf{I} + \mathbf{T}_c) \cdot \hat{\mathbf{r}}, \tag{4.31}$$

and at $r = r_m$,

$$c_m^{(i)} = c_e^{(i)}, \qquad D_m^{(i)} \frac{\partial c_m^{(i)}}{\partial r} = D_e^{(i)} \frac{\partial c_e^{(i)}}{\partial r}, \tag{4.32}$$

$$\mathbf{u}_m = \mathbf{u}_e, \qquad (-p_m\mathbf{I} + \mathbf{T}_m) \cdot \hat{\mathbf{r}} = (-p_e\mathbf{I} + \mathbf{T}_e) \cdot \hat{\mathbf{r}}. \tag{4.33}$$

At the inlet, where $z = 0$, fluid enters through the lumen only. We assume a parabolic inlet fluid velocity profile so that,

$$\mathbf{u}_\alpha = \mathbf{0}\ , w_l = \frac{2Q_{l,0}}{\pi r_c^2}\left(1 - 2\frac{r^2}{r_c^2}\right) \text{ and } u_l = 0, \tag{4.34}$$

where $\alpha = c, m$ and e. We also impose inlet species concentrations in the lumen as,

$$c_l^{(i)} = c_0^{(i)}, \tag{4.35}$$

where $c_0^{(i)}$ is the inlet concentration. In all other layers there is no inlet flux so that,

$$\mathbf{J}_\alpha^{(i)} = 0, \tag{4.36}$$

where $\alpha = c, m$ and e. At the outlet of the bioreactor, where $z = L$, fluid is able to flow out through the lumen and the ECS. Accordingly, we set the diffusive flux to zero so that advective flow may leave

through the outlet. Mass flux out of the lumen and ECS is therefore specified as,

$$D_{\alpha}^{(i)} \nabla c_{\alpha}^{(i)} \cdot \hat{\mathbf{z}} = 0, \tag{4.37}$$

where $\alpha = l$ and e. The pressures at the lumen and ECS outlet are kept constant so that we specify stress by,

$$[-p_{\alpha}\mathbf{I} + \mathbf{K}_{\alpha}] \cdot \hat{\mathbf{z}} = p_{\alpha,L} \cdot \hat{\mathbf{z}}. \tag{4.38}$$

Finally, the outlet in the membrane and cell layers are sealed so that,

$$\mathbf{u}_{\alpha} = \mathbf{0}, \qquad \mathbf{J}_{\alpha}^{(i)} = 0, \tag{4.39}$$

where $\alpha = c$ and m.

Having defined the model: Geometry, governing equations, boundary conditions, constitutive laws, model parameters, and initial conditions, we have a system of 5 equations (see equations 4.1, 4.2, 4.5, 4.6, and 4.15) with 5 unknown dependent variables. We now solve our model for these unknown dependent variables: u_{α}, w_{α}, p_{α}, $c_{\alpha}^{(i)}$ and N. To solve the problem we use the finite element software COMSOL (Ver 5.3), to numerically evaluate experimentally relevant case studies. In these simulations, a free triangle mesh comprised of 102588 elements, of which 9693 were edge elements, was generated, and the system of 107996 degrees of freedom was solved for with 50 regular time steps for the total simulated period. The coarseness of the mesh was selected such that the relative error did not exceeded the tolerance of 0.005.

4.3.5 Initial conditions and parameter selection

For each of the simulations, experimentally relevant parameters were taken. ECs were seeded with a uniform density so that $t = 0, N = N_0$. The cell growth model was parameterised with values determined with the data-driven EC growth model described in supplementary section 4.7.1, the values of which may be seen in appendix 4.7.4 tables 4.15 and 4.16. Experimentally measured parameters were used to define the membrane material properties. The concentration of species of interest in fresh media were assumed to be the same formulation as that in ATCC's F-12k culture medium additionally supplemented with VEGF, in accordance with PromoCell's EC growth media [202, 203]. Finally, the diffusivities of each species of interest in water were taken from the literature. A table of all species of interest fresh media concentrations, diffusivities and membrane material property parameters may be seen in table 4.6.

Table 4.6. Table of EC seeding density, membrane material property parameters, inlet concentrations and diffusivities for the species of interest

Parameter	Value	Unit	Description	Ref.
N_0	5.000E11	$[1/m^3]$	EC seeding density	-
Υ	3.900	-	Membrane tortuosity	[7]
κ	1.890E-14	$[m^2]$	Membrane permeability	[7]
ϕ	88.000	$[\%]$	Membrane porosity	[7]
ρ	0.908	$[g/cm^3]$	Membrane density	[7]
T	310.150	$[K]$	Reactor Temperature	-
$c_f^{(1)}$	24.978	$[mol/m^3]$	Glucose concentration in fresh media	[203]
$c_f^{(2)}$	3.996	$[mol/m^3]$	Glutamine concentration in fresh media	[203]
$c_f^{(4)}$	2.604E-8	$[mol/m^3]$	VEGF concentration in fresh media	[202]
$D_{\mathrm{w}}^{(1)}$	6.000E-10	$[m^2/s]$	Diffusivity of glucose	[182]
$D_{\mathrm{w}}^{(2)}$	8.000E-10	$[m^2/s]$	Diffusivity of glutamine	[204]
$D_{\mathrm{w}}^{(3)}$	2.794E-9	$[m^2/s]$	Diffusivity of O2	[205]
$D_{\mathrm{w}}^{(4)}$	5.550E-11	$[m^2/s]$	Diffusivity of VEGF	[206]
$D_{\mathrm{w}}^{(5)}$	1.100e-09	$[m^2/s]$	Diffusivity of lactate	[207]
$D_{\mathrm{w}}^{(6)}$	1.900e-09	$[m^2/s]$	Diffusivity of ammonia	[208]

The inlet dissolved oxygen concentration were calculated from Henry's law [209], as seen in appendix 4.7.3. The partial pressure of oxygen, $\Pi^{(3)}$ was taken as that of oxygen in air, 21%. The initial

and inlet concentration of oxygen, $c_0^{(3)}$, was thereby found to be 0.23354 mol/m^3. The initial and inlet concentrations of species $i = 1, 2$ and 4 were taken as those in fresh media so that $c_0^{(i)} = c_f^{(i)}$.

Having defined our model with experimentally relevant parameters we now test our hypotheses by evaluating the role of inlet flow rate and the EHFM bioreactor outlet partial pressure on EC growth.

4.4 Results and Discussion

4.4.1 The role of inlet flow rate

As we hypothesise, inlet media flow rate alters the EC growth rates in EHFM bioreactors; we evaluate the effect of inlet flow rate on EC culture dynamics and identify which of the flow rates considered conferred the highest EC growth rate. To do this, we evaluated EC culture dynamics over a range of inlet flow rates, $Q_{l,0}$, between 5E-13 and 5E-9 m^3/s. The initial and inlet concentrations of each species of interest were set as detailed in section 4.3.5, while the lumen and ECS outlet gauge pressures were set so that $p_{l,L} = p_{e,L} = 0$ Pa.

To visualise culture performance the mean concentration of each species of interest, magnitude of shear stress, and cell number in the cell layer were determined, as given by,

$$\overline{\chi} = \frac{\int_0^Z \int_{r_c}^{r_l} (\chi) dr dz}{\int_0^Z \int_{r_c}^{r_l} dr dz}, \tag{4.40}$$

where, $\chi = N, \tau, c^{(i)}$. Time profiles of the mean concentration of each species of interest, magnitude of shear stress, and cell number in the cell layer were then plotted with filled bars showing the range in concentration and magnitude, as seen in figure S4.7 appendix 4.7.5. As seen in the time profiles in figures S4.7 B, C, and D an increase in inlet flow rate resulted in a decrease in the reduction of glucose, glutamine, and oxygen concentration by the end of the 35 day culture period. Conversely, the increase in VEGF, lactate and ammonia concentration, as seen in figures S4.7 E, F, and G, decreases with an

increase in inlet flow rate. Similarly, as seen in figure S4.7 H, the magnitude of shear stress in the cell layer increased with inlet flow rate. The decrease in reduction of glucose, glutamine and oxygen concentration across the culture period may explained by the increase flux of each with an increase in flow rate. The proportional rate at which each were consumed compared with the rate of each entering the system decreases with an increase in inlet flow rate thereby resulting in the reduced decrease in concentration with inlet flow rate seen.

To determine the combined effect that the variation in each species of interest had on EC growth at each inlet flow rate, we consider the change in mean EC growth rate at each inlet flow rate. This was evaluated by taking the mean growth rate between the times at which EC growth started and when it plateaued, as given by,

$$\overline{\zeta} = \frac{\sum_{t_s}^{t_f} \left(\frac{ln \frac{\overline{N_t}}{N_0}}{t} \right)}{n}, \tag{4.41}$$

where t_s and t_f are the first and last time points the percentage change in EC density between time steps is more than 1%, $\overline{N_t}$ is the mean density of ECs at time t_f and n is the number of measured values between these times. By this means, the slope of the EC growth curve, during the growth phase, at each inlet flow rate in figure S4.7A appendix 4.7.5 is displayed as a single point, as seen in figure 4.5.

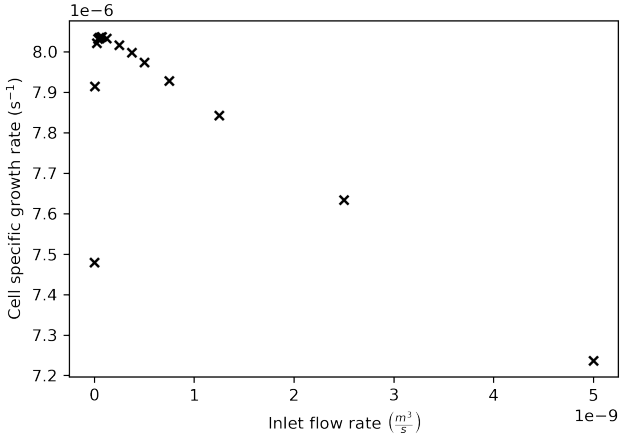


Figure 4.5. Variation in the endothelial cell growth rate with inlet media flow rate

As seen in figure 4.5, the mean EC growth rate was found to initially increase with inlet flow rate, reaching a maximum of 8.036E-6 s^{-1} at an inlet flow rate of 7.5E-11 m^3/s after which it began to decrease. The initial rise in EC growth rate with inlet flow rate may be explained by the increase in the concentration of glucose, glutamine, and oxygen with inlet flow rate as well as the decrease in lactate and ammonia with inlet flow rate, as seen in figures S4.7 B, C, D, F, and G, respectively. The subsequent decrease in EC growth rate may be explained by the decrease in VEGF concentration and increase in shear stress in the cell layer with an increase in inlet flow rate, as seen in figures S4.7 E, and H. As the inlet flow rate continues to increase the increased rate of VEGF removal and shear stress would result in a decrease in cell growth rate and an increase in cell death rate, respectively.

As we hypothesise EHFM bioreactor outlet partial pressures may alter EC growth we now consider their effect.

4.4.2 The role of EHFM bioreactor outlet partial pressures

Experimentally, by narrowing the downstream outlet of the lumen or ECS, it is possible to exert a differential pressure on the fluid leaving through the EHFM bioreactor outlets. By this means, it is possible to route more or less fluid through each outlet. To evaluate the effect of varying the ECS and lumen outlet fluid partial pressures on EC growth, the lumen inlet fluid velocity profile was set according to equation 4.34 with an inlet flow rate, $Q_{l,0}$, of 7.5E-11 m^3/s. The ECS and lumen outlet gauge pressures were set such that the lumen outlet pressure $p_{l,L}$ was taken as the reference pressure, at 0 Pa, and a pressure differential, P_d, was applied to the ECS outlet such that,

$$p_{l,L} = 0, \qquad p_{e,L} = p_{l,L} + (\delta \times P_d), \tag{4.42}$$

where P_d has a value of 30 Pa and δ is the outlet partial pressure variable with a value between -1 and 1. The value for P_d was selected to be 80% of the inlet pressure calculated with an inlet flow rate of

7.5E-11 m^3/s and gauge outlet pressures $p_{l,L} = p_{e,L} = 0$ Pa.

Culture dynamic profiles may be seen in figure S4.8 appendix 4.7.5. As before, the combined effect of varying the outlet partial pressures of the ECS and lumen may be appreciated from the change in EC growth rate may be seen in figure 4.6. As δ increases relative to the lumen outlet, the ECS outlet

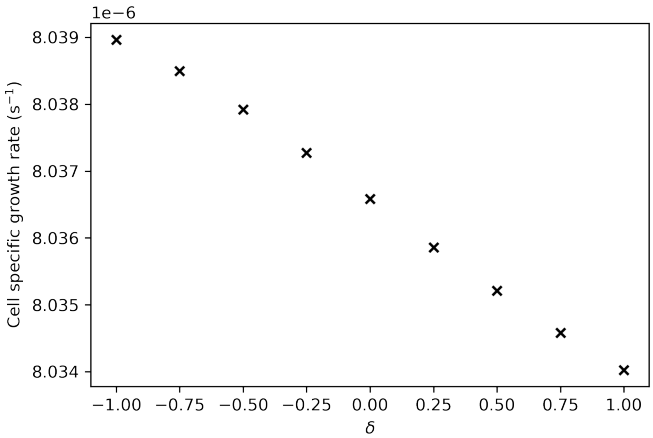


Figure 4.6. Variation in EC growth rate with the change in the proportion of ECS:lumen outlet partial pressure pressures.

pressure increases. Furthermore, as δ increase the reduction in oxygen decreases while the increase in the concentration of VEGF increases, as seen in figure S4.8D, and E, respectively. Similarly, as seen in figure S4.8H, the magnitude of shear stress increases with δ. Collectively, these changes result in a decrease in cell growth rate with δ as seen in figure 4.6. However, it may be noted that the change in the cell specific growth rate is very small. Therefore although there is a slight decrease in cell specific growth rate with an increase in bioreactor outlet pressure functionally there is very little change. It may be that as EC growth is restricted to the lumen that the change in flow path associated with pressure change has little effect. However, the pressure range evaluated is also small, which may have contributed to the small change seen as well. Future studies should evaluate a larger pressure range to determine if this is true.

Collectively, our simulations indicate that of the conditions evaluated, an inlet media flow rate of 7.5E-11 m^3/s with a pressure differential of -30 Pa between the lumen and ECS outlets is best

for lumenal EC growth. To ensure these findings are reliable, we now validate our model against experimental observations of EC growth in a HFM bioreactor.

4.5 Model validation

ECs have been cultured in HFM bioreactors [6]. Using the process parameters used in this study and applying them to our model, simulated and experimentally measured EC growth were compared and used to validate our model. In the exemplar study, the inlet flow rate was set such that the shear stress on the lumen wall was 0.66 Pa. As we assume that the flow through the lumen may be approximated as a parabola as given by equation 4.34. While the system considers a porous tube in which the boundary at the lumen wall is non-slip, comparisons between slip and non-slip solutions reveal a similar parabolic flow profile with low fluid velocities, we, therefore, take this assumption to hold true [210]. Consequently, we take it that the interstitial shear stress on the lumen wall is given by [58],

$$\sigma = \frac{8\mu\overline{w_l}}{2r_c} \tag{4.43}$$

where $\overline{w_l}$ is the mean axial fluid velocity. Accordingly, for our system the inlet media flow rate which yielded 0.66 Pa was found to be 6.005e-11 m^3/s. The experimental EC seeding density was measured to be 4E8 cells/m^2, and as such, the simulated seeding density was set to match. As cell growth rates may vary depending on cell source, the ζ_{max} was determined from the flask EC growth data from the same study and was taken to be given by,

$$\zeta_{max} = max\left(\frac{ln\left(\frac{N_t}{N_0}\right)}{t}\right) \tag{4.44}$$

Where N_t is the EC density at time t, N_0 is the initially EC seeding density, and t is time. ζ_{max} was therefore taken as 3.11E-6 s^{-1}. The media reservoir in the study had an air inlet through a microporous membrane to facilitate gas exchange. The resulting oxygen concentration in the reservoir

was measured and found to be equivalent to a partial pressure of 13.4 %. From equation 4.47, the initial and inlet dissolved oxygen concentration, $c_0^{(3)}$, was therefore calculated to be 0.15 mol/m^3. The reactor configuration in the study included a complete media recycle. The initial concentrations of each species of interest were set so that at $t = 0$, $c_0^{(i)} = c_f^{(i)}$. The inlet concentration of each species of interest were then subsequently taken as,

$$c_0^{(i)} = \overline{c_{l,L}^{(i)}} \tag{4.45}$$

Previously developed models for cell growth in HFM bioreactors have considered the effect of oxygen and shear stress only [196, 197, 198, 199, 58]. By reducing our model to consider the impact of oxygen and shear stress only, we also compare our model to predictions made by a reduced model similar to those previously described in literature.

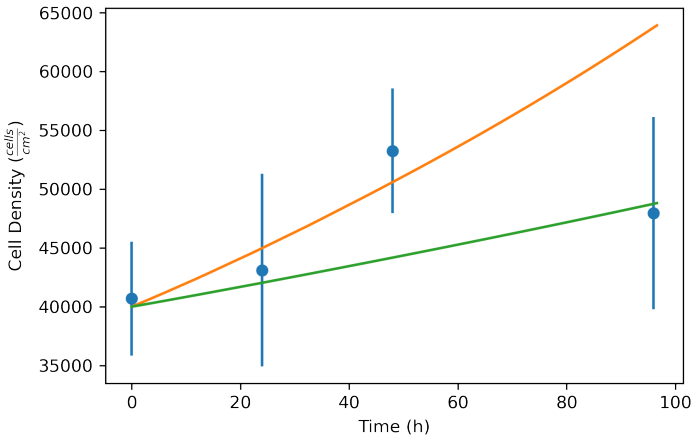


Figure 4.7. The change in simulated EC density as predicted by the full model (green) and reduced model (orange) compared to experimentally measured values taken from [6], as shown as blue points.

As seen in figure 4.7, compared to the full model, the reduced model predicted EC numbers to increase at a higher rate at all times. Across the 96 hour culture period, our full model closely matched the experimentally measured values at 24 and 96 hours but failed to capture the spike in EC density at 48 hours. In contrast, the reduced model was within experimental error for the first 48 hours. However,

by 96 hours, EC density was overestimated.

While comparisons between these experimentally measured values start to validate our simulated results, the porosity and permeability of the membranes used in this exemplar study are not reported. Furthermore, the HFMs used in this study were produced through traditional extrusion and solvent casting while EHFMs are produced through electrospinning. This means that the porosity and permeability of EHFMs and the HFMs used in this study are likely to differ substantially. However, as these values were not reported, we substitute the porosity and permeability of our EHFMs into our simulations. In both the simulations and experimental study ECs are grown in the lumen of the HFM and EHFMs. ECs in the lumen are directly exposed to lumenal fluid shear. Similarly, nutrient supply is not perturbed by the porosity or permeability of the membrane layer. It may be due to these reasons that we see agreement between our simulated and experimental results. To further validate our model comparisons between simulated and experimental results of EC grown in the lumen and ECS of an EHFM bioreactor should be made.

4.6 Conclusion

We present a model of EC growth in a EHFM bioreactor, in which, we model two-dimensional single-phase and porous media fluid flow with the Navier stokes equations and Brinkman equation, respectively. Furthermore, we consider nutrient transport with an advection-diffusion-reaction model. Finally, we model EC growth with a phenomenological data-driven model of endothelial cell metabolism and signalling, sensitive to shear stress, nutrient and signalling molecule concentrations.

We hypothesised that inlet media flow rate and bioreactor outlet partial pressure alters EC growth rate. Indeed we found that, between 5E-13 and 5E-9 m^3/s. EC growth rate increased with inlet media flow rate up to a maximum of 8.036E-6 s^{-1} at 7.5E-11 m^3/s, after which it began to decrease. An increase in lumen to ECS outlet partial pressure, however, was found to decrease EC growth rate.

Collectively our finding suggest that, of the conditions considered, an inlet flow rate of 7.5E-11 m^3/s with a lumen partial pressure differential of -30 Pa conferred the highest EC growth rate. This inlet velocity is particularly noteworthy as it corresponds to a wall shear stress very close to that for in vasculature *in vivo* [6]. Finally, we validated our model with experimental HFM bioreactor EC growth data and compared our model to a reduced version, which considered only the role of oxygen and shear stress. While these studies suggest our finds are valid, to better validate our findings studies evaluating EC growth in a EHFM bioreactor should be used.

4.7 Supplementary section

4.7.1 Development of Endothelial Cell Growth Model

Meta-analyses of quantitative data in the literature with established substrate growth and inhibition models can be used to develop and parameterise a data-driven models. Here, through the analysis of data in the literature describing the dose-dependent behaviour of ECs in response to the concentration of metabolites, cell signalling molecules, and the magnitude of fluid sheer stress, we present a parameterised data-driven model of EC growth and behaviour.

4.7.1.1 Model development method

To obtain data, literature databases: Scopus, PubMed and SciFinder were searched to exhaustively collect and evaluate all data available. Literature was screened for suitability by considering cell source, methodology and range of conditions used in each study. Only studies using human umbilical vein endothelial cells (HUVECs) as the cell source were selected. Methodologies in which EC numbers were counted directly, rather than determined through the use of an assay, were preferentially selected. When data were not tabulated, the raster graphics editor Adobe Photoshop was used to measure off data points from graphs.

Raw cell growth data was subsequently pre-processed to extract cell specific growth, excretion or uptake values as given by equation 4.46.

$$gr = \frac{ln\left(\frac{N(t)}{N_0}\right)}{t} \tag{4.46}$$

where gr is the cell specific growth, excretion or uptake rate, $N(t)$ is the number of cells or concentration of the specifies of interest at time t, and N_0 is the initial number of cells or concentration of the species of interest.

In cases where multiple suitable data sources were identified for a given species of interest, data sets were combined. To account for variability between maximal cell specific growth rates, protein expression and waste metabolite production rates between cells used in different studies, a scaling method was used. To scale data sets, the average cell specific growth rate or expression rate was calculated for each data set considered. A scaling factor for each data set was then calculated by dividing the maximum average rate for all sets by the average rate for a given set. All data were then multiplied by the scaling factor. By this means, the features of each data set were maintained and comparable between studies while creating a unified scaled data set.

To determine a suitable model to describe a given dynamic, ten Monod-based growth kinetic models, the same as those used by Dutta *et al.* and Ingram *et al.* [211, 212], as seen in table 4.7, were fitted to the data from the literature. The application, function, and parameters of these models have previously been reviewed in detail [213, 211, 214, 212]. The Monod model has widely been used as a simplistic model to describe the dose dependent change in bacterial growth as a function of substrate concentration [215, 214]. However, the Monod function fails to capture potential inhibitory effects that may occur at higher substrate concentrations. Subsequently, models such as the Haldane, and Han-Levenspiel models extended upon the seminal Monod model to capture the inhibitory effects of substrates through various means including the incorporation of an S_{max} term, which is the upper concentration of a substrate at which growth rate is reduced to zero [216, 217, 218]. The parameters in the models detailed in table 4.7, with respect to the species of interest i, are; $c^{(i)}$, the concentration, $G^{(i)}$, the cell specific growth, uptake or excretion rate, $V_{max}^{(i)}$, the maximum growth, uptake or excretion rate, $K_s^{(i)}$, the half saturation constant, $n^{(i)}$, the Moser constant, $m^{(i)}$, the Han-Levenspiel constant, $S_{max}^{(i)}$, the maximum substrate concentration, $K^{(i)}$, the growth constant, and $K_I^{(i)}$, the growth inhibition constant.

The parameters for each model were estimated through non-linear regression with an in-house Python script, "Bio-Fit", as seen at: `https://github.com/ristojm/Biofit.git`. To determine the

model of best fit, each of the dynamics was initially qualitatively evaluated to determine whether the data presented with a pseudo logarithmic growth, exponential growth or exponential decay profile. Accordingly, the models were fitted as seen, as the reciprocal, or as the inverse. Additionally, if there was an apparent basal production or consumption, a basal term was added to each. Unless stated otherwise, the R^2 value was used to determine the model which fit the data best. In cases where no model gave an R^2 value of more than 0.9, the model which qualitatively best preserved the features of experimental data was selected at the discretion of the author, while aiming to minimize the number of parameters associated with each model and excluding models which do not capture physiological behavior. Furthermore, owing to the scarcity of dose-response data, the ability to use statistical methods to prevent the overfitting of data was not always possible. This was because in some cases the number of data points was equal to less than the number of parameters associated with the models considered. To overcome these limitations future cellular dose-response studies are required.

4.7.1.2 Sub model selection

Cell growth develops as a function of environmental conditions, including nutrient, waste, and cell signalling molecule concentration, as well as mechanical stimulation and topographic effects. Similarly, the rate of cellular consumption and production of soluble factors and ECM proteins depends on environmental conditions. To model cell growth, it is necessary to determine the species of interest, model the kinetics by which they are produced and consumed, and the influence each has on cell growth and behaviour. Modulatory cell growth mechanisms may broadly be broken up into those mediated by cell signalling and metabolism.

4.7.1.2.1 Endothelial cell metabolism

Cell metabolism serves three primary purposes: energy production, redox homeostasis, and biomass synthesis. Strikingly, cell metabolism is vastly similar between different species in the animal kingdom.

Table 4.7. Suite of substrate limitation and inhibition models evaluated to describe cell specific growth, protein expression, metabolite consumption, and waste metabolite excretion rates.

Model	Equation	Reference
Menten	$G^{(i)} = \frac{V_{max}^{(i)} c^{(i)}}{K_s^{(i)} + c^{(i)}}$	[215]
Reciprocal Monod	$G^{(i)} = V_{max}^{(i)} \frac{K_s^{(i)} + c^{(i)}}{c^{(i)}}$	-
Inverse Monod	$G^{(i)} = \frac{K_s^{(i)} c^{(i)}}{V_{max}^{(i)} - c^{(i)}}$	-
Moser	$G^{(i)} = \frac{V_{max}^{(i)} (c^{(i)})^{n^{(i)}}}{K_s^{(i)} + (c^{(i)})^{n^{(i)}}}$	[219]
Han-Levenspiel	$G^{(i)} = \frac{V_{max}^{(i)} c^{(i)} \left[1 - \frac{c^{(i)}}{S_{max}^{(i)}}\right]^{n^{(i)}}}{c^{(i)} + K_s^{(i)} \left[1 - \frac{c^{(i)}}{S_{max}^{(i)}}\right]^{m^{(i)}}}$	[218]
Luong	$G^{(i)} = \frac{V_{max}^{(i)} c^{(i)}}{K_s^{(i)} + c^{(i)}} \left[1 - \frac{c^{(i)}}{S_{max}^{(i)}}\right]^{n^{(i)}}$	[217]
Yano	$G^{(i)} = \frac{V_{max}^{(i)} c^{(i)}}{K_s^{(i)} + c^{(i)} + \left(\frac{(c^{(i)})^2}{K_I^{(i)}} \left(1 + \frac{c^{(i)}}{K^{(i)}}\right)\right)}$	[220]
Webb	$G^{(i)} = \frac{V_{max}^{(i)} c^{(i)} \left(1 + \frac{c^{(i)}}{K^{(i)}}\right)}{K_s^{(i)} + c^{(i)} + \frac{(c^{(i)})^2}{K_I^{(i)}}}$	[221]
Haldane	$G^{(i)} = \frac{V_{max}^{(i)} c^{(i)}}{K_s^{(i)} + c^{(i)} + \frac{S_{max}^{(i)}}{K_I^{(i)}}}$	[216]
Edwards	$G^{(i)} = V_{max}^{(i)} c^{(i)} \left[e^{\frac{-c^{(i)}}{K_I^{(i)}}} - e^{\frac{-c^{(i)}}{K_s^{(i)}}}\right]$	[222]
Aiba	$G^{(i)} = \frac{V_{max}^{(i)} c^{(i)}}{K_s^{(i)} + c^{(i)}} e^{\frac{-c^{(i)}}{K_I^{(i)}}}$	[223]
Andrews	$G^{(i)} = \frac{V_{max}^{(i)} c^{(i)}}{(K_s^{(i)} + c^{(i)}) \left(1 + \frac{c^{(i)}}{K_I^{(i)}}\right)}$	[224]

It is, therefore, surprising that ECs display metabolic adaptations different to most cell types [225]. In contrast to most healthy cell types, ECs are glycolysis addicts, producing 85% of their ATP glycolytically, converting glucose to lactate [85]. The glycolysis addicted nature of ECs is reflected in the combined data from the literature [226, 227, 228], as seen in figure S4.1, both the uptake [229] of glucose and EC specific growth rate [230] can be seen to increase with glucose concentration.

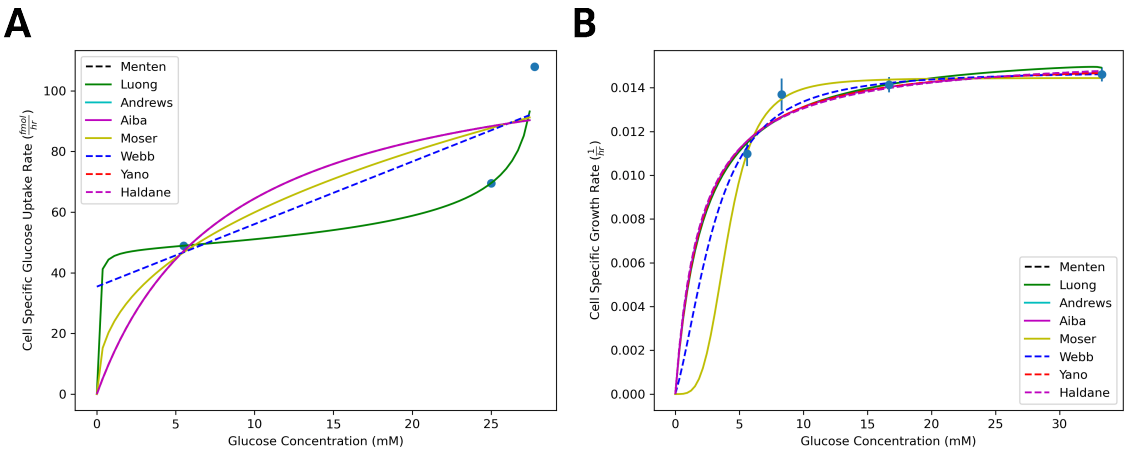


Figure S4.1. (A) Endothelial cell specific glucose uptake rate in response to glucose concentration and (B) Cell specific growth rate as a function of glucose concentration, with associated models, and experimental data from the literature are shown as blue points.

Although the Luong model was found to have the highest R^2 value of 0.999, the Webb function, with an $R^2 = 0.698$, qualitatively appeared to better preserve the features of EC glucose uptake rate compared to the Luong model, which appeared to be overfitted. With an R^2 of 0.984, the Moser equation was found to best describe the glucose dose dependent response of EC growth rate. The kinetic parameters determined to best describe EC glucose uptake and dose dependent growth rate may be seen in table 4.8. While glucose is integral to EC survival, ECs utilise several other metabolites.

Table 4.8. Fitted model parameters for endothelial cell glucose dose dependent cell specific uptake and growth rate.

Name	Expression	Unit	Description
V_{max}	4.478E4	$[mol/s]$	Glucose maximum consumption rate
K_s	1.278e-08	$[mol/m^3]$	Glucose consumption half saturation constant
n	0.417		Glucose consumption Moser constant
G_{max}	0.014	$[mol/s]$	Glucose maximum proliferation rate
K_G	0.244	$[mol/m^3]$	Glucose proliferation half saturation constant
n	3.745		Glucose proliferation Moser constant

Glutamine, the most abundant non-essential amino acid in circulation, is the amino acid most consumed by ECs. Predominantly catabolised by ECs for reactive oxygen species homeostasis, protein and nucleotide production, ECs with deficient glutamine have been found to be more susceptible to oxidative stress and have inhibited proliferation and motility. Surprisingly, in spite of its abundance,

ECs have been found to synthesise negligible amounts of glutamine. However, inhibition of glutamine synthesis was found to inhibit EC proliferation, and migration [87, 225]. Further to glutamine, asparagine, arginine, and serine have been identified to be vital to EC functionality, without which motility and proliferation are inhibited [84]. Considering data from the literature [231], uptake [231], and cell specific growth rate [232] were seen to increase with Glutamine concentration, as seen in figure S4.2.

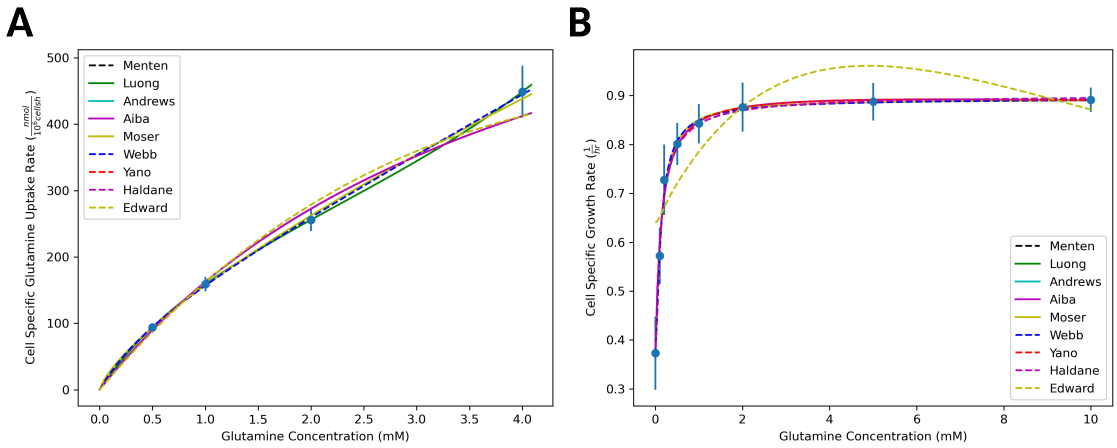


Figure S4.2. (A) Endothelial cell specific glutamine uptake rate in response to glutamine concentration and (B) Cell specific growth rate as a function of glutamine concentration, with associated models, and experimental data from the literature are shown as blue points.

With an R^2 of 1.00, the Luong model was to best fit the EC Glutamine uptake data. However, the Moser equation was selected as it was found to have an R^2 of 0.998 and has a reduced computational demand compared to the Luong function. When considering the change in EC specific growth rate with glutamine, none of the functions were found to have an R^2 greater than 0.9. However, as seen in figure S4.2B, qualitatively, all of the models appeared to fit the experimental data well. The Menten model with a basal production term was therefore selected to model the change in EC cell specific growth rate with Glutamine concentration as it minimises the computational demand of the model. The kinetic parameters for which may be seen in table 4.9.

Ammonia is produced as a waste metabolite produced during EC catabolism of glutamine and as glutamine spontaneously degrades [233]. The production of ammonia due to the catabolism of glutamine may be modelled as a fraction of the rate of glutamine consumed [231]. Data from the

Table 4.9. Fitted model parameters for endothelial cell glutamine dose dependent cell specific uptake and growth rate.

Name	Expression	Unit	Description
V_{max}	2.404E7	$[mol/s]$	Glutamine maximum consumption rate
K_s	9.867E-8	$[mol/m^3]$	Glutamine consumption half saturation constant
n	0.740		Glutamine consumption Moser constant
b	0.364	$[mol/s]$	Glutamine basal proliferation constant
G	0.538	$[mol/s]$	Glutamine maximum proliferation rate
K_G	0.125	$[mol/m^3]$	Glutamine proliferation half saturation constant

literature [234] revealed that as the concentration of ammonia increases, the EC specific growth rate decreases. Of the models considered, the Moser model was found to have the closest fit. However, this fit was poor, with an R^2 of 0.680. Qualitatively, as seen in figure S4.3, the Webb model appeared to give a good approximation to the features of the change in EC specific growth rate with ammonia concentration and was consequently selected. The parameters for ammonia production and the ammonia dose dependent EC growth rate models may be seen in table 4.10.

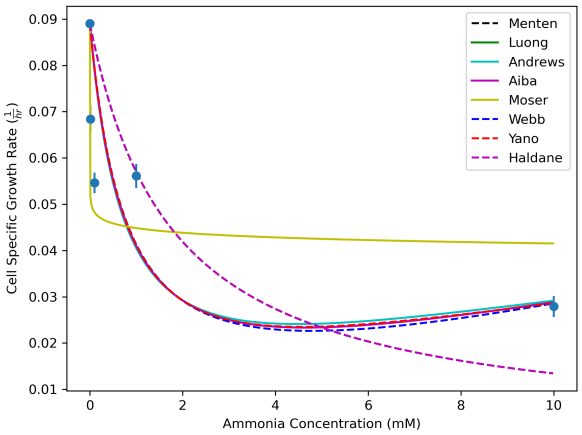


Figure S4.3. Endothelial cell ammonia dose dependent change in cell specific growth rate with associated models and experimental data from the literature shown as blue points.

ECs as glycolysis addicts exhibit a low level of aerobic metabolism, and their proximity to relatively high oxygen concentrations from fresh blood flow can lead to the formation of reactive oxygen species [235, 236]. Collectively, as seen from the data in the literature [235, 236], shown in figure S4.4, these effects yield an initial increase in EC cell specific growth rate with oxygen concentration followed by

Table 4.10. Fitted model parameters for endothelial cell ammonia dose dependent cell specific uptake and growth rate equation parameters.

Name	Expression	Unit	Description
Y	0.964		Ratio of ammonia production for each glutamine consumed
b	11.236	$[mol/s]$	Ammonia basal proliferation constant
G_{max}	6.259	$[mol/s]$	Ammonia maximum proliferation rate
K	3.724	$[mol/m^3]$	Ammonia proliferation constant
K_G	0.007	$[mol/m^3]$	Ammonia proliferation half saturation constant
K_I	1.12E8	$[mol/m^3]$	Ammonia proliferation inhibition constant
Y_{max}	47.710	$[mol/s]$	Ammonia proliferation function normalisation constant

a decrease at super-physical concentrations. While the Webb model was found to have the greatest

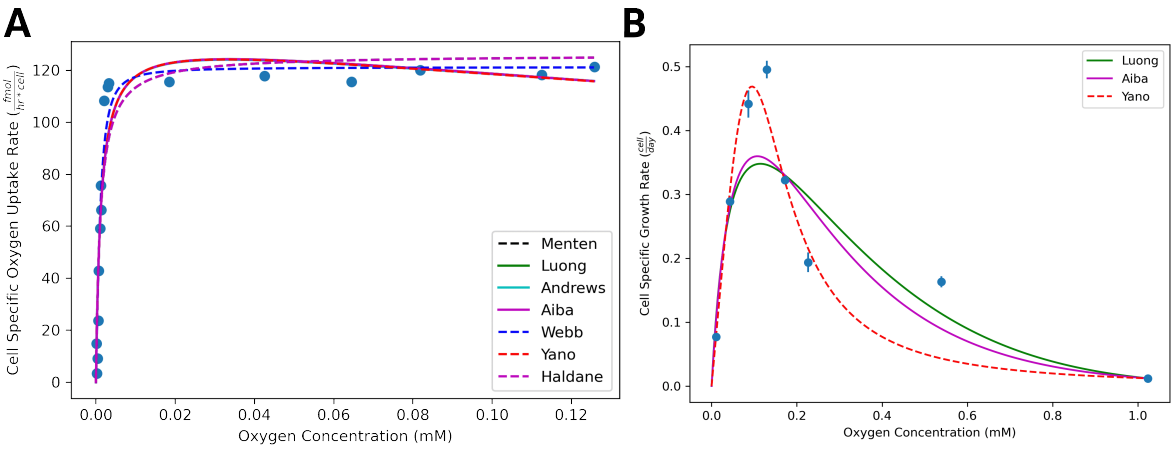


Figure S4.4. (A) Endothelial cell specific oxygen uptake rate in response to oxygen concentration and (B) Cell specific growth rate as a function of oxygen concentration, with associated models, and experimental data from the literature are shown as blue points.

R^2 value, of 0.978, the Menten model had an R^2 of 0.891 and, as seen in figure S4.4, qualitatively appeared to maintain the features of the EC oxygen uptake. The Menten model was, therefore, selected to describe EC uptake with less computational complexity. In contrast, none of the models evaluated to model the oxygen dose dependent change in EC specific growth rate were found to have an R^2 greater than 0.9. As seen in figure S4.4, qualitatively, the Yano model appeared to fit the data well and had an R^2 of 0.896 and so was selected accordingly. The parameters for each model may be seen in table 4.11. Having evaluated the principal metabolites of interest modulating EC growth according to the data available in literature, we now consider the role of cell signalling and fluid shear stress.

Table 4.11. Fitted model parameters for endothelial cell oxygen dose dependent cell specific uptake and growth rate equation parameters.

Name	Expression	Unit	Description
$V_{max}^{(3)}$	119.034	$[mol/s]$	Oxygen maximum consumption rate
$K_s^{(3)}$	969.881	$[mol/m^3]$	Oxygen consumption half saturation constant
$n^{(3)}$	2.435		Oxygen consumption Moser constant
$G_{max}^{(3)}$	1.182E3	$[mol/s]$	Oxygen maximum proliferation rate
$K_G^{(3)}$	951.260	$[mol/m^3]$	Oxygen proliferation half saturation constant
$K_I^{(3)}$	9.490E-05	$[mol/m^3]$	Oxygen proliferation Yano inhibition constant
$K^{(3)}$	0.020	$[mol/m^3]$	Oxygen proliferation Yano constant
$Y_{max}^{(3)}$	0.075	$[mol/s]$	Oxygen proliferation function normalisation constant

4.7.1.2.2 Endothelial cell signalling

Given the complexity of vasculogenesis, it is somewhat surprising that a single soluble growth factor, vascular endothelial growth factor (VEGF), presides as the dominant regulatory factor [78, 80, 81]. To modulate the reversible transition between quiescence and a proliferative phenotype, the growth factor VEGF-A binds with the receptor VEGFR-2. The subsequent tug-of-war interplay between NOTCH and DLL4 expression in adjacent ECs facilitates the VEGF modulation of EC proliferation, vessel branching, and enlargement [80]. Providing further modulatory effect to this process, two isoforms, B and C, mediate the response to VEGF-A and regulate the tip and stalk cell phenotypic specification and lymphangiogenesis respectively [81]. Considering the data from the literature, as seen in figure S4.5, EC VEGF production increases with lactate concentration [237]. Similarly, EC specific growth rate increases with VEGF concentration [221, 216, 219, 222]. The inverse Monod function was found to fit the cell specific release of VEGF data with an R^2 of 0.997. However, none of the models fit the EC VEGF dose dependent change in specific growth rate data with an R^2 greater than 0.9. Of the models evaluated, the Webb model gave the best fit with an R^2 of 0.729 while qualitatively maintaining the main features of the data and was therefore selected. The parameters for the models describing EC VEGF production and VEGF dose dependent cell specific growth rate may be seen in table 4.12.

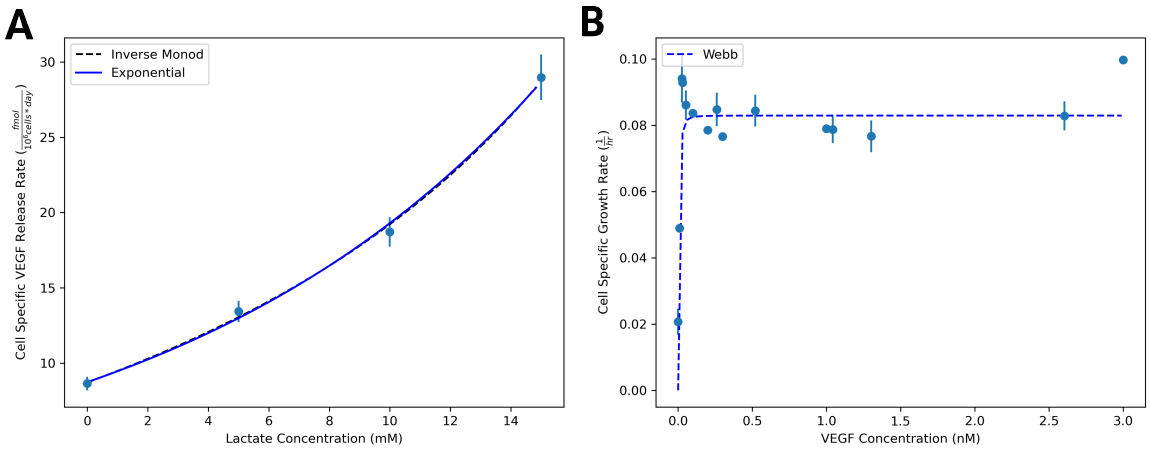


Figure S4.5. Endothelial cell specific VEGF release rate in response to lactate concentration and (B) Cell specific growth rate as a function of VEGF concentration, with associated models, and experimental data from the literature are shown as blue points.

Table 4.12. Fitted model parameters for endothelial cell VEGF dose dependent cell specific uptake and growth rate equation parameters.

Name	Expression	Unit	Description
$a^{(4)}$	8.724	$[mol/s]$	VEGF basal production constant
$V_{max}^{(4)}$	24.665	$[mol/s]$	VEGF maximum production rate
$K_v^{(4)}$	33.496	$[mol/m^3]$	VEGF production maximal Lactate concentration
$G_{max}^{(4)}$	0.110	$[mol/s]$	VEGF function maximum proliferation rate value
$K_G^{(4)}$	2.604E-7	$[mol/m^3]$	VEGF proliferation maximum growth constant
$K_I^{(4)}$	9.49E-5	$[mol/m^3]$	VEGF proliferation inhibition constant
$K^{(4)}$	0.020347	$[mol/m^3]$	VEGF proliferation constant
$Y_{max}^{(4)}$	0.083	$[mol/s]$	VEGF proliferation function normalisation constant

In view of the lactate dependent VEGF release rate, we consider the lactate release kinetics. As seen in figure S4.6A, data collected from the literature shows that lactate production decreases with oxygen concentration [237]. While the inverse Webb model had the highest R^2 value of 0.992, the inverse Moser model had an R^2 of 0.955 and, as illustrated in Figure S4.4, maintained the EC oxygen-dependent lactate production features with the curve falling within the error bars for each data point. Therefore, we selected the inverse Moser model to describe EC uptake due to its reduced computational complexity. This assumption was considered valid as the inverse Moser model accurately reflected the decrease in lactate production with increasing oxygen concentration, with model predictions remaining within the error margins of all oxygen concentration data points in the system. In contrast, the Aiba and Andrews model were deemed to be unacceptable as, although they had had an R^2 above 0.95, the lactate

production appeared to initially decrease with oxygen concentration but then increase again around an oxygen concentration of 0.05 mM, which is not physiologically consistent.

In vivo, subsequent to the formation of immature blood vessels and the onset of vessel perfusion, flow-induced wall shear stress has been shown to evoke a series of intra-cellular cascades shifting cells towards quiescence [82]. This shift towards quiescence with increased wall shear stress is further exacerbated by an associated increase in mass transfer leading to an increase in oxygen availability. This, in turn, results in a decrease in lactate production, which culminates in a further shift towards quiescence [78]. From the data in the literature, [238, 239], seen in figure S4.6, EC death rate increases with wall shear stress [240].

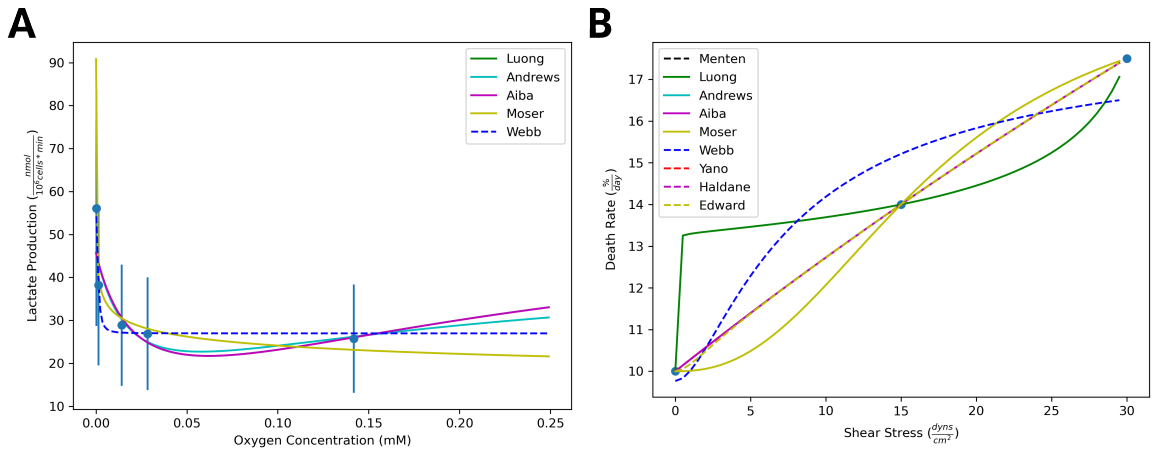


Figure S4.6. (A) Endothelial cell specific Lactate release rate in response to oxygen concentration and (B) Cell specific death rate as a function of shear stress, with associated models, and experimental data from the literature are shown as blue points.

The Menten function was found to describe the effect of shear stress on death rate with an R^2 of 1. The model parameters for both the oxygen concentration dependent lactate production and shear stress dependent death rate may be seen in table 4.13.

Table 4.13. Fitted model parameters for endothelial cell oxygen dose dependent lactate production and shear stress dependent cell specific growth rate.

Name	Expression	Unit	Description
$V_{max}^{(5)}$	652.762	$[mol/s]$	Lactate maximum production rate
$K_s^{(5)}$	2.160E12	$[mol/m^3]$	Lactate production half saturation constant
$n^{(5)}$	0.125		Lactate production Moser constant
$b^{(ss)}$	1.157E-6	$[1/s]$	Shear Stress basal proliferation constant
$G_{max}^{(ss)}$	6.944E-6	$[1/s]$	Shear stress maximum proliferation rate
$K_G^{(ss)}$	20.999	$[Pa]$	Shear Stress proliferation half saturation constant

4.7.1.3 Endothelial cell growth model formulation

4.7.2 Endothelial cell growth model formulation

Considering these findings in conference we formulate a data-driven model to describe the dose-dependent change in endothelial cell growth rate. Substrates found to promote EC growth include: Glucose, Glutamine, and Oxygen. Oxygen concentration was found to modulate the rate of lactate production. In turn, lactate concentration modulated the excretion of VEGF, and VEGF modulated EC growth rate. Ammonia production was found to depend on Glutamine catabolism and spontaneous degradation of glutamine. An increase in Ammonia concentration was found to inhibit EC growth rate. Finally, fluid shear stress was found to promote EC death. Each of these effects are modelled through the application of the sub-models and their respective parameters, as detailed above. Collectively, these sub-models form a parameterised model to describe EC growth, as illustrated in figure 4.1, and detailed in section 4.3.3.

4.7.3 Dissolved gas concentration calculations

The concentration of dissolved gasses were calculated with Henry's law as given by,

$$c_0^{(3)} = H^{(i)}(T) \times \Pi^{(i)} \tag{4.47}$$

where $\Pi^{(i)}$, is the partial pressure of the gaseous species i and $H^{(i)}(T)$ is the Henry's law constant for species i at temperature, T, given by,

$$H^{(i)}(T) = H^{(i)} + e^{\left(k_H^{(i)}\left(\frac{1}{T} - \frac{1}{298.15}\right)\right)} \tag{4.48}$$

where $H^{(i)}$ is the Henry's law solubility constant in water at 298.15 K and $k_H^{(i)}$ is the temperature dependence constant, the values for which may be seen in table 4.14.

Table 4.14. Table of EC seeding density, membrane material property parameters, inlet concentrations and diffusivities for the species of interest

Parameter	Value	Unit	Description	Ref.
$H^{(3)}$	1.2922E-5	$\left[\frac{s^2 \times mol}{kg \times m^2}\right]$	Henry's law oxygen solubility constant in water	[209]
$k_H^{(3)}$	1500	$[K]$	Henry's law oxygen solubility temperature dependence constant in water	[209]

4.7.4 Parameter values

Table 4.15. Endothelial cell reaction model parameter values

Name	Expression	Unit	Description
$V_{max}^{(1)}$	4.478E4	$[mol/s]$	Glucose maximum consumption rate
$K_s^{(1)}$	1.278e-08	$[mol/m^3]$	Glucose consumption half saturation constant
$n^{(1)}$	0.417		Glucose consumption Moser constant
$V_{max}^{(2)}$	2.404E7	$[mol/s]$	Glutamine maximum consumption rate
$K_s^{(2)}$	9.867E-8	$[mol/m^3]$	Glutamine consumption half saturation constant
$n^{(2)}$	0.740		Glutamine consumption Moser constant
$V_{max}^{(3)}$	119.034	$[mol/s]$	Oxygen maximum consumption rate
$K_s^{(3)}$	969.881	$[mol/m^3]$	Oxygen consumption half saturation constant
$n^{(3)}$	2.435		Oxygen consumption Moser constant
$a^{(4)}$	8.724	$[mol/s]$	VEGF basal production constant
$V_{max}^{(4)}$	24.665	$[mol/s]$	VEGF maximum production rate
$K_v^{(4)}$	33.496	$[mol/m^3]$	VEGF production maximal Lactate concentration
$V_{max}^{(5)}$	652.762	$[mol/s]$	Lactate maximum production rate
$K_s^{(5)}$	2.160E12	$[mol/m^3]$	Lactate production half saturation constant
$n^{(5)}$	0.125		Lactate production Moser constant
$Y^{(6,2)}$	0.964		Ratio of ammonia production for each glutamine consumed

Table 4.16. Endothelial cell growth model parameter values

Name	Expression	Unit	Description
ζ_{max}	2.306E-5	$[1/s]$	EC maximum cell growth rate
N_{max}	$9.911E14$	$[1/m^3]$	EC seeding density
N_0	$5.000E11$	$[1/m^3]$	EC seeding density
$b^{(ss)}$	1.157E-6	$[1/s]$	Shear Stress basal proliferation constant
$G_{max}^{(ss)}$	6.944E-6	$[1/s]$	Shear stress maximum proliferation rate
$K_G^{(ss)}$	20.999	$[Pa]$	Shear Stress proliferation half saturation constant
$b^{(6)}$	11.236	$[mol/s]$	Ammonia basal proliferation constant
$G_{max}^{(6)}$	6.259	$[mol/s]$	Ammonia maximum proliferation rate
$K^{(6)}$	3.724	$[mol/m^3]$	Ammonia proliferation constant
$K_G^{(6)}$	0.007	$[mol/m^3]$	Ammonia proliferation half saturation constant
$K_I^{(6)}$	1.12E8	$[mol/m^3]$	Ammonia proliferation inhibition constant
$Y_{max}^{(6)}$	47.710	$[mol/s]$	Ammonia proliferation function normalisation constant
$G_{max}^{(1)}$	0.014	$[mol/s]$	Glucose maximum proliferation rate
$m^{(1)}$	3.745		Glucose proliferation Moser constant
$Y_{max}^{(1)}$	0.014	$[mol/s]$	Glucose proliferation function normalisation constant
$K_G^{(1)}$	0.244	$[mol/m^3]$	Glucose proliferation half saturation constant
$b^{(2)}$	0.364	$[mol/s]$	Glutamine basal proliferation constant
$G_{max}^{(2)}$	0.538	$[mol/s]$	Glutamine maximum proliferation rate
$K_G^{(2)}$	0.125	$[mol/m^3]$	Glutamine proliferation half saturation constant
$Y_{max}^{(2)}$	0.895	$[mol/s]$	Glutamine proliferation function normalisation constant
$G_{max}^{(3)}$	1.182E3	$[mol/s]$	Oxygen maximum proliferation rate
$K_G^{(3)}$	951.260	$[mol/m^3]$	Oxygen proliferation half saturation constant
$K_I^{(3)}$	9.490E-05	$[mol/m^3]$	Oxygen proliferation Yano inhibition constant
$K^{(3)}$	0.020	$[mol/m^3]$	Oxygen proliferation Yano constant
$Y_{max}^{(3)}$	0.075	$[mol/s]$	Oxygen proliferation function normalisation constant
$G_{max}^{(4)}$	0.110	$[mol/s]$	VEGF function maximum proliferation rate value
$K_G^{(4)}$	2.604E-7	$[mol/m^3]$	VEGF proliferation maximum growth constant
$K_I^{(4)}$	9.49E-5	$[mol/m^3]$	VEGF proliferation inhibition constant
$K^{(4)}$	0.020347	$[mol/m^3]$	VEGF proliferation constant
$Y_{max}^{(4)}$	0.083	$[mol/s]$	VEGF proliferation function normalisation constant

4.7.5 Cell culture dynamics profiles

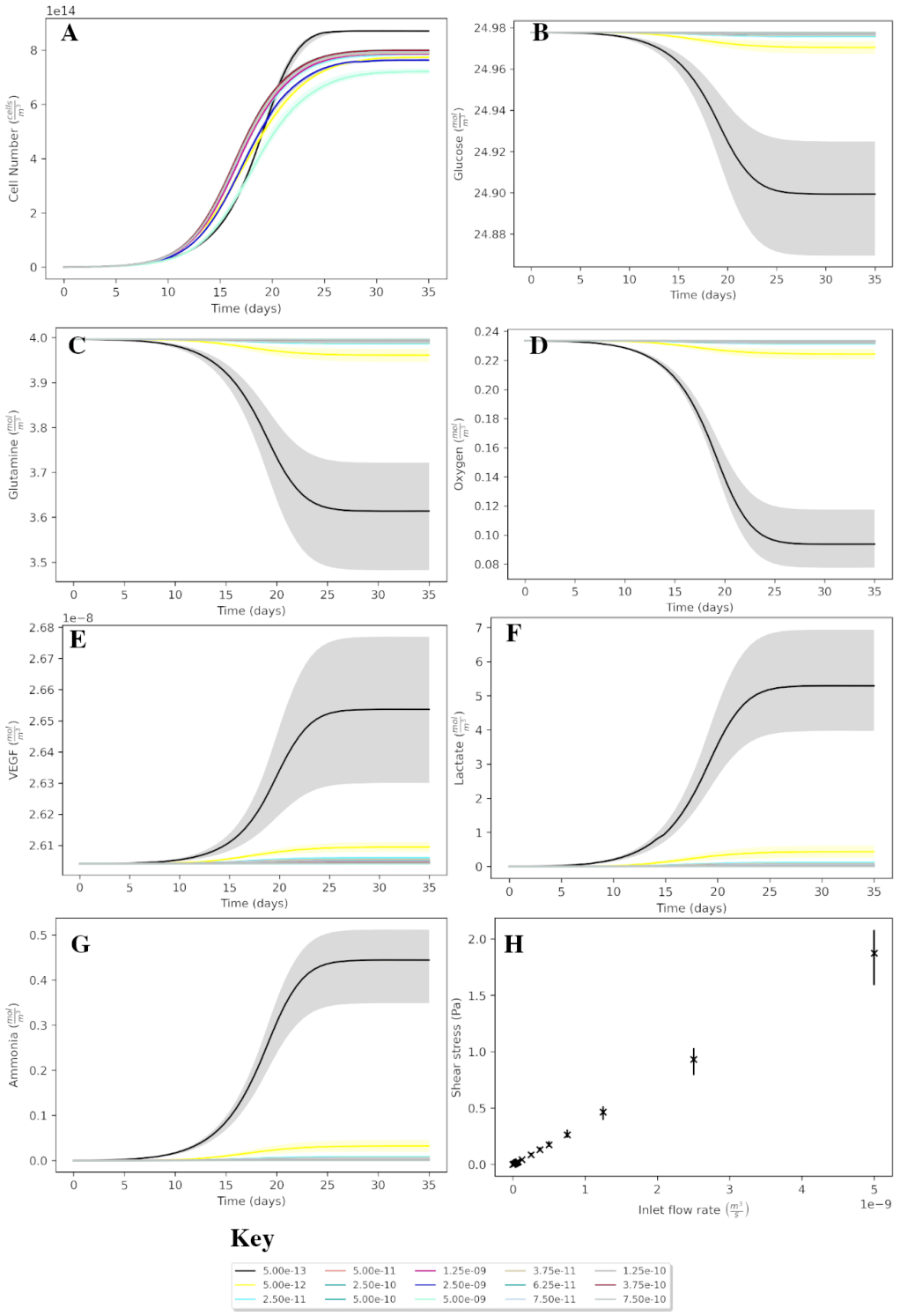


Figure S4.7. (A-G) EC culture dynamic profiles showing the influence of inlet media flow rate on endothelial cell growth and the change in concentration of the species of interest in an electrospun hollow fibre bioreactor, with bars illustrating the range in EC number and concentration in the cell layer. in which the colours shown in the key correspond with the adjacent flow rate in m^3/s. (H) The change in liquid shear stress in the cell layer with inlet flow rate.

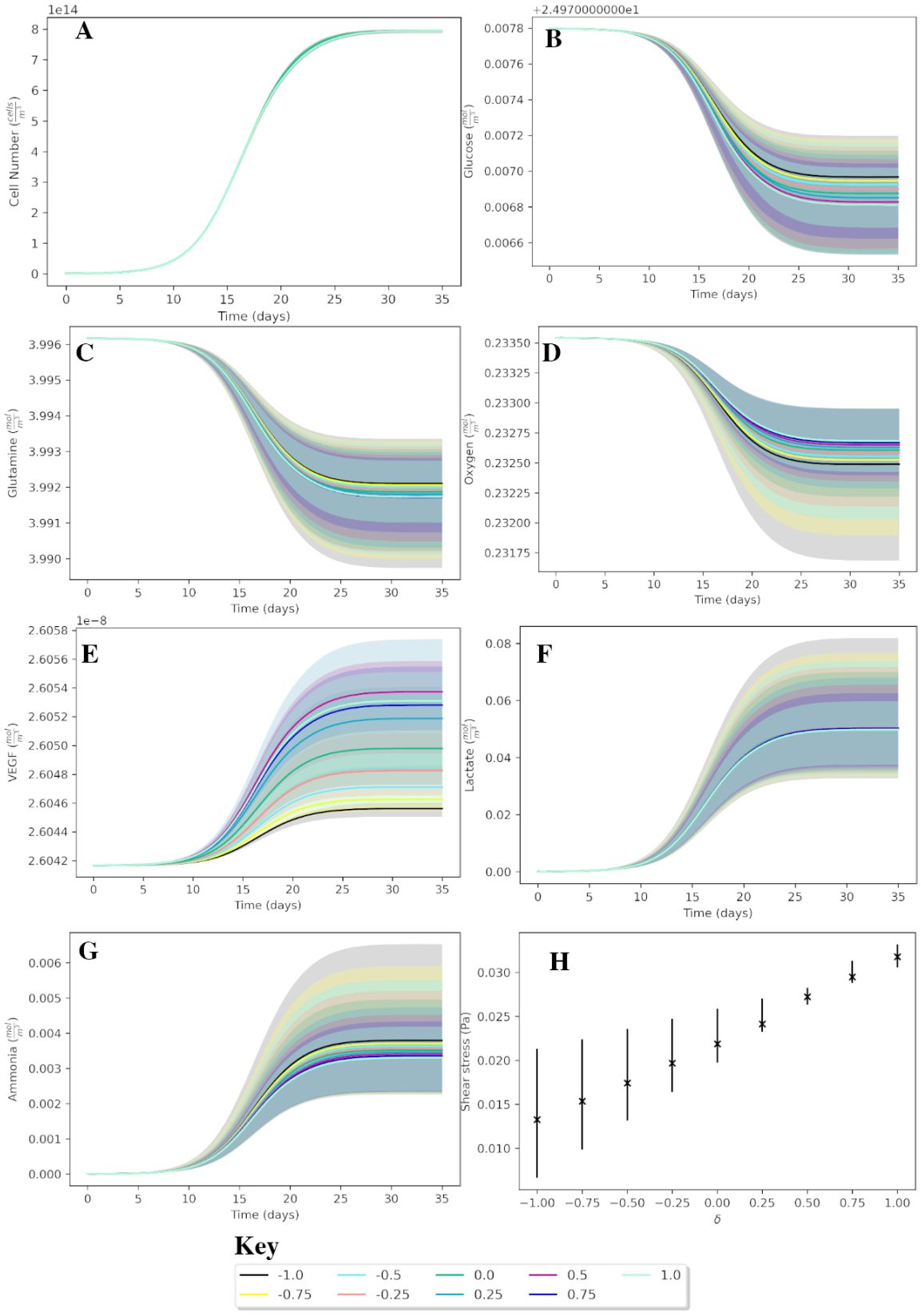


Figure S4.8. (A-G) Culture dynamics profiles showing the influence of the bioreactor ECS and lumen outlet partial pressure differential, δ, on endothelial cell growth and the change in concentration of the species of interest in an electrospun hollow fibre bioreactor, with bars illustrating the range in EC number and concentration in the cell layer. in which the colours shown in the key correspond with the adjacent δ value. (H) The change in liquid shear stress in the cell layer with inlet flow rate.

Statement of Authorship for joint/multi-authored papers for PGR thesis

To appear at the end of each thesis chapter submitted as an article/paper

The statement shall describe the candidate's and co-authors' independent research contributions in the thesis publications. For each publication, there should exist a complete statement that is to be filled out and signed by the candidate and supervisor **(only required where there isn't already a statement of contribution within the paper itself).**

Title of Paper	Endothelial cell growth in an electrospun hollow fibre membrane bioreactor: A mathematical perspective
Publication Status	□Published □ Accepted for Publication □ Submitted for Publication ☒Unpublished and unsubmitted work written in a manuscript style
Publication Details	e.g. Martin, R., Mouthuy, P., Ye, H., Waters, S., (2023) Endothelial cell growth in an electrospun hollow fibre membrane bioreactor: A mathematical perspective

Student Confirmation

Student Name:	Risto John Martin		
Contribution to the Paper	The formulation of the model, simulation work, analysis and writing were carried out by Risto Martin. Prof. Sarah Waters, Prof. Pierre Alexis-Mouthuy, and Prof. Hua (Cathy) Ye provided supervision and advice throughout.		
Signature		Date	06/01/2023

Supervisor Confirmation

By signing the Statement of Authorship, you are certifying that the candidate made a substantial contribution to the publication, and that the description described above is accurate.

Supervisor name and title: Prof Hua Ye		
Supervisor comments The description above is accurate.		
Signature 	Date	6 Jan 2023

This completed form should be included in the thesis, at the end of the relevant chapter.

Chapter 5

Prototyping of an electrospun hollow fibre membrane bioreactor

Electrospun hollow fibre membranes have been developed, as described in chapter 3. To aid the development of an electrospun hollow fibre membrane bioreactor for the culture of human umbilical vein endothelial cells, a model to describe endothelial cell growth and behaviour was developed, in chapter 4. The model was used to evaluate culture conditions to be used in an electrospun hollow fibre membrane bioreactor, thereby informing experimental design decisions and ensuring quality by design.

In this chapter, to evaluate our hypothesis that blended PCL/PDO electrospun hollow fibre membranes may be used as a substrate to support cell growth in 3D tissue culture, we present the development of; a novel EHFM bioreactor, methods for potting EHFMs; and novel methods for the evaluation of cell distribution in tissue engineered scaffold through μCT image analysis. Through the culture of human umbilical vein endothelial cells, the biocompatibility of electrospun PCL/PDO produced up to 50 ppm pyridine is evaluated. To do this, electrospun PCL/PDO is evaluated in both flat sheet and hollow fibre membrane configurations, under hydro-static and hydro-dynamic conditions.

In this section, all experimental work, data analysis and writing were carried out by Risto Martin. Prof. Hua (Cathy) Ye, Prof. Sarah Waters, and Prof. Pierre Alexis-Mouthuy provided supervision and advice throughout.

A vascular mimetic electrospun hollow fibre membrane bioreactor for the culture of human endothelial cells: An *In-Vitro* vascular model

Authors:

Risto Martin[1], Pierre-Alexis Mouthuy [2]*, Sarah Waters[3], Hua (Cathy) Ye[1]*

Affiliations:

[1]*Department of Engineering Science, University of Oxford, Oxford, OX3 7DQ, UK*

[3]*Nuffield Department of Orthopaedic Surgery, The Botnar Research Centre, Institute of Musculoskeletal Sciences, Oxford University, N.O.C. Headington, Oxford, OX3 7LD, UK*

[2]*OCIAM, Mathematical Institute, University of Oxford, Radcliffe Observatory Quarter, Woodstock Road, Oxford, OX2 6GG, UK*

*__Corresponding author__:

hua.ye@eng.ox.ac.uk, pierre-alexis.mouthuy@ndorms.ox.ac.uk

Keywords:

Tissue engineering — Bioreactor — Electrospun — Hollow fibre membrane — Vascular biology

Abstract:

Electrospun hollow fibre membranes (EHFMs) have been developed to: support cell growth in 3D tissue culture scaffolds larger than 200 μm; without disrupting passive mechanical cues; or preventing the use of auxiliary actuation in mechanically dynamic bioreactors. We hypothesised that; blended polycaprolactone (PCL) and polydioxanone (PDO) EHFMs may be used as a substrate to support cell growth in 3D tissue culture. We found that under hydro-static conditions, human umbilical vein

endothelial cell (HUVEC) growth was supported for 28 days on both PCL/PDO electrospun flat sheet membranes and EHFMs. When cultured in EHFMs, by day 22, HUVECs were seen to have reached confluency, align along the long axis of the membrane, have a distinct morphology, and established VE-cadherin cell-cell interactions. Similarly, under hydro-dynamic conditions in an EHFM bioreactor, HUVEC growth was maintained for 28 days. Furthermore, as in the hydro-static culture, at the terminus of the culture period, HUVECs were seen to align along the long axis of the bioreactor in the direction of fluid flow, have a distinct morphology, and have established cell-cell interactions. μCT cell location image analysis revealed HUVEC growth was retained in the lumen, as seeded, throughout the culture period. HUVEC density was greatest at the EHFM lumen inlet and tapered to a plateau within 5000 μm of the entrance, which was then maintained throughout the length of the EHFM fibre. In summary, our findings show that PCL/PDO EHFMs provide a biocompatible substrate for HUVEC growth. Furthermore, EHFMs may be used to support partitioned 3D tissue culture, and μCT image analysis may be used to evaluate full scaffold thickness cell growth distributions.

Introduction

The lack of cell-cell and cell-extracellular matrix has hitherto marred the physiological relevance of two-dimensional tissue culture techniques, which otherwise has been indispensable in elucidating the biochemical and mechanical mechanisms that regulate cell function in health and disease [8, 9]. Three-dimensional (3D) tissue culture techniques, more recently developed, promise to overcome this limitation. However, the short effective range of diffusive mass transfer, of just 200 μm, limits the size of these constructs [12, 13]. By facilitating membrane-bound advective mass transfer, hollow fibre membranes (HFMs) in bioreactors alleviate this size limitation.

Endothelial cells (ECs) were first cultured in the lumen of hollow fibre membranes in 1995 as a model of human vasculature [241]. In this initial culture, it was found that when exposed to hydro-

dynamic shear stress, ECs developed a phenotype more akin to that found *in vivo* [242]. In contrast, in the absence of fluid shear stress, changes in; cytoskeleton structure, cell morphology, proliferation, migration, and gene expression have been observed [243]. In the pursuit of an *in vitro* model of human vasculature, hydro-dynamic conditions are therefore necessary.

In vivo blood vessels are flexible and compliant. In contrast, traditional HFMs are rigid and monolithic. Consequently, HFMs disrupt passive mechanical cues and thereby limit the mimicry of the physiological condition afforded by HFM bioreactors. Thus, to prevent the disruption of passive mechanical cues while facilitating membrane-bound advective mass transfer, electrospun HFMs (EHFMs) have been developed [7].

We hypothesised that EHFMs produced from blended polycaprolactone (PCL) and polydioxanone (PDO), doped with pyridine, may be used as a substrate to support human umbilical vein endothelial cell (HUVEC) growth in 3D tissue culture. Herein, we describe the design of an EHFM bioreactor, means for potting highly porous EHFMs, EHFM bioreactor operation, and culture of ECs on electrospun flat sheet membranes as well as in EHFMs under hydro-static and hydro-dynamic conditions. Furthermore, by considering EC growth kinetics, morphology, distribution, and metabolite profiles, we evaluate the performance of the EHFM bioreactor developed.

5.1 Materials and methods

5.1.1 Preparation of electrospinning solutions

PDO (melting flow rate 4.5 g/10min at 170 °C, Riverpoint Medical, Portland, USA) and PCL (inherent viscosity of 1.11 dl/g Ashland Specialities, Dublin, Ireland) were dissolved in 1,1,1,3,3,3-hexafluoroisopropanol (HFIP, ultra-pure >99.99 %, Halocarbon Product Corporation, Atlanta, USA) at a ratio of 0.43 PCL/PDO with a total mass of 15.86 % w/v. Pyridine (purity >99.5 %, PhEur grade,

EMSURE ACS, Merck, Darmstadt, Germany) was added to the polymer granules along with HFIP at concentrations specified. Before spinning, the final solutions were agitated at room temperature on a roller for at least 24 h to allow for the complete dissolution of the polymer.

5.1.2 Electrospinning

5.1.2.1 EHFMs

EHFMs were fabricated with a single nozzle electrospinning apparatus, as previously described [7]. Briefly, the polymer solution was fed from a syringe pump (World Precision Instruments Limited, Florida, US) at a flow rate of 1 ml/hr, connected to a high voltage power supply system (30 kV, SL30P30/230, Spellman, West Sussex, UK) with a potential difference of 10-13 kV maintained between the nozzle and the collector. Before use, the stainless steel collector wire (600 µm in diameter, Scientific Wire Company LTD, Essex, UK) was washed with 70 % ethanol. The nozzle and the wire collector were placed, with a constant gap of 19 cm, in a glove box constantly circulated with filtered air to eliminate HFIP vapours produced during operation. A distance of 1.5 m was maintained between the tensioner and rotary spool bracket. The wire draw, rotation speed and directional oscillation frequency were maintained at 0.5 mm/s, 75 rpm and 3 rotations, respectively. To eliminate the influence of environmental electrostatic fluctuations, a polystyrene enclosure with holes to let the collector wire in and out each side was placed around the nozzle and collector. The EHFMs were continuously collected on the tensioner spool, which could be removed between spins and stored in a desiccator.

5.1.2.2 Electrospun flat sheet membranes

Electrospun flat sheet membranes were fabricated in an EC-DIG electrospinning system (IME Medical Electrospinning, Geldrop, the Netherlands), maintained at 50 % humidity and 20 °C. A constant gap of 19 cm was maintained between the nozzle and the 8 cm diameter rotating mandrel collector. The nozzle was set to pan the width of the rotating mandrel at 20 mm/s, which in turn

rotated at 50 rpm. The polymer solution was fed from a syringe pump (Harvard Apparatus, Holliston, Massachusetts, United States) at a flow rate of 1 ml/hr, and the potential difference was set between 10-13 kV. Electrospun flat sheet membranes were collected on aluminium foil coating the rotating mandrel, which could be removed for storage.

5.1.3 Membrane pre-hydration testing

Membrane pre-hydration testing, in line with ISO 10993-12 [194], was carried out to determine the volume of media required to saturate the membranes, which was then taken as the volume of cell suspension required for cell seeding. A minimum of 0.1 g of membrane material (n=3) was incubated at 37 °C in a 15 ml falcon tube with 10 ml of deionised water. The membrane material was removed from the tube, and the change in mass was recorded, from which the hydrating volume could be calculated.

5.1.4 Bioreactor Fabrication

Bioreactor assembly was a multi-stage process in which EHFMs were produced as described, while parts, including the outer bioreactor shell and membrane mounts, were 3D printed to be combined for use. A schematic of the bioreactor as assembled may be seen in figure 5.1.

5.1.4.1 Fabrication of 3D printed parts

The bioreactor shell and membrane mounts were drawn with SolidWorks (2022 edition, Dassault Systems SolidWorks Corporation, Waltham, USA) and were 3D printed by Stereolithography with the FormLabs Form 3B+ (Formlabs, Somerville, Massachusetts, USA). All parts were printed out of BioMed Amber V1 Resin (RS-F2-BMAM-01, Formlabs, Somerville, Massachusetts, USA). Printed parts were washed for 20 minutes in the Form Wash (Formlabs, Somerville, Massachusetts, USA) with 100 % isopropyl alcohol (Sigma-Aldrich, Dorset, UK). Washed parts were cured under UV at 75 °C in the Form Cure (Formlabs, Somerville, Massachusetts, USA) for 30 minutes.

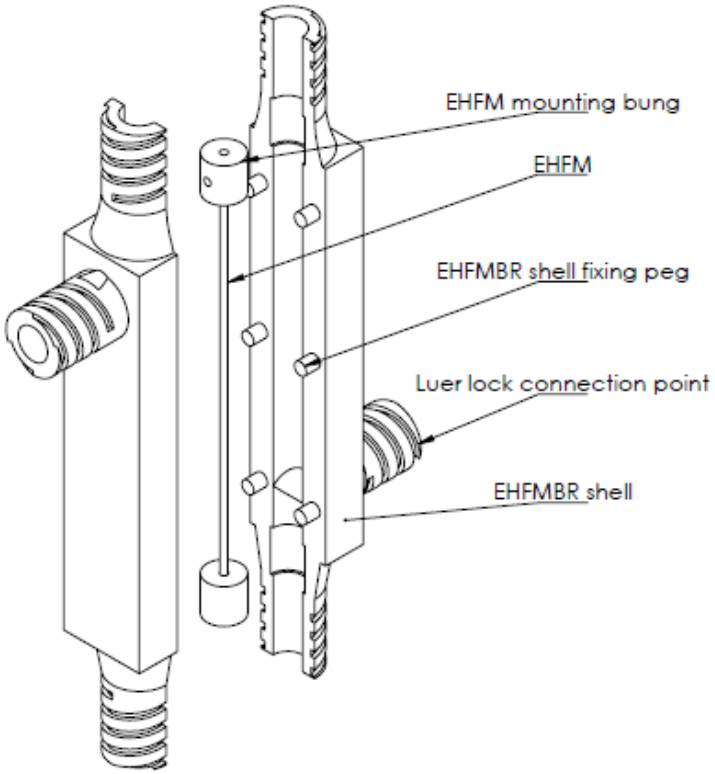


Figure 5.1. A schematic of the assembly of an electrospun hollow fibre membrane bioreactor.

5.1.4.2 Bioreactor Assembly

Sections of EHFM coated wire were cut to 8 cm, membrane mounts were threaded onto the cut section, and the EHFM was wetted with ethanol. The membrane mounts were moved such that a gap of 5 cm was between each. Epoxy resin (Epotek 301, Epoxy Technology Inc., Billerica, USA) was mixed and drawn into a syringe. The mixed epoxy was placed in an oven at 70 °C for 7 minutes to increase the viscosity of the epoxy mixture. A minimal amount of the Epoxy was then injected into each of the membrane mounts side channels. The wire was then removed from the EHFM with fine tweezers. To prevent the epoxy from wicking into the EHFMs, the EHFMs were soaked with ethanol as the epoxy cured. To prevent the membranes from drying out as the epoxy cured, the EHFM and mounts were placed in an ethanol vapour chamber. After 24 h, the mounted EHFMs were removed from the chamber,

and a scalpel was used to trim the excess EHFM from the mounts, as seen in supplementary figure S5.6. To check the patency of the mounted EHFMs, a 30 G blunt hypodermic needle (Temuro Ltd, Surrey) was inserted and removed from each end of the mounted and trimmed EHFM.

To encase the mounted membranes in the bioreactor shell, a minimal amount of epoxy resin (Epotek 301, Epoxy Technology Inc., Billerica, USA) was applied to the edge of each side of the bioreactor shell. The epoxyed membrane was slotted into the corresponding membrane mount slots, and the bioreactor shell closed around it. Clamps were fastened around the shell for 24 h to allow the epoxy to cure, as seen in figure 5.7B. To ensure uniform quality between bioreactors, each EHFM bioreactor was irrigated with deionised water. An EHFM bioreactor was only considered acceptable if the deionised water flowed through the EHFM lumen and was seen to permeate into the extra-capillary space as well.

5.1.5 Cell preparation and cell culture

Single donor human umbilical vein endothelial cells (HUVEC, LOT: 00291, Lonza, Basel, Switzerland) were grown in 170cm^2 flasks (Corning, NY, US) in Lonza Endothelial Cell Growth Medium-2 containing; Fetal Calf Serum 0.02 ml/ml, Hydrocortisone 0.2 μg/ml, hFGF-B 10 ng/ml, VEGF 0.5 ng/ml, R3-IGF-1 20 ng/ml, Ascorbic Acid 1 μg/ml, hEGF 5 ng/ml, Gentamicin 30 mg/ml, Amphotericin 15 ug/ml, Heparin 22.5 µg/ml (Lonza, Basel, Switzerland) and 1 % Antibiotic Antimycotic solution (Sigma-Aldrich, Dorset, UK). Flasks were incubated at 37 °C, 5 % CO2 and the growth medium was replaced every 2–3 days. Cultures were maintained under these conditions until the flasks reached 90 % confluency. Cells were regularly checked for Mycoplasma infection using a MycoAlert testing kit (Lonza, UK), according to the manufacturer's instructions.

5.1.5.1 Static scaffold culture

HUVECs were cultured on the surface of electrospun flat sheet membranes and in the lumen of EHFMs. 8 mm diameter disks of electrospun flat sheet membrane were recovered with a biopsy punch

(Stiefel, North Carolina, USA). Similarly, 1 cm EHFM coated wire sections were cut. The sections were soaked in ethanol and removed from the wire with fine tweezers. The recovered membrane sections were transferred into individual wells of 24 well plates (Corning, UK).

To sterilise the membranes, each well of the 24 well plates was filled with 1 ml of 70 % ethanol and transferred into a tissue culture hood in which they were left for 12 h. The membranes were subsequently washed with PBS for 1, 2, and 12 h. Finally, the PBS was replaced with fresh culture medium for 24 h and the plates were placed in an incubator at 37 °C, 5 % CO2. Sterility was thereby ensured as plates which showed any signs of bacterial or fungal growth after this period were discarded.

To seed the membranes, cultured cells were trypsinised from confluent flasks and re-suspended in fresh medium. A minimum volume of cell suspension, determined as described in section 5.1.3, was pipetted onto the surface of the electrospun flat sheet membranes or injected into the lumen of the EHFMs to yield a seeding density of 6×10^5 cells/cm^2. The seeded membranes were transferred into an incubator for 6 h to allow for cell attachment. Following cell attachment, cell viability was assessed with the PrestoBlue assay, as described in section 5.1.6, and subsequently replaced with 380 μL of fresh media. Cell viability was subsequently assessed every other day with media exchanges for 28 days. Spent media was recovered with each media exchange and transferred into sterile Eppendorf tubes for metabolite analysis, as described in section 5.1.11.

5.1.5.2 Bioreactor Operation

Prior to seeding the bioreactor, all of the tubes and fittings were autoclaved to ensure sterility. While working in a tissue culture hood the EHFM bioreactor was plumbed into the operational circuit, as seen in figure 5.2, and filled with 70 % ethanol. The assembled apparatus was then transferred into an incubator maintained at 37 °C, 5 % CO2. To ensure the sterility of the system 70 % ethanol was circulated for 12h. The system was then washed with PBS three times for 1, 2, and 12 h. Finally, the

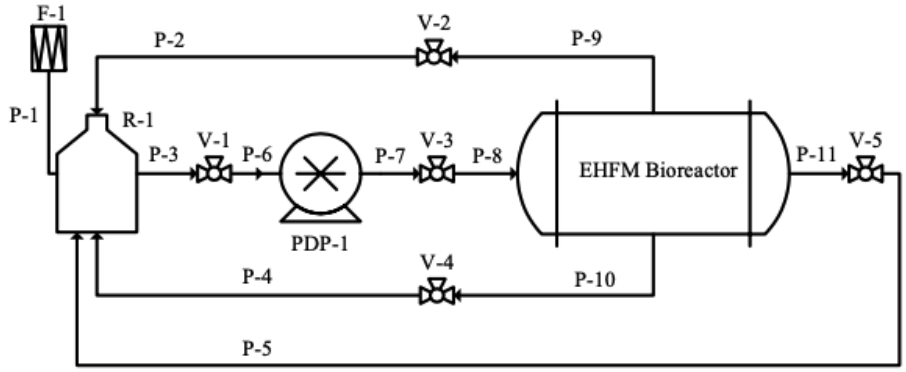


Figure 5.2. (A) piping and instrumentation diagram of the electrospun hollow fibre membrane bioreactor configuration.

PBS was replaced with fresh media and circulated for 24 h, if any signs of infection were detected the bioreactor was discarded and the process restarted.

The total holdup volume of the bioreactor and lines P-8, P-9, P-10, and P-11 was measured to be 3 ml. To seed the bioreactors, cells were trypsinised from the confluent flasks and re-suspended in 3 ml of culture medium at a density of 2×10^5 cells/ml to yield a seeding density of 6×10^5 cells/cm^2. To seed the bioreactor, valves V-5 and V-2 were closed while V-4 was left open. The cell suspension was injected through V-3 to deposit the cells on the lumen wall through dead-end filtration. After allowing 6 h for cell attachment, cell viability was assessed as described in section 5.1.6. Upon the replacement of media, perfusion was started at 50.4 ml/hr.

To prevent the depletion of nutrients and the accumulation of waste metabolites, half media exchanges of the total 20 ml hold-up were performed every other day for the duration of the 28 day culture. To exchange media, the positive displacement pump, PDP-1, was stopped and the EHFM inlet and outlet were isolated by closing valves V-3 and V-5. Spent media in the reservoir, R-1, bioreactor ECS and lines, P-2, P-4, P-9, and P-10 was recovered through V-4 and transferred into sterile Eppendorf tubes, for metabolite analysis, as described in section 5.1.11. Cell viability was then assessed with PrestoBlue, as described in section 5.1.6. Subsequently, media was replaced by reversing the process with a syringe of fresh media depressed through a 0.22 μm syringe filter. Valves V-3 and V-4 were re-opened and the

perfusion of media restarted.

5.1.6 PrestoBlue cell viability assay

Cell viability was assessed with a PrestoBlue (Invitrogen, Paisley, UK) assay. For static membrane cultures, 380 μL of 10 % PrestoBlue solution (v/v in culture medium) was transferred into the wells of a fresh 24 well plate. Membranes were then transferred from the plates containing spent media into those with PrestoBlue solution. Similarly, to carry out the assay in the bioreactor, following the removal of spent media, 3 mL of 10 % PrestoBlue solution (v/v in culture medium) was injected into the bioreactor ECS through valve V-4. After 1 h of incubation at 37 °C, the PrestoBlue samples were recovered and transferred into sterile Eppendorf tubes. 100 μL of PrestoBlue solution was transferred to a black 96-well plate (Corning, UK) for analysis (n=12). Fluorescence was measured using the SpectraMax i3x microplate reader (Molecular Devices, Wokingham, England λ_{ex} = 544 nm, λ_{em} = 590 nm).

5.1.7 Scanning electron microscopy

Samples (n=3) maintained under hydro-static conditions were fixed six hours after seeding and then with every subsequent media exchange in a solution of 4 % (wt/v) glutaraldehyde (Sigma-Aldrich, Dorset, UK) in Sorenson's buffer with a pH of 7.4 for 24 h. Similarly, EHFM bioreactor samples were fixed in the same way at the terminus of the culture period. After washing with Sorenson's buffer, fixed membrane sections were stained with osmium tetroxide 1 % v/v (Merck, Darmstadt, Germany) in the same buffer. Fixed and stained samples were serially dehydrated in ethanol and Sorenson's buffer for 15 minutes in steps of 50:50, 70:30, 90:10, 95:5, and 100:0. Subsequently, samples were also dehydrated in a hexadimethylsilazane:ethanol gradient of 70:30, 90:10, 95:5, and 100:0, before leaving to dry overnight.

Stained membrane sections were gold coated using an SC7620 Mini Sputter Coater System (Quorum Technologies Ltd, East Sussex, UK). High-resolution images were taken using an environmental scanning

electron microscope (SEM, Carl Zeiss Evo LS15 Variable Pressure Scanning Electron Microscope).

5.1.8 Fixed confocal microscopy

EHFMs were fixed in a solution of 4 % (wt/v) glutaraldehyde (Sigma-Aldrich, Dorset, UK) in Sorenson's buffer with a pH of 7.4 for 24 h. Fixed membranes were washed in wash buffer containing 1 % (wt/v) BSA (Sigma-Aldrich, Dorset, UK), 0.5 % (v/v) Tween-20 (Sigma-Aldrich, Dorset, UK), 0.01 % (wt/v) NaN_3 (Sigma-Aldrich, Dorset, UK) in PBS. Due to the limited depth of view afforded by confocal microscopy washed samples were cut in half with a scalpel to reveal the lumen of the EHFMs. Washed and cut samples were permeabilized at room temperature for 3 min in wash buffer supplemented with 0.1 % (v/v) Triton X-100 (Sigma-Aldrich, Dorset, UK). To prevent non-specific binding and excessive auto-florescence, membranes were blocked in wash buffer supplemented with 10 % goat serum (ThermoFisher, Massachusetts, U.S.) and 0.5 M glycine (Sigma-Aldrich, Dorset, UK) for 24 h at 4 °C on an orbital shaker. Blocked membrane sections were incubated with Rabbit VE-Cadherin (33168, AbCam, Cambridge, UK) antibodies in PBS at room temperature for 30 minutes. Thereafter the membranes were incubated with Goat anti-Rabbit IgG (H+L) cross-adsorbed secondary antibody, Alexa Fluor 488 (A-11008, ThermoFisher, Massachusetts, U.S.), for 30 minutes at room temperature. After staining with the secondary antibody, the samples were stained for the cytoskeletal marker F-actin (ActinRed 555 ReadyProbes, ThermoFisher Scientific, R37112) and nuclei (NucBlue Fixed cell staining, Life technologies, R37606) for 10 and 5 minutes, respectively, at room temperature. Finally, stained samples were stored in 0.01 % NaN_3 in PBS at 4°C. Between each step, samples were washed in triplicate in wash buffer for 5 minutes on an orbital shaker at room temperature.

Stained samples were imaged on a Zeiss 880 with an Airyscan inverted confocal microscope with Zeiss Zen Black software. Images were captured in two sequences, the first with a 488 nm argon laser with emission light collected at 495-555 nm (Alexa Fluor 488), and the second with a 405 and 559 nm

diode where emission light was collected at 420–520 nm (DAPI) and 560–650 nm (TRITC). Images were taken with an Olympus UPlanSApo 10x/0.40 ∞/0.17FN26.5 dry microscope lens at a resolution of 1024 x 1024 pixels at an equivalence of 1.204 μm/pixel with Z-stacks acquired in 7 μm slices.

5.1.9 Micro-computed tomography

Membranes recovered from the EHFM bioreactor were fixed and stained with osmium tetroxide, as described in section 5.1.7. The stained samples were mounted in a custom sample holder and placed vertically in the micro computerised tomography machine (μCT, SkyScan 1172, SkyScan, Kontich, Belgium). 35 mm sections of the membranes were scanned with a set voltage of 40 kV, a current of 250 mA, and no filter was used. 1200 projections were then used to reconstruct the images using the NRecon software (SkyScan 1172, SkyScan, Kontich, Belgium) Feldkamp algorithm.

5.1.10 Micro-computed tomography image analysis

Reconstructed μCT images of EHFMs were analysed with an in-house Python image analysis routine to obtain cell locations, and morphological features including EHFM wall thickness, lumen diameter, and fibre aspect ratio.

5.1.10.1 Electrospun hollow fibre membrane morphology

Membrane morphological features were obtained by cutting a square region of interest, an area specified by the user, from the entire image. To attenuate background noise, the pixel values in the residual image array were flattened to a 1D array. A pixel value, below which all pixel values were considered to be background noise, was determined by finding the median absolute deviation of the non-zero background pixel values. All pixel values below this value in the isolated region of interest were set to zero.

The outer membrane boundary was determined by first applying consecutively a 60x60 oval opening,

and closing morphological transformations [244] to the background noise thresholded image. The transformed image was then binarized with Otsu's method [180] and non-critical pixels, i.e. those which do not result in a change in shape, were removed by contouring [178]. The contour with the largest area was isolated, and both the bounding rectangle and oval were found. A binary image of the contoured region within an array of zeros with the dimensions of the bounding rectangle was computed. Similarly, the region within the bounded rectangle from the original image was isolated, with all pixels outside the contoured region set to zero.

To isolate the lumen from the outer bounded membrane, a square region, with size as specified by the user, was isolated from the centre of the isolated outer membrane region. The isolated region was inverted, and a 25x25 oval closing morphological transformation [244] was applied. The transformed image was binarized with Otsu's method and inverted. The distance transform of the inverted image was taken such that the distance to the closest zero pixel for each pixel of the source image was calculated to obtain the derived representation of the binary image. The derived image was thresholded to a pixel value of 230 such that 10 % of each body in the image was removed. The thresholded image was contoured and the largest retained. The residual body was dilated by 10 % of its size. The region associated with this body was set to zero in both the isolated image of the outer membrane layer and the binary mask, leaving an image array with an area of the membrane layer only.

Having isolated the region associated with just the membrane layer and generated a binary image with the same area, the membrane porosity was found by finding the percentage value of the sum of the isolated image over that of the binary image. Furthermore, the membrane wall thickness and aspect ratio could be found. The wall thickness was determined by considering the euclidean distance between 100 points around the lumen and outer wall bounding ovals. The membrane aspect ratio was taken as the ratio of the major and minor axis of the outer wall bounding oval.

5.1.10.2 Cell distribution

To find cell locations, initially, a membrane threshold value was determined. By running the pipeline described in section 5.1.10.1 an image array of only the membrane layer was isolated. The image array was flattened to a 1D array, and the value associated with a median absolute deviation of 3.5 was found. By this means, a minimum pixel threshold value associated with a significant deviation above that of a blank membrane was found. As cells stained with osmium absorb X-rays to a greater extent than polymeric membranes, by thresholding with this value, only the regions associated with cells remain.

Having determined the blank membrane threshold value, the osmium stained cell-laden membrane μCT images were isolated through the same pipeline as used to extract the membrane morphology, as described in section 5.1.10.1. The isolated membrane and cell layers were thresholded using the value determined from the blank membrane samples. The centroids of each residual point in the array were found and recorded with the axial position associated with each image, as seen in supplementary figure S5.7A-E.

The array of centroid locations was queried with a DBSCAN cluster analysis to filter any erroneously isolated regions [245, 246]. The epsilon value in which was set to the size of HUVEC divided by the pixel resolution. Similarly, the minimum number of points within each cluster was set to 6 as for a multidimensional data set the minimum number of points should be twice the number of dimensions. All points not associated with a cluster were removed, as seen in supplementary figure S5.7F.

The radial position of each HUVEC was found by calculating the euclidean distance from the centroid of the largest blob associated with the membrane outer wall of the corresponding axial location. Finally, the number of clusters along the long axis of the EHFM was determined.

5.1.11 Metabolite analysis

Glucose and lactate concentrations in spent culture media taken six hours after seeding and with every subsequent media exchange were measured with a GlucoRx X6 Multi-Functional Meter and an Abbot ARCHITECT system.

5.1.11.1 GlucoRx X6

The GlucoRx X6 (GlucoRx, Henley, UK) measures glucose concentration through the enzymatic action of glucose dehydrogenase, which is oxidised on contact with glucose in the disposable sensor tips. The enzyme is reoxidised by a mediator, which in turn reoxidises the electrode in the sensor's tip thereby creating a current. As the current produced is proportional to glucose concentration, the glucose concentration may be measured. Similarly, lactate concentration is measured with lactate oxidase through the same mechanism as glucose.

5.1.11.2 Abbot ARCHITECT

Glucose and lactate concentrations in spent culture media taken six hours after seeding and with every subsequent media exchange were measured with an ARCHITECT system (Abbott Laboratories, Chicago, Illinois, US). To measure glucose concentrations, glucose is phosphorylated by hexokinase (HK) in the presence of adenosine triphosphate (ATP) and magnesium ions to produce glucose-6-phosphate (G-6-P) and adenosine diphosphate (ADP). Glucose-6-phosphate dehydrogenase (G-6-PDH) specifically oxidizes G-6-P to 6-phosphogluconate with the concurrent reduction of nicotinamide adenine dinucleotide (NAD) to nicotinamide adenine dinucleotide reduced (NADH). One micromole of NADH is produced for each micromole of glucose consumed. The NADH produced absorbs light at 340 nm and can be detected spectrophotometrically as an increased absorbance [247]. Similarly, to determine the lactate concentration is converted to pyruvate and hydrogen peroxide (H2O2) by lactate

oxidase. Peroxidase catalyzes the oxidation of chromogen precursor by H2O2 to produce a colored dye. The increase in absorbance at 572 nm is directly proportional to the lactic acid concentration in the sample [248].

5.1.12 Statistical analysis and reproducibility

All python routines used for the analysis of experimental data presented herein may be found at: `https://github.com/ristojm`. Statistical analysis was performed with the SciPy.stats Python package in each data analysis routine. To determine the statistical significance of the results, distributions were compared using a two-way Mann-Whitney U test. Results were considered significant at $p<0.05$. All measurements were taken with n = >3, unless otherwise stated.

5.2 Results and Discussion

EHFMs and electrospun flat sheet membranes produced from blended PCL and PDO have previously been morphologically and functionally characterised [7]. While found to be non-cytotoxic, electrospun membranes must be biocompatible for use as a substrate for cell growth. Furthermore, while pyridine was used to augment the morphological and functional characteristics of the membranes produced, it must not cause biocompatibility issues, and its effect was therefore considered.

5.2.1 Membrane morphology

EHFMs previously described had a lumen diameter and wall thickness of around 100 and 300 μm [7], respectively. To enable the seeding of HUVECs into the lumen and aid with the ease of handling, EHFMs with larger lumen diameters were produced for this study, as seen in figure 5.3A & B. μCT image analysis was used to evaluate the wall thickness and gross morphology of EHFMs produced with a 600 μm collector wire. As seen in figure 5.3C-E, the median lumen diameter, wall thickness, and aspect ratio was measured to be 638 μm, 124 μm, and 0.788, respectively.

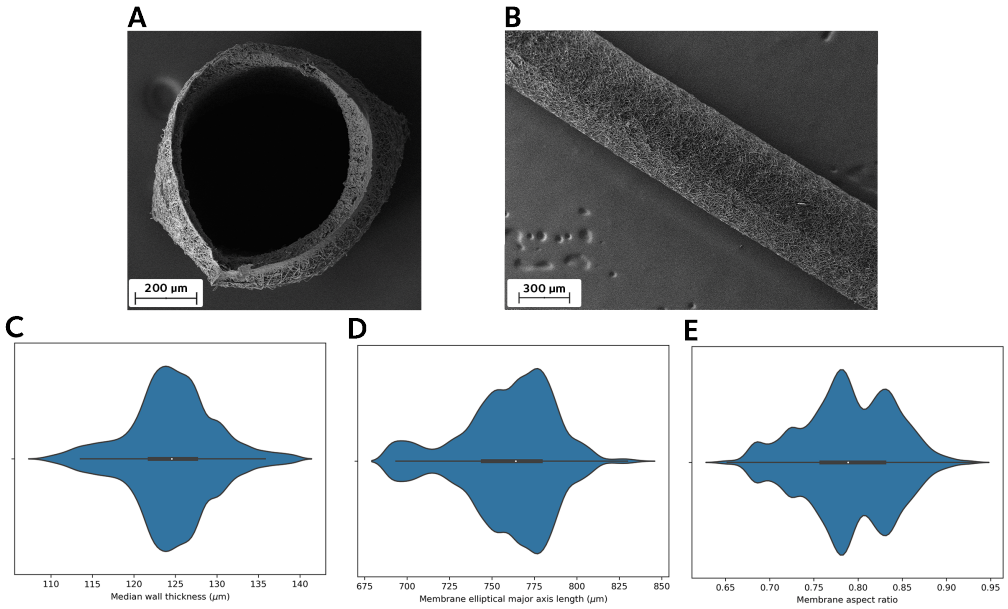


Figure 5.3. (A) Profile and (B) Side view SEM micrographs of EHFM. Quantified EHFM morphological characteristics, including the (C) median wall thickness, (D) elliptical major axis length, and (E) aspect ratio, as measured by μCT image analysis.

5.2.2 Static HUVEC culture

To initially evaluate the biocompatibility of electrospun blended PCL and PDO doped with up to 50 ppm pyridine, HUVECs were cultured on electrospun flat sheet membranes for 28 days under hydro-static conditions.

5.2.2.1 Hydro-static culture of HUVECs on electrospun flat sheet membranes

Irrespective of the pyridine concentration, HUVEC viability was maintained throughout the 28 day culture period, as seen in supplementary figure S5.1A. Irrespective of pyridine concentration, the measured fold change in fluorescence increased until day 14 before reaching a plateau, with the greatest increase associated with membranes produced with 25 and 50 ppm pyridine. Considering the HUVEC doubling time at the point at which the growth began to plateau, the doubling time associated with HUVECs cultured on membranes produced with 25 and 50 ppm pyridine were 8.83 and 8.92, respectively. Compared to HUVECs culture on regular tissue culture plastic, with an estimated doubling time of 2 to 2.5 days, the HUVEC growth rate on these electrospun flat sheet membranes is significantly

reduced [249].

The fold change in fluorescence measured with HUVECs cultured on electrospun flat sheet membranes, produced with 25 ppm pyridine, may be seen in figure 5.4A.

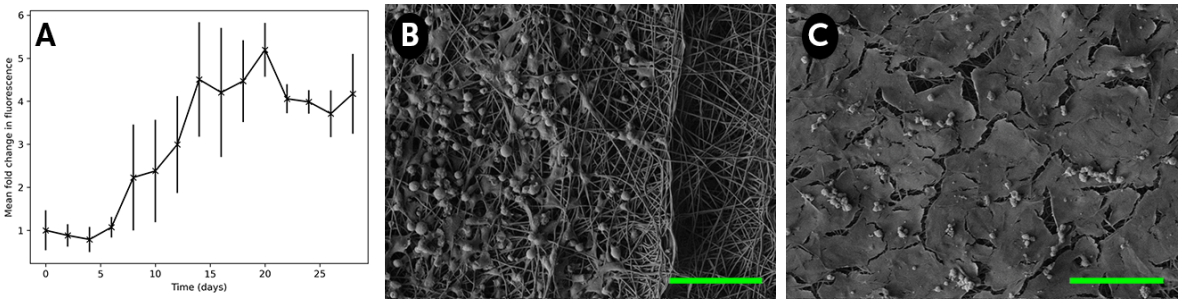


Figure 5.4. (A) Change in HUVEC viability as quantified by the change in PrestoBlue fluorescence relative to day 0 when cultured under hydro-static conditions on electrospun PCL/PDO flat sheet membranes doped with 25 ppm pyridine. (B) SEM micrographs of HUVECs cultured; on electrospun flat sheet membranes for (B) 6 hours, and (C) 2 days, in which scale bars are 60 μm.

SEM imaging of HUVEC growth on electrospun flat sheet membranes revealed that 6 hours after seeding, when media was supplemented, the HUVECs had predominantly a globular morphology with some beginning to flatten and spread out, as seen in figure 5.4B. By day 2, as seen in figure 5.4C, the HUVECs had flattened to form a layer on the surface of the electrospun material. Throughout the rest of the culture period, the HUVECs maintained this flat morphology, as seen in supplementary figure S5.3. However, throughout the culture period, it was not possible to differentiate between cells in this surface layer with SEM imaging. Finally, as seen in supplementary figure S5.4A, upon seeding, the HUVECs initially form a circle in the shape of the droplet of cell suspension placed on the membrane during seeding. Throughout the culture period, it does not appear that the HUVECs disbursed across the surface of the electrospun material as the cell layer remained in the circular droplet shape on the final day of culture, as seen in figure S5.4B.

5.2.2.2 Hydro-static culture of HUVECs in EHFMs

As before, HUVEC viability when cultured in EHFMs was maintained throughout the 28 day culture period irrespective of the pyridine concentration, as seen in supplementary figure S5.1B. The greatest increase in measured fluorescence associated with HUVECs cultured in EHFMs was with those produced with 10 ppm pyridine. As with the electrospun flat sheet membranes, on day 14, HUVECs cultured in EHFMs produced with 10 ppm pyridine were found to have a maximum doubling time of 8.77 days. Again, this suggests that HUVEC growth rates in EHFMs under static conditions are significantly reduced compared to that on traditional tissue culture plastic [249].

By comparing figures 5.4A and 5.5A, it can be seen that measured fluorescence of HUVECs cultured on electrospun flat sheet membranes increases more than that of those cultured in the lumen of EHFMs, with a 5 and 3 fold increase in each, respectively. Furthermore, the increase in fluorescence of HUVECs cultured electrospun flat sheet membranes was initially exponential, while in EHFMs the increase was more linear.

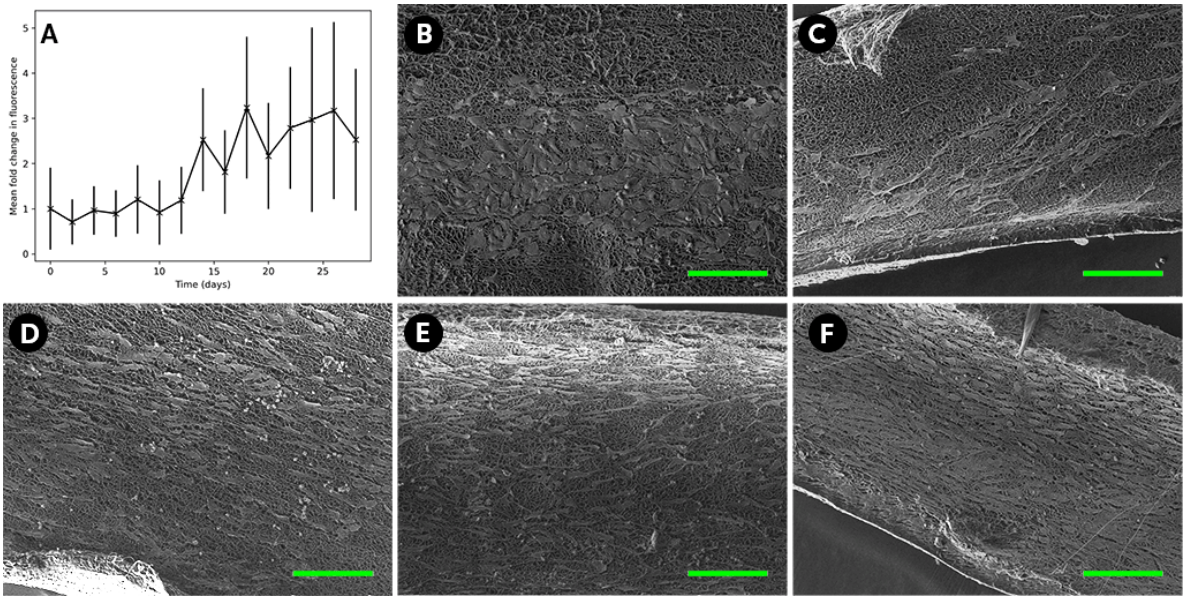


Figure 5.5. (A) Change in HUVEC viability as quantified by the change in PrestoBlue fluorescence relative to day 0 when cultured under hydro-static conditions on EHFMs. SEM micrographs of HUVECs cultured on EHFMs for (B) 6 h, (C) 2, (D) 8, (E) 22, and (F) 28 days, in which the scale bar represents 200 μm.

By cutting the EHFMs in half HUVECs cultured in the EHFM lumen could be imaged with SEM. As seen in figure 5.5B, 6 hours after seeding, HUVEC morphology was flattened and less spherical compared to those cultured on electrospun flat sheet membranes. By day 2, the HUVEC morphology had completely flattened out, as seen in figure 5.5C. In contrast with those cultured on electrospun flat sheet membranes, HUVECs cultured on the EHFMs were seen to have a distinct cell boundary. Between days 2 and 8, the number of HUVECs increased, as seen in figure 5.5D, and began to spread along the length and breadth of the EHFM. Across the same period, the HUVEC morphology was seen to elongate and appeared to align along the long axis of the EHFM. The trend in increasing cell numbers and alignment continued throughout the culture period until day 28, at point confluency had reached approximately 95-100 %, as seen in figures 5.5F. The change in HUVEC number, morphology, and alignment may be appreciated with more granularity from supplementary figure S5.3. The degree of cell coverage by D28 may be better appreciated when considering more of the membrane area, as seen in supplementary figure S5.4C.

While the SEM micrographs illustrated the increase in HUVEC numbers and morphology, by visualising HUVEC nuclei, F-actin cytoskeleton, and cell-cell adhesion VE-cadherin proteins with confocal microscopy, cell remodelling and interaction may be appreciated.

5.2.2.3 Confocal microscopy imaging of HUVEC growth under hydro-static conditions

Again, the EHFMs were cut in half so that the HUVECs cultured in the EHFM lumen could be imaged with confocal microscopy. Confocal microscopy of HUVEC growth on EHFMs showed an increase in cell number until day 18-22, at which confluency was reached, as seen in figure 5.6. As in the SEM micrographs, 6 hours after seeding, the HUVECs may be seen to have a predominately rounded morphology, as seen in supplementary figure S5.5. By day 2, the HUVECs had flattened and elongated, and by day 8, they were largely aligned along the long axis of the EHFM. Initially, there is

little cell-cell adhesion, as seen by the primarily purple colour of the stained cells. Between 6 hours and day 22, the degree of cell adhesion was seen to increase, as shown by the shift in cell colour from purple to yellow between 6 h after seeding and day 8. Subsequently, cell adhesion increases further, demarcated by the continued shift in colour from yellow-green between days 8-22. From day 22, there appears to be no further change in cell number, morphology, or expression in VE-cadherin.

In conference, these findings demonstrate that EHFMs produced from blended PCL and PDO doped with 25 and 50 ppm pyridine perform similarly as a substrate to support HUVEC growth. Qualitative differences in the ease of use of each of the materials were therefore used to decide on the selection of the material which would be used to produce an EHFM bioreactor. Specifically, membranes produced with 50 ppm pyridine were easier to electrospin compared to those with 25 ppm. Furthermore, an increase in pyridine concentration has previously been associated with an improvement in the ease of separation of electrospun materials from the collector [176]. This finding was echoed in our work as the wire collector was more readily removed from EHFMs produced with higher pyridine concentrations. Consequently, EHFMs produced with 50 ppm pyridine were selected for use in the production of EHFM bioreactors described herein.

5.2.3 Culture of HUVECs under hydro-dynamic conditions in an EHFM bioreactor

Due to the number of design decision variables when developing novel bioreactor platforms progression is typically slow due to the commonly adopted trial-and-error design evolution strategy. However, these design decisions may be aided by mathematical modelling, as a means to providing a rationale for experimental design decisions [132]. Previously, through the application of experimentally measured functional characteristics, we mathematically modelled HUVEC growth in an EHFM bioreactor with a number of inlet flow rates [250]. By substituting the new EHFM geometry into this model, it was determined that of those considered, the highest specific HUVEC growth rate would be achieved with

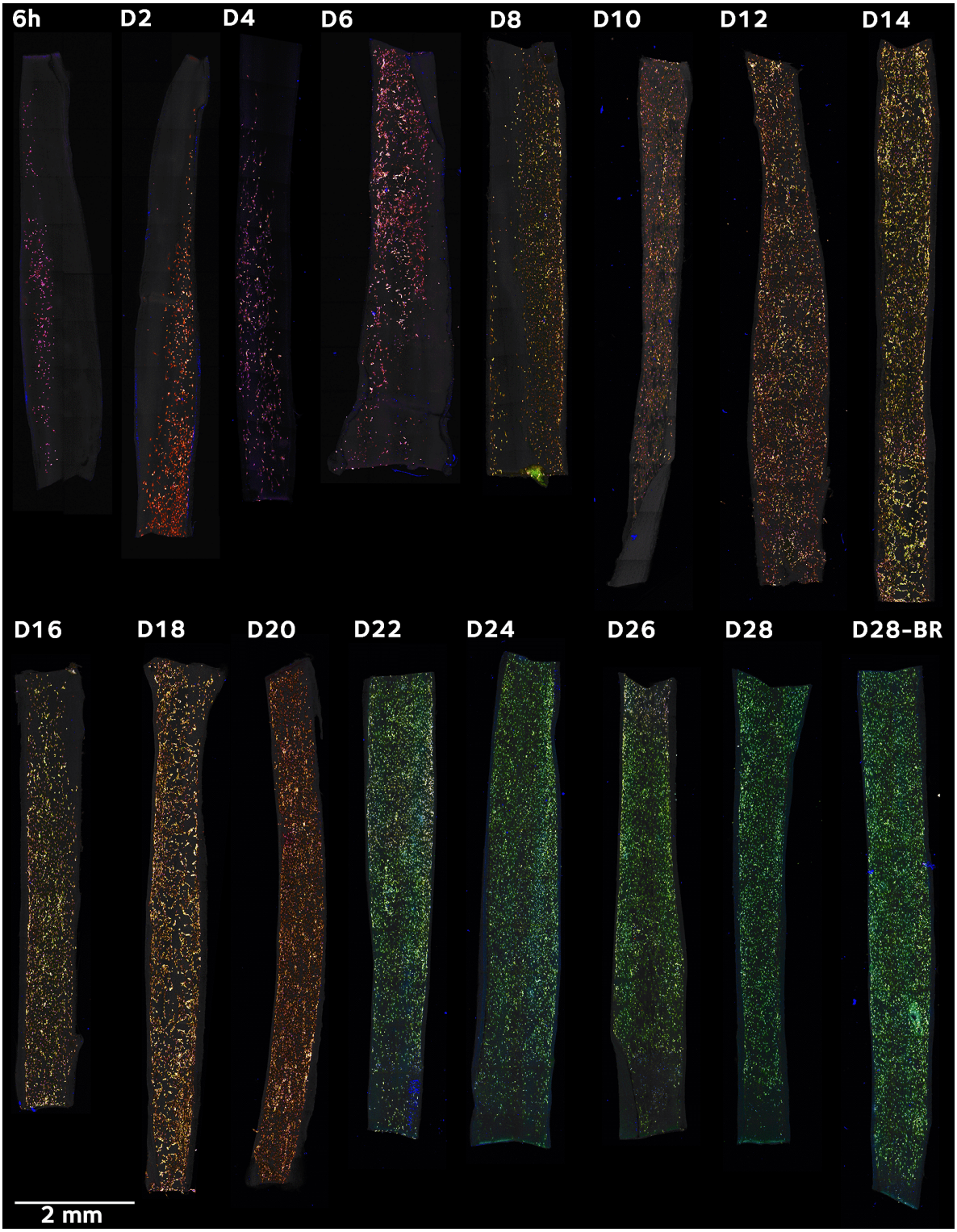


Figure 5.6. Confocal microscopy micrographs of HUVECs cultured on EHFMs, for 6 hours - 28 days under static conditions, or within an EHFM bioreactor when designated with a BR, stained for nuclei (blue), F-actin (red), and VE-cadherin (green).

a lumen inlet volumetric flow rate of 50.4 ml/hr. Consequently, this inlet flow rate was selected for use in the culture of HUVECs in the EHFM bioreactor. To evaluate the performance of the EHFM bioreactor as a vascular mimetic platform to support cell growth, HUVECs were cultured in the lumen of the EHFMs for 28 days.

EHFM bioreactors were produced by mounting EHFMs in mounting bungs, as seen in figure 5.7A, encasing the mounted membranes in a clamshell and sealing it with epoxy glue while being held within a clamp, as seen in 5.7B. The assembled EHFM bioreactor was plumbed in accordance with the block flow diagram seen in figure 5.2 and mounted onto an incubator tray, as seen in figure 5.7C.

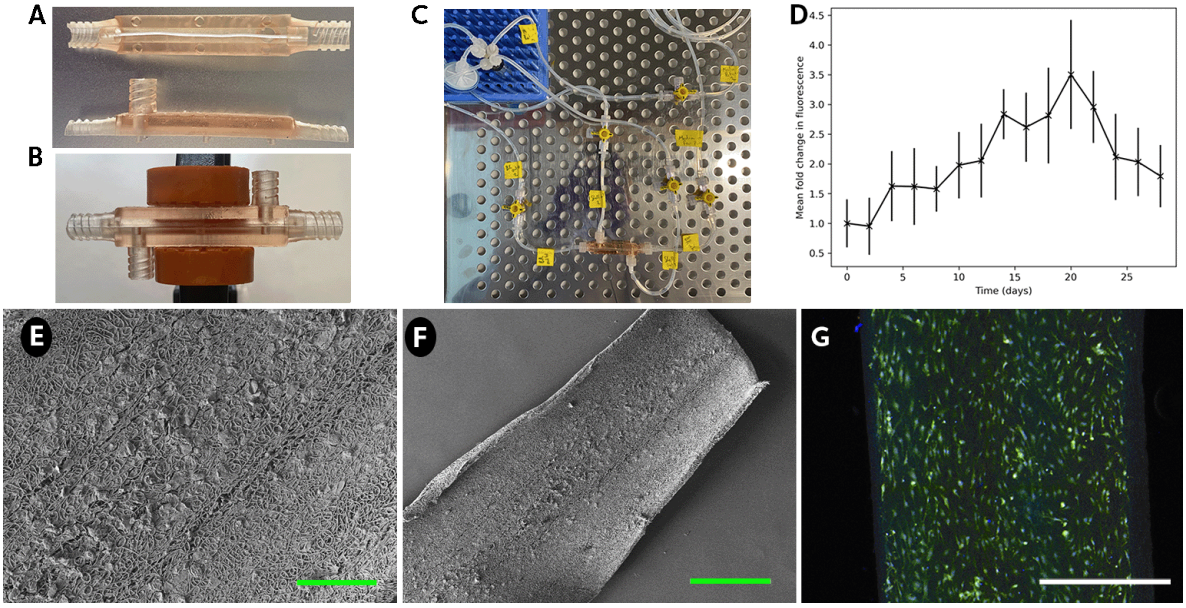


Figure 5.7. (A) EHFM mounted in bungs with open enclosure (B) Clamped EHFM bioreactor enclosure with epoxy. (C) EHFM bioreactor plumbed in the piping configuration in accordance with block flow diagram seen in figure 5.2. (D) Change in HUVEC viability as quantified with PrestoBlue fluorescence relative to day 0 when cultured under hydro-dynamic conditions in an EHFM bioreactor (n=3). SEM micrographs of HUVECs cultured in an EHFM bioreactor under hydro-dynamic conditions for 28 days, with a scale bar equivalent to (E) 100 μm, and (F) 600 μm. (G) Confocal micrograph of HUVECs cultured in an EHFM bioreactor under hydro-dynamic conditions for 28 days, stained for nuclei (blue), F-actin (red), and VE-cadherin, with scale bar equivalent to 500 μm.

When cultured in an EHFM bioreactor, HUVEC viability was maintained throughout the 28 day culture period, as seen in figure 5.7D. As with those cultured under static conditions, the measured fold change in fluorescence initially increased until day 14, after which it began to plateau. The mean

HUVEC doubling time by day 14 was found to be 9.08, which is significantly reduced compared to that associated with traditional tissue culture plastic [249]. However, this growth rate is very similar to that under static conditions on both electrospun flat sheet membranes and EHFMs.

By cracking the EHFM bioreactor at its seam EHFMs could be recovered at the terminus of the culture period. Cutting the recovered EHFMs in half enabled the imaging of the HUVECs cultured in the EHFM lumen with SEM, as seen in figure 5.7E & F. SEM imaging revealed that on day 28 of culture the HUVECs had reached full confluency. In contrast to HUVECs cultured under hydro-static conditions, there was no clear boundary between HUVECs cultured under hydro-dynamic conditions. Instead, a monolithic HUVEC layer integrated into the micro-fibre membrane layer was seen.

Similarly, a fully confluent layer of HUVECs was seen under confocal microscopy, as seen in figure 5.7G. Confocal microscopy enabled the clear visualisation of the cell boundaries, from which it was evident that the HUVECs had a long flatted morphology and were aligned along the long axis of the EHFM. The full confocal image from which the central region was taken may be seen in supplementary figure 5.6.

5.2.3.1 Cell distribution

SEM and confocal imaging are frequently used to visualise cell location and morphology. However, without sectioning SEM may only be used to image the sample surface, while confocal enables the imaging of at most 100 μm below the sample surface. μCT provides a means by which cell location may be imaged through the entire cross-sectional depth of tissue-engineered scaffolds, without the need for scaffold dissection. Through μCT imaging and μCT image analysis, the radial and longitudinal distribution of HUVECs in the bioreactor were analysed, as seen in figure 5.8.

Considering the radial HUVEC distribution, as seen in figure 5.8B, the majority of cells detected

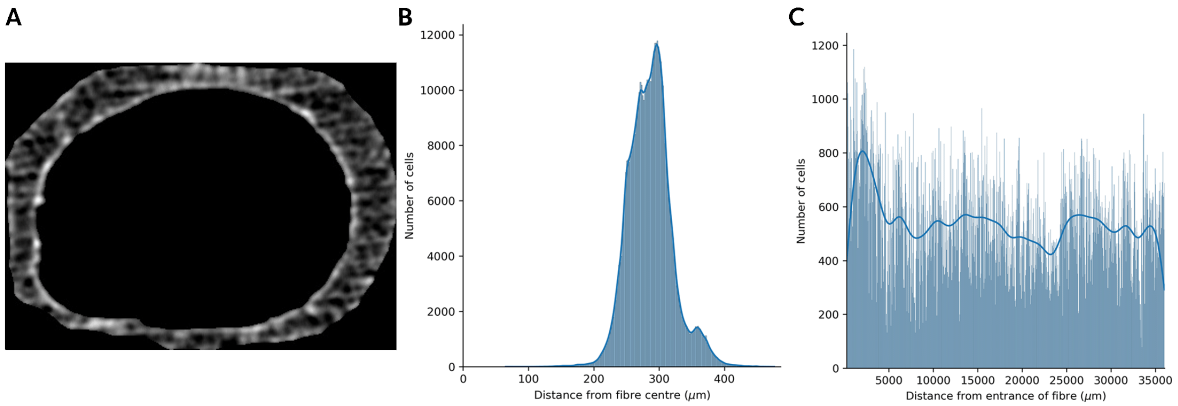


Figure 5.8. (A) μCT image of EHFM bioreactor hollow fibre with HUVECs in lumen isolated through pipeline described in section 5.1.10.2 and seen in supplementary figure S5.7. (B) The radial and (C) longitudinal HUVEC distribution in an EHFM bioreactor as determined through μCT image analysis.

were found 300 μm from the EHFM centre. As the EHFMs in the bioreactor were found to have a median inner diameter of roughly 632 μm, as seen in figure 5.3B, it is inferred that HUVEC growth was maintained predominately in the lumen of the EHFMs as seeded. A small shoulder in cell numbers may be seen within 50 μm of the 300 μm point, this is due to the membrane deforming to an oval shape, as seen in the range of membrane aspect ratios in figure 5.3C, thereby resulting in the appearance of some cells being closer or further away from the centre of the EHFM.

Considering the distribution of cells along the length of the bioreactor in figure 5.8C, it can be seen that there is a greater number of HUVECs closest to the inlet to the EHFM. Moving down the length of the EHFM, the number of HUVECs initially decreases, reaching a plateau around 5000 μm from the EHFM lumen inlet, which is maintained for the rest of the length of the EHFM.

Considering the SEM, confocal microscopy and μCT image analysis data in conference, it is evident that by day 20, a layer of HUVECs is established in the EHFM lumen under static conditions, which is maintained throughout the 28 day culture period. Similarly, under hydro-dynamic conditions, a layer of HUVECs may be seen to be maintained throughout the length of the bioreactor at the terminus of the 28 day culture. In addition to cell number and morphology, culture performance may be considered

through the evaluation of metabolite profiles.

5.2.3.2 Metabolic profiles

By considering metabolic profiles, it is possible to determine whether the feeding regimen used was sufficient to prevent glucose limited growth and, similarly, if the build up of waste metabolites inhibited cell growth. The glucose concentration was seen to increase from around 5 mM to a plateau of approximately 7 mM as measured by the Architect system, as seen in figure 5.9A. Similarly, lactate concentration increased from 0.35 to 0.5 mM from 6 h to day 20, after which it began to decrease, as measured with the Architect system.

The glucose profile measured with the GlucoRx meter followed the same trend as the Architect system. However, after day four, each reading with the GlucoRx meter was higher than that measured with the Architect system. The architect system measures glucose concentrations through the action of HK mediated phosphorilation of ATP to ADP and the concurent reduction of NAD to NADH. As NAH absorbs like a concentration of glucose may be determined. The GlucoRx meter on the otherhand operates on the principal of electron transfer associated with enzyme mediated oxidation of glucose. As the oxidation corresponds to a rate of electron transfer (i.e. an electrical current), a glucose concentration may be determined. As the Architect system is calibrated for blood and serum samples it is likely that the GlucoRx readings are more reliable as there are numerous potential interfearing agents which may perturb the Architect measurements.

The increase in glucose concentration may have been due to evaporation through the gas exchange membrane throughout the culture period. At each media exchange, it was observed that the volume of media in the reservoir had dropped to between 1-4 ml from the original 7 ml, which supports this hypothesis. The total hold up volume of the EHFM bioreactor platform was only 20 ml, a change in volume of 5 ml due to evaporation would therefore have resulted in a change in glucose concentration of

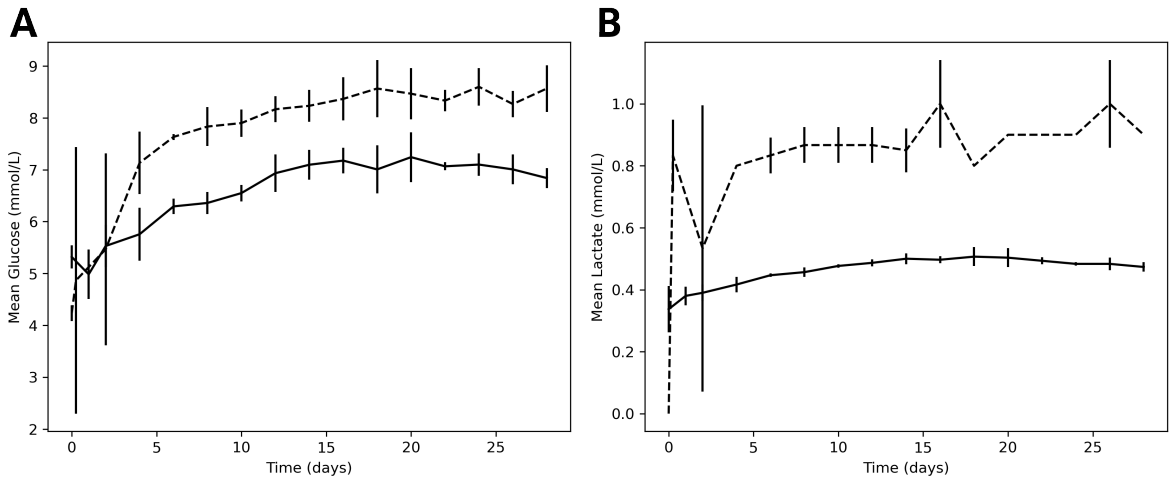


Figure 5.9. Change in (A) Glucose and (B) Lactate concentrations (n=3) in an EHFM bioreactor during the culture of HUVECs over a 28 day period, as measured with the GlucoRx meter (dashed line) and Architect system (solid line).

1.6 mM. Serial accumulation of glucose due to evaporation, therefore, can explain this trend in glucose and lactate profiles. HUVEC specific growth and glucose uptake rates have been shown to increase logarithmically between 5 - 30 mM [240]. Consequently, the increase in glucose concentration would have aided HUVEC growth.

Lactate is produced as a waste product from the catabolism of pyruvate, a product of glycolysis; lactate is then oxidised in the mitochondria. HUVEC specific lactate production has been shown to be insensitive to glucose concentration [251], but increases exponentially with a decrease in oxygen concentration [237]. Normal physiological circulating lactate concentrations are below 2 mM, while lactate acidosis occurs at concentrations above 4 mM [252, 253], the circulating concentrations of lactate may therefore have constituted a reduction in the HUVEC growth rate. The reduction in lactate concentration after day 20, as seen in figure 5.9, may be due to the dilution of the lactate in the system as there is a similar drop in glucose concentration in the same period. However, the decrease in PrestoBlue fluorescence readings, seen in figure 5.7D, at the same period suggests that there is a reduction in metabolic activity or a reduction in cell number. As it can be seen in both the SEM and confocal image data, in supplementary figures S5.3 and 5.6, that by day 20 confluency has been reached and is

sustained under static conditions. If confluency is reached by the same point in the EHFM bioreactor, the reduction in both the lactate concentration and PrestoBlue fluorescence readings may be due to a decrease in metabolic activity. As confluence would have been reached, the demand for carbon to feed the one-carbon metabolism required for mitosis would be reduced to support the turnover of cells rather than for the expansion of cell numbers [254]. This reduction in PrestoBlue fluorescence readings, in spite of cell number being maintained, illustrates the shortcomings of indirect metabolic activity cell viability assays.

Although these profiles provide some insight into the glucose and lactate concentrations over the culture period, they do not fully capture the potential spike and decay profiles that may occur due to the bolus media exchanges between each time point. To give a better insight into the change of metabolite concentrations, future bioreactor operation should include on-line sensors to enable their continuous measurement. These sensors could be connected to a secondary supply of fresh media to elevate the dependency on bolus infusions of fresh media, in favour of a dynamic supply of fresh media and removal of spent media. Such a system would also aid with reducing the risk of infection throughout the culture period.

5.3 Conclusion

We present the development of a novel EHFM bioreactor. Previously EHFMs have been produced from blended PCL/PDO to mimic the micro-topographical and mechanical characteristics of medium sized human arteries. Furthermore, pyridine was used to augment the morphological and functional characteristics of these membranes. It was hypothesised that these EHFMs may be used as a substrate to support cell growth in 3D tissue culture. We demonstrate that PCL/PDO electrospun flat sheet membranes and EHFMs support HUVEC growth for 28 days under hydro-static and hydro-dynamic conditions. After 2 days, a layer of flat HUVECs was shown to form on the surface of electrospun flat

sheet membranes under hydro-static conditions. However, distinct morphologies could not be seen between the cells in the layer, and the HUVECs did not disperse out from the point at which they were seeded. In contrast, after 2 days, HUVECs with distinct flattened morphology could be seen on the surface of the EHFMs, under hydro-static conditions. By day 8 in EHFMs, in addition to an increase in HUVEC numbers and spread of cells, they were seen to align along the long axis of the EHFM. By day 22, as imaged with confocal microscopy, HUVECs were seen to have reached confluency, which was sustained until the end of the culture period. Within the same time period, cell-cell interactions were seen to increase, as seen by an increase in VE-cadherin expression. Similarly, SEM and confocal imaging showed a confluent HUVEC layer on day 28 of the hydro-dynamic EHFM bioreactor culture. μCT image analysis showed that in the EHFM bioreactor, HUVEC growth was retained to the lumen of the EHFMs. HUVEC density was greatest near the EHFM bioreactor lumen inlet and decreases to a plateau within 5000 μm of the EHFM inlet. Both glucose and lactate concentrations were seen to increase. However, the increase in glucose concentration should have increased HUVEC growth rates, while lactate may have inhibited HUVEC growth. Comparisons of the HUVEC growth rate on electrospun flat sheet membranes and EHFMs with that associated with traditional tissue culture plastic revealed that HUVEC growth rates were significantly reduced. As there was no significant variation between HUVEC growth rates with those cultured under static and dynamic culture conditions, this reduction may have been due to lactate induced growth inhibition. Future work should therefore monitor metabolite concentrations with on-line sensors, so that the media supplies may be altered dynamically to avoid the build-up of lactate and other waste metabolites. We, therefore, conclude that in concert these findings show that EHFMs may be used as a substrate to support HUVEC growth while partitioning the lumen and the extra capillary space. EHFMs, therefore, provide an interesting platform for further research of 3D tissue culture and may be combined with a second substrate to support complex geometries or partitioned co-cultures.

5.4 Appendix

5.5 Supplementary section

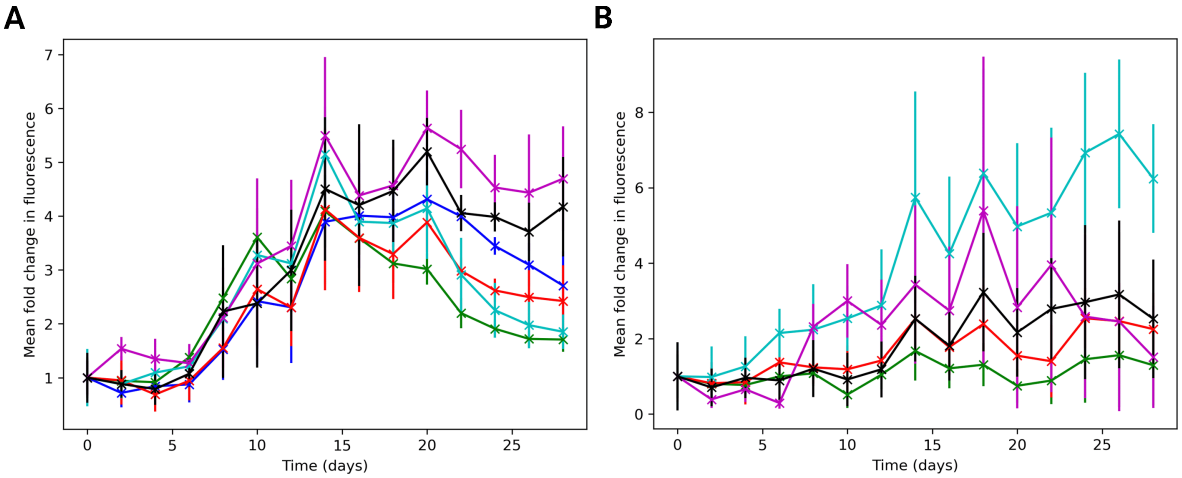


Figure S5.1. Change in HUVEC viability as quantified by the change in PrestoBlue fluorescence relative to day 0 when cultured under hydro-static conditions on (A) electrospun flat sheet membranes, and (B) electrospun hollow fibre membranes (n=3) produced with 0 (Blue), 1 (Green), 5 (Red), 10 (Cyan), 25 (Magenta), 50 (Black) ppm pyridine.

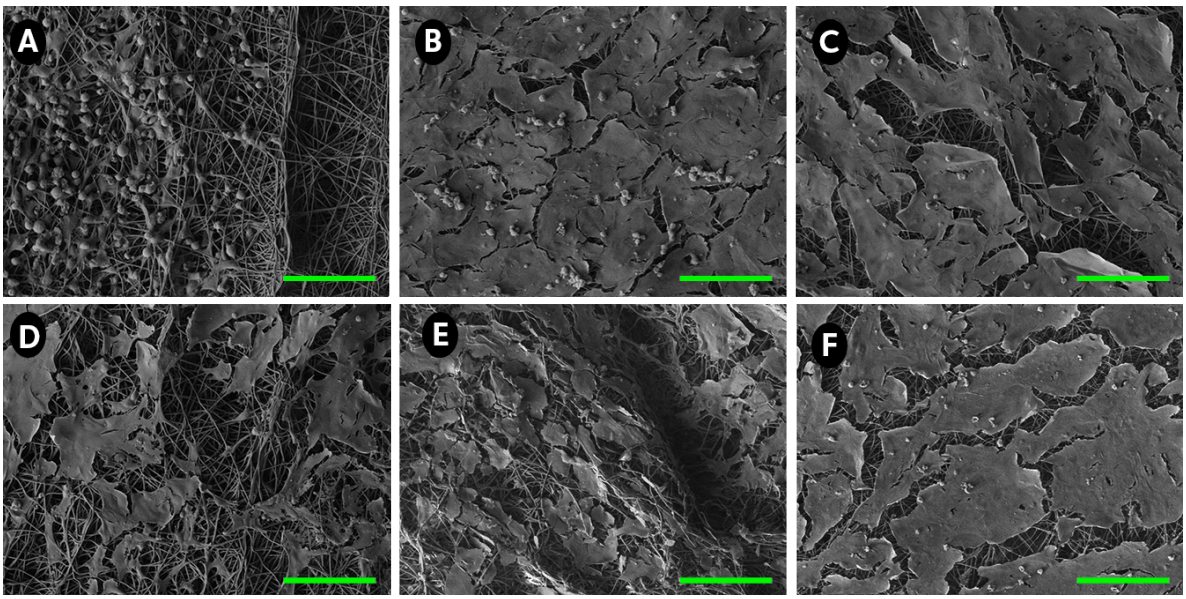


Figure S5.2. SEM micrographs of HUVECs cultured on electrospun flat sheet membranes for (A) 6 hours, (B) 2, (C) 4, (D) 6, (E) 8, and (F) 10 days, in which scale bars are 60 μm.

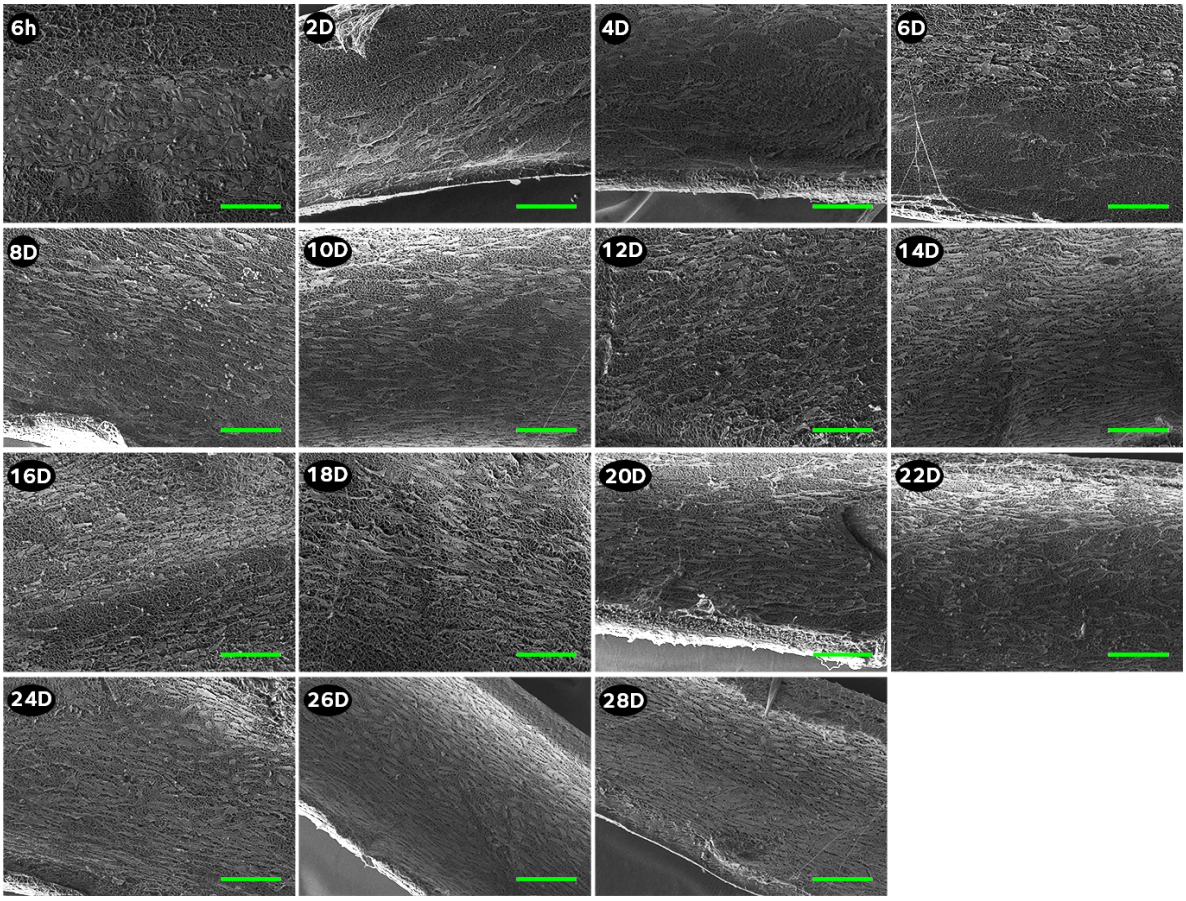


Figure S5.3. SEM micrographs of HUVECs cultured on EHFMs for 6 hours, and 2, 4, 6, 8, 10, 12, 14, 16, 18, 20, 22, 24, 26, and 28 days, in which scale bars are 100 μm.

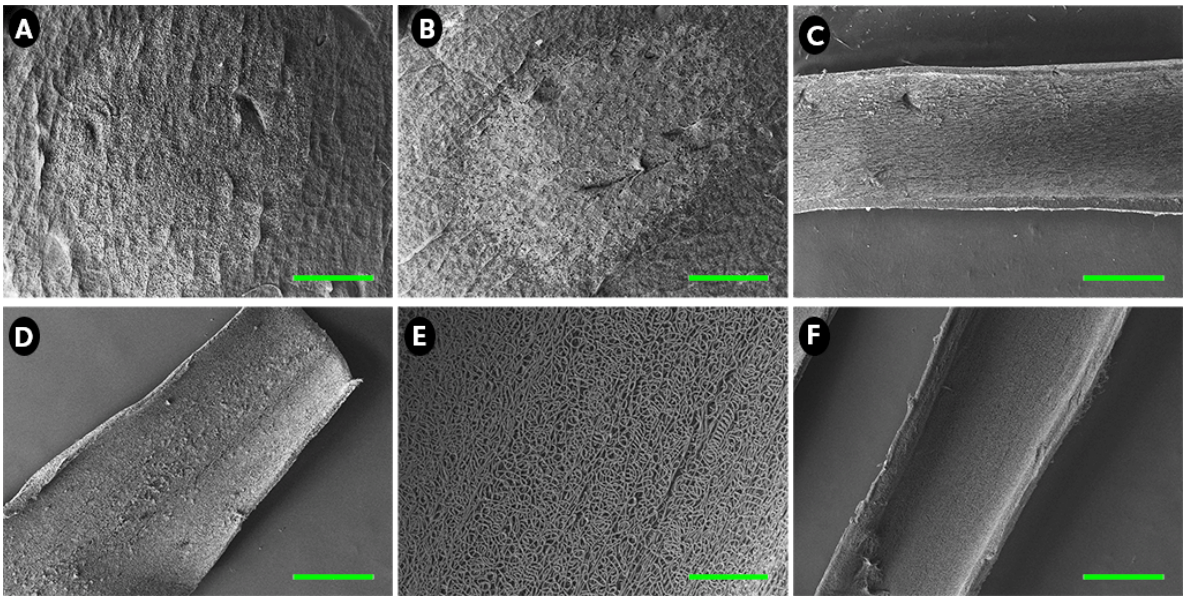


Figure S5.4. SEM micrographs of; HUVECs cultured on electrospun flat sheet membranes for (A) 6 hours and 10 days, in which scale bars are 600 μm. HUVECs cultured on EHFMs under hydro-static conditions (C), and hydro-dynamic conditions (D), in which scale bars are 600 μm. Blank EHFMs treated with osmium staining as used in all SEM and μCT samples.

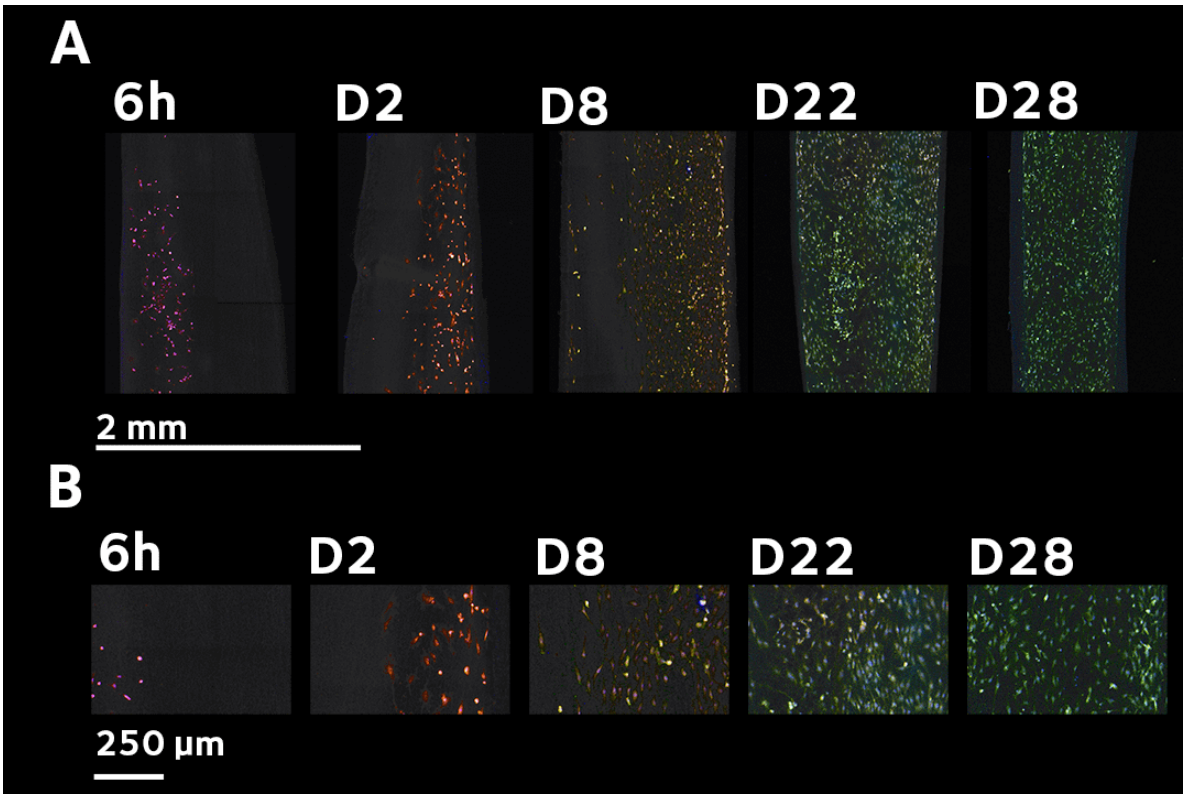


Figure S5.5. Central cuts of confocal microscopy micrographs of HUVECs cultured on EHFMs, for 6 hours - 28 days under static conditions, stained for nuclei (blue), F-actin (red), and VE-cadherin (green), in which the scale bar is equivalent to (A) 2 mm and (B) 250 μm. Uncut versions of the confocal micrographs for the full 28 day culture period may be seen in supplementary figure 5.6.

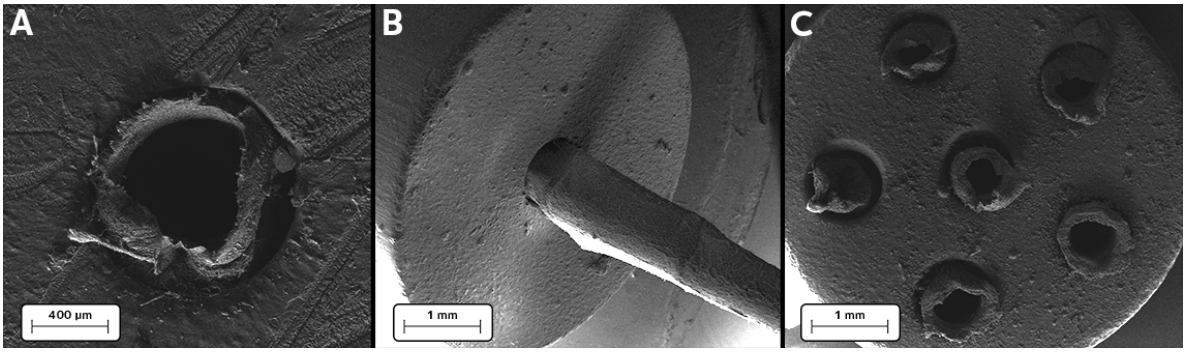


Figure S5.6. (A) Profile and (B) Side view SEM micrograph of single EHFM mounted into mounting bung and fixed with epoxy glue. (C) Profile Side view SEM micrograph of multiple EHFMs mounted into mounting bung and fixed with epoxy glue.

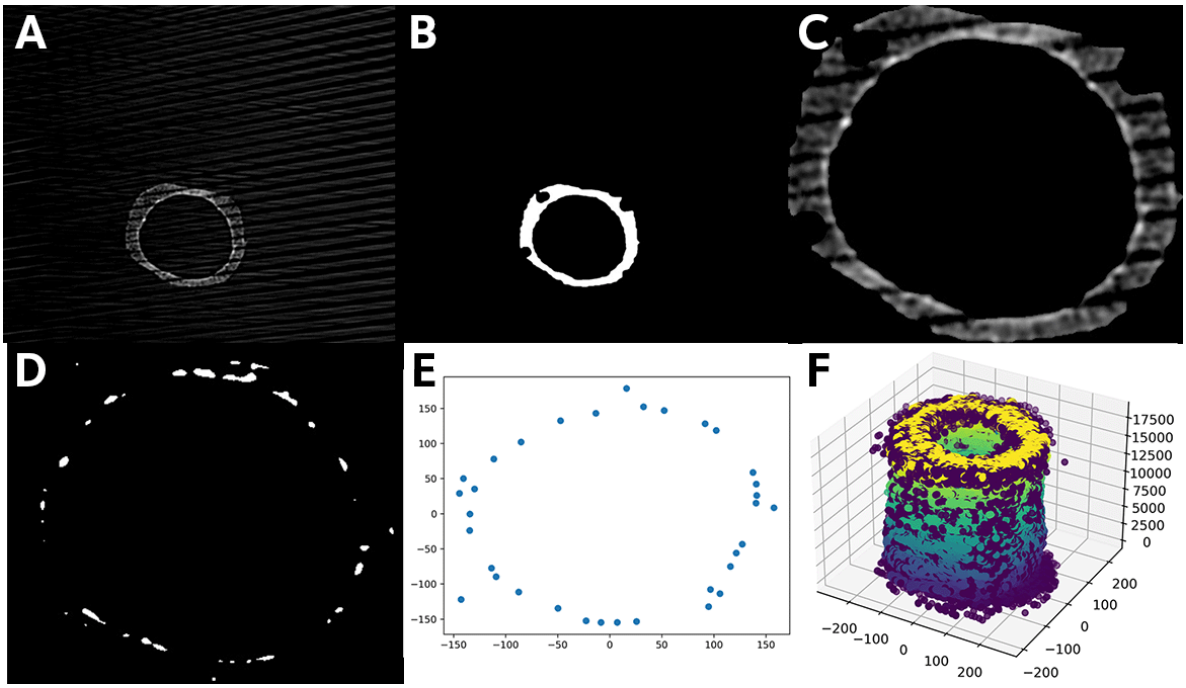


Figure S5.7. (A) Raw μCT image of EHFM bioreactor hollow fibre with HUVECs in the lumen. (B) Binary mask of μCT EHFM bioreactor fibre (C) Isolated μCT image of EHFM bioreactor hollow fibre with HUVECs in the lumen. (D) Thresholded image of μCT image of EHFM bioreactor hollow fibre showing regions which have pixel values significantly greater than that of a blank EHFM. (E) Centroid location of blobs in a single thresholded μCT EHFM image. (F) DBSCAN clusters of centroids along the entire EHFM bioreactor fibre, those highlighted in purple are considered outliers and removed as noise in final cluster distribution analyses.

Statement of Authorship for joint/multi-authored papers for PGR thesis

To appear at the end of each thesis chapter submitted as an article/paper

The statement shall describe the candidate's and co-authors' independent research contributions in the thesis publications. For each publication, there should exist a complete statement that is to be filled out and signed by the candidate and supervisor **(only required where there isn't already a statement of contribution within the paper itself).**

Title of Paper	A vascular mimetic electrospun hollow fibre membrane bioreactor for the culture of human endothelial cells: An In-Vitro vascular model
Publication Status	□Published □ Accepted for Publication □ Submitted for Publication ☒Unpublished and unsubmitted work written in a manuscript style
Publication Details	e.g. Martin, R., Mouthuy, P., Waters, S., Ye, H., (2023) A vascular mimetic electrospun hollow fibre membrane bioreactor for the culture of human endothelial cells: An In-Vitro vascular model

Student Confirmation

Student Name:	Risto John Martin		
Contribution to the Paper	All experimental work, data analysis and writing were carried out by Risto Martin. Prof. Pierre Alexis-Mouthuy, Prof. Sarah Waters, and Prof. Hua (Cathy) Ye provided supervision and advice throughout.		
Signature		Date	06/01/2023

Supervisor Confirmation

By signing the Statement of Authorship, you are certifying that the candidate made a substantial contribution to the publication, and that the description described above is accurate.

Supervisor name and title: Prof Hua Ye		
Supervisor comments The description above is accurate.		
Signature 	Date	6 Jan 2023

This completed form should be included in the thesis, at the end of the relevant chapter.

Chapter 6

Conclusions, and future directions

Current situation

The size limitation, due to the short effective range of diffusive mass transfer, of 3D tissue culture techniques must be overcome so that clinically relevant sized tissue engineered constructs may be realised [8, 9, 255]. Unconfined advective mass transfer is unacceptable as it leaves the cellular niche liable to disruption, ablating clinical relevance [44, 45, 46, 11, 10]. To date, HFMs used in tissue engineering to facilitate confined advective mass transfer are structurally and mechanically divorced from their closest physiological analogue, blood vessels. Good procedural outcomes in coronary artery bypass surgery are associated with good morphological and mechanical matches between the artery transplanted and bypassed [71]. To prevent the disruption of passive mechanical cues and enable the use of multi-modal mechanically dynamic bioreactors, HFMs used in tissue engineered constructs should, therefore, morphologically and mechanically mimic blood vessels of similar size [73, 74].

Conclusion

This thesis aimed to answer the questions

1. Can HFMs be fabricated continuously by electrospinning in a reproducible way to mimic the morphological and mechanical properties of native vasculature and;

2. facilitate nutrients exchange in static and dynamic culture conditions as a substrate for biomedical research?

The meta-analysis, presented in chapter 2 of this thesis, of mechanical data of existing TEVGs in the literature compared to that of a mechanical profile of medium sized blood vessels revealed that PCL and PDO most frequently had mechanical properties similar to that of medium sized blood vessels.

In chapter 3, a novel method for the fabrication of electrospun HFMs is presented. This method

overcomes the limited length of tubular electrospun materials associated with batch mandrel production based techniques. Furthermore, for the first time it was demonstrated that PCL and PDO may be solvent blended to produce defect-free micro-fibre meshes at a mass ratio of PCL/PDO of 0.43. Using this blend, electrospun micro fibres diameter could be shifted between 1.03 and 1.75 μm in diameter by changing either polymer or pyridine concentration. μCT image and gravimetric analysis were used to demonstrate the porosity of the membranes ranged between 88-92%. Tortuosity was found to decrease with pyridine concentration, from 6.0 - 3.9, while permeability and particle rejection size ranged between 1.21 - 1.89 $\times 10^{-14}$ m^2, and 5.8 - 4.8 μm respectively. Consequently, irrespective of pyridine concentration, blended PCL/PDO was shown to be non-cytotoxic, and cell ingress into the membrane layer is unlikely. Furthermore, the EHFMs presented in chapter 3 were found to match more mechanical properties than any of the TEVGs reviewed in the meta-analysis presented in chapter 2. From these findings, we concluded that EHFMs display morphological and functional characteristics akin to that of medium sized human arteries and can be used as a substrate to support cell growth without disrupting passive mechanical cues.

In view of the highly interconnected nature of biological systems, quality by design through mathematical modelling is key to accelerating the otherwise slow development associated with trial-and-error system evolution. Chapter 4 presents a novel model to describe EC growth in an electrospun HFM bioreactor. To describe the system, we model two-dimensional single-phase and porous media fluid flow with the Navier Stokes equations and Brinkman equations; nutrient transport with an advection-diffusion-reaction model; and finally, EC growth with a novel data-driven model. Consequently, It was found that EC growth rate increased with the inlet media flow rate up to a maximum of 8.036E-6 s^{-1} at 7.5E-11 m^3/s, after which it began to decrease. While an increase in the lumen to ECS outlet partial pressure was found to decrease the EC growth rate. However, the range of pressures evaluated was small, as too was the effective change in cell growth rate. Future studies should therefore evaluate

a wider range on pressures. While models describing EC growth have been presented in literature before [89, 139, 141, 143, 149], these models depend on parameter estimation. The model presented in chapter 4 is parameterised from data in the literature. Furthermore, previous models have considered the role of the immune system on vessel growth and repair, as there is no immune system *in vitro* these considerations do not apply in an electrospun HFM bioreactor. Furthermore, due to the novelty of electrospun hollow fibre membranes, no models exist in the literature to describe them.

Finally, the fabrication of a novel electrospun HFM bioreactor is presented in chapter 5. Under hydro-static conditions, throughout the 28 day culture, HUVECs were seen to increase in number, align with the long axis of the membrane and disperse across the EHFMs. Confocal imaging conferred these findings while revealing an increase in VE-cadherin expression throughout the culture period. Following the assembly of a novel prototype EHFM bioreactor, HUVEC growth in EHFMs under hydro-dynamic conditions was presented. Using culture conditions informed by the mathematical model presented in chapter 4, HUVEC viability was maintained throughout the 28 day culture period. At the terminus of the culture, in contrast to the hydro-static culture, no distinct morphologies were seen between HUVECs through SEM imaging. However, imaging with confocal microscopy revealed that on day 28 of the culture period HUVECs were confluent, aligned along the long axis of the membrane in the direction of fluid flow, and expressed VE-cadherin. μCT image analysis revealed HUVEC growth was restricted to the lumen wall of the EHFM, and there was no cell ingress into the membrane wall. Furthermore, HUVEC density peaked within 5000 μm of the fibre inlet and declined to a plateau, which was then maintained along the rest of the fibre. However, compared to HUVEC growth on traditional tissue culture plastic the growth rate was significantly reduced. Future work may therefore evaluate the use of chemically grafted cell adhesion peptides on electrospun materials to aid cell growth.

We, therefore, conclude that in concert, these findings show that:

1. It is possible continuously fabricate EHFMs in a controlled, reproducible manner.

2. That EHFMs may be produced to mimic the morphological and mechanical properties of similar sized blood vessels,

3. and that EFHMs may be used as a substrate for biomedical research while facilitating advective mass transfer and nutrient exchange, with the potential for use in therapeutic applications.

6.1 Limitations

Throughout these studies, there have been limitations to be considered and improved upon in future works. For example, in developing a novel electrospun HFM collector, the platform depends on a wire upon which the membrane layer is collected. The need to subsequently remove this wire limits the length of the membrane, which can be extracted to, at most, around 20 cm. Future studies should investigate alternative collector materials; water-soluble filaments that can be earthed would present an ideal replacement for the current wire.

In formulating models for biological systems, parameterisation has continued to be a significant issue. Existing mechanistic models of biological systems, other than being highly computationally expensive, have relied on parameter estimation studies. To aid with the parameterisation of future models, dose-response studies formulated and analysed through the design of experiments statistical methods would posit a significant aid to the development of well-parameterised useful biological models.

The development of a novel electrospun HFM bioreactor was presented in this thesis. However, future studies of EC growth in this platform with a greater resolution of data are still required for the validation of the mathematical models presented in this thesis. While the PrestoBlue metabolic assay data provides an estimation of the change in HUVEC number, the potential for changes in HUVEC metabolic activity to perturb these data suggests alternative methods are required. μCT image analysis

data was presented as a method by which cell numbers may be evaluated with spatial resolution. Future studies may evaluate EC growth in EHFMs, fixing samples at regular time points such that a spatial-temporal map of the change in EC numbers may be developed. Comparisons between these data and the estimated profiles predicted by the mathematical model presented in this thesis may provide irrefutable validation.

6.2 Future directions

In this work EHFMs were designed to facilitate confined advective mass transfer without disrupting passive mechanical cues; in achieving this, the EHFMs presented are flexible, biodegradable, and vascular mimetic.

In the future EHFMs may be integrated into multi-modal mechanically dynamic bioreactor systems, such as the humanoid bioreactor platform developed by Mouthuy et al. [11]. Currently, this and similar platforms depend on unconfined advective mass transfer, leaving the cellular niche in these platforms susceptible to disruption from fluid shear forces. By incorporating EHFMs into the bioreactor platform, sufficient nutrient transfer may be ensured without the disruption of passive mechanical cues and fluid shear forces, which currently disrupt the cellular niche. Given the extreme lengths such a humanoid bioreactor platform goes to mimic the mechanical stimulation and cellular niche in tendons *in vivo*, the addition of EHFMs to such a system would aid these efforts.

Further to the use of EHFMs as a platform for biomedical research, they may be used as TEVGs. The profile of medium sized blood vessels may be used to identify materials suitable for use in TEVGs. Comparison with this profile revealed that blended PCL/PDO EHFMs mimicked the profile well. Further evaluations of EHFMs as TEVGs through Murine studies would therefore be interesting. The process developed for the continuous fabrication of EHFMs may also be used for the continuous production of TEVGs, relieving the dependency on traditional batch-style mandrel techniques otherwise used to date.

Other potential points which merit further research include the potential investigation of a water soluble collector, which may be used to alleviate the dependency on a metal wire as a collector so that longer EHFMs may be practically used in future applications. Furthermore, investigations with EHFM bioreactors should consider the application of μCT image analysis as a potential method for the creation of a spatiotemporal map of cell populations in these platforms.

References

[1] Ramkumar Tiruvannamalai-Annamalai, David Randall Armant, and Howard W.T. Matthew. A glycosaminoglycan based, modular tissue scaffold system for rapid assembly of perfusable, high cell density, engineered tissues. *PLoS ONE*, 9(1), 2014.

[2] Chitral J. Angammana and Shesha H. Jayaram. Fundamentals of electrospinning and processing technologies. *Particulate Science and Technology*, 34(1):72–82, 2016.

[3] H. Strathmann, Lidietta Giorno, and Enrico Drioli. Basic Aspects in Polymeric Membrane Preparation. In *Comprehensive Membrane Science and Engineering*. 2010.

[4] Susan Standring. *Gray's Anatomy, The Anatomical Basis of Clinical Practice*. Elsevier Ltd, 41st edition, 2015.

[5] Yanina Zócalo, Daniel Bia, Edmundo I. Cabrera-Fischer, Sandra Wray, Cintia Galli, and Ricardo L. Armentano. Structural and Functional Properties of Venous Wall: Relationship between Elastin, Collagen, and Smooth Muscle Components and Viscoelastic Properties. *ISRN Physiology*, 2013:1–9, 2013.

[6] Anna Ciechanowska, Piotr Ladyzynski, Grazyna Hoser, Stanislawa Sabalinska, Jerzy Kawiak, Piotr Foltynski, Cezary Wojciechowski, and Andrzej Chwojnowski. Human endothelial cells hollow fiber membrane bioreactor as a model of the blood vessel for in vitro studies. *Journal of Artificial Organs*, 19(3):270–277, 2016.

[7] Risto Martin, Sarah Waters, Cathy Ye, and Pierre-Alexis Mouthuy. Morphological and functional characterisation of vascular inspired electrospun hollow fibre membranes. 2022.

[8] Kayla Duval, Hannah Grover, Li-Hsin Han, Yongchao Mou, Adrian F. Pegoraro, Jeffery Fredberg,

and Zi Chen. Modeling Physiological Events in 2D vs. 3D Cell Culture. *Physiology*, 32(4):266–277, 2017.

[9] Magdalena Jedrzejczak-Silicka. History of Cell Culture. In *New Insights into Cell Culture Technology*, volume i, page 13. InTech, 5 2017.

[10] Pierre-Alexis Mouthuy and Andrew Carr. Growing tissue grafts on humanoid robots: A future strategy in regenerative medicine? *Science Robotics*, 2(4), 3 2017.

[11] Pierre-Alexis Mouthuy, Sarah Snelling, Rafael Hostettler, Alona Kharchenko, Sarah Salmon, Alan Wainman, Jolet Mimpen, Claudia Paul, and Andrew Carr. Humanoid robots to mechanically stress human cells grown in soft bioreactors. *Communications Engineering*, 1(1):2, 12 2022.

[12] Jeroen Rouwkema, Nicolas C. Rivron, and Clemens A. van Blitterswijk. Vascularization in tissue engineering. *Trends in Biotechnology*, 26(8):434–441, 2008.

[13] Mark C. Allenby, Asma Tahlawi, José C.F. Morais, Kang Li, Nicki Panoskaltsis, and Athanasios Mantalaris. Ceramic hollow fibre constructs for continuous perfusion and cell harvest from 3D hematopoietic organoids. *Stem Cells International*, 2018, 2018.

[14] Katia Bilodeau, Frédéric Couet, Francesca Boccafoschi, and Diego Mantovani. Thoughts and Progress: Design of a Perfusion Bioreactor Specific to the Regeneration of Vascular Tissue Under Mechanical tresses. *Artificial Organs*, 29(December 2004):906–922, 2005.

[15] Angela H. Huang, Jenna L. Balestrini, Brooks V. Udelsman, Kevin C. Zhou, Liping Zhao, Jacopo Ferruzzi, Barry C. Starcher, Michael J. Levene, Jay D. Humphrey, and Laura E. Niklason. Biaxial Stretch Improves Elastic Fiber Maturation, Collagen Arrangement, and Mechanical Properties in Engineered Arteries. *Tissue Engineering Part C: Methods*, 22(6):524–533, 2016.

[16] Masaki Ito and Kiyohiro Houkin. Cell culture. *Cell Therapy against Cerebral Stroke: Comprehensive Reviews for Translational Researches and Clinical Trials*, 1612:49–72, 2017.

[17] Jessica Hoarau-Véchot, Arash Rafii, Cyril Touboul, and Jennifer Pasquier. Halfway between 2D and animal models: Are 3D cultures the ideal tool to study cancer-microenvironment interactions? *International Journal of Molecular Sciences*, 19(1), 2018.

[18] Tingli Lu, Yuhui Li, and Tao Chen. Techniques for fabrication and construction of three-dimensional scaffolds for tissue engineering. *International Journal of Nanomedicine*, page 337, 1 2013.

[19] Francis J Giles. Acute Myeloid Leukemia. *Hematology*, 2002(1):73–110, 2002.

[20] Youssef Mohamed Mosaad. Hematopoietic stem cells: An overview. *Transfusion and Apheresis Science*, 51(3):68–82, 2014.

[21] Abdalla Eltom, Gaoyan Zhong, and Ameen Muhammad. Scaffold Techniques and Designs in Tissue Engineering Functions and Purposes: A Review. *Advances in Materials Science and Engineering*, 2019, 2019.

[22] Isaac A Chaim, Marcos A Sabino, Mayela Mendt, Alejandro J Müller, and Diana Ajami. Evaluation of the potential of novel PCL-PPDX biodegradable scaffolds as support materials for cartilage tissue engineering. *Journal of Tissue Engineering and Regenerative Medicine*, 6(4):272–279, 4 2012.

[23] Bradley Ladewig and Muayad Nadhim Zemam Al-Shaeli. *Fundamentals of Membrane Bioreactors*. Springer Transactions in Civil and Environmental Engineering. Springer Singapore, Singapore, 2017.

[24] Teresa Mortera Blanco, Athanasios Mantalaris, Alexander Bismarck, and Nicki Panoskaltsis. The development of a three-dimensional scaffold for ex vivo biomimicry of human acute myeloid leukaemia. *Biomaterials*, 31(8):2243–2251, 2010.

[25] Osama A. M. Abdelaal and Saied M. H. Darwish. Review of Rapid Prototyping Techniques for Tissue Engineering Scaffolds Fabrication. In *Characterization and Development of Biosystems and Biomaterials*, volume 29, pages 33–54. 2013.

[26] J. F. Cooley. Improved Methods of and Apparatus for Electrically Separating the Relatively Volatile Liquid Component from the Component of Relatively Fixed Substances of Composite Fluids, 1900.

[27] Nick Tucker, Jonathan J. Stanger, Mark P. Staiger, Hussam Razzaq, and Kathleen Hofman. The History of the Science and Technology of Electrospinning from 1600 to 1995 1Nick. *Journal of engineered fibers and fabrics*, (SPECIAL ISSUE - July 2012), 2012.

[28] Jiajia Xue, Jingwei Xie, Wenying Liu, and Younan Xia. Electrospun Nanofibers: New Concepts, Materials, and Applications. *Accounts of Chemical Research*, 50(8):1976–1987, 2017.

[29] Roxanna Elizabeth Abhari, Andrew Jonathan Carr, and Pierre-Alexis Mouthuy. *Electrofluidodynamic Technologies (EFDTs) for Biomaterials and Medical Devices: Principles and Advances*. Woodhead Publishing Series in Biomaterials, 2018.

[30] Seeram Ramakrishna, Kazutoshi Fujihara, Wee-Eong Teo, Teik-Cheng Lim, and Zuwei Ma. An Introduction to Electrospinning and Nanofibers. (June), 2005.

[31] G. Taylor. Electrically Driven Jets. *Proceedings of the Royal Society A: Mathematical, Physical and Engineering Sciences*, 313(1515):453–475, 1969.

[32] Adnan Haider, Sajjad Haider, and Inn Kyu Kang. A comprehensive review summarizing the effect of electrospinning parameters and potential applications of nanofibers in biomedical and biotechnology. *Arabian Journal of Chemistry*, 11(8):1165–1188, 2018.

[33] Zheng Ming Huang, Y. Z. Zhang, M. Kotaki, and S. Ramakrishna. A review on polymer

nanofibers by electrospinning and their applications in nanocomposites. *Composites Science and Technology*, 63(15):2223–2253, 2003.

[34] M. M. Demir, I. Yilgor, E. Yilgor, and B. Erman. Electrospinning of polyurethane fibers. *Polymer*, 43(11):3303–3309, 2002.

[35] Jing Zeng, Xiaoyi Xu, Xuesi Chen, Qizhi Liang, Xinchao Bian, Lixin Yang, and Xiabin Jing. Biodegradable electrospun fibers for drug delivery. *Journal of Controlled Release*, 92(3):227–231, 2003.

[36] Cheryl L. Casper, Jean S. Stephens, Nancy G. Tassi, D. Bruce Chase, and John F. Rabolt. Controlling surface morphology of electrospun polystyrene fibers: Effect of humidity and molecular weight in the electrospinning process. *Macromolecules*, 37(2):573–578, 2004.

[37] Vahid Shabafrooz, Masoud Mozafari, Daryoosh Vashaee, and Lobat Tayebi. Electrospun nanofibers: from filtration membranes to highly specialized tissue engineering scaffolds. *Journal of nanoscience and nanotechnology*, 14:522–34, 2014.

[38] Damien Lacroix, Marzia Brunelli, Cécile Perrault, Adrien Baldit, Ana Campos, and Marin Andre. *Multiscale Mechanobiology in Tissue Engineering*. 2018.

[39] Eline van Haaften, Carlijn Bouten, and Nicholas Kurniawan. Vascular Mechanobiology: Towards Control of In Situ Regeneration. *Cells*, 6(3):19, 2017.

[40] Ke Li, Chunqiu Zhang, Lulu Qiu, Lilan Gao, and Xizheng Zhang. Advances in Application of Mechanical Stimuli in Bioreactors for Cartilage Tissue Engineering. *Tissue Engineering Part B: Reviews*, 23(4):399–411, 2017.

[41] Jolanda Rita Vetsch, Ralph Müller, and Sandra Hofmann. The evolution of simulation techniques for dynamic bone tissue engineering in bioreactors. *Journal of Tissue Engineering and Regenerative Medicine*, 9(8):903–917, 8 2015.

[42] Angela Hai Huang, Elizabeth A. Calle, Michael Boyle, Jay D. Humphrey, Laura E. Niklason, Yong-Ung Lee, and Barry C. Starcher. Design and Use of a Novel Bioreactor for Regeneration of Biaxially Stretched Tissue-Engineered Vessels. *Tissue Engineering - Part C: Methods*, 21(8):841–851, 2015.

[43] Jos Malda, Travis J. Klein, and Zee Upton. The Roles of Hypoxia in the In Vitro Engineering of Tissues . *Tissue Engineering*, 13(9):2153–2162, 2007.

[44] Yibo Ling, Jamie Rubin, Yuting Deng, Catherine Huang, Utkan Demirci, Jeffrey M. Karp, and Ali Khademhosseini. A cell-laden microfluidic hydrogel. *Lab on a Chip*, 7(6):756–762, 2007.

[45] Su Eun Chung, Wook Park, Sunghwan Shin, Seung Ah Lee, and Sunghoon Kwon. Guided and fluidic self-assembly of microstructures using railed microfluidicchannels. *Nature Materials*, 7(7):581–587, 2008.

[46] A. Lee, A. R. Hudson, D. J. Shiwarski, J. W. Tashman, T. J. Hinton, S. Yerneni, J. M. Bliley, P. G. Campbell, and A. W. Feinberg. 3D bioprinting of collagen to rebuild components of the human heart. *Science*, 365(6452):482–487, 8 2019.

[47] Marcel Mulder. *Basic Principles of Membrane Technology*. Springer Netherlands, Dordrecht, 1996.

[48] Kang Li. *Ceramic Membranes for Separation and Reaction*. John Wiley & Sons, Ltd, Chichester, UK, 3 2007.

[49] Ramalingam Balamurugan, Subramanian Sundarrajan, and Seeram Ramakrishna. Recent trends in nanofibrous membranes and their suitability for air and water filtrations. *Membranes*, 1(3):232–248, 2011.

[50] Xiaoyao Tan and Kang Li. *Inorganic Membrane Reactors*. John Wiley & Sons, Ltd, Chichester, UK, 11 2014.

[51] Hadis Eghbali, Michele M. Nava, Davod Mohebbi-Kalhori, and Manuela T. Raimondi. Hollow fiber bioreactor technology for tissue engineering applications. *International Journal of Artificial Organs*, 39(1):1–15, 2016.

[52] Lidietta Giorno and Rosalinda Mazzei. Encyclopedia of Membranes. *Encyclopedia of Membranes*, 2015.

[53] Loredana De Bartolo. Encyclopedia of Membranes. *Encyclopedia of Membranes*, 2015.

[54] Robert J. Whittaker, Richard Booth, Rosemary Dyson, Clare Bailey, Louise Parsons Chini, Shailesh Naire, Sevil Payvandi, Zimei Rong, Hannah Woollard, Linda J. Cummings, Sarah L. Waters, Lina Mawasse, Julian B. Chaudhuri, Marianne J. Ellis, Vipin Michael, Nicola J. Kuiper, and Sarah Cartmell. Mathematical modelling of fibre-enhanced perfusion inside a tissue-engineering bioreactor. *Journal of Theoretical Biology*, 256(4):533–546, 2009.

[55] J. M. Osborne, R. D. O'Dea, J. P. Whiteley, H. M. Byrne, and S. L. Waters. The Influence of Bioreactor Geometry and the Mechanical Environment on Engineered Tissues. *Journal of Biomechanical Engineering*, 132(5):051006, 2010.

[56] R. J. Shipley, A. J. Davidson, K. Chan, J. B. Chaudhuri, S. L. Waters, and M. J. Ellis. A strategy to determine operating parameters in tissue engineering hollow fiber bioreactors. *Biotechnology and Bioengineering*, 108(6):1450–1461, 2011.

[57] Nelly Wung, Samuel M. Acott, David Tosh, and Marianne J. Ellis. Hollow fibre membrane bioreactors for tissue engineering applications. *Biotechnology Letters*, 36(12):2357–2366, 2014.

[58] Lloyd A.C. Chapman, Jonathan P. Whiteley, Helen M. Byrne, Sarah L. Waters, and Rebecca J. Shipley. Mathematical modelling of cell layer growth in a hollow fibre bioreactor. *Journal of Theoretical Biology*, 418(December 2016):36–56, 2017.

[59] Nazely Diban and Dimitrios Stamatialis. Polymeric hollow fiber membranes for bioartificial organs and tissue engineering applications. *Journal of Chemical Technology and Biotechnology*, 89(5):633–643, 2014.

[60] Loredana De Bartolo, Antonella Piscioneri, Giuseppina Cotroneo, Simona Salerno, Franco Tasselli, Carla Campana, Sabrina Morelli, Maria Rende, Maria Cristina Caroleo, Marcello Bossio, and Enrico Drioli. Human lymphocyte PEEK-WC hollow fiber membrane bioreactor. *Journal of Biotechnology*, 132(1):65–74, 2007.

[61] Mark C. Allenby, Nicki Panoskaltsis, Asma Tahlawi, Susana Brito Dos Santos, and Athanasios Mantalaris. Dynamic human erythropoiesis in a three-dimensional perfusion bone marrow biomimicry. *Biomaterials*, 188(August 2018):24–37, 2019.

[62] Iwan Roberts, Stefano Baila, R. Brent Rice, Michiel Etienne Janssens, Kim Nguyen, Nathalie Moens, Ludmila Ruban, Diana Hernandez, Pete Coffey, and Chris Mason. Scale-up of human embryonic stem cell culture using a hollow fibre bioreactor. *Biotechnology Letters*, 34(12):2307–2315, 2012.

[63] Toon Lambrechts, Ioannis Papantoniou, Brent Rice, Jan Schrooten, Frank P. Luyten, and Jean Marie Aerts. Large-scale progenitor cell expansion for multiple donors in a monitored hollow fibre bioreactor. *Cytotherapy*, 18(9):1219–1233, 2016.

[64] Michael T. Zaucha, William Wan, Rudolph L. Gleason Jr., Julia Raykin, Robert Gauvin, Francois A. Auger, Lucie Germain, and Thomas E. Michaels. A novel cylindrical biaxial computer-controlled bioreactor and biomechanical testing device for vascular tissue engineering. *Tissue Engineering - Part A*, 15(11):3331–3340, 2009.

[65] N. S. Abdullah, Diganta B. Das, H. Ye, and Z. F. Cui. 3D bone tissue growth in hollow fibre mem-

brane bioreactor: Implications of various process parameters on tissue nutrition. *International Journal of Artificial Organs*, 29(9):841–851, 2006.

[66] Hua Ye, Zhidao Xia, David J.P. Ferguson, James T. Triffitt, and Zhanfeng Cui. Studies on the use of hollow fibre membrane bioreactors for tissue generation by using rat bone marrow fibroblastic cells and a composite scaffold. *Journal of Materials Science: Materials in Medicine*, 18(4):641–648, 2007.

[67] George S. Hussey, Jenna L. Dziki, and Stephen F. Badylak. Extracellular matrix-based materials for regenerative medicine. *Nature Reviews Materials*, 3(7):159–173, 5 2018.

[68] R. K. Viswanadham and Edward J. Kramer. Elastic properties of reconstituted collagen hollow fibre membranes. *Journal of Materials Science*, 11(7):1254–1262, 1976.

[69] Koji Kuraoka, Takashi Hirano, and Tetsuo Yazawa. High-selectivity , high-flexibility glass hollow-fiber membrane for gas. pages 664–665, 2002.

[70] Miki Yoshimune and Kenji Haraya. Flexible carbon hollow fiber membranes derived from sulfonated poly(phenylene oxide). *Separation and Purification Technology*, 75(2):193–197, 2010.

[71] Brenda Martínez-González, Cynthia Guadalupe Reyes-Hernández, Alejandro Quiroga-Garza, Víctor E. Rodríguez-Rodríguez, Claudia N. Esparza-Hernández, Rodrigo E. Elizondo-Omaña, and Santos Guzmán-López. Conduits used in coronary artery bypass grafting: A review of morphological studies. *Annals of Thoracic and Cardiovascular Surgery*, 23(2):55–65, 2017.

[72] Colin D. Mathers and Dejan Loncar. Projections of global mortality and burden of disease from 2002 to 2030. *PLoS Medicine*, 3(11):2011–2030, 2006.

[73] Nasser K. Awad, Haitao Niu, Usman Ali, Yosry S. Morsi, and Tong Lin. Electrospun fibrous scaffolds for small-diameter blood vessels: A review. *Membranes*, 8(1):1–26, 2018.

[74] Young Min Ju, Jin San Choi, Anthony Atala, James J. Yoo, and Sang Jin Lee. Bilayered scaffold for engineering cellularized blood vessels. *Biomaterials*, 31(15):4313–4321, 2010.

[75] J Gordon Betts. *Anatomy & physiology*. 2013.

[76] Wojciech Pawlina Michael H. Ross. *Histology: A Text and Atlas*. Lippincott Williams and Wilkins, 7th edition, 2015.

[77] Sandip Sarkar, Thomas Schmitz-Rixen, George Hamilton, and Alexander M. Seifalian. Achieving the ideal properties for vascular bypass grafts using a tissue engineered approach: A review. *Medical and Biological Engineering and Computing*, 45(4):327–336, 2007.

[78] Ralf H. Adams and Kari Alitalo. Molecular regulation of angiogenesis and lymphangiogenesis. *Nature Reviews Molecular Cell Biology*, 8(6):464–478, 2007.

[79] Kenneth Kaushansky, Marshall Lichtman, Josef Prchal, Marcel M Levi, Oliver Press, Linda Burns, and Michael Caligiuri. *Hematology*. 2016.

[80] L. K. Phng and Holger Gerhardt. Angiogenesis: A Team Effort Coordinated by Notch. *Developmental Cell*, 16(2):196–208, 2009.

[81] Peter Carmeliet and Rakesh K. Jain. Molecular mechanisms and clinical applications of angiogenesis. *Nature*, 473(7347):298–307, 2011.

[82] Michael Potente, Holger Gerhardt, and Peter Carmeliet. Basic and therapeutic aspects of angiogenesis. *Cell*, 146(6):873–887, 2011.

[83] Katerina Rohlenova, Koen Veys, Ines Miranda-Santos, Katrien De Bock, and Peter Carmeliet. Endothelial Cell Metabolism in Health and Disease. *Trends in Cell Biology*, 28(3):224–236, 2018.

[84] Xuri Li, Anil Kumar, and Peter Carmeliet. Metabolic Pathways Fueling the Endothelial Cell Drive. *Annual Review of Physiology*, 81(1):483–503, 2 2019.

[85] Katrien De Bock, Maria Georgiadou, Sandra Schoors, Anna Kuchnio, Brian W. Wong, Anna Rita Cantelmo, Annelies Quaegebeur, Bart Ghesquière, Sandra Cauwenberghs, Guy Eelen, Li-Kun Phng, Inge Betz, Bieke Tembuyser, Katleen Brepoels, Jonathan Welti, Ilse Geudens, Inmaculada Segura, Bert Cruys, Franscesco Bifari, Ilaria Decimo, Raquel Blanco, Sabine Wyns, Jeroen Vangindertael, Susana Rocha, Russel T. Collins, Sebastian Munck, Dirk Daelemans, Hiromi Imamura, Roland Devlieger, Mark Rider, Paul P. Van Veldhoven, Frans Schuit, Ramon Bartrons, Johan Hofkens, Peter Fraisl, Sucheta Telang, Ralph J. DeBerardinis, Luc Schoonjans, Stefan Vinckier, Jason Chesney, Holger Gerhardt, Mieke Dewerchin, and Peter Carmeliet. Role of PFKFB3-Driven Glycolysis in Vessel Sprouting. *Cell*, 154(3):651–663, 8 2013.

[86] Guy Eelen, Pauline De Zeeuw, Michael Simons, and Peter Carmeliet. Endothelial cell metabolism in normal and diseased vasculature. *Circulation Research*, 116(7):1231–1244, 2015.

[87] Kim D. Falkenberg, Katerina Rohlenova, Yonglun Luo, and Peter Carmeliet. The metabolic engine of endothelial cells. *Nature Metabolism*, 1(10):937–946, 2019.

[88] R. A. Macrae, K. Miller, and B. J. Doyle. Methods in Mechanical Testing of Arterial Tissue: A Review. *Strain*, 52(5):380–399, 2016.

[89] Takehiko Azuma and Masamitsu Hasegawa. Distensibility of the vein: from the architectural point of view. *Biorheology*, 10(3):469–479, 1973.

[90] A. P. Ebrahimi. Mechanical properties of normal and diseased cerebrovascular system. *J. Vasc. Interv. Neurol.*, 2(2):155–162, 2009.

[91] Koon Sung Cheng, Alok Tiwari, Cara R. Baker, Richard Morris, George Hamilton, and Alexan-

der M. Seifalian. Impaired carotid and femoral viscoelastic properties and elevated intima-media thickness in peripheral vascular disease. *Atherosclerosis*, 164(1):113–120, 2002.

[92] Maarten Groenink, Susan E. Langerak, Ed Vanbavel, Ernst E. Van Der Wall, Barbara J.M. Mulder, Allard C. Van Der Wal, and Jos A.E. Spaan. The influence of aging and aortic stiffness on permanent dilation and breaking stress of the thoracic descending aorta. *Cardiovascular Research*, 43(2):471–480, 1999.

[93] International Standards Organization. BS EN ISO 7198 : 2017 BSI Standards Publication Cardiovascular implants and extracorporeal systems — Vascular prostheses — Tubular vascular grafts and vascular patches (ISO 7198 : 2016). 2017.

[94] Maria Stekelenburg, Marcel C.M. Rutten, Luc H.E.H. Snoeckx, and Frank P.T. Baaijens. Dynamic Straining Combined with Fibrin Gel Cell Seeding Improves Strength of Tissue-Engineered Small-Diameter Vascular Grafts. *Tissue Engineering Part A*, 15(5):1081–1089, 5 2009.

[95] Abdol-Mohammad Kajbafzadeh, Reza Khorramirouz, Seyede Maryam Kameli, Javad Hashemi, and Amin Bagheri. Decellularization of Human Internal Mammary Artery: Biomechanical Properties and Histopathological Evaluation. *BioResearch Open Access*, 6(1):74–84, 2017.

[96] Lorenzo Soletti, Yi Hong, Jianjun Guan, John J. Stankus, Mohammed S. El-Kurdi, William R. Wagner, and David A. Vorp. A bilayered elastomeric scaffold for tissue engineering of small diameter vascular grafts. *Acta Biomaterialia*, 6(1):110–122, 1 2010.

[97] T. Khamdaeng, J. Luo, J. Vappou, P. Terdtoon, and E. E. Konofagou. Arterial stiffness identification of the human carotid artery using the stress-strain relationship in vivo. *Ultrasonics*, 52(3):402–411, 2012.

[98] L V Antonova, R A Mukhamadiyarov, A V Mironov, E A Velikanova, O D Sidorova, O L

Barbarash, and L S Barbarash. VASCULAR GRAFT OF SMALL DIAMETER FROM POLY-HYDROXYBUTYRATE / VALERATE AND POLYCAPROLACTONE. 2015.

[99] Chang Min Suh, Sung Ho Kim, Ken L. Monson, and Werner Goldsmith. Tensile characteristics and behavior of blood vessels from human brain in uniaxial tensile test. *KSME International Journal*, 17(7):1016–1025, 2003.

[100] Y Aggoun. Mechanical properties of the common carotid artery in Williams syndrome. *Heart*, 84(3):290–293, 2000.

[101] Gerhardt Konig, Todd N. McAllister, Nathalie Dusserre, Sergio A. Garrido, Corey Iyican, Alicia Marini, Alex Fiorillo, Hernan Avila, Wojciech Wystrychowski, Krzysztof Zagalski, Marcin Maruszewski, Alyce Linthurst Jones, Lech Cierpka, Luis M. de la Fuente, and Nicolas L'Heureux. Mechanical properties of completely autologous human tissue engineered blood vessels compared to human saphenous vein and mammary artery. *Biomaterials*, 30(8):1542–1550, 2009.

[102] Stéphane Laurent, Xavier Girerd, Jean Jacques Mourad, Patrick Lacolley, Lionel Beck, Pierre Boutouyrie, Jean Pierre Mignot, and Michel Safar. Elastic modulus of the radial artery wall material is not increased in patients with essential hypertension. *Arteriosclerosis, Thrombosis, and Vascular Biology*, 14(7):1223–1231, 1994.

[103] G Gamble, J Zorn, G Sanders, S MacMahon, and N Sharpe. Estimation of arterial stiffness, compliance, and distensibility from M-mode ultrasound measurements of the common carotid artery. *Stroke*, 25(1):11–6, 1 1994.

[104] Sarra de Valence, Jean Christophe Tille, Damiano Mugnai, Wojciech Mrowczynski, Robert Gurny, Michael Möller, and Beat H. Walpoth. Long term performance of polycaprolactone vascular grafts in a rat abdominal aorta replacement model. *Biomaterials*, 33(1):38–47, 2012.

[105] Shannon L M Dahl, Alan P Kypson, Jeffrey H Lawson, Juliana L Blum, Justin T Strader, Yuling

Li, Roberto J Manson, William E Tente, Louis DiBernardo, M Taylor Hensley, Riley Carter, Tiare P Williams, Heather L Prichard, Margaret S Dey, Keith G Begelman, and Laura E Niklason. Readily available tissue-engineered vascular grafts. *Science translational medicine*, 3(68):68ra9, 2011.

[106] Yanzhong Zhang, Hongwei Ouyang, Teck Lim Chwee, Seeram Ramakrishna, and Zheng Ming Huang. Electrospinning of gelatin fibers and gelatin/PCL composite fibrous scaffolds. *Journal of Biomedical Materials Research - Part B Applied Biomaterials*, 72(1):156–165, 2005.

[107] Cho Hay Mun, Youngmee Jung, Sang-Heon Kim, Sun-Hee Lee, Hee Chan Kim, Il Keun Kwon, and Soo Hyun Kim. Three-Dimensional Electrospun Poly(Lactide-Co-Caprolactone) for Small-Diameter Vascular Grafts. *Tissue Engineering Part A*, 18(15-16):1608–1616, 2012.

[108] Yiwa Pan, Xin Zhou, Yongzhen Wei, Qiuying Zhang, Ting Wang, Meifeng Zhu, Wen Li, Rui Huang, Ruming Liu, Jingrui Chen, Guanwei Fan, Kai Wang, Deling Kong, and Qiang Zhao. Small-diameter hybrid vascular grafts composed of polycaprolactone and polydioxanone fibers. *Scientific Reports*, 7(1):1–11, 2017.

[109] Krishna Kumar Sankaran, Kirthanashri Srinivasan Vasanthan, Uma Maheswari Krishnan, and Swaminathan Sethuraman. Development and evaluation of axially aligned nanofibres for blood vessel tissue engineering. *Journal of Tissue Engineering and Regenerative Medicine*, 8(8):640–651, 8 2014.

[110] Wei He, Zuojun Hu, Anwu Xu, and Ruiming Liu. The Preparation and Performance of a New Polyurethane Vascular Prosthesis. pages 855–866, 2013.

[111] Jamil A. Matthews, Gary E. Wnek, David G. Simpson, and Gary L. Bowlin. Electrospinning of collagen nanofibers. *Biomacromolecules*, 3(2):232–238, 2002.

[112] Catherine P. Barnes, Charles W. Pemble, David D. Brand, David G. Simpson, and Gary L. Bowlin.

Cross-Linking Electrospun Type II Collagen Tissue Engineering Scaffolds with Carbodiimide in Ethanol. *Tissue Engineering*, 13(7):1593–1605, 2007.

[113] A. A. Salifu, B. D. Nury, and C. Lekakou. Electrospinning of nanocomposite fibrillar tubular and flat scaffolds with controlled fiber orientation. *Annals of Biomedical Engineering*, 39(10):2510–2520, 2011.

[114] Kathryn A. McKenna, Monica T. Hinds, Rebecca C. Sarao, Ping Cheng Wu, Cheryl L. Maslen, Robert W. Glanville, Darcie Babcock, and Kenton W. Gregory. Mechanical property characterization of electrospun recombinant human tropoelastin for vascular graft biomaterials. *Acta Biomaterialia*, 8(1):225–233, 2012.

[115] Jingchen Gao, Yaping Wang, Siyuan Chen, Di Tang, Li Jiang, Deling Kong, and Shufang Wang. Electrospun poly-ϵ-caprolactone scaffold modified with catalytic nitric oxide generation and heparin for small-diameter vascular graft. *RSC Advances*, 7(30):18775–18784, 2017.

[116] M. J. McClure, S. A. Sell, C. E. Ayres, D. G. Simpson, and G. L. Bowlin. Electrospinning-aligned and random polydioxanone-polycaprolactone-silk fibroin-blended scaffolds: Geometry for a vascular matrix. *Biomedical Materials*, 4(5), 2009.

[117] Young Min Ju, Hyunhee Ahn, Juan Arenas-Herrera, Cheil Kim, Mehran Abolbashari, Anthony Atala, James J. Yoo, and Sang Jin Lee. Electrospun vascular scaffold for cellularized small diameter blood vessels: A preclinical large animal study. *Acta Biomaterialia*, 59:58–67, 2017.

[118] H. Wu, J. Fan, C. C. Chu, and J. Wu. Electrospinning of small diameter 3-D nanofibrous tubular scaffolds with controllable nanofiber orientations for vascular grafts. *Journal of Materials Science: Materials in Medicine*, 21(12):3207–3215, 2010.

[119] Claudia M. Vaz, S. van Tuijl, C. V C Bouten, and F. P T Baaijens. Design of scaffolds for blood

vessel tissue engineering using a multi-layering electrospinning technique. *Acta Biomaterialia*, 1(5):575–582, 2005.

[120] Chi Hun Kim, Myung Seob Khil, Hak Yong Kim, Hyun Uk Lee, and Kwang Yeop Jahng. An improved hydrophilicity via electrospinning for enhanced cell attachment and proliferation. *Journal of Biomedical Materials Research Part B: Applied Biomaterials*, 78B(2):283–290, 8 2006.

[121] Krishna Kumar Sankaran, Uma Maheswari Krishnan, and Swaminathan Sethuraman. Axially aligned 3D nanofibrous grafts of PLA-PCL for small diameter cardiovascular applications. *Journal of Biomaterials Science, Polymer Edition*, 25(16):1791–1812, 2014.

[122] Joseph L. Lowery, Néha Datta, and Gregory C. Rutledge. Effect of fiber diameter, pore size and seeding method on growth of human dermal fibroblasts in electrospun poly(ϵ-caprolactone) fibrous mats. *Biomaterials*, 31(3):491–504, 2010.

[123] Marek Rychter, Anna Baranowska-korczyc, and Janina Lulek. Progress and perspectives in bioactive agent delivery via electrospun vascular grafts. *RSC Advances*, pages 32164–32184, 2017.

[124] Hong-yong Duan, Lin Ye, Xin Wu, Qiang Guan, Xiao-fei Yang, Feng Han, Ning Liang, Zhen-Feng Wang, and Zhong-gao Wang. The in vivo characterization of electrospun heparin-bonded polycaprolactone in small-diameter vascular reconstruction. *Vascular*, 23(4):358–365, 8 2015.

[125] Anlin Yin, Rifang Luo, Jiukai Li, Xiumei Mo, Yunbing Wang, and Xingdong Zhang. Coaxial electrospinning multicomponent functional controlled-release vascular graft : Optimization of graft properties. *Colloids and Surfaces B: Biointerfaces*, 152:432–439, 2017.

[126] L. V. Antonova, A. Yu. Burago, A. V. Mironov, V. G. Matveeva, E. A. Velikanova, R. A. Mukhamadiyarov, T. V. Glushkova, Y. A. Kudryavtseva, O. L. Barbarash, and L. S. Barbarash.

Polyhydroxybutyrate/valerate/polycaprolactone small-diameter vascular graft: Experimental study of integration into organism. 020010(2015):020010, 2015.

[127] Jeffrey J D Henry, Jian Yu, Aijun Wang, Natasha Maurmann, Daniela P Pereira, and Daniela Burguez. Electrospun scaffolds functionalized with heparin and vascular endothelial growth factor increase the proliferation of endothelial progenitor cells Electrospun scaffolds functionalized with heparin and vascular endothelial growth factor increase the proli. 2017.

[128] Hua Li, Chenguang Zhao, Zhexiang Wang, Hong Zhang, Xiaoyan Yuan, and Deling Kong. Controlled Release of PDGF-bb by Coaxial Electrospun Dextran/Poly(L-lactide-co-ϵ-caprolactone) Fibers with an Ultrafine Core/Shell Structure. *Journal of Biomaterials Science, Polymer Edition*, 21(6-7):803–819, 1 2010.

[129] Nick Huettner, Tim R. Dargaville, and Aurelien Forget. Discovering Cell-Adhesion Peptides in Tissue Engineering: Beyond RGD. *Trends in Biotechnology*, 36(4):372–383, 2018.

[130] Wenting Zheng, Zhihong Wang, Lijie Song, Qiang Zhao, Jun Zhang, Dong Li, Shufang Wang, Jihong Han, Xi Long Zheng, Zhimou Yang, and Deling Kong. Endothelialization and patency of RGD-functionalized vascular grafts in a rabbit carotid artery model. *Biomaterials*, 33(10):2880–2891, 2012.

[131] Cheng-hung Lee, Shang-hung Chang, Yu-huang Lin, Shih-jung Liu, Chao-jan Wang, Ming-yi Hsu, Kuo-chun Hung, Yung-hsin Yeh, Wei-jan Chen, I-chang Hsieh, and Ming-shien Wen. Biomaterials Acceleration of re-endothelialization and inhibition of neointimal formation using hybrid biodegradable nano fi brous rosuvastatin-loaded stents. *Biomaterials*, 35(15):4417–4427, 2014.

[132] Rachel H. Coy, Owen R. Evans, James B. Phillips, and Rebecca J. Shipley. An integrated

theoretical-experimental approach to accelerate translational tissue engineering. *Journal of Tissue Engineering and Regenerative Medicine*, 12(1):e53–e59, 2018.

[133] C. J. Chuong and Y. C. Fung. Three-Dimensional Stress Distribution in Arteries. *Journal of Biomechanical Engineering*, 105(3):268–274, 8 1983.

[134] Keiichi Takamizawa and Kozaburo Hayashi. Strain energy density function and uniform strain hypothesis for arterial mechanics. *Journal of Biomechanics*, 20(1):7–17, 1 1987.

[135] Jungsil Kim and Jessica E. Wagenseil. Bio-Chemo-Mechanical Models of Vascular Mechanics. *Annals of Biomedical Engineering*, 43(7):1477–1487, 2015.

[136] P. B. Dobrin and T. R. Canfield. Elastase, collagenase, and the biaxial elastic properties of dog carotid artery. *American Journal of Physiology-Heart and Circulatory Physiology*, 247(1):H124–H131, 7 1984.

[137] HARVEY WOLINSKY and SEYMOUR GLAGOV. Structural Basis for the Static Mechanical Properties of the Aortic Media. *Circulation Research*, 14(5):400–413, 5 1964.

[138] Martin A. Zulliger, Pierre Fridez, Kozaburo Hayashi, and Nikos Stergiopulos. A strain energy function for arteries accounting for wall composition and structure. *Journal of Biomechanics*, 37(7):989–1000, 7 2004.

[139] Victoria P. Le, Russell H. Knutsen, Robert P. Mecham, and Jessica E. Wagenseil. Decreased aortic diameter and compliance precedes blood pressure increases in postnatal development of elastin-insufficient mice. *American Journal of Physiology-Heart and Circulatory Physiology*, 301(1):H221–H229, 7 2011.

[140] Gerhard A. Holzapfel and Hans W. Weizsäcker. Biomechanical behavior of the arterial wall and its numerical characterization. *Computers in Biology and Medicine*, 28(4):377–392, 7 1998.

[141] T. Christian Gasser, Ray W Ogden, and Gerhard A Holzapfel. Hyperelastic modelling of arterial layers with distributed collagen fibre orientations. *Journal of The Royal Society Interface*, 3(6):15–35, 2 2006.

[142] N.A. Hill and M.K. Spendiff. A model for the interaction between intimal hyperplasia and blood flow. 2001.

[143] K. S. Miller, Y. U. Lee, Y. Naito, C. K. Breuer, and J. D. Humphrey. Computational model of the in vivo development of a tissue engineered vein from an implanted polymeric construct. *Journal of Biomechanics*, 47(9):2080–2087, 2014.

[144] Kristin S. Miller, Ramak Khosravi, Christopher K. Breuer, and Jay D. Humphrey. A hypothesis-driven parametric study of effects of polymeric scaffold properties on tissue engineered neovessel formation. *Acta Biomaterialia*, 11(1):283–294, 2015.

[145] Jason M. Szafron, Abhay B. Ramachandra, Christopher K. Breuer, Alison L. Marsden, and Jay D. Humphrey. Optimization of Tissue-Engineered Vascular Graft Design Using Computational Modeling. *Tissue Engineering - Part C: Methods*, 25(10):561–570, 2019.

[146] Pedro Aparício, Mark S. Thompson, and Paul N. Watton. A novel chemo-mechano-biological model of arterial tissue growth and remodelling. *Journal of Biomechanics*, 49(12):2321–2330, 2016.

[147] J. D. Humphrey, S. Baek, and L. E. Niklason. Biochemomechanics of cerebral vasospasm and its resolution: I. A new hypothesis and theoretical framework. *Annals of Biomedical Engineering*, 35(9):1485–1497, 2007.

[148] S. Baek, A. Valentín, and J. D. Humphrey. Biochemomechanics of cerebral vasospasm and its resolution: II. Constitutive relations and model simulations. *Annals of Biomedical Engineering*, 35(9):1498–1509, 2007.

[149] Linda Irons and Jay D. Humphrey. Cell signaling model for arterial mechanobiology. *PLoS Computational Biology*, 16(8):1–22, 2020.

[150] Minki Hwang, Marc Garbey, Scott A. Berceli, Rongling Wu, Zhihua Jiang, and Roger Tran-Son-Tay. Rule-Based Model of Vein Graft Remodeling. *PLoS ONE*, 8(3):1–11, 2013.

[151] Colin J. Boyle, Alexander B. Lennon, and Patrick J. Prendergast. In silico prediction of the mechanobiological response of arterial tissue: Application to angioplasty and stenting. *Journal of Biomechanical Engineering*, 133(8):1–11, 2011.

[152] Marc Garbey and Scott A. Berceli. A dynamical system that describes vein graft adaptation and failure. *Journal of Theoretical Biology*, 336:209–220, 2013.

[153] Paula Budu-Grajdeanu, Richard C. Schugart, Avner Friedman, Christopher Valentine, Anil K. Agarwal, and Brad H. Rovin. A mathematical model of venous neointimal hyperplasia formation. *Theoretical Biology and Medical Modelling*, 5:1–9, 2008.

[154] Michele Marino, Giuseppe Pontrelli, Giuseppe Vairo, and Peter Wriggers. A chemo-mechano-biological formulation for the effects of biochemical alterations on arterial mechanics: The role of molecular transport and multiscale tissue remodelling. *Journal of the Royal Society Interface*, 14(136), 2017.

[155] Ramak Khosravi, Abhay B. Ramachandra, Jason M. Szafron, Daniele E. Schiavazzi, Christopher K. Breuer, and Jay D. Humphrey. A computational bio-chemo-mechanical model of in vivo tissue-engineered vascular graft development. *Integrative biology : quantitative biosciences from nano to macro*, 12(3):47–63, 2020.

[156] Francesca Donadoni, Cesar Pichardo-Almarza, Matthew Bartlett, Alan Dardik, Shervanthi Homer-Vanniasinkam, and Vanessa Díaz-Zuccarini. Patient-specific, multi-scale modeling of neointimal hyperplasia in vein grafts. *Frontiers in Physiology*, 8(APR):1–20, 2017.

[157] Maziyar Keshavarzian, Clark A. Meyer, and Heather N. Hayenga. Mechanobiological model of arterial growth and remodeling. *Biomechanics and Modeling in Mechanobiology*, 17(1):87–101, 2018.

[158] Erman Pektok, Benjamin Nottelet, Jean Christophe Tille, Robert Gurny, Afksendiyos Kalangos, Michael Moeller, and Beat H. Walpoth. Degradation and healing characteristics of small-diameter poly(ϵ-caprolactone) vascular grafts in the rat systemic arterial circulation. *Circulation*, 118(24):2563–2570, 2008.

[159] B. Nottelet, E. Pektok, D. Mandracchia, J. C. Tille, B. Walpoth, R. Gurny, and Michael Möller. Factorial design optimization and in vivo feasibility of poly(ϵ-caprolactone)-micro- and nanofiber-based small diameter vascular grafts. *Journal of Biomedical Materials Research - Part A*, 89(4):865–875, 2009.

[160] Andrew Krishna Ekaputra, Yefang Zhou, Simon McKenzie Cool, and Dietmar Werner Hutmacher. Composite Electrospun Scaffolds for Engineering Tubular Bone Grafts. *Tissue Engineering Part A*, 15(12):3779–3788, 2009.

[161] Sang Jin Lee, Jie Liu, Se Heang Oh, Shay Soker, Anthony Atala, and James J. Yoo. Development of a composite vascular scaffolding system that withstands physiological vascular conditions. *Biomaterials*, 29(19):2891–2898, 7 2008.

[162] Thi Hiep Nguyen, Andrew R. Padalhin, Hyung Seok Seo, and Byong Taek Lee. A hybrid electrospun PU/PCL scaffold satisfied the requirements of blood vessel prosthesis in terms of mechanical properties, pore size, and biocompatibility. *Journal of Biomaterials Science, Polymer Edition*, 24(14):1692–1706, 2013.

[163] Costantino Del Gaudio, Enrico Ercolani, Pierluca Galloni, Federico Santilli, Silvia Baiguera, Leonardo Polizzi, and Alessandra Bianco. Aspirin-loaded electrospun poly(ϵ-caprolactone)

tubular scaffolds: potential small-diameter vascular grafts for thrombosis prevention. *Journal of Materials Science: Materials in Medicine*, 24(2):523–532, 2 2013.

[164] Nuoxin Wang, Wenfu Zheng, Shiyu Cheng, Wei Zhang, Shaoqin Liu, and Xingyu Jiang. In vitro evaluation of essential mechanical properties and cell behaviors of a novel polylactic-co-glycolic acid (PLGA)-based tubular scaffold for small-diameter vascular tissue Engineering. *Polymers*, 9(8), 2017.

[165] Primana Punnakitikashem, Danh Truong, Jyothi U Menon, Kytai T Nguyen, and Yi Hong. Electrospun biodegradable elastic polyurethane scaffolds with dipyridamole release for small diameter vascular grafts. *Acta Biomaterialia*, 10(11):4618–4628, 2014.

[166] Jingchen Gao, Siyuan Chen, Di Tang, Li Jiang, Jie Shi, and Shufang Wang. Mechanical Properties and Degradability of Electrospun PCL/PLGA Blended Scaffolds as Vascular Grafts. *Transactions of Tianjin University*, (0123456789):1–9, 2018.

[167] Catherine P. Barnes, Scott A. Sell, Eugene D. Boland, David G. Simpson, and Gary L. Bowlin. Nanofiber technology: Designing the next generation of tissue engineering scaffolds. *Advanced Drug Delivery Reviews*, 59(14):1413–1433, 2007.

[168] Juan Zhou, Chuanbao Cao, and Xilan Ma. A novel three-dimensional tubular scaffold prepared from silk fibroin by electrospinning. *International Journal of Biological Macromolecules*, 45(5):504–510, 2009.

[169] Benedetto Marelli, Antonio Alessandrino, Silvia Farè, Giuliano Freddi, Diego Mantovani, and Maria Cristina Tanzi. Compliant electrospun silk fibroin tubes for small vessel bypass grafting. *Acta Biomaterialia*, 6(10):4019–4026, 2010.

[170] Benedetto Marelli, Matteo Achilli, Antonio Alessandrino, Giuliano Freddi, Diego Mantovani,

Maria Cristina Tanzi, and Silvia Fare. Collagen-Reinforced Electrospun Silk Fibroin Tubular Construct as Small Calibre Vascular Graft a. pages 1566–1574, 2012.

[171] Zhihong Wang, Yifan Wu, Jianing Wang, Chuangnian Zhang, Hongyu Yan, Meifeng Zhu, Kai Wang, Chen Li, Qingbo Xu, and Deling Kong. Effect of Resveratrol on Modulation of Endothelial Cells and Macrophages for Rapid Vascular Regeneration from Electrospun Poly([U+03F5]-caprolactone) Scaffolds. *ACS Applied Materials and Interfaces*, 9(23):19541–19551, 2017.

[172] Leah Soffer, Xianyan Wang, Xiaohui Zhang, Jonathan Kluge, Luis Dorfmann, David L. Kaplan, and Gary Leisk. Silk-based electrospun tubular scaffolds for tissue-engineered vascular grafts. *Journal of Biomaterials Science, Polymer Edition*, 19(5):653–664, 2008.

[173] Michael J. McClure, Scott A. Sell, David G. Simpson, Beat H. Walpoth, and Gary L. Bowlin. A three-layered electrospun matrix to mimic native arterial architecture using polycaprolactone, elastin, and collagen: A preliminary study. *Acta Biomaterialia*, 6(7):2422–2433, 2010.

[174] Larisa Antonova, Alexander M Seifalian, Anton G Kutikhin, Victoria V Sevostyanova, Evgeniya O Krivkina, Andrey V Mironov, Andrey Burago, Elena Velikanova, Vera G. Matveeva, Tatiana V. Glushkova, Evgeniya A. Sergeeva, Georgiy Y. Vasyukov, Yuliya A. Kudryavtseva, Olga L. Barbarash, and Leonid S. Barbarash. Bioabsorbable bypass grafts biofunctionalised with RGD have enhanced biophysical properties and endothelialisation tested in vivo. *Frontiers in Pharmacology*, 7(MAY):1–10, 2016.

[175] A. K. Moghe, R. Hufenus, S. M. Hudson, and B. S. Gupta. Effect of the addition of a fugitive salt on electrospinnability of poly(ϵ-caprolactone). *Polymer*, 50(14):3311–3318, 2009.

[176] Antonina A Lach, Hayley L Morris, Joana A Martins, Edward T Stace, Andrew J. Carr, and Pierre-Alexis Mouthuy. Pyridine as an additive to improve the deposition of continuous electrospun filaments. *PLOS ONE*, 14(4):e0214419, 4 2019.

[177] Nathan A. Hotaling, Kapil Bharti, Haydn Kriel, and Carl G. Simon. DiameterJ: A validated open source nanofiber diameter measurement tool. *Biomaterials*, 61:327–338, 2015.

[178] Satoshi Suzuki and KeiichiA Be. Topological Structural Analysis of Digitized Binary Images by Border Following. 46:32–46, 1985.

[179] Andrew W Fitzgibbon, Robert B Fisher, Forrest Hill, and Edinburgh Eh. A Buyer's Guide to Conic Fitting *. pages 513–522, 1995.

[180] N Otsu. A Threshold Selection Method from Gray-Level Histograms. *IEEE Transactions on Systems, Man, and Cybernetics*, C(1):62–66, 1979.

[181] Olaf Dietrich. Diffusion Coefficients of Water, 2022.

[182] Hazwani Suhaimi, Shuai Wang, Tom Thornton, and Diganta Bhusan Das. On glucose diffusivity of tissue engineering membranes and scaffolds. *Chemical Engineering Science*, 126:244–256, 2015.

[183] C.Chenu and E.B.Roberson. Diffusion of glucose in microbial extracellular polysaccharide as affected by water potential. *Soil Biology and Biochemistry*, 28(7):877–884.

[184] Bengt A Westrin and Anders Axelsson. A diaphragm diffusion cell applied to ethanol diffusion in agarose gel: A reproducibility study. *Biotechnology Techniques volume*, 5(4):303–306, 1991.

[185] Ashish Aher, Joseph Papp, Andrew Colburn, Hongyi Wan, Evan Hatakeyama, Prakhar Prakash, Ben Weaver, and Dibakar Bhattacharyya. Naphthenic acids removal from high TDS produced water by persulfate mediated iron oxide functionalized catalytic membrane, and by nanofiltration. *Chemical Engineering Journal*, 327:573–583, 11 2017.

[186] Y. Brito, M. A. Sabino, G. Ronca, and A. J. Müller. Changes in crystalline morphology, thermal,

and mechanical properties with hydrolytic degradation of immiscible biodegradable PPDX/PCL blends. *Journal of Applied Polymer Science*, 110(6):3848–3858, 12 2008.

[187] Katarzyna Wielemborek-Musial, Katarzyna Szmigielska, Joanna Leszczynska, and Anna Jegier. Blood Pressure Response to Submaximal Exercise Test in Adults. *BioMed Research International*, 2016, 2016.

[188] Boqi Xiao, Wei Wang, Xian Zhang, Gongbo Long, Jintu Fan, Hanxin Chen, and Lin Deng. A novel fractal solution for permeability and Kozeny-Carman constant of fibrous porous media made up of solid particles and porous fibers. *Powder Technology*, 349:92–98, 5 2019.

[189] Triantafyllos Stylianopoulos, Maria Kokonou, Stefanos Michael, Antonia Tryfonos, Claus Rebholz, Andreani D. Odysseos, and Charalambos Doumanidis. Tensile mechanical properties and hydraulic permeabilities of electrospun cellulose acetate fiber meshes. *Journal of Biomedical Materials Research Part B: Applied Biomaterials*, 100B(8):2222–2230, 11 2012.

[190] Looh Tchuin (Simon) Choong, Zafarullah Khan, and Gregory C. Rutledge. Permeability of electrospun fiber mats under hydraulic flow. *Journal of Membrane Science*, 451:111–116, 2014.

[191] Zeman Liu, Yiqi Wang, and Fei Guo. An Investigation into Hydraulic Permeability of Fibrous Membranes with Nonwoven Random and Quasi-Parallel Structures. *Membranes*, 12(1):54, 12 2021.

[192] British Standards. Biological evaluation of medical devices, Part 1: Evaluation and testing. (June 2009), 2010.

[193] British Standards. Biological Evaluation of Medical Devices, Part 5: Tests for in vitro cytotoxicity. 26(7):54, 2009.

[194] British Standards. Biological Evaluation of Medical Devices, Part 12: Sample preparation and reference materials. 2012.

[195] Zofia Modrzejewska and Wojciech Eckstein. Chitosan Hollow Fiber Membranes. *Biopolymers*, 73(1):61–68, 2004.

[196] Yahya Elsayed, Constantina Lekakou, and Paul Tomlins. Modeling, simulations, and optimization of smooth muscle cell tissue engineering for the production of vascular grafts. *Biotechnology and Bioengineering*, 116(6):1509–1522, 2019.

[197] Hua Ye, Diganta B. Das, James T. Triffitt, and Zhanfeng Cui. Modelling nutrient transport in hollow fibre membrane bioreactors for growing three-dimensional bone tissue. *Journal of Membrane Science*, 272(1-2):169–178, 2006.

[198] Natalie C. Pearson, Rebecca J. Shipley, Sarah L. Waters, and James M. Oliver. Multiphase modelling of the influence of fluid flow and chemical concentration on tissue growth in a hollow fibre membrane bioreactor. *Mathematical Medicine and Biology*, 31(4):393–430, 2014.

[199] Natalie C. Pearson, Sarah L. Waters, James M. Oliver, and Rebecca J. Shipley. Multiphase modelling of the effect of fluid shear stress on cell yield and distribution in a hollow fibre membrane bioreactor. *Biomechanics and Modeling in Mechanobiology*, 14(2):387–402, 2015.

[200] COMSOL AB. *CFD Module User's Guide*. 2021.

[201] Matthias Ehrhardt. An Introduction to Fluid-Porous Interface Coupling. (September), 2010.

[202] PromoCell. Endothelial Cell Growth Medium 2, 2020.

[203] ATCC. Formulation for F-12K Medium. Technical report, ATCC, 2020.

[204] L. G. Longsworth. Diffusion Measurements, at 25°, of Aqueous Solutions of Amino Acids, Peptides and Sugars. *Journal of the American Chemical Society*, 75(22):5705–5709, 1953.

[205] *Rotating Electrode Methods and Oxygen Reduction Electrocatalysts*. Elsevier, 2014.

[206] Daniel A. Nunez. Experimental Estimate of the Diffusivity of Vascular Endothelial Growth Factor. page 17, 2006.

[207] Ana C.F. Ribeiro, Victor M.M. Lobo, Derek G. Leaist, Joaquim J.S. Natividade, Luís P. Veríssimo, Marisa C.F. Barros, and Ana M.T.D.P.V. Cabral. Binary diffusion coefficients for aqueous solutions of lactic acid. *Journal of Solution Chemistry*, 34(9):1009–1016, 2005.

[208] Cristian Picioreanu. Modelling biofilms with cellular automata. *Final report to European Environmental Research Organisation*, (January), 1996.

[209] Rolf Sander. NIST Oxygen web book, 2020.

[210] Javaria Farooq, Jae Dong Chung, Muhammad Mushtaq, Dianchen Lu, Muhammad Ramazan, and Umer Farooq. Influence of slip velocity on the flow of viscous fluid through a porous medium in a permeable tube with a variable bulk flow rate. *Results in Physics*, 11:861–868, 12 2018.

[211] K. Dutta, V. Venkata Dasu, B. Mahanty, and A. Anand Prabhu. Substrate inhibition growth kinetics for cutinase producing pseudomonas cepacia using tomato-peel extracted cutin. *Chemical and Biochemical Engineering Quarterly*, 29(3):437–445, 2015.

[212] Haydn Rhys Ingram, Risto John Martin, and James Benjamin Winterburn. Optimized cell growth and poly(3-hydroxybutyrate) synthesis from saponified spent coffee grounds oil. *Applied Microbiology and Biotechnology*, 106(18):6033–6045, 9 2022.

[213] N.S. Panikov. *Microbial Growth Kinetics*. Springer Dordrecht, 1 edition, 1995.

[214] Mpho Muloiwa, Stephen Nyende-Byakika, and Megersa Dinka. Comparison of unstructured kinetic bacterial growth models. *South African Journal of Chemical Engineering*, 33:141–150, 7 2020.

[215] J Monod. The Growth of Bacterial Cultures. *Annual Review of Microbiology*, 3(1):371–394, 10 1949.

[216] J. B. S. Haldane. *Enzymes*. MIT Press, 1965.

[217] J. H. T. Luong. Generalization of monod kinetics for analysis of growth data with substrate inhibition. *Biotechnology and Bioengineering*, 29(2):242–248, 2 1987.

[218] Keehyun Han and Octave Levenspiel. Extended monod kinetics for substrate, product, and cell inhibition. *Biotechnology and Bioengineering*, 32(4):430–447, 8 1988.

[219] Anton Moser. *Bioprocess Technology*. Springer New York, New York, NY, 1988.

[220] Toshimasa Yano, Tadaatsu Nakahara, Shigeo Kamiyama, and Koichi Yamada. Kinetic Studies on Microbial Activities in Concentrated Solutions. Part. I. *Agricultural and Biological Chemistry*, 30(1):42–48, 1966.

[221] John Leyden. Webb. *Enzyme and metabolic inhibitors*. Academic Press, New York, 1963.

[222] Victor H. Edwards. The influence of high substrate concentrations on microbial kinetics. *Biotechnology and Bioengineering*, 12(5):679–712, 9 1970.

[223] S. Aiba, M. Shoda, and M. Nagatani. Kinetics of product inhibition in alcohol fermentation. *Biotechnology and Bioengineering*, 10(6):845–864, 11 1968.

[224] John F. Andrews. A mathematical model for the continuous culture of microorganisms utilizing inhibitory substrates. *Biotechnology and Bioengineering*, 10(6):707–723, 11 1968.

[225] Xuri Li, Xiaodong Sun, and Peter Carmeliet. Hallmarks of Endothelial Cell Metabolism in Health and Disease. *Cell Metabolism*, 30(3):414–433, 2019.

[226] Julia V. Busik, Susanne Mohr, and Maria B. Grant. Hyperglycemia-Induced reactive oxygen species toxicity to endothelial cells is dependent on paracrine mediators. *Diabetes*, 57(7):1952–1965, 2008.

[227] Mayumi Abe, Junko Ono, Yasufumi Sato, Toshimitsu Okeda, and Ryosaburo Takaki. Effects of glucose and insulin on cultured human microvascular endothelial cells. *Diabetes Research and Clinical Practice*, 9(3):287–295, 1990.

[228] Francesc Viñals, Aachim Gross, Xavier Testar, Manuel Palacín, Peter Rösen, and Antonio Zorzano. High glucose concentrations inhibit glucose phosphorylation, but not glucose transport, in human endothelial cells. *Biochimica et Biophysica Acta - Molecular Cell Research*, 1450(2):119–129, 1999.

[229] L. Bergandi, F. Silvagno, I. Russo, C. Riganti, G. Anfossi, E. Aldieri, D. Ghigo, M. Trovati, and Amalia Bosia. Insulin Stimulates Glucose Transport Via Nitric Oxide/Cyclic GMP Pathway in Human Vascular Smooth Muscle Cells. *Arteriosclerosis, Thrombosis, and Vascular Biology*, 23(12):2215–2221, 2003.

[230] Junko N. Hayashi, Hideki Ito, Toshie Kanayasu, Noriko Asuwa, Ikuo Morita, Toshiharu Ishii, and Sci itsu Murota. Effects of glucose on migration, proliferation and tube formation by vascular endothelial cells. *Virchows Archiv B Cell Pathology Including Molecular Pathology*, 60(1):245–252, 1991.

[231] Guoyao Wu, Tony E. Haynes, Hui Li, and Cynthia J. Meininger. Glutamine metabolism in endothelial cells: Ornithine synthesis from glutamine via pyrroline-5-carboxylate synthase. *Comparative Biochemistry and Physiology - A Molecular and Integrative Physiology*, 126(1):115–123, 2000.

[232] Kelly J. Peyton, Xiao ming Liu, Yajie Yu, Benjamin Yates, Ghazaleh Behnammanesh, and

William Durante. Glutaminase-1 stimulates the proliferation, migration, and survival of human endothelial cells. *Biochemical Pharmacology*, 156(March):204–214, 2018.

[233] D. B. Rubin, E. A. Drab, and K. D. Bauer. Endothelial cell subpopulations in vitro: cell volume, cell cycle, and radiosensitivity. *Journal of Applied Physiology*, 67(4):1585–1590, 10 1989.

[234] Edhi S. Gunawan, Shingo Tsuji, Masahiko Tsujii, Wei-Hao Sun, Zulfikar Ali, Yutaka Sasaki, Masatsugu Hori, and Sunao Kawano. Cetraxate, an antiulcer agent, abolishes ammonia-induced suppression of angiogenesis. *Gastroenterology*, 118(4):A1242, 2000.

[235] Martin L. Decaris, Chang I. Lee, Mervin C. Yoder, Alice F. Tarantal, and J. Kent Leach. Influence of the oxygen microenvironment on the proangiogenic potential of human endothelial colony forming cells. *Angiogenesis*, 12(4):303–311, 2009.

[236] Ilias Attaye, Yvo M. Smulders, Monique C. de Waard, Heleen M. Oudemans-van Straaten, Bob Smit, Michiel H. Van Wijhe, Rene J. Musters, Pieter Koolwijk, and Angelique M. E. Spoelstra–de Man. The effects of hyperoxia on microvascular endothelial cell proliferation and production of vaso-active substances. *Intensive Care Medicine Experimental*, 5(1):1–17, 2017.

[237] S. Mertens, T. Noll, R. Spahr, A. Krutzfeldt, and H. M. Piper. Energetic response of coronary endothelial cells to hypoxia. *American Journal of Physiology - Heart and Circulatory Physiology*, 258(3 27-3), 1990.

[238] Yuan Zhang, Ting Wang, Ke Yang, Ji Xu, Lijie Ren, Weiping Li, and Wenlan Liu. Cerebral microvascular endothelial cell apoptosis after ischemia: Role of enolase-phosphatase 1 activation and aci-reductone dioxygenase 1 translocation. *Frontiers in Molecular Neuroscience*, 9(AUG):1–14, 2016.

[239] Ye Ji Jeong, Myung Gu Jung, Yeonghoon Son, Jun Ho Jang, Yoon Jin Lee, Sung Ho Kim, Young Gyo Ko, Yun Sil Lee, and Hae June Lee. Coniferyl aldehyde attenuates radiation enteropa-

thy by inhibiting cell death and promoting endothelial cell function. *PLoS ONE*, 10(6):1–16, 2015.

[240] J. Q. Yu, X. F. Liu, L. K. Chin, A. Q. Liu, and K. Q. Luo. Study of endothelial cell apoptosis using fluorescence resonance energy transfer (FRET) biosensor cell line with hemodynamic microfluidic chip system. *Lab on a Chip*, 13(14):2693–2700, 2013.

[241] Barbara J. Ballermann and Mark J. Ott. Adhesion and Differentiation of Endothelial Cells by Exposure to Chronic Shear Stress: A Vascular Graft Model. *Blood Purification*, 13(3-4):125–134, 1995.

[242] E M Redmond, P A Cahill, and J V Sitzmann. Perfused transcapillary smooth muscle and endothelial cell co-culture–a novel in vitro model. *In vitro cellular & developmental biology. Animal*, 31(8):601–9, 9 1995.

[243] Shu Chien. Mechanotransduction and endothelial cell homeostasis: The wisdom of the cell. *American Journal of Physiology - Heart and Circulatory Physiology*, 292(3), 2007.

[244] G. Bradski. The OpenCV Library. *Dr. Dobb's Journal of Software Tools*, 2000.

[245] Anant Ram, Sunita Jalal, Anand S. Jalal, and Manoj Kumar. A Density Based Algorithm for Discovering Density Varied Clusters in Large Spatial Databases. *International Journal of Computer Applications*, 3(6):1–4, 6 2010.

[246] Erich Schubert, Jörg Sander, Martin Ester, Hans Peter Kriegel, and Xiaowei Xu. DBSCAN Revisited, Revisited. *ACM Transactions on Database Systems*, 42(3):1–21, 8 2017.

[247] ABBOTT LABORATORIES. Architect Glucose - 3L82-21. pages 1–8, 2017.

[248] ABBOTT LABORATORIES. Architect Lactate - 9P18-21. (April):1–6, 2018.

[249] ATCC. HUVEC/TERT 2 - CRL-4053, 2023.

[250] Risto Martin, Pierre-Alexis Mouthuy, Cathy Ye, and Sarah Waters. Endothelial cell growth in vascular mimetic electrospun hollow fibre membranes: A mathematical modelling prospective. 2022.

[251] M. Artwohl, B. Brunmair, C. Fürnsinn, T. Hölzenbein, G. Rainer, A. Freudenthaler, E. M. Porod, N. Huttary, and S. M. Baumgartner-Parzer. Insulin does not regulate glucose transport and metabolism in human endothelium. *European Journal of Clinical Investigation*, 37(8):643–650, 2007.

[252] Christopher D. Foucher and Robert E. Tubben. *Lactic Acidosis*. 2022.

[253] Barrie Phypers and JM Tom Pierce. Lactate physiology in health and disease. *Continuing Education in Anaesthesia Critical Care & Pain*, 6(3):128–132, 6 2006.

[254] Gregory S Ducker and Joshua D Rabinowitz. One-Carbon Metabolism in Health and Disease. *Cell metabolism*, 25(1):27–42, 2017.

[255] NASA. NASA Vascular Tissue Challenge, 2022.